Turbulence modelling of fluid-particle interaction

Submitted by

Matthew James Riella

to the University of Exeter as a thesis for the degree of Doctor of Philosophy in Engineering, May 2019.

I certify that all material in this thesis which is not my own work has been identified and that no material has previously been submitted and approved for the award of a degree by this or any other University.

Matthew James Riella

This page is intentionally left blank.

Abstract

The accurate prediction of turbulent fluid-particle behaviour has been a complex and elusive topic for researchers for several decades. The momentum and energy exchange between the fluid and particles, across the whole spectrum of spatial and temporal scales, leads to an abundance of rich physical behaviour which has ensured that significant advances in the area have proven challenging. This contribution seeks to shine a small ray of light on a vast and murky abyss in which the true nature of turbulent fluid-particle flows may allude us for some time still.

This thesis presents a multi-scale continuum approach to modelling fluid-particle flows i.e. Eulerian-Eulerian (E-E). A fully-coupled Reynolds-Averaged Two-Fluid Model (RA-TFM) for turbulent fluid-particle flow, with particular emphasis on the near-wall region, is developed. The coupling is provided both mathematically i.e. the fluid-particle momentum and energy coupling across all spatial and temporal scales and numerically i.e. the RA-TFM governing equations are solved within a block-coupled matrix.

The RA-TFM is derived, applied and validated against a plethora of benchmark experimental and Direct Numerical Simulation data in which a wide range of physical processes are present. Finally, the RA-TFM's implementation within the open-source CFD toolbox OpenFOAM is detailed.

This page is intentionally left blank.

Dedicated to the Underclass of Cardiff, Wales.

University of Exeter, September 2016 - May 2019.

This page is intentionally left blank.

Preface

The main contributions of the thesis make up four papers and correspond to Chapters 5 - 8, respectively:

Paper 1 Riella, M., Kahraman, R., Tabor, G. (2018).
'Reynolds-Averaged Two-Fluid Model prediction of moderately dilute fluid-particle flow over a backward-facing step'
Int. J. Multiphase Flow, 106:95-108.

Paper 2 Riella, M., Kahraman, R., Tabor, G. (2019).
'Near-wall modelling in Eulerian-Eulerian Simulations'
Computers and Fluids. 190:206-216.

Paper 3 Riella, M., Kahraman, R., Tabor, G. (2019).
'Inhomogeneity and anisotropy in Eulerian-Eulerian near-wall modelling'
Int. J. Multiphase Flow, 114:9-18.

Paper 4 Riella, M., Kahraman, R., Tabor, G. (2019).
'Fully-coupled pressure-based two-fluid solver for the solution of turbulent fluid-particle systems'
Computer and Fluids. (Under review).

This page is intentionally left blank.

Examined by *Prof. Hrvoje Jasak & Dr. David Moxey.*
- 20/06/19.

This page is intentionally left blank.

Acknowledgements

This work has been carried out thanks to a PhD Studentship awarded by the College of Engineering, Mathematics and Physical Sciences and is gratefully acknowledged. I would like to thank Prof. Tabor for his continued encouragement throughout my PhD, in particular giving me the freedom to pursue my own thoughts and ideas.

I'd like to especially thank Dr. Kahraman who has provided invaluable guidance throughout this PhD and through countless discussions (mainly over coffee) has greatly influenced this thesis.

Finally, I would like to thank my family and a small handful of friends. Without the love of the former and the affection of the latter this thesis would not exist.

This page is intentionally left blank.

Nomenclature

Greek letters

α_i	volume fraction, [−]
$\alpha_{p,max}$	maximum particle volume fraction, [−]
β	momentum exchange coefficient, [kgm^{-3}s^{-1}]
ϵ_i	turbulent kinetic energy dissipation, [m^{2}s^{-3}]
ϵ_{ij}	fluid-particle dissipation velocity covariance, [m^{2}s^{-3}]
η	Kolmogorov length scale, [m]
Γ_i	generic diffusive term w.r.t each phase, [m^{2}s^{-1}]
κ_p	particle fluctuation energy, [m^{2}s^{-2}]
$\kappa_{\Theta s}$	diffusion coefficient for granular energy, [kgm^{-1}s^{-1}]
μ_i	shear viscosity, [kgm^{-1}s^{-1}]
$\mu_{i,t}$	turbulent shear viscosity, [kgm^{-1}s^{-1}]
ν_i	kinematic viscosity, [m^{2}s^{-1}]
$\nu_{i,t}$	turbulent kinematic viscosity, [m^{2}s^{-1}]

$\overline{\boldsymbol{\sigma}}_f$ fluid phase stress tensor,[kgm^{-1}s^{-2}]

$\overline{\boldsymbol{\sigma}}_p$ particle phase stress tensor, [kgm^{-1}s^{-2}]

ϕ specularity coefficient, [−]

ϕ_i generic flux term w.r.t each phase, [ms^{-3}]

Π_{ij} mixed turbulent energy production w.r.t each phase, [m^2]s^{-3}]

Π_i turbulent energy production w.r.t each phase, [m^2]s^{-3}]

ρ_i density, [kgm^{-3}]

σ_{pk} turbulent Prandtl number, [-]

τ_f characteristic flow time, [s]

τ_p particle response time, [s]

τ_η turnover time of Kolmogorov eddy, [s]

Θ granular temperature, [m^{2}s^{-2}]

Θ_f pseudo-turbulent kinetic energy, [m^{2}s^{-2}]

u_η velocity of Kolmogorov eddy, [ms^{-1}]

Roman letters

$(\cdot)_f$ cell to face interpolation

$\mathbf{A}_i$ main diagonal of coefficients obtained from the discretisation procedure, [s^{-1}]

$\mathbf{H}_i$ off-diagonal of coefficients obtained from the discretisation procedure, [ms^{-2}]

$\mathbf{n}$ unit vector normal to the wall, [−]

$\mathbf{S}_f$ surface area vector

$\mathbf{u}_f'''$ fluid velocity fluctuation w.r.t PA velocity, [ms^{-1}]

$\mathbf{u}_{p,i}''^2$ particle Reynolds stress component in direction i, [ms^{-1}]

$\mathbf{u}_p''$ particle velocity fluctuation w.r.t PA velocity, [ms^{-1}]

$\mathbf{u}_i$ velocity, [ms^{-1}]

$\mathbf{u}_{p,w}$ particle slip velocity parallel to the wall, [ms^{-1}]

$\mathbf{u}_r$ relative velocity between phases, [ms^{-1}]

$\mathbf{u}_w$ wall velocity, [ms^{-1}]

$\mathbf{v}$ mesoscale instantaneous velocity, [ms^{-1}]

$\mathbf{x}$ location of control volume's arbitrary cell centre

$\mathbf{x}_p$ location of control volume's cell centre

$\mathcal{A}$ Fluid momentum coupling, [$\mathrm{kgm}^{-3}\mathrm{s}^{-1}$]

d_p particle diameter, [m]

Re_p particle Reynolds number, [−]

Sc_{fp} dispersion correction term, [−]

$\overline{\mathbf{P}}_i$ pressure stress tensor w.r.t each phase, [Pa]

$\overline{v_{ij}^2}$ fluid-particle wall normal velocity covariance, [$\mathrm{m}^2\mathrm{s}^{-2}$]

$\overline{v_i^2}$ wall normal component of the Reynolds-stress tensor w.r.t each phase, [$\mathrm{m}^2\mathrm{s}^{-2}$]

$\mathbf{q}$ total granular energy flux, [$\mathrm{m}^3\mathrm{s}^{-3}$]

C_D drag coefficient, [−]

D_p pressure diffusivity matrix, [$\mathrm{kg}^{-1}\mathrm{sm}^3$]

e total granular energy, [$\mathrm{m}^2\mathrm{s}^{-2}$]

f elliptic relaxation function, [s^{-1}]

$f(\mathbf{x}, \mathbf{v}, t)$ particle velocity distribution function, [−]

f_x interpolation factor

g_0 radial distribution coefficient, [−]

k_i turbulent kinetic energy, [$\mathrm{m}^2\mathrm{s}^{-2}$]

k_{ij} fluid-particle turbulent kinetic energy velocity covariance, [m^2s^{-2}]

p_i pressure w.r.t each phase, [Pa]

St Stokes number, [−]

t time, [s]

V_p Control volume of interest

$d_{,i}$ numerical coefficient ratio

L_p particle turbulent length scale, [m]

T_p particle turbulent time scale, [s]

D pipe diameter, [m]

g gravity, [ms^{-2}]

Kn Knudsen number, [−]

L fluid turbulent length scale, [m]

L pipe length, [m]

N control volume's neighbouring cell centre

P control volume's cell centre

P phases

T fluid turbulent time scale, [s]

Subscripts

f face value

f fluid

i cell i

j cell j

k general index denoting a phase

N	control volume's neighbouring cell centre
P	control volume's cell centre
p	particle
r	relative
T	total
x	x direction
y	y direction
z	z direction
i	general index

Superscripts

$*$	predicted
$\perp$	surface normal gradient
ϕ	generic variable
$k-1$	values at previous iteration
k	values at current iteration
$t-1$	old time step
t	current time step

Acronyms

BBO	Basset-Boussinesq-Ossen
CFD	Computational Fluid Dynamics
CFL	Courant-Friedrichs-Lewy number
DNS	Direct Numerical Simulation
E-E	Eulerian-Eulerian

PA phase average

PDE partial differential equation

RA Reynolds average

RA-TFM Reynolds-Averaged Two-Fluid Model

RANS Reynolds-Averaged Navier-Stokes

RHS right hand side

TFM Two-Fluid Model

VFM Finite Volume Method

Special notation

$\langle \cdot \rangle$ Reynolds averaging operator

$\langle \cdot \rangle_i$ phase averaging operator w.r.t phase i

Contents

List of Figures

This page is intentionally left blank.

1 Introduction

1.1 Overview

In this chapter the theoretical background of turbulent fluid-particle flow is presented. The equation for singular particle motion is given in which the governing physical mechanisms, that are present in this study, are described. Within this picture, the numerical prediction of the turbulent fluid-particle flows is presented with a particular emphasis on Eulerian-Eulerian (E-E) modelling. A literature review detailing several shortcomings within the current E-E modelling approaches of turbulent fluid-particle flows is then provided.

This chapter comprises:

- Background and theory of turbulent motion;
- Characterisation of fluid-particle interaction and motion;
- Literature review of Eulerian-Eulerian modelling for fluid-particle turbulence and near-wall interaction;
- Literature review of Eulerian-Eulerian numerical solution algorithms.

1.2 Background

A whole range of turbulent flows can be seen in everyday life. From running a bath, blending food, smoke from a cigarette or visible vortices in the sky from a passing plane. It is evident from this eclectic mix that the chaotic and random behaviour gives rise to a wide spectrum of spatial and temporal scales. This broad range of flows can be described by a set of partial differential equations (PDEs) called the Navier-Stokes equations [142]. The equations are an extension of the Euler equations which are inviscid, by including viscosity. Under limiting 2D cases, solutions to the equations were found by George Stokes. Owing to the Navier-Stokes' inherent non-linear nature a general solution to the complete Navier-Stokes does not exist for turbulent flows [1] i.e. high Reynolds number. Thus, numerical approximation is necessary.

If one considers the natural and engineering occurrences of turbulent flows, one is struck by the abundance of fluid-particle flows. There are numerous examples of this e.g. dust clouds on the planet Mars, sediment transport, sand storms, fluidised bed combustion processes, volcanic ash, dispersion of pollutants and pneumatic transport. If one thinks more abstractly we can even consider the transportation of blood cells in ones own blood stream. In fact it is this analogy between the micro- and the macro-scales that will provide some crucial insights into the modelling of fluid-particle flows. A well anchored example of this analog between scales is the Boussinesq eddy-viscosity assumption [19]. The assumption employs a result from kinetic theory i.e. molecular motion can be described by a molecular stress (defined by mean flow gradients), and applies it at the turbulent macroscale. This results in a closure for turbulence induced stress.

In single-phase flow, the flow is characterised by the Reynolds number [142] and the smallest turbulent scales can be described with the Kolmogorov time and length scales. This framework, used for understanding and describing turbulent single-phase flow is used as a basis for turbulent fluid-particle flow. The complexity is

increased with the addition of particles. The characteristics of the turbulent fluid-particle flow now become dependent on the particles diameter, density and volume fraction.

Differing particle diameters and densities influence the particle response times, which dictates how quickly the particles react to the surrounding fluid. Variations in the particle volume fraction results in drastically different behaviour in a turbulent flow, comprising of: one-way, two-way and four-way coupling. One-way coupling is when the particles behave as flow tracers and have no influence on the carrier flow. Two-way coupling is when there is a momentum exchange between the fluid and the particles. Lastly, four-way coupling is when the volume fraction is so high that the particle interactions begin to take place influence the flow. The aforementioned characteristics of turbulent fluid-particle flow are not mutually exclusive and as we will see later can influence one another.

The prediction of turbulent fluid-particle interaction is of significant interest for a variety of industrial flows e.g. spray drying that is used for foods, detergents and pharmaceuticals [123] a process in which liquid material is atomised in a chamber subject to hot gases and dried into a powder. A major aspect of this is predicting the correct drying of the powder to ensure impingement and accumulation is avoided. Another example is the removal of particulates from industrial effluents [98] in which several devises are used to separate particles from gases. Finally, pneumatic transport is widely used to transport cement, metal powders, grains, ores, etc. [102]. It is clear that there is considerable motivation for developing a numerical framework for the correct prediction of fluid-particle behaviour.

The governing equations of the fluid and particle behaviour are known (presented in Chapter 2) and these equations can be resolved across all scales. From this, the particle paths can be tracked and their interaction with the fluid ascertained (Eulerian-Lagrangian). As with Direct Numerical Simulation (DNS) in single-phase flow, the Reynolds number provides a constraint on the viability of its solution. This level of description in two-phase flow, resolving both the smallest eddies and

the boundary layer around a particle, for high Reynolds number flow is computationally very expensive. Even if this level of description was sought it is largely redundant when applied to engineering applications as only a handful of flow characteristics are of interest.

For solving challenging industrial problems the Reynolds-Averaged Navier-Stokes (RANS) equations are often employed. The effect of turbulence fluctuations are modelled instead of being explicitly solved for, which greatly reduces the computational cost. This methodology can also be applied to multiphase flows. Typically, two Eulerian fields are assumed in which both the fluid- and particle-phase are treated as inter-penetrating continua i.e. the Eulerian-Eulerian (E-E) approach [7]. This approach gives rise to increased versatility and flexibility akin to the RANS vs DNS pay-off in single-phase flow. Unlike in single-phase flows this approach leads to complicated inter-phase energy exchange terms, multi-scale closure of the particle stress and a more complicated energy cascade process that has proved challenging to researchers. It is this aspect in particular that concerns this thesis. Throughout we put a particular emphasis on how the fundamental physical processes can be modelled within the E-E approach.

1.2.1 Fundamentals of turbulence

Turbulent motion is extremely common in nature and engineering applications. Its exact nature has eluded researchers, scientists and engineers alike for centuries [68]. Its intrinsically chaotic and random nature has made its successful prediction elusive but not without progress. One prevailing (and contested [95, 96]) picture of turbulence is the energy cascade of Richardson [155] with the *Kolmogorov hypotheses*.

The energy cascade was first proposed by Richardson [155] and marks an important step forward in our understanding of turbulent flows. The underpinning philosophy is that the turbulent kinetic energy is produced by the largest scales of motion. Beyond this, the turbulent kinetic energy is transmitted via decreasing eddy size

through inviscid processes until the energy is finally dissipated by viscous forces i.e. heat. Essentially, the large eddies continue to break-up into smaller and smaller eddies thus creating a cascading effect of energy. The large eddies are assumed to be inherently anisotropic and unstable, this continues until they reach stability which marks the end of the cascade process. Once a sufficiently small scale is reached the molecular viscosity can dominate, which finally dissipates the turbulent kinetic energy.

Kolmogorov added to and formalised this theory of turbulence through his hypotheses and in particular identified the smallest scales of turbulence [103, 142]. The formalising was facilitated by the introduction of and relationship between the velocity, u the eddy timescale, τ eddy size, η and their characteristic length, l. This comprises three hypotheses [103]:

Kolmogorov's hypothesis of local isotropy: *At sufficiently high Reynolds number, the small-scale turbulent motions ($l < l_0$) are statistically isotropic.*

Kolmogorov's first similarity hypothesis: *In every turbulent flow at sufficiently high Reynolds number, the statistics of the small-scale motions ($l < l_{EI}$) have a universal form that is uniquely determined by ν and ε.*

Kolmogorov's second similarity hypothesis: *In every turbulent flow at sufficiently high Reynolds number, the statistics of the motions of scale l in the range $l_0 \geq l \geq \eta$ have a universal form that is uniquely determined by ε and independent of ν.*

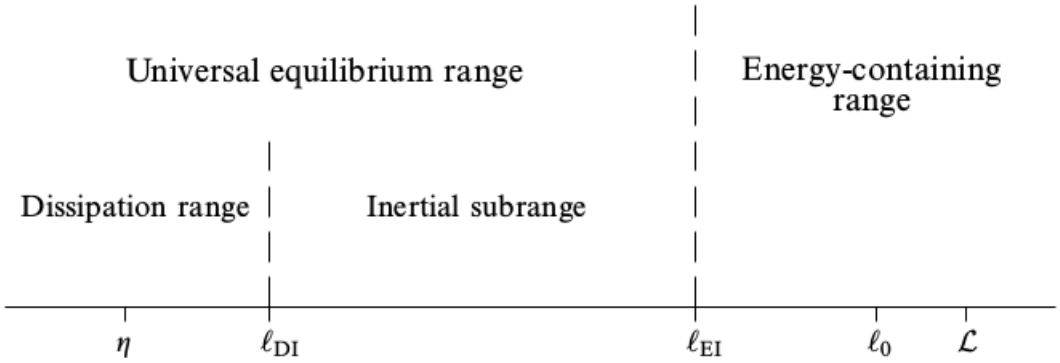

Figure 1.1: Eddy sizes l at very high Reynolds number, showing a spectrum of length scales and ranges [Adapted from Pope [142]].

The first hypothesis states that as the large, anisotropic eddies dissipate energy and decrease in size until they lose their directional dependency and reach an equilibrium amongst the velocity components and become isotropic. This theory is universal and applies to all small scale motion. The second hypothesis explains by which mechanisms this dissipation is occurring. It states that at the dissipative range to the inertial sub-range the turbulent kinetic energy dissipation is in balance with the energy transfer rate. Finally, the third states that the turbulent kinetic energy dissipation is in balance with the production and determines the rate of dissipative transfer i.e. how quickly the large eddies will shorten in length.

The Kolmogorov scales are determined by two prevailing parameters, the kinematic viscosity (ν) and the turbulent kinetic energy dissipation (ε) [142]:

$$\eta = (\nu^3/\varepsilon)^{1/4}, \tag{1.1}$$

where η is the scale of the smallest dissipative eddies. The velocity of the Kolmogorov eddies is

$$u_\eta = (\varepsilon\nu)^{1/4}, \tag{1.2}$$

with the turnover time over the smallest eddies given as

$$\tau_\eta = (\nu/\varepsilon)^{1/2}. \tag{1.3}$$

A Reynolds number based on the Kolmogorov scales can be written as, $\eta u_\eta/\nu = 1$, which corroborates the idea that as the cascade proceeds to smaller and smaller scales the Reynolds number is small enough for the dissipation to be effective. Finally, the turbulent kinetic energy dissipation is

$$\varepsilon = \nu(u_\eta/\eta)^2 = \nu/\tau_\eta^2. \tag{1.4}$$

The separation of the scales across the range of eddy sizes can be seen in Fig. 1.1. At the energy containing range the transfer of energy, if the eddy sizes are comparable, can be determined through the turbulent kinetic energy dissipation rewritten as:

$$\varepsilon = u(l)^2/\tau(l). \tag{1.5}$$

Hence we have a purely dissipative process from the large scale production of turbulence to the small scale dissipation of turbulence. This acts across the whole range of eddy sizes and is *usually* in balance, meaning that production and dissipation are approximately in equilibrium.

1.2.2 Classification of turbulent fluid-particle flow

The classification of turbulent fluid-particle flows can be complex, largely due to the abundance of differing physical interactions occurring dependent on the various properties of the turbulent flow. When considering the classification of turbulent fluid-particle flow one must build on the concepts grounded in single-phase flows. As mentioned previously, single-phase flows can be characterised by the Reynolds number:

$$Re = \frac{ul}{\nu}. \tag{1.6}$$

In addition to this, the characterisation of the particles and their interaction with the fluid must be ascertained. Elghobashi [59] provides a classification of the fluid-particle interactions based on particle volume fraction, α_p and the Stokes number,

St. The Stokes number is the ratio between the particle response time, τ_p and the characteristic flow time, τ_f. This number along with the particle Reynolds number (defined later) are two of the most important characteristics of fluid-particle flow. The Stokes number reads:

$$St = \frac{\tau_p}{\tau_f}, \tag{1.7}$$

the particle response time, τ_p is a measure of the how quickly the particle can respond to the surrounding fluid velocity. This quantity is essentially a drag time scale - the formulation of which will be presented later. The correct modelling of this term is essential for predicting the correct Stokes dependant behaviour as seen in Fig. 1.2. This has important consequences as the fluid- and particle-phase turbulent kinetic energy can be very similar for low Stokes numbers and vastly different for high Stokes number. Some physical intuition can be built by examining Fig. 1.2 in which particles in a plane wake are shown. The particles are discreetly modelled in a numerical simulation and are coupled to the flow through their inter-phase drag. It is evident across all four plots that quite clear and distinct differing behaviour can be seen.

For, $St \ll 1$ the particles behave as passive scalars and closely follow the fluid wake behaviour. $St = 1$ is a somewhat special case as particles fall in-between the eddies and the surrounding fluid showing global focusing. This term is used to describe particles that are forced into thin regions of the flow characterised here by the boundaries of the vortex structures. As the Stokes number is increased it becomes clear that it takes longer and longer for the particles to react to the surrounding fluid. Looking at, $St = 100$ it can be seen that the particles are convected some way downstream (x/s $\approx$ 9) before the momentum of the particles is changed by the carrier flow.

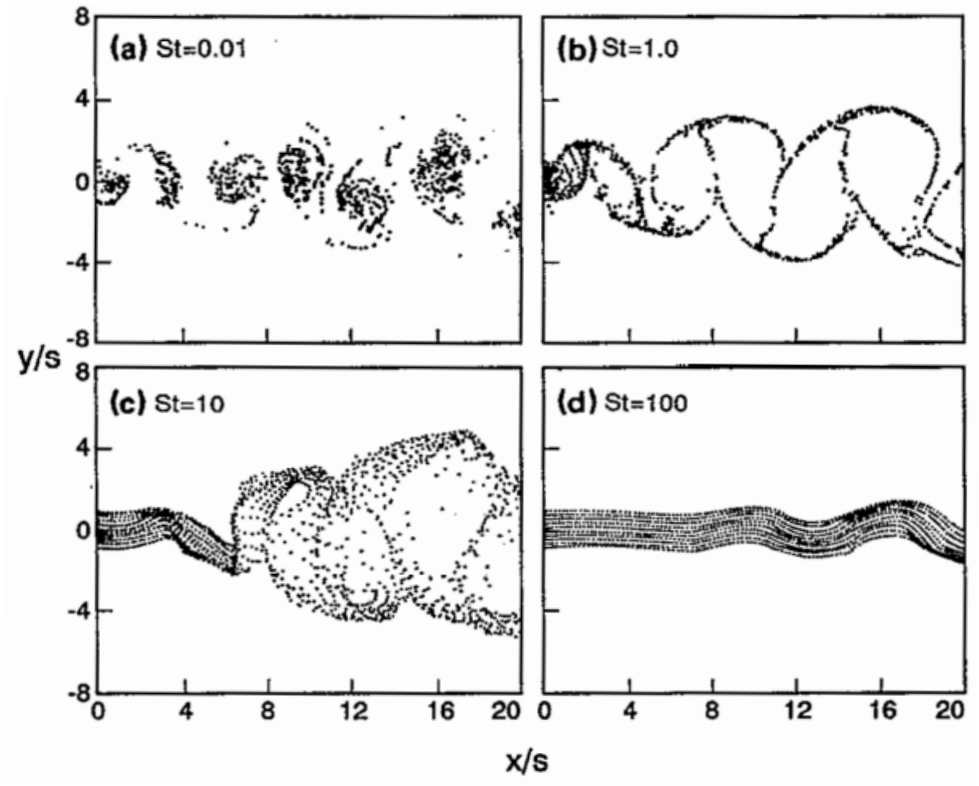

Figure 1.2: Instantaneous particle dispersion patterns with varying Stokes number [Adapted from Tang et al. [187]]

Plotting the Stokes number vs particle volume fraction, α_p, Elghobashi [59] produced a schematic detailing several distinct regions that make up turbulent fluid-particle interaction, this can be seen in Fig. 1.3. The characteristic time scale, τ_f is given here as the eddy turnover time. For small particle volume fractions, $\alpha_p \ll 10^{-6}$, the fluid-phase is unaffected by the presence of the particles i.e. the so-called one-way coupled regime where by the particles can be treated as passive scalars. In the regime, $10^{-6} < \alpha_p < 10^{-3}$ momentum transfer between the particles and the fluid-phase becomes relevant and can either enhance turbulence or attenuate it. This is the so-called two-way coupling regime and is very complex with the cause of turbulence modulation having a range of contributing factors: fluid-particle, particle-particle or particle-wall interaction. Moving to denser regimes, $\alpha_p > 10^{-3}$ particle-particle collisions begin to affect the flow. This is the so-called four-way coupling regime and can have significant effects on the carrier flow.

The challenges of modelling this behaviour, especially within wall-bounded flows, will be explored in §1.5 & §1.6.

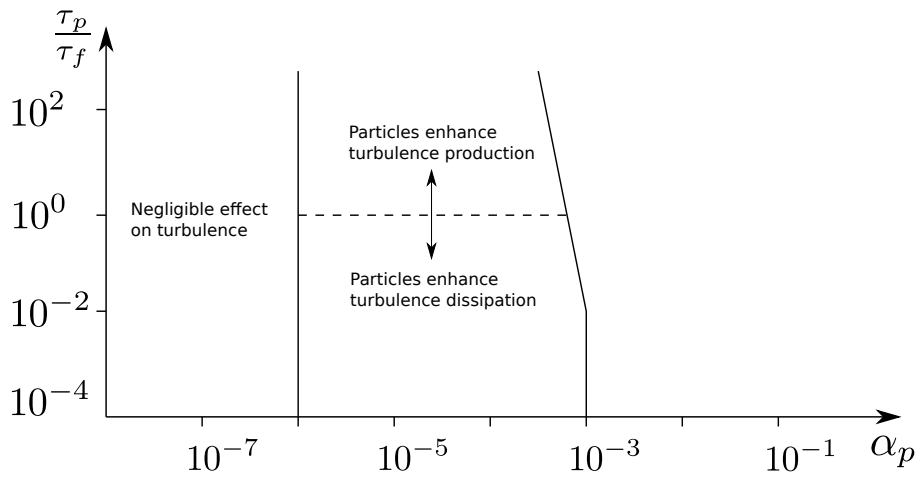

Figure 1.3: Classification of flow regimes given by Elghobashi [59]

When examining Fig. 1.3 one must be careful to not think entirely in terms of statics (as schematics often do) but in terms of dynamics. As particles are being carried by a turbulent flow they can be constantly fluctuating into and out of these classifications. There can be clustering of particles affecting their effective diameter and consequently their particle response time. Additionally, there can be near-wall effects in wall-bounded flows in which the particle response time increases dramatically resulting in an extremely high Stokes number and particle-wall collisions. Moreover, the classifications may not be so clear cut. For example, Wu et al. [214] found experimentally for particle volume fractions as low as 6 x 10^{-7} two-way coupling effects were present. Despite this, within a Reynolds-Averaged framework the schematic provides an adequate basis for understanding the expected fluid-particle interaction.

1.2.3 Singular particle motion

The Basset-Boussinesq-Ossen (BBO) equation [170] describes the motion of a single particle subject to an unsteady flow at $Re_p < 1$. The equation is essentially

Newton's second law for a single particle with explicit forces on a particle that govern its motion. Introducing the BBO for single particle motion enables the dominant forces determining its motion to be ascertained. The BBO equation is presented to elucidate some of the critical physical mechanisms investigated in this work and is not explicitly solved for. First, the particle Reynolds number reads:

$$Re_p = \frac{\rho_f d_p |\mathbf{u}_p - \mathbf{u}_f|}{\mu_f}, \tag{1.8}$$

where d_p is the particle diameter, $\mathbf{u}_i$ is the velocity of the each respective phase, ρ_f is the density of the fluid and μ_f is the dynamic viscosity of the fluid. The BBO equation reads:

$$\begin{aligned} \frac{\pi}{6}\rho_p d_p^3 \frac{d\mathbf{u}_p}{dt} = & \underbrace{\frac{\pi}{6} d_p^3 \nabla p}_{\text{Pressure gradient}} - \underbrace{3\pi\mu_f d_p(\mathbf{u}_f - \mathbf{u}_p)}_{\text{Stokes drag}} - \underbrace{\frac{\pi}{12}\rho_f d_p^3 \frac{d}{dt}(\mathbf{u}_f - \mathbf{u}_p)}_{\text{Added mass}} \\ & + \underbrace{\frac{3}{2} d_p^2 \sqrt{\pi \rho_f \mu_f} \int_{-t_0}^{t} \frac{1}{\sqrt{t-\tau}} \frac{d}{d\tau}(\mathbf{u}_f - \mathbf{u}_p) d\tau}_{\text{Basset force}} + \underbrace{F_g}_{\text{Buoyancy and/or gravity}} . \end{aligned} \tag{1.9}$$

The first term on the right-hand-side (RHS) is the force exerted on the particle due to the pressure gradient. The second term is the Stokes drag and dictates the momentum exchange between phases. The third term represents the acceleration or deceleration of the surrounding fluid in which the particle displaces as it accelerates or decelerates. The fourth term represents the Basset force [11] which accounts for the lagging boundary layer development due to a change in relative velocity, a term that is often relevant when the particle is being accelerated at a high rate. The final term represents buoyancy and a body force of gravity. The former is mainly prevalent in low-density ratios (one may think of a marble in oil) and the latter is relevant for capturing the correct physical behaviour in the majority of fluid-particle flows.

The relative velocity between the particle and the surrounding fluid-phase results in a pressure gradient and viscous drag, the so-called Stokes drag. This force represents the fluids effect through momentum on the particle's motion. As the particle Reynolds number increases beyond 1, the Stokes drag approximation is

no longer valid. Thus, just considering the drag force in the BBO equation and rewriting the equation considering a generic form of the drag around a spherical particle [170] as:

$$\mathbf{F}_D = \frac{\pi}{6}\rho_p d_p^3 \frac{d\mathbf{u}_p}{dt} = \frac{1}{2} C_d \frac{\pi d_p^2}{4} \rho_f |\mathbf{u}_f - \mathbf{u}_p|(\mathbf{u}_f - \mathbf{u}_p). \tag{1.10}$$

Defining the particle Reynolds number and dividing through by the particle mass gives:

$$\frac{d\mathbf{u}_p}{dt} = \frac{18\mu_f}{d_p^2 \rho_p} \frac{C_d Re_p}{24} (\mathbf{u}_f - \mathbf{u}_p), \tag{1.11}$$

where in the Stokes flow limit the factor $C_D Re_p/24$ approaches unity and the remaining terms define a particle response time as:

$$\tau_p = \frac{d_p^2 \rho_p}{18\mu_f}, \tag{1.12}$$

as it can be seen the particle response time is defined by the material properties of each phase. Therefore, we can now write:

$$\frac{d\mathbf{u}_p}{dt} = \frac{1}{\tau_p}(\mathbf{u}_f - \mathbf{u}_p). \tag{1.13}$$

For larger particle Reynolds number, the factor C_D is no longer at unity and needs to be adjusted. Schiller and Naumann [167] introduced a multiplicative drag factor, absorbing the Re_p into the formulation, which is valid up to particle Reynolds numbers of 1000, and is written as:

$$C_d = \frac{24}{Re_p}\left[1 + 0.15 Re_p^{0.287}\right]. \tag{1.14}$$

Since this development, variations to account for correlations due to particle Reynolds numbers higher than 1000 have been proposed. In this work both Schiller and Naumann [167] and Wen and Yu [211] are employed. The drag force,

$$\mathbf{F}_D = \beta(\mathbf{u}_f - \mathbf{u}_p), \tag{1.15}$$

with the drag time scale, β as,

$$\beta = \frac{3}{4} C_d \frac{\rho_f}{d_p} |\mathbf{u}_f - \mathbf{u}_p|, \tag{1.16}$$

with the drag coefficient as,

$$C_d = \begin{cases} \frac{24}{Re_p}\left[1 + 0.15 Re_p^{0.287}\right] & \text{if } Re_p < 1000 \\ 0.44 & \text{if } Re_p \geq 1000. \end{cases} \tag{1.17}$$

The drag coefficient (or factor) is then used to provide a multiplicative factor in front of the drag law depending on the particles Reynolds number. This term has important ramifications as it dictates the energy transfer between each phase. Note that the derivation of these models is concerned with single particles and as such can not capture the effects of clustering. The interested reader is referred to the energy minimisation multiscale drag model (EMMS) method of Li et al. [111], Yang et al. [218] and the DNS filtered equations of Agrawal et al. [3], Ozel et al. [131], respectively as this phenomenon remains outside the scope of this study as it requires expensive modelling techniques.

For the particles investigated in this work, we concern ourselves with high density ratios $\rho_p/\rho_f \gg 1$, the so-called small heavy particle regime. Looking at the BBO equation, this results in two dominant forces on the particle - drag and gravity. In a fully turbulent regime, the relative motion between the phases can result in the production of turbulent kinetic energy, leading to a mixture of production mechanisms [30], although in this work the only production mechanism is the mean shear. With an understanding of the governing mechanisms of the particle behaviour we now concern ourselves with the fundamental aspects of the numerical modelling.

1.3 Modelling approaches for fluid-particle flows

There are two main approaches for predicting turbulent fluid-particle flows: the Euler-Lagrange (E-L) and the Euler-Euler (E-E) method. Both of which rely on

the same underlying principles. Fig. 1.4 shows a schematic detailing the modelling approaches available.

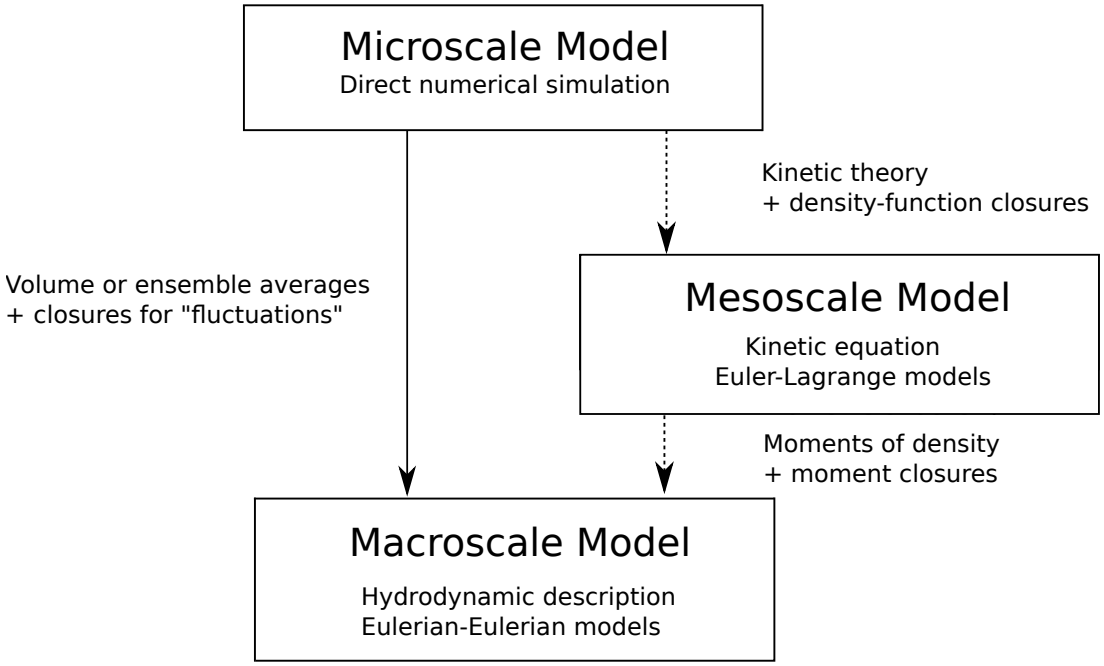

Figure 1.4: Modelling approaches for fluid-particle flows [122].

We define the *microscale* as the level of description in which the no-impermeability constraint and the no-slip boundary condition is imposed at the surface of each particle [9, 10, 188, 216], this is often referred to in the literature as 'true' DNS. These equations resolve the whole range of length and time scales as well as the inter-phase coupling term. The *mesoscale* denotes a description in which the discrete particle elements are replaced by a point-particle approximation, typically used when the particle diameters are smaller than the Kolmogorov length scale. The momentum transfer between the fluid and particle is then modelled as a point source [27] reducing the computational cost. Finally, the *macroscale* is used to denote models that employ a hydrodynamic description and contain two averaged continuum equations of continuity, momentum and energy with constitutive equations used for the closure of unclosed terms. The inter-phase transfer is accounted for through an averaged force coupling term.

1.3.1 Euler-Lagrange methods

The E-L method relies on solving the fluid-phase in an Eulerian approach and the particle-phase in a Lagrangian approach i.e. particle tracking [55]. The microscale or 'true' DNS simulations are often conducted to record hard-to-access quantities such as instantaneous drag, lift and virtual mass forces [5, 153, 189, 219]. Additionally, it has been employed to ascertain the effects of turbulent energy exchange between phases [6, 181, 191]. This method provides key insights but due to their computational cost and reliance on simulating small-scale interactions the approach is unfeasible for large particulate systems. There also exists a hybrid approach in which the microscale model i.e. discrete particles are coupled with the macroscale model in the fluid-phase [74, 194, 195]. These models have had some success with the mesoscale approach receiving more attention [70] as there is a clear distinction between time and length scales.

Within the context of the mesoscale model, each point-particle is a statistical representation of its underlying kinetic equation (presented in §2.2.1), similar to simulations carried out in the direct-simulation Monte-Carlo method [15]. Essentially, the kinetic equation is discretised into a number of individually tracked stochastic particles. This is then coupled with the carrier flow through momentum exchange terms. This is the overwhelming popular approach in the literature [69, 122] as this provides a reasonable trade-off between physical and statistical approximation. The approach has been used for understanding fundamental phenomena e.g. clustering [27, 186], transition [30] and verifying experimental observations [80, 115]. Again, for large particulate systems in which the macroscale effects e.g. turbulence, dominate the system these simulations are still computationally expensive. This is exacerbated by the fact that a large number of stochastic particles are required in order to control the statistical errors [15].

1.3.2 Euler-Euler methods

The E-E approach models both the fluid- and particle-phase as interpenetrating continua resulting in both phases acting as 'fluids'. This results in two sets of momentum and continuity equations for the fluid- and particle-phase and a shared pressure field, respectively. This reduces the computational cost considerably, as the range of fully resolved scales in E-L simulations are modelled. This approach then relies on constitutive relations to close the unclosed terms in the governing equations and leads to a computationally flexible approach to modelling turbulent fluid-particle flows.

Microscale based macroscale models

As seen in Fig. 1.4, two approaches for deriving an E-E model exist. The first E-E models were found by either ensemble- or volume-averaging [7, 53, 88] the microscale model i.e. local instantaneous NSE. The fundamental idea behind this approach is as follows: at a fixed time and location in a multiphase flow field, the cell or point will contain either the pure phase or a mixture of each. To arrive at such a description then, the microscopic governing equations are multiplied by a phasic indicator function, and then averaged to find governing equations i.e. continuity and momentum for each respective phase. This then leads to unclosed terms in the fluid-phase i.e. velocity fluctuations which are typically closed using the Boussinesq approximation, as well as unclosed terms in the particle-phase i.e. the pressure-stress tensor and the velocity fluctuations, which are closed using kinetic theory (KT).

Historically, E-E models were developed for dense fluidised bed applications [7, 59, 76, 198] owing to their industrial relevance. This encapsulates a whole plethora of physics including bubbling beds [197], reactions [133], transition from bubbling to circulating [8], drag force [225], etc. Under these dense conditions in which the particles are highly collisional, an analog with the KT of molecular gases [17,

38] was drawn. This behaviour, the velocity fluctuations being the analog of the temperature of a molecular gas, leads to a balance equation through a normal solution to the Boltzmann equation [93, 94], through which constitutive relations can be found for the pressure-stress tensor and heat-flux. Under the conditions found in a dense fluidised bed the particle fluctuations are well represented by this analogy as they belong to a largely uncorrelated random velocity field. Once these models were extended to more dilute or turbulent regimes e.g. the chamber of a circulating fluidised bed, it was found that the approach was inadequate [141].

As the particles, under high Re and/or dilute conditions, are influenced by the large scale turbulence of the fluid-phase the particles are no longer in uncorrelated random motion as the analog suggests. The kinetic contributions increase dramatically which render the dense constitutive relations inaccurate i.e. kinetic contributions are neglected, and as such the constitutive models were revised for dilute conditions [3, 85, 224]. Moreover, ad-hoc coupling terms were introduced in order to capture the macroscale turbulence [141, 174, 198]. Even so, in high Re number flows this still did not provide satisfactory results [16, 52, 118, 175]. It was only recently that the underlying physical basis of the approach was found to be conceptually inadequate and efforts have been made to rectify this [70].

As mentioned previously, the constitutive equations and particle fluctuations are closed using KT. This closure represents the Achilles' heel of the approach in the context of high Re number flow. As shown by Février et al. [67], two contributions to the particle fluctuation energy exist. These are the *turbulent kinetic energy* and the *kinetic collisional energy* and neglecting the former results in the breakdown of the particles behaviour where macroscale correlated motion is relevant [67, 71].

In the microscale-based approach then, the particle fluctuations at the macroscale (from the unclosed momentum equation) are equated to the particle fluctuations at the microscale. The particle fluctuations of individual particles is analogous to the KT of molecular gases Boltzmann [17], Chapman and Cowling [38] in which the pressure tensor arises due to velocity fluctuations of individual gas molecules

i.e. internal energy. This then does not represent the macroscale turbulence of which the model's governing equations now represents. To be more precise, in the particle phase, the particle fluctuations can arise from more than one source i.e. both kinetic collisional energy and turbulent kinetic energy. This approach, using the KT closure at the macroscale, has been applied by many authors (to name but a few) [13, 48, 49, 61, 84, 141, 179, 183, 198, 201, 226] in high Re flow, with varying degrees of success.

Upon further investigation, the source of the particle fluctuation energy in these models suffer from a further problem, as first identified by Fox [71]. For this discussion it is useful to bear in mind that the unclosed fluctuations in the macroscale model are being equated to the energy derived from a collisional Boltzmann equation (see §2.2.1) to describe stochastic small-scale particle behaviour.

The distribution of particles in KT are described using a kinetic equation (i.e. collisional Boltzmann equation). The velocity distribution then represents an instantaneous field of varying particle velocities. Linearising the collisional operator and employing an appropriate mathematical approximation, the hydrodynamic equations can be found. These comprise of the volume fraction, velocity and granular temperature which then appear as random variables in a one-point p.d.f model.

When modelling turbulence a one-point probability density function (p.d.f) representing the velocity distribution is used [142]. This represents an infinite number of realisations of the turbulent flow, each of which contains a unique particle number density and velocity at a time and location. This is used to describe the velocity fluctuations in turbulent flow. In effect, the p.d.f used in KT belongs to a completely different realisation of the flow than the p.d.f used to describe turbulence. In the literature these two are often equated, using the notation used later in this work, we denote the granular temperature as $\langle\Theta\rangle_p$, particle turbulent kinetic energy as k_p, and the fluctuating kinetic energy as $\frac{1}{2}\langle\mathbf{u}_p''\cdot\mathbf{u}_p''\rangle_p$. The statement following Peirano and Leckner [141] is as follows, $\frac{3}{2}\langle\Theta\rangle_p = \frac{1}{2}\langle\mathbf{u}_p''\cdot\mathbf{u}_p''\rangle_p$. This then omits the contribution of the correlated macroscale turbulence as the granular temperature

is used in its stead. As previously touched upon, there exist two contributions to the fluctuation energy which will be explored in more detail in the subsequent section. This closure then makes modelling high Re number flows challenging as the macroscale energy is omitted.

In this work, the model of Peirano and Leckner [141] hereby denoted Modified Peirano Model (MPM), is compared and contrasted against a model in which the separation of particle fluctuation energy *is* made in Chapter 5. The model is tested on a challenging high Re case and it will be shown how omitting the particle turbulent kinetic energy results in the breakdown of the particle mean statistics.

Kinetic theory based macroscale models

Looking again at Fig. 1.4, an alternative approach to arriving at a macroscale model exists. Recently, Fox [71] has shown that this two-step process can result in a clear distinction between the contributions that make up the particle fluctuation energy. Beginning with the kinetic (mesoscale) equation [73], the particle-phase is coupled with the fluid-phase through a momentum coupling term. Then the low order moments of the kinetic equation are found and closed using the the Chapman-Enskog expansion (see §2.2.1) which leads to the hydrodynamic description of the system. The resulting system of equations for volume fraction, momentum and granular energy can then be Reynolds-Averaged (RA) to find the macroscale turbulence model. Once the equations have undergone RA the appropriate closures are adopted and the full set of equations that make up the Reynolds-Averaged Two-Fluid model (RA-TFM) are found.

This approach leads to separate transport equations for the particle turbulent kinetic energy k_p and the granular temperature $\langle\Theta\rangle_p$ which represent correlated macroscale and uncorrelated mesoscale energy, respectively. Moreover, through the derivation of the macroscale turbulent kinetic energy, the particle turbulent kinetic energy dissipation ε_p is defined. This in turn appears as a source term in the transport equation of the granular temperature. This introduces a cascade

of energy meaning that as macroscale correlated energy is dissipated it produces mesoscale uncorrelated energy. This distinction is crucial and will be shown to be very advantageous to its numerical solution in subsequent chapters.

This approach then leads to the particle fluctuation energy being written as $\kappa_p = k_p + 1.5\langle\Theta\rangle_p$. Février et al. [67] found that even for non-collisional flow, separate transport equations for k_p and $\langle\Theta\rangle_p$ were essential, a direct result of the energy cascade outlined previously. Vance et al. [199] also corroborated these findings but for collisional flow; in their work the particles were found to preferentially concentrate their energy into uncorrelated energy with increasing particle response time. Given these recent advances in the field, the modelling of previously challenging turbulent fluid-particle interactions in the Eulerian-Eulerian framework has become clearer and their successful prediction more likely.

As a final note it should be stressed that when working with either E-E or E-L models that have been derived from the mesoscopic model, their predictions for the moments should be the same if the statistical and mathematical errors are reduced [51, 135, 137]. This enables the E-E model to be validated against the E-L methods, thus resulting in more accurate hydrodynamical models. This is not possible with a microscale-based-macroscale model due to the lack of physical and mathematical basis for the velocity fluctuations.

1.4 Partitioning effect of particle inertia

Looking again at the equation for the particle fluctuation energy, $\kappa_p = k_p + 1.5\langle\Theta\rangle_p$ it can be seen that there are two contributions: macroscale turbulent kinetic energy and mesoscale kinetic collisional energy. The underlying mechanism for this particle fluctuation energy separation is the particle's inertia. Sommerfeld [178] describes how important particle inertia is in fluid-particle flows, revealing how it dictates the interaction between the particles and the whole spectrum of time and length scales in turbulent flow. Typically, this has been investigated to ascertain its effect

on preferential concentration (particle volume fraction distribution), even in the absence of wall-bounded flow, which can be induced by regions of low vorticity and/or high strain rate. This can have a substantial influence on the collisional rate of particle flows [148, 181, 206].

It has been shown by Février et al. [67] that particle inertia not only leads to preferential concentration but also results in a correlation of the velocities in neighboring particles and can be seen in Figs. 1.5 & 1.6. Two distinct behaviours, which pertain to correlated and uncorrelated motion are displayed. In Fig. 1.5, the St is small i.e. small-inertia particles, the neighboring particle velocity field becomes spatially correlated through the inter-phase interaction e.g. drag with the fluid velocity field. The energy contained in the correlated particles is represented by the macroscale turbulent kinetic energy.

In Fig. 1.6, St is large i.e. large-inertia particles with response times much larger than the integral time scale of the fluid. The neighboring particle velocity field remains uncorrelated with the surrounding velocity field as the particles tend to contain 'memory' effects with long distant and independent eddies. For the simulations conducted in Février et al. [67] inter-particle collisions were absent, despite this the particle fluctuation energy still needed to be separated into two separate types of energy in order to correctly account for correlated motion. This is due to the the uncorrelated motion containing both collisional and kinetic energy [38]. The energy contained within the large-inertia particles, of which collisions are typically included [199], is then described by $\langle \Theta \rangle_p$.

It has been shown that there exists a two-particle velocity distribution with asymptotic behaviour [2] in each inertial limit. In the large-inertia limit the p.d.f of the particle velocity distribution satisfies the assumption of molecular chaos and thus KT can be employed as suggested by Reeks [150]. This suggests that in the large-inertia limit the particle velocity distribution cannot be assumed to remain correlated with the fluid. This further strengthens the theory that there exists a separation of correlated and uncorrelated velocity fields due to particle inertia.

In the small-inertia limit, the spatial correlation function between any two velocities should be accurately modelled by a decaying exponential, analogous to the correlation describing the fluid turbulence [83]. In the large-inertial limit, the motion of the particle becomes stochastically similar to Brownian motion with independent random velocities [2, 150] i.e. random spatially uncorrelated velocity. This corroborates the presence of correlated particle turbulent kinetic energy and the particle collisional energy, the rigorous derivation of which will be presented in Chapter 2.

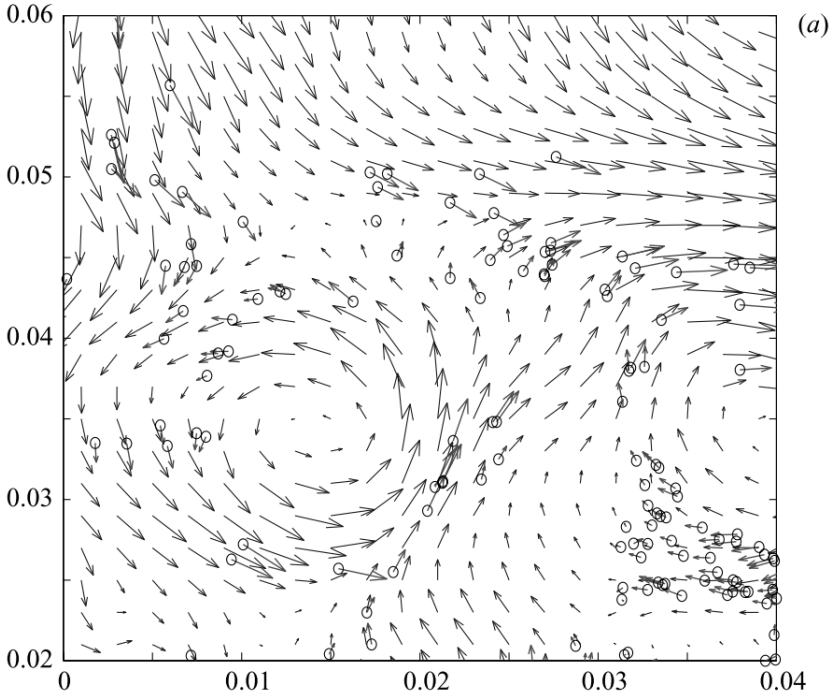

Figure 1.5: Instantaneous fluid and particle velocity vectors with particle relaxation time of $0.13\tau_f$. Adopted from Février et al. [67].

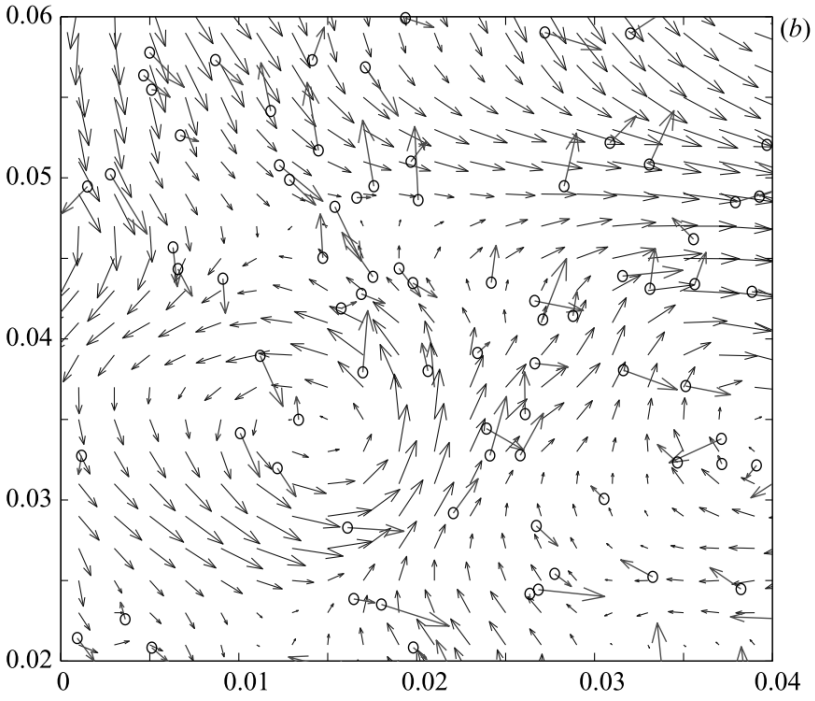

Figure 1.6: Instantaneous fluid and particle velocity vectors with particle relaxation time of $2.17\tau_f$. Adopted from Février et al. [67].

1.5 Fluid-particle turbulence interaction

Fluid-particle turbulence interaction constitutes the exchange of momentum and energy across both fluid- and particle-phases, the classification of which has been presented in §1.2.1. This accounts for the coupling between the phases and can be caused by drag, lift, virtual mass, buoyancy or the Basset force. Owing to the effect of the particle's inertia the turbulence of the carrier phase can be augmented - this is *turbulence modulation*.

Modulation of turbulence is a complex two-way coupled phenomenon [59] and can be caused by several processes including fluid-particle interaction, particle-particle interaction and particle-wall interaction. Modulation of turbulence is primarily dominated by the reduction of the fluid-phase fluctuating velocities, i.e. attenuation of the turbulence. Attenuation is especially prevalent in the presence of small heavy particles and is well established in the literature [60, 77, 82, 106, 192, 203, 217]. This can be further influenced by the inhomogeneity of wall-bounded flow [202], leading to more complex mechanisms governing turbulence attenuation. In contrast to this, the fluid-phase turbulence kinetic energy can be increased due to coupling [77], for example when the particle Reynolds number is high, resulting in particle vortex shedding [141].

A particular issue in capturing this two-way coupled phenomenon is the fluid-particle covariance term, the so-called cross-correlation term. This term appears in the turbulence transport equations of both respective phases and dictates the energy transfer between the two. Essentially, it accounts for the turbulent kinetic energy exchange between phases through drag. This should be correlated in $St < 1$ and uncorrelated in $St > 1$.

Due to the lack of particle inertia induced energy separation this term has proven challenging to model correctly. As such, this term has received considerable attention by researchers with various model forms being suggested [4, 13, 37, 40, 48, 79, 141, 145, 216, 226]. Writing the unclosed covariance term as, $\langle \mathbf{u}_p'' \cdot \mathbf{u}_f''' \rangle_p$ (defined in

App. B) we see that it incorporates the fluctuating component from of each phase. In the literature, a standard form Peirano and Leckner [141], Sinclair and Mallo [176] $\langle \mathbf{u}_p'' \cdot \mathbf{u}_f''' \rangle_p = \sqrt{\Theta k_f}$ is often adopted. The form of this term models energy exchange between large-scale turbulent kinetic energy and small-scale collisional energy - the ramifications of this are explored in Chapter 5.

Recently, with the energy separating effect of particle inertia a new form has been proposed by Fox [71] and reads $\langle \mathbf{u}_p'' \cdot \mathbf{u}_f''' \rangle_p = \sqrt{k_p k_f}$, in which both variables represent the large-scale turbulent kinetic energy of each respective phase. This form was validated for isotropic homogeneous turbulence showing the correct decaying behaviour. In Chapters 5, 6 and 7 we show that the form of the velocity covariance shows the correct behaviour for two-way coupled phenomena.

As the volume fraction increases, the likelihood of particle collisions increases, giving rise to inter-particle collisions. The effect of this so-called four-way coupled phenomenon has been studied by numerous authors [129, 181, 185, 204, 205, 217]. Vreman et al. [204] found that the inclusion of the inter-particle collisions enabled to particles to diffuse the particle kinetic energy in the wall-normal direction. This results in a flattening of both the fluid- and particle-phase velocity profile, this finding is also consistent with that of Yamamoto et al. [217] and Tanaka et al. [186]. With a flattening of the particle velocity profile the numerical predictions were able to closely align with the experimental observations of Kulick et al. [106]. With this redistribution of particle kinetic energy the spatial distribution of the particle volume fraction is also changed which can impinge on predicting crucial particle behaviour i.e. particle deposition in the boundary layer. In Chapter 6, this four-way coupled type behaviour is explored on the experimental data of Kulick et al. [106].

The collisional frequency has also been investigated in isotropic turbulence, through two- [181] and one-way [205] coupled DNS simulations of isotropic turbulence to study turbulence modulation. Results suggest that the rate of viscous dissipation of turbulence energy is enhanced by particles - similar to the case in the two-way

coupled regime. Owing to its isotropic nature any direction dependent phenomena were not recorded. This suggests that the fluid turbulence dissipation transport equations may need adjusting in the presence of particles through an adjustment of the turbulence model constants or the presence of an extra dissipative term. This type of behaviour is out of the scope of this work but it is important to note that this is another area requiring investigation.

1.6 Near-wall fluid-particle behaviour

It is well established that in turbulent wall-bounded flow particles tend to accumulate in the near-wall region. This phenomenon, known as turbophoresis, was first identified by Caporaloni et al. [31], Reeks [149], Young and Leeming [220], and is responsible for particles drifting from regions of high turbulence intensity to low turbulence intensity. The form of the turbophoretic velocity proposed reads as:

$$u_{p,y} = -\frac{1}{\tau_p}\frac{du''_{p,y}}{dx} \tag{1.18}$$

where $u_{p,y}$ is the velocity in the wall normal direction and $u''_{p,y}$ is the wall-normal stress component. In inhomogeneous flow the particles will migrate from regions of high to low turbulence intensities i.e. wall-drift. Additionally, a dependence on the particles relaxation time is present. This means that for low St number the velocity should be higher in magnitude.

In low St, wall-bounded flow with particles tightly coupled to the fluid through drag the region of highest turbulence intensity variation is in the near-wall region. There is a band of low turbulence intensity just below the peak of production in the boundary layer ($y^+ \approx 11.6$), with a slow decay in turbulent kinetic energy as the core of the flow is approached. As the particles are closely correlated with the carrier flow, through the covariance term, the inhomogeneity of the turbulent kinetic energy close to the wall results in a net drift of the particles towards the wall [177]. This wall-induced drift results in an accumulation of particles in the

near-wall region. The particles are then trapped in the near-wall viscous region and can not migrate back into the core of the flow. This phenomenon is called particle deposition.

The effects of turbophoresis and particle deposition has been investigated by numerous authors; almost exclusively in the context of E-L modeling [112, 119, 126, 132, 177]. Largely due to its ability to resolve turbulent scales to a high resolution the simulations can provide crucial insights into fundamental phenomena and its appropriate modelling. The prevailing physical explanation suggests that particles are pushed towards the wall and into the viscous sublayer by the span-wise motion of turbulence (vortex) and as a result the particles experience a net transverse drift which concentrates them in the near-wall region [23, 132]. This behaviour is of significant interest for a number of applications, ranging from new gas cleaning devices to sizing and control of surface chemical reactions [119] and its successful prediction can exert stark changes to the particle turbulence kinetic energy and particle viscosity predictions.

Strömgren et al. [180] investigated the effect of the turbophoresis force within an E-E framework and found that even for small volume fractions, $\alpha_p = 2\text{x}10^{-4}$, two-way coupling effects are non-negligible in the near-wall region and require special attention. This is due to the concentration of particles being at its largest in the near-wall region - a phenomenon caused by turbophoresis. Due to the accumulation of particles in the boundary layer, inter-particle and particle-wall collisions then become more relevant. This leads to an increase in skin friction [204] as the particle-wall interaction behaves as an additional drag source on the fluid-phase.

In E-E model, turbophoresis and particle deposition presents two challenges: the first, being that typically in the fluid-phase where the mean velocity gradients are steepest wall functions are often employed. Secondly, the phenomenon is governed by the wall-normal fluctuating velocity, meaning that the particles move down the wall-normal gradient towards the wall. In standard RA modelling the kinematic blocking of the wall is not explicitly modelled and we close the term by modelling

the pressure redistribution (along with the triple correlation) by a gradient-diffusion hypothesis [142], combined with the Boussinesq approximation, assuming that the deviatoric Reynolds stress is proportional to the mean rate of strain. This limits the turbulent viscosity due to the y-wall dependence i.e. turbulent viscosity does not actually depend on k_f^2/ε_f, which is known to lead to an over-prediction in the near-wall region (Durbin and Reif [58]) causing further limitations.

To correctly model the turbophoresis and particle deposition in the boundary layer these constraints need to be alleviated, which is the concern of Chapters 6 & 7. It will be shown that the inter-particle collisions and the explicit modelling of the fluid-phase wall-normal stress component allows the particles to drift to the wall. To complicate the picture further, as particles deposit in the near-wall region, the particles begin to affect the fluid-phase through two- and four-way coupling effects, as the volume fraction increases.

In the near-wall region there exists a strongly inhomogeneous region which requires special attention to model in a Reynolds-Averaged framework. Due to the no impermeability constraint, a kinematic blocking effect is introduced that leads to image vorticity [86, 190] (discussed in Chapter 2 - §2.5). This non-local effect on the Reynolds-Stress i.e. the no-flux condition on the normal component of velocity $\mathbf{u} \cdot \mathbf{n} = 0$, results in an anisotropic distribution amongst the fluctuating velocity components in the vicinity of a wall, mainly felt as a suppression of energy transfer into the wall-normal component. This is not accounted for in standard turbulence modelling as the Reynolds stress is closed using a one-point closure i.e. a turbulent viscosity and symmetric velocity gradient.

The isotropic limitation is introduced in the definition of the turbulent viscosity which comprise of a velocity and length scale. The velocity and length scale (that represent the size of the eddies transporting momentum and their respective velocity) are chosen to represent the fluctuating quantities of the flow. This results in the turbulent kinetic energy, $k = 0.5(\mathbf{u}_x \cdot \mathbf{u}_x)$ being used as a velocity scale by taking the square root and then defining a length scale to complement this choice.

The definition of k, that is used as a measure of the averaged turbulence intensity, relies on assuming all the fluctuating components in each direction are equal. This introduction of isotropy results in an overestimation of the turbulent kinetic energy in the near-wall region as in general the statement, $\langle \mathbf{u}_x'' \mathbf{u}_x'' \rangle > \langle \mathbf{u}_y'' \mathbf{u}_y'' \rangle$ is true as the stream-wise components dominate the wall-normal. Therefore, there is a suppression of momentum transfer in the wall-normal direction and without accounting for this, a large over-prediction of the turbulent viscosity is experienced in the near-wall region Durbin and Reif [58]. This phenomenon is present in both phases, within a E-E framework, and this aspect of modelling forms the basis of Chapters 6 & 7.

1.7 Numerical solution of E-E models

In Computational Fluid Dynamics (CFD), the coupling of pressure and velocity has proven to be one of the major challenges when solving the Navier-Stokes equations (NSE) [64, 138]. Traditionally, this problem has been tackled by solving the NSE in a decoupled manner [7, 64]. First, an estimate for the velocity field is found by the momentum equation using an initial guess of the pressure field. Then a Poisson equation for pressure is solved for by taking the divergence of the momentum equation. After its solution, the velocity field is corrected to ensure continuity is satisfied.

This pressure-based (meaning a pressure-correction equation is formulated) approach make up two of the most widely used algorithms in CFD; SIMPLE [138] and PISO [89]. As the latter is employed in this work we shall focus our attention on its general procedure in a Finite-Volume framework. As the Finite-Volume-Method (FVM) is used throughout this work we assume it's notation and discretisation procedures throughout. A full treatise of the FVM is provided in Chapter 3.

We start by writing the NSE for single-phase incompressible flow,

$$\nabla \cdot \mathbf{u} = 0, \tag{1.19}$$

$$\frac{\partial \mathbf{u}}{\partial t} + \nabla \cdot (\mathbf{uu}) - \nabla \cdot (\nu \nabla \mathbf{u}) = -\nabla p. \tag{1.20}$$

where p is the kinematic pressure. First, we discretise the implicit contributions of the temporal, convective and diffusive terms and denote them, $\mathbf{A}$. Then grouping the neighbouring coefficients (multiplied by the velocity) and the source terms from the explicit contributions of the aforementioned terms into the $\mathbf{H}$ operator (full details are given in Chapter 4). The semi-discretised form of the momentum equation can then be written as:

$$\mathbf{Au} = \mathbf{H} - \nabla p, \tag{1.21}$$

with the pressure gradient being omitted from the discretisation in line with a Rhie-Chow like procedure [154]. Then an expression for the velocity can be written as:

$$\mathbf{u} = \frac{\mathbf{H}}{\mathbf{A}} - \frac{1}{\mathbf{A}} \nabla p. \tag{1.22}$$

Velocities on the cell face i.e. flux can be found by interpolating Eq. 1.22 (details of which will be shown in Chapter 4) which reads as:

$$\mathbf{u}_f = \left(\frac{\mathbf{H}}{\mathbf{A}}\right)_f - \left(\frac{1}{\mathbf{A}}\right)_f (\nabla p)_f. \tag{1.23}$$

Then the flux form of the predicted velocities Eq. 1.23 is inserted into the discretised continuity equation which then leads to the Poisson-like equation for pressure,

$$\nabla \cdot \left(\frac{1}{\mathbf{A}} \nabla p\right) = \nabla \cdot \left(\frac{\mathbf{H}}{\mathbf{A}}\right). \tag{1.24}$$

The solution of this equation then leads to an updated pressure field but the velocities (both fluxes and cell centered velocity values) do not currently contain the influence of the pressure gradient and need to be updated. This is then achieved by updating the face flux with Eq. 1.23 and then correcting the velocity field with Eq. 1.22, this then results in a velocity field that satisfies continuity.

These steps are some of the essential ingredients that make up the PISO algorithm. In short, the momentum equation, with a predicted pressure field, is used

to estimate a velocity field. The field is then interpolated onto cell faces to find the predicted mass flux which is then inserted into the continuity equation to formulate a Poisson-like equation for pressure. Once solved the velocity fluxes are updated and the cell centre velocities are corrected to satisfy the new pressure field i.e. conservation. This procedure is then repeated until some user defined tolerance is found and then the solution is advanced in time.

The velocity and pressure are decoupled within the solution matrix with each variable being solved separately. The unknowns in each respective equation i.e. pressure in the momentum equation and momentum in the pressure equation, are treated explicitly. The computational overhead required to store and operate on a single variable matrix is relatively cheap and this lead to its widespread use as when these algorithms were developed computational memory was at a premium. As the matrices are solved sequentially the emphasis is then put on the time taken to do repeated operations as opposed to storage. Two of the major drawbacks of these algorithms is the use of arbitrary under-relaxation factors, due to high rates of change in dependent variables and the slow convergence rates, due to the decoupling of velocity and pressure. In transient flows, the time-step size is used as an effective under-relaxation method in order to cope with abrupt rates of change in the dependant variable as it represents actual physical time.

Owing to the rapid increase of computational power an alternative to the decoupled solution algorithm has received renewed interest. These methods were available around the same time as the segregated solution [200] but received little attention due to their high computational memory requirements. In particular, methods that employ a pressure-correction equation have been employed within FVM frameworks [39, 46, 47, 215] - here denoted as block-coupled. Alternatives to this approach rely on the type of grid used i.e. staggered, in which a direct method on the primitive form of the NSE are employed [20, 34, 99, 124, 125, 200] or co-located grids within a control volume finite element framework (CVFEM) [20, 34, 99, 124, 125, 200].

Within the block-coupled framework the system of equations are solved within

one single block-matrix in which the influence of velocity-pressure coupling can be introduced through inter-equation coupling terms. This ensures that the system of equations are solved implicitly using the current iteration values. As a single block-matrix of coefficients needs to be solved for, the computational overhead is high, unlike in the segregated approach. This then puts an emphasis on the computational memory in order to store the matrix of coefficients. This approach has significant advantages over the segregated formulation as arbitrary under-relaxation is no longer needed and dramatic improvements in convergence, stability and robustness are experienced.

The pressure-based approach was first applied to co-located grids in the CVFEM framework by Webster [208, 209]. The approach shows dramatic improvements in convergence on both structured and unstructured grids in comparison to the SIMPLE algorithm and shows superior performance on denser meshes. This framework [87, 147, 208, 209] has since been extended to multiphase applications - namely the two-fluid model [25]. In this approach the entire system is coupled i.e. two momentum equations and a pressure field leading to tighter inter-equation coupling. The coupled solver showed far superior performance over its segregated counterpart with improvements in the number of iterations and computational time.

The two-fluid model is particularly well placed for such an extension due to the formulation of the governing equations. Two phase-momentum equations are coupled via a shared pressure field with inter-phase coupling through drag. When solved within a segregated framework the system of equations are solved in a decoupled manner in which the decoupled phase-velocity-pressure and inter-phase drag terms are treated explicitly, putting a computational constraint on the solution time and adversely affecting convergence.

In a FVM framework, Darwish et al. [45] has recently proposed a two-fluid fully-coupled pressure-based solver in which their single-phase framework [46, 47] is extended to a multiphase framework. The governing equations are solved within a fully conservative formulation i.e. the volume fraction and density are left in

the momentum equations, typically used to capture compressibility effects. They derived their model in a 2D framework and verify their results on 1D laminar test cases showing a rate of solution acceleration between 1.3 and 4.6.

More recently, Ferreira et al. [63] proposed a fully-coupled pressure-based multi-fluid framework. In their work they solve the phase-intensive formulation i.e. dividing out by volume fraction and density and employing the Compact Momentum Interpolation (CMI) practice of Cubero et al. [44] and guess-and-correct procedure shown in Darwish et al. [45]. Overall, this treatment was shown to enhance stability and convergence through the correct treatment of the temporal, drag and body force interpolation especially when a large drag force was present. The multi-fluid solver is verified on 2D laminar test cases showing superior performance when compared to the segregated solver reporting computational speedups from 4.6 to 9.3 times.

In Chapter 4, the two-fluid methodology in this work will be derived and implemented in a pressure-based segregated and block-coupled manner. Both algorithms will be compared in terms of performance and convergence in Chapter 8.

1.8 Present Contributions

The following contributions to the field of Eulerian-Eulerian numerical modelling that are presented in this thesis:

- An E-E (RA-TFM) framework is presented that accounts for the particle inertia induced energy separation in wall-bounded turbulent particle-fluid flows. This is particularly relevant for high Re number flow in which the fluid- and particle-phases energy can be correlated in the main core of the flow;
- A segregated solution algorithm is derived and implemented within the open-source CFD tool-box OpenFOAM;

- A fully-coupled solution algorithm is derived and implemented within the open-source CFD tool-box OpenFOAM;
- Boundary conditions to incorporate the particle-wall interaction of the new particle-phase turbulence energy statistics have been derived following Johnson and Jackson [97];
- The model has been compared against the conventional model found in existing open-source and commercial CFD codes [141]. This particular aspect highlights the inherit shortcomings in the existing methodology;
- A elliptic relaxation model is derived and presented. It was found to be an effective modelling approach for the near-wall region within E-E simulations. This provided the resolution of the fluid boundary layer and incorporated the suppression of the wall-normal fluctuating component. This model was derived within the current RA-TFM methodology but it is a generic formulation and can be applied to existing E-E model;
- A elliptic relaxation model for the particle-phase was validated against DNS data;
- A comparison of the implemented segregated and coupled solution algorithms within the E-E framework was presented and their behaviour contrasted;
- The RA-TFM was validated on a range of benchmark experimental data including DNS. This comprises of a range of particle classifications, coupling mechanisms and geometric configurations;
- Finally, the CFD codes developed throughout this work are made available online (see Appendix D). This comprises of two main solvers: `ratfmFoam` and `ratfmCoupledFoam`. They are used throughout Chapters 5-8 and Chapter 8, respectively.

2 Multiphase turbulence modelling

2.1 Overview

In this chapter both Eulerian-Eulerian (E-E) frameworks and modelling methodologies are presented. The two-step E-E framework is presented first. We begin at a collisional Boltzmann equation and follow the derivation of Garzó and Santos [72] to arrive at the hydrodynamic balance equations. We then follow Fox [71] in which this system of equations are Reynolds-Averaged to arrive at a set of Reynolds-Averaged E-E equations. The second modelling methodology is then presented. We follow the derivation of Anderson and Jackson [7] which begins at a microscale model for fluid-particle flows. This is then volume-averaged to arrive at the hydrodynamic governing equations at the macroscale. These models are then contrasted to highlight the key underpinning differences between them. Finally, two novel elliptic relaxation models are derived within the RA E-E framework to account for the near-wall region in multiphase simulations. The particle wall-boundary conditions that are required to capture the correct particle-wall interaction are also detailed.

This chapter comprises of:

- Derivation of the two-step E-E methodology;
- Details of the mathematical modelling and appropriate closures are presented;
- Description of the microscale-to-macroscale E-E model methodology;
- Presentation of both the two-step and one-step E-E model equations.
- Derivation/presentation of the elliptic relaxation models for both the fluid- and particle-phase.
- Presentation of the particle wall boundary conditions used in E-E simulations.

2.2 Euler-Euler modelling

As shown in Section 1.3 there exist two main approaches for deriving an Euler-Euler model (see Fig. 1.4). This section will present both approaches and compare their fundamental differences.

2.2.1 Mesoscale modelling

Throughout this section we present the fundamental governing equations for collisional fluid-particle multiphase flows by starting at the *mesoscale* level. The first step, deriving the mesoscale model, involves physical modelling and physics-based simplifications in order to arrive at a closed and complete kinetic equation i.e. collisional Boltzmann equation. As indicated by the schematic (Fig. 1.4) this is a model of the microscale model in which modelling decisions can be discerned from the overall picture once arriving at the macroscale model.

The second step, deriving the macroscale model from the mesoscale model, involves mathematical approximations (Chapman-Enskog) to find a normal solution to the kinetic equation [93] i.e. the hydrodynamic equations. Then, applying Reynolds-Averaging to the hydrodynamic equations to find the macroscale turbulence model. This approach has a distinct advantage over the one-step average as there is a

clear distinction between the physical and mathematical errors. In addition, the mesoscale model can be compared, term-by-term, to the microscale model a feature that provides invaluable validation [29, 71].

Boltzmann equation

We begin then by first deriving the Boltzmann equation using classical heuristic arguments similar to those made by Boltzmann [17] himself and follow the procedure found in Garzó and Santos [72]. A more thorough exposition can be found in Cercignani et al. [35], Chapman and Cowling [38].

We begin by considering a dilute monatomic gas of $\mathcal{N}$ identical particles of mass m interacting through a pair-wise central interaction potential of finite range. At the kinetic level the state of the system can be described by a one-particle velocity function $f(\mathbf{x}, \mathbf{v}; t)$, defined in a such a way that $f(\mathbf{x}, \mathbf{v}; t)d\mathbf{x}d\mathbf{v}$ is the average number of particles which at time t reside in the volume $d\mathbf{x}$ centred at the point $\mathbf{x}$ and moving with velocities in the range $d\mathbf{v}$ about $\mathbf{v}$. The average number of particles per unit volume is then the number density, $n(\mathbf{x}, t)$, related to f through the integral,

$$n(\mathbf{x}, t) = \int d\mathbf{v} f(\mathbf{x}, \mathbf{v}; t). \tag{2.1}$$

The average velocity of the particles located around point $\mathbf{x}$ at time t defines the local flow velocity $\mathbf{u}(\mathbf{x}, t)$ as

$$\mathbf{u}(\mathbf{x}, t) = \frac{1}{n(\mathbf{x}, t)} \int d\mathbf{v}\mathbf{v} f(\mathbf{x}, \mathbf{v}; t). \tag{2.2}$$

The average kinetic energy measured moving with the flow velocity defines a nonequilibrium local temperature $\Theta(\mathbf{x}, t)$ as

$$\frac{3}{2} n(\mathbf{x}, t) k_B \Theta(\mathbf{x}, t) = \frac{m}{2} \int d\mathbf{v} [\mathbf{v} - \mathbf{u}(\mathbf{r}, t)]^2 f(\mathbf{x}, \mathbf{v}; t), \tag{2.3}$$

where $k_B = 1.38054 \times 10^{-23}$J/K is the Boltzmann constant which throughout the derivation is typically neglected [93]. The approach then is to arrive at an equation

that describes the rate of change of f in time. The derivative can be expressed, recognising the two sources of temporal change: free streaming and collisions, in the form,

$$\frac{\partial f}{\partial t} = \frac{\partial f}{\partial t}\Big|_{str} + \frac{\partial f}{\partial t}\Big|_{coll}, \tag{2.4}$$

where the RHS represents the change of f due to the free motion of particles under the action of an external force, $\mathbf{F}$. It is important to note that $\mathbf{F}$ represents any external force, in this work for example it will contain the drag force from the fluid phase. The second term refers to the change due to collisions among the particles. To arrive at an equation for the free streaming contribution it is assumed that the interactions are absent i.e. low density gas. In such a case, the particles that at time t are located at point $\mathbf{x}$ and moving with velocity $\mathbf{v}$ will be located at $\mathbf{x}' = \mathbf{x} + \mathbf{v}\delta t$ having a velocity $\mathbf{v}' = \mathbf{v} + m^{-1}\mathbf{F}\delta t$ at a later time $t' = t + \delta t$, where δt represents an infinitesimal time interval. This leads to

$$f(\mathbf{x}, \mathbf{v}; t)d\mathbf{x}d\mathbf{v} = f(\mathbf{x}', \mathbf{v}'; t')d\mathbf{x}'d\mathbf{v}'. \tag{2.5}$$

Then recognising that,

$$f(\mathbf{x}', \mathbf{v}'; t') = f(\mathbf{x}, \mathbf{v}; t) + \mathbf{v} \cdot \nabla f \delta t + \frac{\mathbf{F}}{m} \cdot \frac{\partial f}{\partial \mathbf{v}}\delta t + \frac{\partial f}{\partial t}\delta t + \mathcal{O}(\delta t^2), \tag{2.6}$$

and that the Jacobian of the transformation $(\mathbf{x}, \mathbf{v}) \rightarrow (\mathbf{x}', \mathbf{v}')$ yields

$$d\mathbf{x}'d\mathbf{v}' = \left[1 + \frac{\partial}{\partial \mathbf{v}} \cdot \frac{\mathbf{F}}{m}\delta t + \mathcal{O}(\delta t^2)\right] d\mathbf{x}d\mathbf{v}. \tag{2.7}$$

Thus subbing Eq. 2.7 into Eq. 2.5 leads to

$$\frac{\partial f}{\partial t}\Big|_{str} = -\mathbf{v} \cdot \nabla f - \frac{\partial}{\partial \mathbf{v}} \cdot \left(\frac{\mathbf{F}}{m} f\right). \tag{2.8}$$

Then finally inserting Eq. 2.8 into Eq. 2.4 leads to,

$$\frac{\partial f}{\partial t} + \mathbf{v} \cdot \nabla f + \frac{\partial}{\partial \mathbf{v}} \cdot \left(\frac{\mathbf{F}}{m} f\right) = \frac{\partial f}{\partial t}\Big|_{coll}. \tag{2.9}$$

The collision term on the RHS is difficult to deal with as it is nonlinear through f therefore we omit its treatment here. The term, $\frac{\partial f}{\partial t}\Big|_{coll}$ is typically replaced with the expression $J[\mathbf{v}|f,f]$ and would make up the *Boltzmann equation*. The collisional term represents a bilinear operator acting on the velocity distribution function. To summarise then, the equation is a nonlinear equation for f and is a function of three spatial coordinates, three velocity components and time. In order to arrive at the hydrodynamic equations, a necessary requirement in describing the system as a continuum, simplifications are sought. The first simplification is linearising the collisional operator through the Boltzmann hypothesis of molecular chaos i.e. the collisions of particles do not start in a correlated state. This means that the collisional operator can be expressed through a one-particle velocity distribution function, the one employed in this work is the Enskog collisional operator [38] and is presented without derivation.

We thus present the Enskog kinetic equation [21, 22, 73], in which the external force in Eq. 2.9 has been neglected and the right hand side has been replaced with the Enskog collisional operator, which reads:

$$\frac{\partial f}{\partial t} + \mathbf{v}\cdot\nabla f = J_E[\mathbf{x},\mathbf{v}|f,f]. \tag{2.10}$$

Here the terms, moving from left to right, represent accumulation, free transport and finally particle-particle collisions. In which the last term is expressed as:

$$\begin{aligned} J_E[\mathbf{x},\mathbf{v}|f,f] =& d_p^{d-1}\int \mathrm{d}\mathbf{v}_2 \int \mathrm{d}\overline{\boldsymbol{\sigma}}\, H(\overline{\boldsymbol{\sigma}}\cdot\mathbf{g}_{12})(\overline{\boldsymbol{\sigma}}\cdot\mathbf{g}_{12}) \\ &\times \Big(e^{-2}\chi(\mathbf{x},\mathbf{x}-\boldsymbol{\sigma})f(\mathbf{x},\mathbf{v}_1';t)f(\mathbf{x}-\boldsymbol{\sigma},\mathbf{v}_2';t) \\ &- \chi(\mathbf{x},\mathbf{x}+\boldsymbol{\sigma})f(\mathbf{x},\mathbf{v}_1;t)f(\mathbf{x}+\boldsymbol{\sigma},\mathbf{x}_2;t)\Big), \end{aligned} \tag{2.11}$$

is the Enskog collision operator [73]. Here, d is dimensionality of the system (d=2 for disks and 3 for spheres), e is the coefficient of restitution, $\boldsymbol{\sigma} = d_p\overline{\boldsymbol{\sigma}}$, with $\overline{\boldsymbol{\sigma}}$ being a unit vector pointing in the direction from the centre of particle 1 to the centre of particle 2, H is the Heaviside step function, $\mathbf{g}_{12} = \mathbf{v}_1 - \mathbf{v}_2$ and $\chi = \frac{1-0.5\phi}{(1-\phi)^3}$

which is a shape factor for spheres. The primes on the velocities denote the initial values $\{\mathbf{v}_1', \mathbf{v}_2'\}$ that lead to $\{\mathbf{v}_1, \mathbf{v}_2\}$ following a binary collision:

$$\mathbf{v}_1' = \mathbf{v}_1 - 0.5(1+e^{-1})(\overline{\boldsymbol{\sigma}} \cdot \mathbf{g}_{12})\overline{\boldsymbol{\sigma}}, \quad \mathbf{v}_2' = \mathbf{v}_2 - 0.5(1+e^{-1})(\overline{\boldsymbol{\sigma}} \cdot \mathbf{g}_{12})\overline{\boldsymbol{\sigma}}. \tag{2.12}$$

Chapman-Enskog expansion

From here the macroscopic equations for the system can be found, bearing in mind the definitions of each hydrodynamic variable given in Eqs. 2.1 - 2.3, by multiplying Eq. 2.10 by $\{1, m\mathbf{v}, \frac{1}{2}m\mathbf{v}^2\}$ and integrating over the phase velocity, $\mathbf{v}$ respectively. This then leads to three balance equations for continuity, momentum and temperature, which read as:

$$\frac{\partial(\alpha_p \rho_p)}{\partial t} + \nabla \cdot (\alpha_p \rho_p \mathbf{u}_p) = 0, \tag{2.13}$$

$$\frac{\partial(\alpha_p \rho_p \mathbf{u}_p)}{\partial t} + \nabla \cdot (\alpha_p \rho_p \mathbf{u}_p \mathbf{u}_p + \alpha_p \rho_p \overline{\mathbf{P}}_p) = 0, \tag{2.14}$$

$$\frac{\partial(\alpha_p \rho_p \Theta)}{\partial t} + \nabla \cdot \left(\alpha_p \rho_p \Theta \mathbf{u}_p + \frac{2}{3}\alpha_p \rho_p \mathbf{q}\right) = -\frac{2}{3}\alpha_p \rho_p \overline{\mathbf{P}}_p : \nabla \mathbf{u}_p, \tag{2.15}$$

where α_p is the volume fraction, $\mathbf{u}_p$ is the particle mean velocity and Θ is the granular temperature i.e. the hydrodynamic variables. Noting that $mn = \rho_p$ and the collisional operator vanishes as momentum is conserved and finally multiplying through by the phase indicator α_p. The difficulty now arises as the pressure-stress tensor, $\overline{\mathbf{P}}_p$ and the heat flux $\mathbf{q}$ are expressed as a function of f leaving them unclosed. To circumvent this then the equations need to be fully described by the hydrodynamic fields, this can be achieved through the Chapman-Enskog (CE) approximation. The approach assumes a normal solution to the Eq. 2.10 such that all space and time dependence of the distribution function occurs through the hydrodynamic fields.

$$f(\mathbf{x}, \mathbf{v}, t) = f[\mathbf{v}|n, \mathbf{u}, \Theta]. \tag{2.16}$$

The RHS shows that there exists a functional dependence on the density, flow velocity and temperature. Therefore, if we are to determine f at any given point $\mathbf{x}$ knowledge of the hydrodynamic fields in the whole system are required.

For small spatial variations i.e. low Knudsen numbers, The dependency can be localised in space via an expansion in the gradients of the hydrodynamic fields. This essentially says that the system can be completely described by the hydrodynamic fields as the velocity distribution is assumed to have reached an equilibrium. To realise this, f is written in a series expansion in a formal parameter ϵ measuring the non-uniformity of the system

$$f = f^{(0)} + \epsilon f^{(1)} + \epsilon^2 f^{(2)} + \dots, \tag{2.17}$$

where each factor of ϵ means an implicit gradient of a hydrodynamic field and is mainly used for book-keeping to label the orders of magnitude of different terms. This expansion also generates similar terms for the momentum and heat fluxes. To obtain the hierarchy of equations pertaining to each approximation of order $f^{(k)}$ from the Eq. 2.10, the operator ∇ is replaced with $\epsilon\nabla$ and the time derivative is expanded to read

$$\partial_t = \partial_t^{(0)} + \epsilon\partial_t^{(1)} + \epsilon^2\partial_t^{(2)}. \tag{2.18}$$

Since $f = f^{(0)}$, $\epsilon f^{(1)}$, $\epsilon^2 f^{(2)}$, ... only depend on time through the hydrodynamic fields, the operator $\partial_t^{(k)}$ is

$$\partial_t^{(k)} = (\partial_t^{(k)} n)\frac{\partial}{\partial n} + (\partial_t^{(k)}\mathbf{u})\cdot\frac{\partial}{\partial \mathbf{u}} + (\partial_t^{(k)}\Theta)\frac{\partial}{\partial \Theta}. \tag{2.19}$$

The macroscopic equations up to the Navier-Stokes order can then be found by expanding the terms in Eq. 2.10 up to the first order, collecting terms of the same order in ϵ, multiplying through by $\{1, m\mathbf{v}, \frac{1}{2}m\mathbf{v}^2\}$ and integrating over the phase velocity, $\mathbf{v}$ respectively. After lengthy algebra one then arrives at the same equations arrived at at the top of the section but this time the pressure-tensor and heat flux can be closed in terms of the hydrodynamic fields.

This then leads to:

$$\frac{\partial(\alpha_p\rho_p)}{\partial t} + \nabla\cdot(\alpha_p\rho_p\mathbf{u}_p) = 0, \tag{2.20}$$

$$\frac{\partial(\alpha_p\rho_p\mathbf{u}_p)}{\partial t} + \nabla\cdot(\alpha_p\rho_p\mathbf{u}_p\mathbf{u}_p + \alpha_p\rho_p\overline{\mathbf{P}}_p) = 0, \tag{2.21}$$

$$\frac{\partial(\alpha_p\rho_p\Theta)}{\partial t} + \nabla\cdot\left(\alpha_p\rho_p\Theta\mathbf{u}_p + \frac{2}{3}\alpha_p\rho_p\mathbf{q}\right) = -\frac{2}{3}\alpha_p\rho_p\overline{\mathbf{P}}_p : \nabla\mathbf{u}_p. \tag{2.22}$$

As their functional dependence on the distribution function f has been removed due to the CE approximation, constitutive relations for both the pressure tensor and heat flux can be derived. Both the pressure-tensor and heat flux comprise a kinetic and collisional contribution and constitutive relations will be provided for both later on.

This system of macroscopic equations then represent continuity, momentum and granular energy (temperature), respectively and make up the kinetic-theory-based continuum model [73, 93, 94].

2.2.2 Complete kinetic-theory-based continuum model

The kinetic-theory-based continuum model presented in §2.2.1 was derived without any coupling with the fluid-phase. In order to couple the model to the fluid-phase there are two options: one can couple the model at the continuum level or include the coupling term at the kinetic level. The former has been shown to lead to mathematical inaccuracies and can not be directly compared with E-L simulations [71, 73]. The latter approach provides a more mathematically exact approach and theoretically leads to the same solution as an E-L simulation if the mathematically and statistical errors are reduced accordingly [70]. Here, we follow the latter approach but omit a rigorous derivation and provide the main conceptual changes to the approach carried out in the previous section. The interested reader is refereed to Garzó et al. [73] for a rigorous derivation.

We begin by presenting the Enskog kinetic equation for a single particle velocity distribution function and include both a fluid force coupling term and a body force term leading to the form

$$\frac{\partial f}{\partial t} + \mathbf{v} \cdot \nabla f + \frac{\partial}{\partial \mathbf{v}}[\mathcal{A}f] + \mathbf{g} \cdot \frac{\partial f}{\partial \mathbf{v}} = J_E[\mathbf{x}, \mathbf{v}|f, f]. \tag{2.23}$$

The fluid-phase momentum coupling is provided through the force term, $\mathcal{A}$ and include the dominant physical mechanisms as highlighted in §1.9. The term is then written as:

$$\mathcal{A} = \frac{1}{\tau_p}(\mathbf{u}_f - \mathbf{v}) - \frac{1}{\rho_p}\nabla p_f, \tag{2.24}$$

where $\mathbf{u}_f$ is the instantaneous fluid velocity, τ_p is the particle relaxation time and p_f is the fluid pressure. The particles are assumed large enough to have their own inertia which allows the particle to deviate from the fluid velocity. The change in granular energy (temperature) due to the same forces [71, 73, 189] can be written as

$$\mathcal{E} = \frac{1}{\tau_p}\mathbf{v} \cdot (\mathbf{u}_f - \mathbf{v}) - \frac{3}{\tau_p}(\Theta_f - \Theta) - \frac{1}{\rho_p}\mathbf{v} \cdot \nabla p_f, \tag{2.25}$$

where Θ_f is the pseudo-turbulent kinetic energy of the fluid i.e. fluid velocity fluctuations due to particle wakes. This contribution is neglected due to the low particle Reynolds number investigated in this work. The drag term comprises of two separate contributions: the first is due to the exchange of kinetic energy between the phases and the second is due to the granular energy between the two phases.

From here the hydrodynamic model for the particle-phase can be derived by following an identical procedure to the one outlined in §2.2.1. This procedure then leads to a set of hydrodynamic equations that are coupled to the fluid-phase.

The continuity, momentum and granular energy transport equations for the complete kinetic-theory-based continuum model [73, 93, 94] reads:

$$\frac{\partial(\alpha_p\rho_p)}{\partial t} + \nabla\cdot(\alpha_p\rho_p\mathbf{u}_p) = 0, \tag{2.26}$$

$$\frac{\partial(\alpha_p\rho_p\mathbf{u}_p)}{\partial t} + \nabla\cdot(\alpha_p\rho_p\mathbf{u}_p\mathbf{u}_p + \alpha_p\rho_p\overline{\mathbf{P}}_p) = \alpha_p\rho_p(\mathcal{A}+\mathbf{g}), \tag{2.27}$$

$$\frac{\partial(\alpha_p\rho_p\Theta)}{\partial t} + \nabla\cdot\left(\alpha_p\rho_p\Theta\mathbf{u}_p + \frac{2}{3}\alpha_p\rho_p\mathbf{q}\right) = -\frac{2}{3}\alpha_p\rho_p\overline{\mathbf{P}}_p : \nabla\mathbf{u}_p + \alpha_p\rho_p(\mathcal{E}+\mathbf{u}_p\cdot\mathbf{g}). \tag{2.28}$$

From KT, the constitutive relations for the pressure tensor $\overline{\mathbf{P}}_p$ and the total granular energy flux $\mathbf{q}$ can be derived - these closure models can be found in §A.5.1 & §A.5.2. The relations directly rely on the three instantaneous values of the hydrodynamic variables and are a function of α_p, Θ and the rate of deformation tensor $\nabla\mathbf{u}_p + \nabla\mathbf{u}_p^T$ due to the CE expansion.

Now we can introduce the total granular energy:

$$e = \frac{1}{2}(\mathbf{u}_p\cdot\mathbf{u}_p + 3\Theta). \tag{2.29}$$

Then rewriting Eq. 2.28 into its conservative form:

$$\frac{\partial(\alpha_p\rho_p e)}{\partial t} + \nabla\cdot\left(\alpha_p\rho_p\mathbf{u}_p e + \alpha_p\rho_p\overline{\mathbf{P}}_p\cdot\mathbf{u}_p + \alpha_p\rho_p\mathbf{q}\right) = \alpha_p\rho_p(\mathcal{E}+\mathbf{u}_p\cdot\mathbf{g}). \tag{2.30}$$

This ensures that the naturally conserved variables of the particle-phase are α_p, $\mathbf{u}_p$ and e. We simply find Θ by invoking Eq. 2.29. Finally, the whole system of equations for the particle-phase read:

$$\frac{\partial(\alpha_p\rho_p)}{\partial t} + \nabla\cdot(\alpha_p\rho_p\mathbf{u}_p) = 0, \tag{2.31}$$

$$\frac{\partial(\alpha_p\rho_p\mathbf{u}_p)}{\partial t} + \nabla\cdot(\alpha_p\rho_p\mathbf{u}_p\mathbf{u}_p + \alpha_p\rho_p\overline{\mathbf{P}}_p) = \alpha_p\rho_p(\mathcal{A}+\mathbf{g}), \tag{2.32}$$

$$\frac{\partial(\alpha_p\rho_p e)}{\partial t} + \nabla\cdot\left(\alpha_p\rho_p\mathbf{u}_p e + \alpha_p\rho_p\overline{\mathbf{P}}_p\cdot\mathbf{u}_p + \alpha_p\rho_p\mathbf{q}\right) = \alpha_p\rho_p(\mathcal{E}+\mathbf{u}_p\cdot\mathbf{g}). \tag{2.33}$$

The corresponding equations for the fluid-phase can be found by invoking conservation of the volume fraction, $\alpha_p + \alpha_f = 1$. Thus, the continuity, momentum and energy for the fluid-phase read:

$$\frac{\partial(\alpha_f \rho_f)}{\partial t} + \nabla \cdot (\alpha_f \rho_f \mathbf{u}_f) = 0, \tag{2.34}$$

$$\frac{\partial(\alpha_f \rho_f \mathbf{u}_f)}{\partial t} + \nabla \cdot (\alpha_f \rho_f \mathbf{u}_f \mathbf{u}_f + \alpha_f \rho_f \overline{\mathbf{P}}_f) = -\alpha_p \rho_p \rho_f \mathcal{A} + \alpha_f \rho_f \mathbf{g}, \tag{2.35}$$

$$\frac{\partial(\alpha_f \rho_f e_f)}{\partial t} + \nabla \cdot (\alpha_f \rho_f \mathbf{u}_f e_f + \alpha_f \rho_f \overline{\mathbf{P}}_f \cdot \mathbf{u}_f + \alpha_f \rho_f \mathbf{q}_f) = -\alpha_p \rho_p \rho_f \mathcal{E} + (\alpha_f \mathbf{u}_f) \cdot \mathbf{g}. \tag{2.36}$$

The RHS contain the momentum coupling through drag and buoyancy. Here we define the fluid-phase pressure tensor as,

$$\overline{\mathbf{P}}_f = \frac{1}{\rho_f \alpha_f}(p_f \mathbf{I} - \overline{\boldsymbol{\sigma}}_f), \tag{2.37}$$

where the closure for the viscous stress tensor can be found in Table C.2. In this work the flow is assumed to be incompressible and therefore within the numerical implementation of the balance equations the density is divided out. In the fluid-phase, the energy equation is only required for compressible flows as the equation of state is required to formulate pressure. As this is not the case in this work, the equation is not solved nor is it presented in the further derivation of the Reynolds-Averaged model. From this full set of equations the final step of RA can be applied to find the macroscale turbulence model. Looking back briefly at Fig. 1.4, it can be seen that this makes up the necessary first step to arrive at a conceptual adequate model for the prediction of turbulent fluid-particle flows.

The full set of hydrodynamic equations are first RA (see Appendix A for the derivation) and then re-expressed in their Phase-Average (PA) or conditionally averaged form (Appendix B) in order to express the equations in their most compact form.

2.3 Reynolds-Averaged Two-Fluid Model

In this section the RA-TFM equations first presented by Fox [71] are given. The RA transport equations are presented in their conservative form and for clarity

the PA notation has been dropped. The full definition of the variables and the constitutive equations can be found in Appendix C and Tables C.1 & C.2.

The particle-phase continuity equation reads:

$$\frac{\partial(\alpha_p\rho_p)}{\partial t} + \nabla\cdot(\alpha_p\rho_p\mathbf{u}_p) = 0, \tag{2.38}$$

where α_p is the volume fraction of particles, ρ_p is the density of the particles and $\mathbf{u}_p$ is the particle-phase velocity.

The momentum balance equation for the particulate phase is given as:

$$\begin{aligned}\frac{\partial(\alpha_p\rho_p\mathbf{u}_p)}{\partial t} + \nabla\cdot(\alpha_p\rho_p\mathbf{u}_p\mathbf{u}_p) = \nabla\cdot(\alpha_p\rho_p\overline{\mathbf{R}}_{\mathrm{eff,p}}) + \beta\left[(\mathbf{u}_f-\mathbf{u}_p) - \frac{\nu_{ft}}{\mathrm{Sc}_{fs}\alpha_p\alpha_f}\nabla\alpha_p\right] \\ -\nabla p_p - \alpha_p\nabla p_f + \alpha_p\rho_p\left[1 - C_p\alpha_f\left(1-\frac{\rho_f}{\rho_p}\right)\right]\mathbf{g},\end{aligned} \tag{2.39}$$

where the first term on the RHS contains the particle Reynolds stress tensor that comprises two components: the particles laminar viscosity i.e. from uncorrelated granular temperature and the particles turbulent viscosity i.e. correlated turbulent kinetic energy. The second term is the momentum transfer term and contains both the slip velocity and a turbulent dispersion term. Through the denominator of the dispersion term $\mathrm{Sc}_{fp} = (k_f/k_p)^{1/2}$ a Stokes number (St) dependency is introduced, which accounts for dispersion for moderate to large St. The form of this equation enforces the correct behaviour, when there is a small St the particle turbulent kinetic energy $k_p \to k_f$ meaning Sc_{fp} is unity; for a large St, where k_p is deviates from k_f can either reduce or enhance dispersion through Sc_{fp}.

The third term is the gradient of particle pressure which is determined from the solution of the granular temperature equation (defined in App. C). The fourth term represents the coupling with the fluid-phase through its pressure gradient. The last term contains the body forces (i.e. gravity) and the velocity-fluid-pressure-gradient covariance term. This term represents the correlations between the velocity and pressure gradients which arise from buoyancy.

The particle Reynolds stress tensor is modelled by grouping the kinematic and turbulent viscosity into an effective viscosity, $\nu_{\text{eff,p}} = \nu_p + \nu_{pt}$ and employing the Boussinesq hypothesis [19]. Now, we can write the Reynolds stress tensor in the form:

$$\overline{\mathbf{R}}_{\text{eff,p}} = -2\nu_{\text{eff,p}}\overline{\mathbf{S}}_{\mathbf{p}} + \frac{2}{3}\mathbf{I}k_p. \tag{2.40}$$

The drag force defined as F_D and the drag transfer coefficient defined as β in Chapter 1 - Eq. 1.16 an expression for the inter-phase momentum coupling through drag can be written as:

$$F_D = \frac{\rho_p \alpha_p}{\tau_p}(\mathbf{u}_f - \mathbf{u}_p), \tag{2.41}$$

$$\beta = \frac{\rho_p \alpha_p}{\tau_p} = \frac{3}{4}\frac{\alpha_p \alpha_f \rho_f \mathbf{u}_r}{d_p} C_d, \tag{2.42}$$

$$C_d = \begin{cases} \frac{24}{Re_p}\left[1 + 0.15 Re_p^{0.287}\right] & \text{if } Re_p < 1000 \\ 0.44 & \text{if } Re_p \geq 1000, \end{cases} \tag{2.43}$$

where the expression, β has been multiplied by the fluid-phase volume fraction. This was shown in Rusche [164], Weller [210] to ensure that the drag term did not tend to 0 during its numerical implementation as the equations are implemented in their phase-intensive form i.e. divided by volume-fraction.

The fluid-phase continuity equation reads:

$$\frac{\partial(\alpha_f \rho_f)}{\partial t} + \nabla \cdot (\alpha_f \rho_f \mathbf{u}_f) = 0. \tag{2.44}$$

The momentum balance equation for the fluid-phase is given as:

$$\begin{aligned} \frac{\partial(\alpha_f \rho_f \mathbf{u}_f)}{\partial t} + \nabla \cdot (\alpha_f \rho_f \mathbf{u}_f \mathbf{u}_f) = \nabla \cdot (\alpha_f \rho_f \overline{\mathbf{R}}_{\text{eff,f}}) + \beta\left[(\mathbf{u}_p - \mathbf{u}_f) + \frac{\nu_{ft}}{\text{Sc}_{fs}\alpha_p \alpha_f}\nabla \alpha_p\right] \\ -\alpha_f \nabla p_f + \alpha_p \nabla p_f + \alpha_f \rho_f \left[1 + C_p \alpha_p \left(\frac{\rho_p}{\rho_f} - 1\right)\right]\mathbf{g}. \end{aligned} \tag{2.45}$$

The particle- and fluid-phase momentum equations are almost symmetric but with some key differences. The second term on the RHS includes the turbulence dispersion with an opposite sign, to ensure an exchange of forces between them. The third term is the mean fluid pressure gradient and the fourth term represents the buoyancy coupling with the particle-phase.

The fluid Reynolds stress tensor is modelled by grouping the kinematic and turbulent viscosity into an effective viscosity, $\nu_{\text{eff,f}} = \nu_f + \nu_{ft}$ and employing the Boussinesq hypothesis. Now, we can write the fluid Reynolds stress tensor in the form:

$$\overline{\mathbf{R}}_{\text{eff,f}} = -2\nu_{\text{eff,f}}\overline{\mathbf{S}}_{\mathbf{f}} + \frac{2}{3}\mathbf{I}k_f. \tag{2.46}$$

The turbulent kinetic energy transport equation for the fluid-phase takes the form:

$$\begin{aligned}\frac{\partial(\alpha_f\rho_f k_f)}{\partial t} + \nabla\cdot(\alpha_f\rho_f k_f\mathbf{u}_f) = \nabla\cdot\left[\left(\mu_f + \frac{\mu_{ft}}{\sigma_{fk}}\right)\nabla k_f\right] + \alpha_f\rho_f\Pi_f - \alpha_f\rho_f\varepsilon_f \\ +2\beta(k_{fp} - k_f) + \alpha_p\rho_p\Pi_{fp} + \alpha_p\rho_p\Pi_{\rho f},\end{aligned} \tag{2.47}$$

where the first term on the RHS is the fluid-phase turbulent kinetic energy flux. The second term Π_f represents kinetic energy production due to mean shear, with the third term being the turbulent kinetic energy dissipation. The remaining three terms are the coupling terms: velocity correlations, mean slip and volume-fraction-velocity correlations, respectively.

The turbulent kinetic energy dissipation transport equation for the fluid-phase reads as:

$$\begin{aligned}\frac{\partial(\alpha_f\rho_f\varepsilon_f)}{\partial t} + \nabla\cdot(\alpha_f\rho_f\varepsilon_f\mathbf{u}_f) = \nabla\cdot\left[\left(\mu_f + \frac{\mu_{ft}}{\sigma_{fk}}\right)\nabla\varepsilon_f\right] + \frac{\varepsilon_f}{k_f}\left[C_1\alpha_f\rho_f\Pi_f - C_2\alpha_f\rho_f\varepsilon_f\right] \\ +2C_3\beta(\varepsilon_{fp} - \varepsilon_f) + C_4\frac{\varepsilon_p}{k_p}\alpha_p\rho_p\Pi_{fp} + C_5\frac{\varepsilon_p}{k_p}\alpha_p\rho_p\Pi_{\rho f},\end{aligned} \tag{2.48}$$

where the first term on the RHS is the fluid-phase turbulent kinetic dissipation energy flux. The second term Π_f is kinetic energy production due to mean shear with the third term is dissipation. The remaining three terms are the coupling

terms: velocity correlations, mean slip and volume-fraction-velocity correlations, respectively. The forms of these are as follows:

$$\Pi_f = 2\nu_{ft}\overline{\mathbf{S}}_\mathbf{f} : \overline{\mathbf{S}}_\mathbf{f} + \frac{2}{3}k_f \nabla \cdot \mathbf{u}_f, \tag{2.49}$$

$$\Pi_{fp} = \left[C_g(\mathbf{u}_p - \mathbf{u}_f) - \frac{\nu_{ft}}{Sc_{fp}\alpha_p\alpha_f}\nabla\alpha_p\right] \cdot \left[\beta(\mathbf{u}_p - \mathbf{u}_f) + \frac{1}{\rho_p}\nabla p_f\right], \tag{2.50}$$

$$\Pi_{\rho f} = C_\rho\left(1 - \frac{\rho_f}{\rho_p}\right)\left[C_g\alpha_p\alpha_f(\mathbf{u}_p - \mathbf{u}_f) - \frac{\nu_{ft}}{Sc_{fp}}\nabla\alpha_p\right] \cdot \mathbf{g}, \tag{2.51}$$

where Π_f is the production of the turbulent kinetic energy, Π_{fp} is due to mean slip and $\Pi_{\rho f}$ is due to volume-fraction-velocity correlations.

The co-variance or cross-coupling terms take the form of $k_{fp} = \beta_k\sqrt{k_f k_p}$ and $\varepsilon_{fp} = \beta_\varepsilon\sqrt{\varepsilon_f\varepsilon_p}$, where the correlation coefficients are $0 < \beta_k,\ \beta_\varepsilon \leq 1$. These terms represent the fluid-velocity covariance and their exact closure is still uncertain, a detailed discussion on this point can be found in [71]. This form is adopted as it shows correct limiting behaviour for large St as well as diminishing to zero in the absence of the particulate phase.

The particle-phase turbulent kinetic energy, which represents the correlated macroscale energy, reads as:

$$\begin{aligned}\frac{\partial(\alpha_p\rho_p k_p)}{\partial t} + \nabla\cdot(\alpha_p\rho_p k_p\mathbf{u}_p) = \nabla\cdot\left[\left(\mu_p + \frac{\mu_{pt}}{\sigma_{pk}}\right)\nabla k_p\right] + \alpha_p\rho_p\Pi_p - \alpha_p\rho_p\varepsilon_p \\ +2\beta(k_{fp} - k_p) + \alpha_p\rho_p\Pi_{\rho p},\end{aligned} \tag{2.52}$$

where the first term on the RHS is the particle-phase turbulent kinetic energy flux. The second term Π_p is kinetic energy production due to mean shear with the third term being the particle turbulent kinetic energy dissipation. The remaining two terms are the coupling terms: velocity correlations, and the combination of the buoyancy induced and mean slip terms.

The particle-phase turbulent kinetic energy dissipation transport equation reads:

$$\frac{\partial(\alpha_p\rho_p\varepsilon_p)}{\partial t}+\nabla\cdot(\alpha_p\rho_p\varepsilon_p\mathbf{u}_p)=\nabla\cdot\left[\left(\mu_p+\frac{\mu_{pt}}{\sigma_{pk}}\right)\nabla\varepsilon_p\right]+\frac{\varepsilon_p}{k_p}(C_1\alpha_p\rho_p\Pi_p-C_2\alpha_p\rho_p\varepsilon_p)$$
$$+2C_3\beta(\varepsilon_{fp}-\varepsilon_p)+C_5\frac{\varepsilon_p}{k_p}\alpha_p\rho_p\Pi_{\rho p}, \tag{2.53}$$

where the first term on the RHS is the particle-phase turbulent kinetic dissipation energy flux. The second term Π_p is kinetic energy production due to mean shear with the third term being its dissipation. The remaining two terms are the coupling terms: velocity correlations, and the combination of the buoyancy induced and mean slip terms. The second term contains, Π_p which is the production of the turbulent kinetic energy and is expressed as:

$$\Pi_p=2\nu_{pt}\overline{\mathbf{S}}_\mathbf{p}:\overline{\mathbf{S}}_\mathbf{p}+\frac{2}{3}k_p\nabla\cdot\mathbf{u}_p. \tag{2.54}$$

It should be noted here that the final term on the RHS is a compressive term that appears in compressible turbulence modelling and plays a similar role to the bulk viscosity found in the typical granular temperature formulations in the literature [141], [198]. Finally, the buoyancy-induced source term $\Pi_{\rho f}$ is added to the mean slip Π_{fp} to be reformulated as $\Pi_{\rho p}$ which is read as:

$$\Pi_{\rho p}=C_\rho C_p\alpha_f\left(1-\frac{\rho_f}{\rho_p}\right)(\mathbf{u}_p-\mathbf{u}_f)\cdot\mathbf{g}. \tag{2.55}$$

The granular temperature equation, which represents the uncorrelated collisional energy, reads:

$$\frac{3}{2}\left[\frac{\partial(\alpha_p\rho_p\Theta)}{\partial t}+\nabla\cdot(\alpha_p\rho_p\Theta\mathbf{u}_p)\right]=\nabla\cdot\left[\left(\kappa_\Theta+\frac{3\mu_{pt}}{2Pr_{pt}}\right)\nabla\Theta\right]+2\mu_p\overline{\mathbf{S}}_\mathbf{p}:\overline{\mathbf{S}}_\mathbf{p}$$
$$-p_p\nabla\cdot\mathbf{u}_p+\alpha_p\rho_p\varepsilon_p-3\beta\Theta-\gamma, \tag{2.56}$$

where the first term on the RHS is the granular temperature flux which is made up of two contributions, the granular conductivity flux and the turbulent granular flux. The former consists of a constitutive closure that is given by Syamlal and O'Brien [184] and is used as it correctly tends to zero in the dilute limit [198]. The latter term is the turbulent flux and includes the particle turbulent viscosity. The

second term is a laminar source term due to viscous stresses. The third term is a pressure dilation term which accounts for compressibility. The fourth term is of particular interest, as it represents the turbulent particle kinetic energy dissipation which appears here as a source term. The physical interpretation of this means that as large scale particle turbulent kinetic energy is dissipated, small scale granular temperature is produced. The two remaining terms represent decrease of granular temperature due to drag and decrease of granular temperature due to inelastic collisions.

The full form of the equations have been presented here with no mention of their relevance to the flow regime being simulated in this work. As the density ratio is high the buoyancy induced terms are expected to be negligible. The coefficient $C_g \to 0$ and $C_p \to 0$ due to the small mass loading and high density ratios respectively, used in this work, a more thorough discussion on this topic can be found in [27, 28, 71]. Similarly, the compressible turbulence correction terms depend on the particle-phase Mach number, which is expected to be large for large St. Given the St numbers used in this study this is not expected to be the case. In general these terms are neglected throughout this work unless otherwise stated.

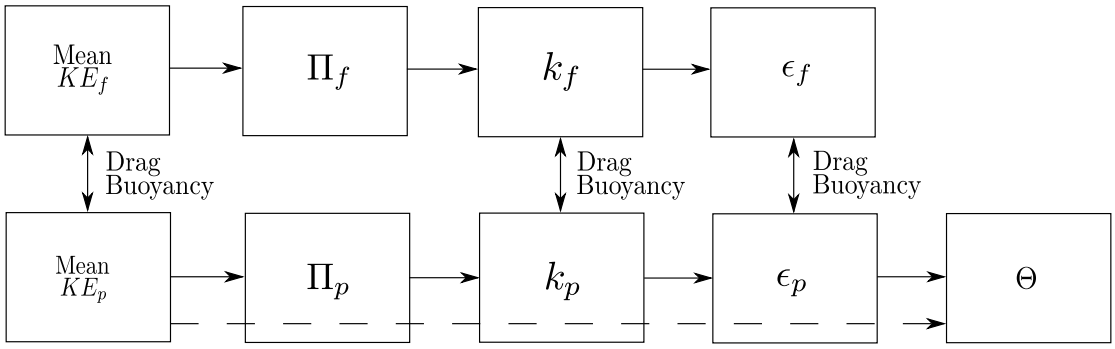

Figure 2.1: Schematic showing the energy cascade between each variable within the multiphase model [71]. The interaction between each quantity is shown along with their respective energy transfer mechanisms. The dashed line represents the energy flow in the (mesoscale) laminar model.

Fig. 2.1 shows an overall picture of the RA-TFM. As can be seen the energy cascade is almost identical in both phases. Starting with the mean particle kinetic

energy $\frac{1}{2}\mathbf{u}_p \cdot \mathbf{u}_p$, the energy transfer to the turbulent particle kinetic energy is given by the production term which is Π_p i.e. the shear. This then generates k_p and is dissipated by the turbulent kinetic energy dissipation equation. Finally, this dissipation term ε_p appears in the granular temperature Θ as a source term, meaning that as the particle turbulent kinetic energy dissipates, granular energy is produced. Both turbulent quantities interact via drag and buoyancy terms in the same way the governing equations do. If there is dissipation due to collisions, the granular temperature is reduced due to particle heating.

2.4 Microscale-based-macroscale model

In the literature many two-fluid models have been derived by applying an averaging procedure to the microscale model to arrive at a macroscale model [7, 54, 88]. For the sake of brevity the basic idea behind the approach will be outlined with the crucial modelling decisions being highlighted. For a full treatise the interested reader is referred to [7, 54, 62, 141].

The most commonly used derivation for fluid-particle flows is that of Anderson and Jackson [7]. In their work a local spatial average of the variables in the system of interest, taken over regions small compared with the length scale of the problem considered i.e. volume-averaging. Although alternatives exist in which one can average at each point over an ensemble of macroscale equivalent systems. Both lead to a very similar system of equations Zhang and Prosperetti [223].

Firstly, a mathematical definition of local mean variables is defined in order to translate the local instantaneous Navier-Stokes equations for the fluid-phase and Newton's equation of motion for a single particle into continuum equations. These then represent the continuity and momentum of each phase, respectively. The local instantaneous variables are first volume-averaged over regions that are larger than the particle diameter to arrive at expressions for the average of a point property e.g. velocity. These averaging rules are then applied to the point continuity and momentum balances resulting in a macroscale system of equations that has been derived from a local average of the microscale.

From here the particle-pressure tensor is closed using an analogy from kinetic theory Chapman and Cowling [38]. This constitutes a kinetic and collisional contribution and are largely based on the relations derived by Lun et al. [117]. The exact closures can be found in Appendix C. As described previously (see §1.3) a direct analogy between the thermodynamic temperature for gases in introduced. The granular temperature is introduced as a measure of the particle velocity fluctuations, $\frac{3}{2}\langle\Theta\rangle_p = \frac{1}{2}\langle\mathbf{u}_p'' \cdot \mathbf{u}_p''\rangle_p$. From here the temperature equation derived from

the collisional Boltzmann equation can be used to describe the particle fluctuation energy.

We begin at the E-E equations presented by Anderson and Jackson [7], Peirano and Leckner [141] which will be hereafter labelled the Modified Peirano Model (MPM). Note here that we compare against the form of the RA-TFM equations that have been simplified i.e. neglecting buoyancy correlation terms. These are presented in Chapter 5 and as such will be forward referenced.

The continuity equations for each phase read:

$$\frac{\partial(\alpha_p\rho_p)}{\partial t} + \nabla\cdot(\alpha_p\rho_p\mathbf{u}_p) = 0, \tag{2.57}$$

$$\frac{\partial(\alpha_f\rho_f)}{\partial t} + \nabla\cdot(\alpha_f\rho_f\mathbf{u}_f) = 0. \tag{2.58}$$

The momentum balance equation for the particle-phase:

$$\frac{\partial(\alpha_p\rho_p\mathbf{u}_p)}{\partial t} + \nabla\cdot(\alpha_p\rho_p\mathbf{u}_p\mathbf{u}_p) = \nabla\cdot(\alpha_p\rho_p\overline{\mathbf{R}}_{\text{eff,p}}) + \beta\left[(\mathbf{u}_f-\mathbf{u}_p) - \frac{\nu_{ft}}{\text{Sc}_{fs}\alpha_p\alpha_f}\nabla\alpha_p\right] - \nabla p_p - \alpha_p\nabla p_f + \alpha_p\rho_p\mathbf{g}. \tag{2.59}$$

In the momentum equation for the particle-phase it can be seen that when comparing term-by-term with Eq. 4.2 there is one main differences - the effective viscosity within the particles Reynolds stress tensor. The effective viscosity just contains the granular contribution i.e. ν_p as the turbulent viscosity contribution does not exist within this methodology.

The momentum balance equation for the fluid-phase:

$$\frac{\partial(\alpha_f\rho_f\mathbf{u}_f)}{\partial t} + \nabla\cdot(\alpha_f\rho_f\mathbf{u}_f\mathbf{u}_f) = \nabla\cdot(\alpha_f\rho_f\overline{\mathbf{R}}_{\text{eff,p}}) + \beta\left[(\mathbf{u}_p-\mathbf{u}_f) + \frac{\nu_{ft}}{\text{Sc}_{fs}\alpha_p\alpha_f}\nabla\alpha_p\right] - \alpha_f\nabla p_f + \alpha_f\rho_f\mathbf{g}. \tag{2.60}$$

In the momentum equation for the fluid-phase it can be seen that the equations are identical with Eq. 4.4 as the buoyancy contribution has been neglected.

In order to close the particle-phase momentum equation the particle fluctuation energy is closed using KT. The temperature is defined such that

$$\Theta = \frac{1}{3}(\mathbf{u}_p'' \cdot \mathbf{u}_p''), \tag{2.61}$$

where $\mathbf{u}_p''$ is the particle fluctuation velocity which represents the uncorrelated energy. The derivation of the temperature transport equation is identical to the one followed in §2.2.1. The form here is slightly different due to the inclusion of covariance terms. The granular temperature equation [76, 141] is then:

$$\begin{aligned}\frac{3}{2}\left[\frac{\partial(\alpha_p\rho_p\Theta)}{\partial t} + \nabla\cdot(\alpha_p\rho_p\Theta\mathbf{u}_p)\right] = \nabla\cdot(\kappa_\Theta\nabla\Theta) + \overline{\boldsymbol{\sigma}} : \nabla\mathbf{u}_p + p_p\mathbf{I} : \nabla\mathbf{u}_p \\ + J_{vis} + J_{slip} - \gamma_p,\end{aligned} \tag{2.62}$$

where the first term on the RHS is the granular temperature flux (dissipation) which is the granular conductivity or heat flux in the terminology used in §2.2.1. The second and third terms fluctuation energy created by the shearing and pressure in the particle-phase i.e. kinetic and collisional contributions. The remaining terms are energy source/sink terms due to viscous damping, drag and inter-particle collisions.

The particle pressure and inter-particle collision term are defined in Appendix. C. We write the particle stress tensor as

$$\overline{\boldsymbol{\sigma}} = \mu_p[\nabla\mathbf{u}_p + \nabla^T\mathbf{u}_p] + (\lambda - \frac{2}{3}\mu_p)(\nabla\cdot\mathbf{u}_p)\mathbf{I}. \tag{2.63}$$

Finally, J_{vis} and J_{slip} are dissipation of granular temperature due to viscous damping and creation of granular temperature from the energy exchange between the fluid- and particle-phases. Both terms can be written more intuitively to read:

$$J_{vis} + J_{slip} = \beta(\mathbf{u}_p'' \cdot \mathbf{u}_p'' - \mathbf{u}_p'' \cdot \mathbf{u}_f'''). \tag{2.64}$$

The first term can be modeled as 3Θ according to Gidaspow [76] and the last term can be modeled as k_{pf}, which is the fluid-particle covariance term and its closure will be presented later.

Comparing Eq. 2.62 with its counterpart in the RA-TFM - Eq. 2.56 highlights some conceptual differences. Firstly, the dissipative term contains a secondary contribution in the latter equation from the turbulent viscosity. Secondly, the source term ε_p does not exist in the current methodology as the macroscale correlated energy is not accounted for. Lastly, velocity covariance, k_{pf} term exists in the granular temperature equation meaning that the granular temperature exchanges energy with both the mean momentum equations through, $3\beta\Theta$ and the fluid-phase energy through $k_{pf} = c_{pf}\sqrt{k_f\Theta}$ [176].

The transport equations for the fluid-phase turbulence model $k_f - \varepsilon_f$ reads as follows:

$$\frac{\partial(\alpha_f\rho_f k_f)}{\partial t}+\nabla\cdot(\alpha_f\rho_f k_f\mathbf{u}_f) = \nabla\cdot\left[\left(\mu_f+\frac{\mu_{ft}}{\sigma_{fk}}\right)\nabla k_f\right]+\alpha_f\rho_f\Pi_f-\alpha_f\rho_f\varepsilon_f+\Pi_{kf}, \quad (2.65)$$

$$\frac{\partial(\alpha_f\rho_f\varepsilon_f)}{\partial t}+\nabla\cdot(\alpha_f\rho_f\varepsilon_f\mathbf{u}_f) = \nabla\cdot\left[\left(\mu_f+\frac{\mu_{ft}}{\sigma_{fk}}\right)\nabla\varepsilon_f\right]+\frac{\varepsilon_f}{k_f}\left[C_1\alpha_f\rho_f\Pi_f-C_2\alpha_f\rho_f\varepsilon_f+C_3\Pi_{kf}\right], \quad (2.66)$$

where all the terms have an identical meaning to those presented in §2.3 except for the final term, Π_{kf} which introduces the particle velocity covariance term. This physically represents the velocity fluctuation correlation of each phase and is written as,

$$\Pi_{kf} = -\beta(2k_f - k_{pf} - |\mathbf{u}_r|\mathbf{u}_d), \quad (2.67)$$

where the term $\mathbf{u}_d$ accounts for turbulence dispersion and is also known as the drift velocity. Here it is given from the formulation of Simonin [173].

$$\mathbf{u}_d = -\nu_{ft}\left(\frac{1}{\alpha_p}\nabla\alpha_p - \frac{1}{\alpha_f}\nabla\alpha_f\right). \quad (2.68)$$

Comparing the macroscale turbulence modelling in the MPM with the RA-TFM i.e. Eqs. 2.47 & 2.48 reveals some interesting differences. Firstly, the coupling term due to velocity correlations has a different characteristic energy i.e. Θ in MPM and k_p in RA-TFM. This has some important ramifications that are explored within

Chapter 5. Both contain a production term due to mean slip i.e. dispersion, although the adopted form is slightly different.

The most fundamental difference between the modes is the fact that in the MPM the energy exchange mechanisms occur across the the granular energy equation and the fluid-phase momentum and turbulent kinetic energy i.e. Θ with the $k_f - \varepsilon_f$ equation. These exchange energy through drag. As discussed in §1.3 the granular energy represents mesoscale interactions i.e. kinetic collisional energy that is conceptually on a different scale to the mean fluid-phase equations. Omitting this leads to a granular temperature equation in which two energy exchange mechanisms are present.

When the MPM equations are solved, numerically artificial bounding is common as the granular temperature equation can only dissipate energy through inelastic collisions or drag. The drag coupling is provided through Π_{kf} which couples the macroscale turbulence of the fluid-phase with the mesoscale granular temperature - two physically different mechanisms. Usually, from the author's experience, this ensures that a large spike of production is experienced throughout the simulation as the mean momentum and energy contribute to the granular/fluctuation energy production. Conversely, in the RA-TFM a dissipative length scale exists, ε_p that ensures the energy cascades towards viscous heating (see Fig. 2.1). This acts as its own "soft" limit throughout the simulation as the energy is produced and dissipated through physically and mathematically similar sources. This has the auxiliary benefit of increasing the robustness of the numerical solution as the terms evolve "naturally" resulting in less iterations e.g. high spikes in source terms require smaller time steps.

2.5 Fluid-phase elliptic relaxation model

In this section the elliptic relaxation model of Durbin [56] is derived within the RA-TFM framework in order to circumvent the near-wall region issues highlighted in §1.6. The model provides two additional transport equations which are solved in conjunction with the $k_f - \varepsilon_f$ transport equations and will be investigated further in Chapter 6.

As discussed in §1.6 there exists an adverse effect on the single-point closure employed in RA turbulence modelling due to the presence of the wall. Figure 2.2 offers two ways of interpretation the effect of the wall. The first suggests that there is an additional source i.e. wall echo that adds a reflected pressure wave. The incorporation of this methodology into the Reynolds stress transport equation is tricky and results in a wall sensitive model [75] that retains the same issues as damping functions. The second approach, seen on the right, suggests that image vorticity exists that accounts for the blocking effect of the wall.

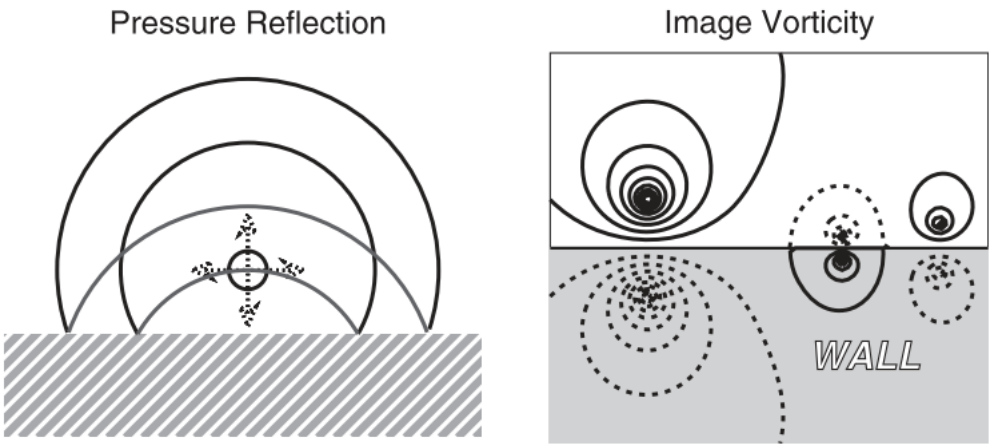

Figure 2.2: Schematic representation of nonlocal wall influences. The left shows pressure reflection characterised as a pressure wave. On the right, image vorticity characterises the blocking effect of a solid wall Durbin and Reif [58].

This kinematic blocking constraint arises due to the no-flux condition, $\mathbf{u} \cdot \mathbf{n} = 0$

and is a continuity effect and thus can not be found via manipulation of the Navier-Stokes equation. It ultimately results in the solution of Laplace's equation which holds the attractive quality of being wall-independent. This does not depend on Reynolds stress dynamics but works to suppress momentum transfer into the wall-normal component as the wall is approach which seems intuitive when examining the right hand side of Fig. 2.2.

The effect of this process indirectly enters the Reynolds stress transport equation via the velocity-pressure gradient. As the wall is approached the gradient is altered in the wall-normal direction. The term of interest is the pressure-strain in the exact RA Reynolds Stress transport Eq. 2.69. From this equation the elliptic relaxation model of Durbin [56] can be derived within a RA-TFM methodology.

We begin with the exact RA Reynolds Stress transport equation for the fluid-phase which is found by Reynolds-Averaging the PA velocity tensor transport equation and subtracting the PA fluid-phase mean velocity tensor transport equation. The derivation of which can be found in Appendix A - Eq. A.32.

$$\begin{aligned}\frac{\partial\langle\alpha_f\rangle\langle\mathbf{u}_f'''\otimes\mathbf{u}_f'''\rangle_f}{\partial t}+\nabla\cdot\langle\alpha_f\rangle\langle\mathbf{u}_f\rangle_f\otimes\langle\mathbf{u}_f'''\otimes\mathbf{u}_f'''\rangle_f &= -\nabla\cdot\langle\alpha_f\rangle\langle\mathbf{u}_f'''\otimes\mathbf{u}_f'''\otimes\mathbf{u}_f'''\rangle_f \\ &\quad -\underbrace{\langle\alpha_f\rangle(\langle\mathbf{u}_f'''\otimes\mathbf{u}_f'''\rangle_f\cdot\nabla\langle\mathbf{u}_f\rangle_f)}_{\text{Production}}+\frac{1}{\rho_f}\nabla\cdot\langle\overline{\boldsymbol{\sigma}}_f\otimes\mathbf{u}_f'''\rangle-\frac{1}{\rho_f}\nabla\langle p_f\mathbf{u}_f'''\rangle \\ &\quad +\underbrace{\frac{1}{\rho_f}\langle p_f\nabla\mathbf{u}_f'''\rangle}_{\text{pressure strain, }\phi_{f,yy}}-\underbrace{\frac{1}{\rho_f}\langle\overline{\boldsymbol{\sigma}}_f\cdot\nabla\mathbf{u}_f'''\rangle}_{\text{dissipation, }\varepsilon_{f,yy}}+\langle\alpha_f\rangle\beta(\underbrace{\langle\mathbf{u}_f'''\otimes\mathbf{u}_p''\rangle_p-\langle\mathbf{u}_f'''\otimes\mathbf{u}_f'''\rangle_p}_{\text{velocity correlations}})\end{aligned} \tag{2.69}$$

Many of these terms are familiar from the compressible Reynolds stress transport equations. The first term on the right hand side is the transport due to turbulent flux term with the second responsible for turbulence production. The terms of particular interest are the pressure strain, responsible for redistribution, and dissipation.

The velocity correlations which arise due to phase coupling are modelled analogously to those terms found in the $k_f-\varepsilon_f$ transport equations. We set the covariance of the fluctuations $\langle\mathbf{u}_f'''\otimes\mathbf{u}_p''\rangle_p=\overline{v_{fp}^2}=\beta_v\sqrt{\overline{v_p^2}\overline{v_f^2}}$, where $\overline{v_p^2}=2/3k_p$ owing to its

definition. The correlation factor, $\beta_v = 1$ along with the correlation factors found in the transport equations for turbulent kinetic energy and dissipation are all set to 1. This is a crude first approximation and the correlation factor should depend on both mass loading and Stokes number. This is out of the scope of this work as only a weak dependency through the relatively low mass loadings is expected.

Following the approach used in classic eddy-viscosity turbulence models, the divergence terms appearing in the transport equation are closed by the eddy-viscosity approximation [142]. This reads as:

$$\nabla \cdot \left[\frac{\mu_{ft}}{\sigma_{fk}} \nabla \langle \mathbf{u}_f''' \otimes \mathbf{u}_f''' \rangle_f \right] \approx -\nabla \cdot \langle \alpha_f \rangle \langle \mathbf{u}_f''' \otimes \mathbf{u}_f''' \otimes \mathbf{u}_f''' \rangle_f + \frac{1}{\rho_f} \nabla \cdot \langle \overline{\boldsymbol{\sigma}}_f \otimes \mathbf{u}_f''' \rangle - \frac{1}{\rho_f} \nabla \langle p_f \mathbf{u}_f''' \rangle. \tag{2.70}$$

Finally, the terms left to close are the pressure strain and dissipation terms. These terms are explicitly modelled in the $\overline{v_f^2} - f$ model equations and are grouped into a source term denoted $k_f f$,

$$k_f f = \underbrace{\phi_{f,yy}}_{\text{pressure strain}} - \underbrace{\varepsilon_{f,yy}}_{\text{dissipation}} + \alpha_f \rho_f 6 \frac{\overline{v_f^2}}{k_f} \varepsilon_f. \tag{2.71}$$

The source term effectively redistributes turbulence energy from the stream-wise Reynolds stress component to the wall-normal component. This is intuitive as previously discussed, when one considers a fully developed turbulent boundary layer as the wall-normal Reynolds stress component's production is zero due to the mean stream-wise flow gradient. Therefore, turbulent kinetic energy can only enter the wall-normal component through redistribution. The original form of the source term has been shown to overproduce in regions relatively far away from the wall and the correction of Davidson et al. [50] is thus employed, this then reads:

$$\overline{v_f^2}_{source} = \min\left\{ k_f f,\ -\frac{1}{T}\left[(C_1 - 6)\overline{v_f^2} - \frac{2k_f}{3}(C_1 - 1) \right] + C_2 \Pi_f \right\}. \tag{2.72}$$

Finally, setting the wall-normal component of the fluid-phase Reynolds stress tensor $\langle \mathbf{u}_f''' \otimes \mathbf{u}_f''' \rangle_f$ to $\overline{v_f^2}$ a transport equation can be written as:

$$\frac{\partial(\alpha_f\rho_f\overline{v_f^2})}{\partial t}+\nabla\cdot(\alpha_f\rho_f\overline{v_f^2}\mathbf{u}_f)=\nabla\cdot\left[\left(\mu_f+\frac{\mu_{ft}}{\sigma_{fk}}\right)\nabla\overline{v_f^2}\right]+\alpha_f\rho_f\overline{v_f^2}_{source}-\alpha_f\rho_f 6\frac{\overline{v_f^2}}{k_f}\varepsilon_f +2\beta(\overline{v_{fp}^2}-\overline{v_f^2}). \tag{2.73}$$

The reader should note that the third term on the RHS is a sink term that is used to balance the source term $k_f f$. This is a modification proposed by Lien and Kalitzin [114] and ensures that the source term $k_f f \to 0$ as it approaches the wall.

Equation 2.73 contains no sensitivity to the wall, this is introduced through a modified Helmholtz equation which forms an elliptic relaxation equation. The form of this equation accounts for anisotropy close to walls and is also independent of Reynolds number and y^+ value which reads:

$$L^2\frac{\partial^2 f}{\partial x^2}-f=\underbrace{\frac{C_1}{T}\left(\frac{\overline{v_f^2}}{k_f}-\frac{2}{3}\right)}_{\phi_{f,yy,S}}-\underbrace{C_2\frac{\Pi_f}{k_f}}_{\phi_{f,yy,R}}-\frac{1}{T}\left(6\frac{\overline{v_f^2}}{k_f}-\frac{2}{3}\right). \tag{2.74}$$

The terms $\phi_{f,yy,S}$ and $\phi_{f,yy,R}$ are the so-called slow and rapid pressure-strain terms [108, 142]. It's important to recall here that the modified Helmholtz equation is a re-expression of the Poissons equation of the exact pressure-rate-of-strain tensor [142]. The form of the slow pressure-strain term is similar to Rotta's return to isotropy model [160] in which the rate of the return to isotropy is related to the anistropy of the flow via a linear relationship. Physically this model suggests that as the turbulence decays it has a tendency to become more isotropic. The rapid term contains the mean-flow gradients through the production of turbulent kinetic energy and as such can respond to immediate changes in the flow. The final term being used to ensure far field behaviour i.e. that the elliptic relaxation function diminishes away from walls.

In the original formulation of this equation as given by Durbin [56] the boundary condition for f contains the wall distance to the fourth power in its denominator. This lead to computational stiffness and numerical oscillations in the near-wall region. This issue was resolved by Lien and Kalitzin [114] by introducing the terms: $6\frac{\overline{v_f^2}}{k_f}$ as a sink and source in the $k_f f$ source term, the $\overline{v_f^2}$ transport equation

and the elliptical relaxation equation, f. This ensures that f tends to 0 at the wall enabling a Dirichlet boundary condition to be prescribed. The turbulent viscosity is calculated from the solution of the $\overline{v_f^2} - f$ model and due to the near-wall behaviour of k_f a correction is employed to avoid singularities. The correction of Davidson et al. [50] is employed and the definition of the turbulent viscosity now reads

$$\nu_{ft} = \min\Big\{C_{f\mu} k_f^2/\varepsilon_f,\ C_\mu \overline{v_f^2} T\Big\}, \tag{2.75}$$

where the turbulent time and length scales are defined as

$$T = \max\left(\frac{k_f}{\varepsilon_f}, 6\sqrt{\frac{\nu_f}{\varepsilon_f}}\right), \tag{2.76}$$

$$L = \max\left(\frac{k_f^{3/2}}{\varepsilon_f}, C_\eta \frac{\nu_f^{3/4}}{\varepsilon_f^{1/4}}\right). \tag{2.77}$$

Both time and length scales are limited in regions close to the wall. This is achieved by introducing a dependency on Kolmogorov scales which are only active in regions very close to the wall i.e. $\mathrm{y}^+ < 5$. This ensures that a singularity is not introduced into the solution matrix and that the scales collapse at the wall. Another modification close to the wall is to modify the "constant" $C_{\varepsilon 1}$ by damping it in the near-wall region by employing the following formulation

$$C_{\varepsilon 1} = 1.4\left(1 + 0.05\sqrt{k_f/\overline{v_f^2}}\right). \tag{2.78}$$

Wall boundary conditions for ε_f can be found by a Taylor expansion around the no-slip condition at the wall [142] and the employing the aforementioned modifications from Lien and Kalitzin [114] which reads as

$$\varepsilon_f \to 2\nu_f \frac{k_f}{\mathrm{y}^2}. \tag{2.79}$$

For the remaining variables the following boundary conditions at the wall are prescribed, $k_f = \overline{v_f^2} = f = 0$.

2.6 Particle-phase elliptic relaxation model

In this section we propose a elliptic relaxation model for the particle-phase. Within the E-E framework we assume continuous inter-penetrating phenomena and both phases share their pressure field. Additionally, we assume the presence of correlated particle-phase turbulent kinetic energy thus ensuring that the macroscale i.e. integral scale, exists. Recognising this is crucial for justifying the modelling decisions. We propose that the pressure reflection caused by the wall is felt in both phases and as a result a elliptic relaxation model can be relevant for each phase.

In an analogous manner to the fluid-phase, the transport equation for the Reynolds stress tensor can be found by Reynolds-Averaging the PA velocity tensor transport equation and subtracting the PA particle-phase mean velocity tensor transport equation, a derivation of which can be found in Appendix A - Eq. A.22.

$$\begin{aligned}\frac{\partial\langle\alpha_p\rangle\langle\mathbf{u}_p''\otimes\mathbf{u}_p''\rangle_p}{\partial t}+\nabla\cdot\langle\alpha_p\rangle\langle\mathbf{u}_p\rangle_p\otimes\langle\mathbf{u}_p''\otimes\mathbf{u}_p''\rangle_p &= -\nabla\cdot\langle\alpha_p\rangle\langle\mathbf{u}_p''\otimes\mathbf{u}_p''\otimes\mathbf{u}_p''\rangle_p \\ &\underbrace{-\langle\alpha_p\rangle(\langle\mathbf{u}_p''\otimes\mathbf{u}_p''\rangle_p\cdot\nabla\langle\mathbf{u}_p\rangle_p)}_{\text{Production}}+\frac{1}{\rho_p}\nabla\cdot\langle\overline{\boldsymbol{\sigma}}_p\otimes\mathbf{u}_p''\rangle-\frac{1}{\rho_p}\nabla\langle p_p\mathbf{u}_p''\rangle \\ +\underbrace{\frac{1}{\rho_p}\langle p_p\nabla\mathbf{u}_p''\rangle}_{\text{pressure strain, }\phi_{p,yy}} &\underbrace{-\frac{1}{\rho_p}\langle\overline{\boldsymbol{\sigma}}_p\cdot\nabla\mathbf{u}_p''\rangle}_{\text{dissipation, }\varepsilon_{p,yy}}+\langle\alpha_p\rangle\beta(\underbrace{\langle\mathbf{u}_f'''\otimes\mathbf{u}_p''\rangle_p-\langle\mathbf{u}_p''\otimes\mathbf{u}_p''\rangle_p}_{\text{velocity correlations}})\end{aligned} \tag{2.80}$$

We postulate that an imaginary particle-phase wall normal component transport equation can be derived with adequate closure to the terms presented in Eq 2.80. Firstly, we recognise that the production term is a function of the mean flow gradients in the stream-wise direction therefore it is dropped.

The velocity correlations which arise due to phase coupling are dominant in this work and have been shown to display the correct behaviour in one-way coupled flow Fox [71]. We therefore adopt the same form for their closure by setting the co-variance of the fluctuations $\langle\mathbf{u}_f'''\otimes\mathbf{u}_p''\rangle_p = \overline{v_{fp}^2} = \sqrt{\overline{v_p^2}\,\overline{v_f^2}}$, and as we now have access to both wall normal components this is the form adopted.

Following the standard approach used in classic eddy-viscosity turbulence models,

the divergence terms appearing in the transport equation are closed by the eddy-viscosity approximation [142].

$$\nabla \cdot \left[\frac{\mu_{pt}}{\sigma_{pk}} \nabla \langle \mathbf{u}_p'' \otimes \mathbf{u}_p'' \rangle_p \right] \approx -\nabla \cdot \langle \alpha_p \rangle \langle \mathbf{u}_p'' \otimes \mathbf{u}_p'' \otimes \mathbf{u}_p'' \rangle_p + \frac{1}{\rho_p} \nabla \cdot \langle \overline{\boldsymbol{\sigma}}_p \otimes \mathbf{u}_p'' \rangle - \frac{1}{\rho_p} \nabla \langle p_p \mathbf{u}_p'' \rangle \tag{2.81}$$

Finally, the terms left to close are the pressure strain and dissipation terms. These terms are explicitly modelled in the $\overline{v_p^2} - f$ transport equation and are grouped into a source term denoted $k_p f$.

$$k_p f = \underbrace{\phi_{p,yy}}_{\text{pressure strain}} - \underbrace{\varepsilon_{p,yy}}_{\text{dissipation}} + \alpha_p \rho_p 6 \frac{\overline{v_p^2}}{k_p} \varepsilon_p. \tag{2.82}$$

The source term effectively redistributes turbulence energy from the stream-wise Reynolds stress component to the wall-normal component close to walls. This means that particle turbulence energy can only enter the wall-normal component through redistribution. The source term has been shown to overproduce in regions relatively far away from the wall and the correction of Davidson et al. [50] is employed.

$$\overline{v_p^2}_{source} = \min\left\{ k_p f,\ -\frac{1}{T}\left[(C_1 - 6)\overline{v_p^2} - \frac{2k_p}{3}(C_1 - 1) \right] + C_2 \Pi_p \right\}. \tag{2.83}$$

Now setting the wall-normal component of the fluid-phase Reynolds stress tensor $\langle \mathbf{u}_p'' \otimes \mathbf{u}_p'' \rangle_p$ to $\overline{v_p^2}$ a transport equation can be written as:

$$\frac{\partial(\alpha_p \rho_p \overline{v_p^2})}{\partial t} + \nabla \cdot (\alpha_p \rho_p \overline{v_f^2} \mathbf{u}_p) = \nabla \cdot \left[\left(\mu_p + \frac{\mu_{pt}}{\sigma_{pk}} \right) \nabla \overline{v_p^2} \right] + \alpha_p \rho_p \overline{v_p^2}_{source} - \alpha_p \rho_p 6 \frac{\overline{v_p^2}}{k_p} \varepsilon_p + 2\beta(\overline{v_{fp}^2} - \overline{v_p^2}). \tag{2.84}$$

The reader should note that the third term is a sink term that is used to balance the source term $k_p f$. This is a modification proposed by Lien and Kalitzin [114] and ensures that the source term $k_p f \to 0$ as it approaches the wall.

Equation 2.84 contains no sensitivity to the wall distance and thus a modified Helmholtz equation is constructed to form an elliptic relaxation equation. The

form of this equation accounts for anisotropy close to walls and is also independent of Reynolds number and y^+ value which reads

$$L_p^2 \frac{\partial^2 f}{\partial x^2} - f = \underbrace{\frac{C_1}{T_p}\left(\frac{\overline{v_p^2}}{k_p} - \frac{2}{3}\right)}_{\phi_{p,yy,S}} - \underbrace{C_2 \frac{\Pi_p}{k_p}}_{\phi_{p,yy,R}} - \frac{1}{T_p}\left(6\frac{\overline{v_p^2}}{k_p} - \frac{2}{3}\right). \tag{2.85}$$

The terms $\phi_{p,yy,S}$ and $\phi_{p,yy,R}$ are the so-called slow and rapid pressure-strain terms [108, 142] with the final term being used to ensure far field behaviour i.e. that the elliptic relaxation function diminishes away from walls. The eddy viscosity is calculated from the solution of the $\overline{v_p^2} - f$ model, again the correction proposed by Davidson et al. [50] is used.

$$\nu_{pt} = \min\left\{C_{p\mu} k_p^2/\varepsilon_p,\ C_\mu \overline{v_p^2} T_p\right\}, \tag{2.86}$$

where the turbulent time and length scales are defined in analogy to those in the fluid-phase, we can define a characteristic length and time scale based on the particle turbulent flow variables as:

$$\mathrm{T}_p = \max\left(\frac{k_p}{\varepsilon_p}, 6\sqrt{\frac{\nu_f}{\varepsilon_f}}\right), \tag{2.87}$$

$$\mathrm{L}_p = \max\left(\frac{k_p^{3/2}}{\varepsilon_p}, C_\eta \frac{\nu_f^{3/4}}{\varepsilon_f^{1/4}}\right). \tag{2.88}$$

Both time and length scales are limited in regions close to the wall. In regions close to the wall k_p need not be zero but due to one-way coupling (which will be used to validate the model in Chapter 7) the mean slip $\to 0$ therefore the particles remain correlated. In regions close to the wall the particle characteristic time scale can reduce below the Kolmorgorov scale, hence limiting is applied. It is instructive to note that as the particle relaxation time increases closer to the wall and the particles become less responsive to the main flow, uncorrelated energy Θ is created. Hence, at the correlated macro-scale k_p, the production due to the velocity covariance is dominant but as the particle response time increases uncorrelated mesoscale energy

Θ is produced. As the fluid-particle flow remains correlated the scaling is retained. Therefore, we set a Neumann wall boundary condition for each turbulence statistic variable.

2.7 Particle wall boundary conditions

The wall boundary conditions for the particle-phase require additional modelling due to the fact that the velocity need not be zero on the wall. Recently, Capecelatro et al. [28] started from the Johnson and Jackson [97] wall boundary conditions and derived wall boundary conditions for the particle turbulence quantities k_p, ε_p and Θ. Here we present the boundary conditions in their implemented form applicable for FVM codes and begin with the wall boundary condition for the particle velocity $\mathbf{u}_p$.

$$\mu_p \nabla \mathbf{u}_{p,w} \cdot \mathbf{S}_f = -\frac{\pi}{6} \frac{\alpha_p}{\alpha_{p,max}} \phi_{spec} \rho_p g_0 \sqrt{3\Theta} \mathbf{u}_{p,w} \tag{2.89}$$

Here we define $\mathbf{u}_{p,w}$ as the particle slip velocity parallel to the wall, $\mathbf{u}_{p,w} = \mathbf{u}_p - \mathbf{u}_w$ and $\mathbf{S}_f$ as the surface area vector. Then Eq. 2.89 is recast into a more compact form

$$\mu_p \nabla \mathbf{u}_{p,w} \cdot \mathbf{S}_f = -\mathcal{D}_w \mathbf{u}_{p,w} \tag{2.90}$$

where the term $\mathcal{D}_w = \phi_{spec} \mathcal{V}_w$ representing ϕ_{spec}, the specularity coefficient and the term $\mathcal{V}_w = \frac{\pi}{6} \frac{\alpha_p}{\alpha_{p,max}} \rho_p \sqrt{3\Theta} g_0$ which contains the tangential momentum $\frac{\pi}{6} \frac{\alpha_p}{\alpha_{p,max}} \rho_p$ (omitting the particle slip velocity parallel to the wall $\mathbf{u}_{p,w}$) and the collisional frequency$\sqrt{3\Theta} g_0$. This boundary condition prescribes a particle partial-slip velocity at the wall. From this condition it follows that the components of the Reynolds stress tensor $\langle \mathbf{u}_p'' \mathbf{u}_p'' \rangle_p$ need not be zero at the wall unlike in the fluid-phase. As we are interested in modelling the particle-wall interaction of the particle turbulent kinetic energy k_p we assume isotropy in the fluctuating components.

$$k_p = \frac{1}{2}(\mathbf{u}''^2_{p,x} + \mathbf{u}''^2_{p,y} + \mathbf{u}''^2_{p,z}) \tag{2.91}$$

Equating the principal Reynolds stress components ($\mathbf{u}''^2_{p,x} \equiv \mathbf{u}''^2_{p,y} \equiv \mathbf{u}''^2_{p,z}$) one arrives at $k_p = 1.5\,\mathbf{u}''^2_p$ and substituting into Eq. 2.90 by employing the PA decomposition (see Appendix B) the wall boundary condition for k_p reads

$$\mu_p \nabla k_p \cdot \mathbf{S}_f = -2\mathcal{D}_w k_p \tag{2.92}$$

Following on from this a condition for the particle turbulent kinetic energy dissipation rate ε_p can be prescribed:

$$\mu_p \nabla \varepsilon_p \cdot \mathbf{S}_f = -2\mathcal{D}_w \varepsilon_p \tag{2.93}$$

Finally, the wall boundary condition for the granular temperature can be found by Reynolds averaging the wall boundary condition of Johnson and Jackson [97] which reads as

$$\frac{3}{2}\boldsymbol{q}_\Theta \cdot \mathbf{S}_f = \phi \mathcal{D}_w |\mathbf{u}_{p,w}|^2 - \frac{3}{2}\mathcal{D}_\kappa \Theta \tag{2.94}$$

where $\boldsymbol{q}_\Theta$ is the granular temperature flux and with $\mathcal{D}_\kappa = (1 - \mathrm{e}_w)^2 \mathcal{D}_w$ and e_w is the restitution of coefficient with the wall. It follows from this that this term represents the energy loss through particle collisions with the wall. The first term on the RHS represents the increase of the granular temperature due to the relative slip velocity with the wall. This means that the slip condition at the wall is capable of increasing the granular temperature.

2.8 Closure

This chapter presented the derivation of the two-step E-E begin at a collisional Boltzmann equation. From the kinetic equation the Chapman-Enskog method is employed to arrive at the hydrodynamic model in the small Knudsen limit. This comprises of continuity, momentum and energy for the particle and fluid-phase. From this description of the mesoscale, the equations are then Reynolds-Averaged

to find the macroscale turbulence model. The fully closed RA hydrodynamic model is then presented with an explanation of the physical mechanisms of each term. Additionally, the energy cascade effect that results from this approach is presented. Lastly, the second approach for deriving E-E models, microscale-based-macroscale models, is presented with the main differences between the methodologies detailed. Two novel elliptic relaxation models were derived within the RA E-E modelling framework, these models are proposed in order to account for the near-wall region in multiphase simulations. Lastly, wall boundary conditions for the particle phase were detailed and presented.

3 Finite Volume discretisation

3.1 Overview

In this chapter the Finite Volume discretisation practices adopted in this work are presented. The continuous PDEs associated with the E-E model are discretised into a system of algebraic equations. This then enables a numerical solution to be sought, the solution of which is the concern of Chapter 4.

This chapter comprises of:

- Discretisation of the computational domain into non-overlapping sub-domains.
- Equation discretisation of the governing PDEs into a system of algebraic equations.
- A description of the discretisation schemes used throughout this work.

3.2 Discretisation in a Finite Volume framework

The PDEs presented in the preceding chapter describe the behaviour of their continuous dependant variables. For a solution or approximation to the system of PDEs to be achieved they need to be replaced with a discrete approximation to their solution. This discrete approximation can be achieved by a two-step process of domain and equation discretisation.

The former requires the generation of a computational mesh. In the finite volume framework this consists of a subdivision of the computational domain into control volumes. The control volumes are non-overlapping and fill the domain entirely. We can then seek a discretisation procedure that describes how the solution varies between cell centroids. The latter, equation discretisation, requires an assumption about the variation of the dependant variable, $\phi = \phi(x, t)$ in space and time at the cell centroid. These will be discussed later but for a more comprehensive treatment see Ferziger and Peric [64].

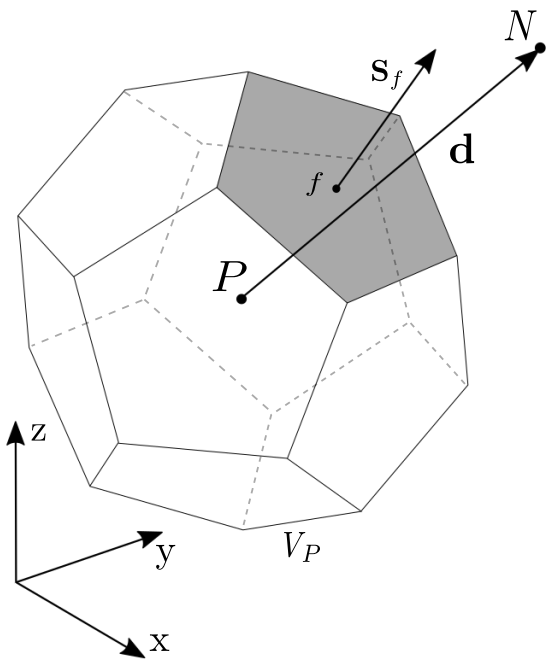

Figure 3.1: Polyhedron control volume adapted from Jasak [92].

A arbitrary control volume can be seen in Fig. 3.1. The computational point P is located at the cells centroid of the control volume, $\mathbf{x}_P$ such that:

$$\int_{V_p} (\mathbf{x} - \mathbf{x}_P) \mathrm{dV} = 0. \tag{3.1}$$

The face area vector $\mathbf{S}_f$ is normal to the face of each cell and its magnitude is equal to the area of the face. It is orientated out of the cell of interest P into the neighbouring cell N. The normal unit vector $\mathbf{n}$ is defined as $\mathbf{n} = \mathbf{S}_f/|\mathbf{S}_f|$. $\mathbf{d}$ denotes the vector between the centre of the cell of interest P and the centre of the neighbouring cell N, i.e. $\mathbf{d} = \mathbf{x} - \mathbf{x_P}$. A computational mesh is orthogonal when $\mathbf{d}$ is parallel to the surface face vector $\mathbf{S}_f$. The topology of the mesh cell is completely arbitrary within a FVM framework and is one of the major benefits on the approach.

3.3 Equation discretisation

Equation discretisation replaces the exact continuous PDE with a discrete system of algebraic equations, the solution of which produces the approximate behaviour of the dependant variables at fixed predetermined positions in time and space. Most of the equations in CFD, and all of those in the proceeding chapter, take the form of a generic transport equation which can be written as:

$$\frac{\partial \rho\phi}{\partial t} + \nabla \cdot (\rho \mathbf{u} \phi) = \nabla \cdot (\gamma \nabla \phi) + S_\phi, \tag{3.2}$$

where ρ, $\mathbf{u}$, ϕ and γ is the density, velocity, generic scalar and diffusivity respectively with S_ϕ representing source terms. The equation can be represented in its integral form by integrating over the control volume P as shown in Fig. 3.1 and time.

$$\begin{aligned} \int_t^{t+\Delta t} \left[\frac{\partial}{\partial t} \int_{V_P} \rho\phi \, \mathrm{dV} + \int_{V_P} \nabla \cdot (\rho \mathbf{u} \phi) \mathrm{dV} - \int_{V_P} \nabla \cdot (\gamma \nabla \phi_i) dV \right] \mathrm{dt} \\ = \int_t^{t+\Delta t} \left(\int_{V_P} S_\phi \mathrm{dV} \right) \mathrm{dt}. \end{aligned} \tag{3.3}$$

In the remainder of this chapter the discretisation practices utilised to approximate the volume integrals in Eq. 3.3 are presented. The procedures shown here are by no means exhaustive and readers are referred to texts such as Ferziger and Peric [64], Jasak [92] for a full treatise.

3.3.1 Face Interpolation

Interpolation of the cell-centred values onto the face centres is a crucial component of the finite volume method - largely due to the need to evaluate the mass flux coming in and out of a cell. Satisfying continuity is pivotal to any numerical solution of the Navier-Stokes and this fundamental property is satisfied by the geometric and numerical approach of the finite volume method.

As previously mentioned a function of the variation of the flow property needs to be assumed in order to approximate the face centre value. In a finite volume approach the cell neighbours are used to create a stencil around the face centre and then interpolate on to the face. A variety of approaches are available - in this work the central difference and upwind method are used unless stated otherwise. For the sake of brevity we therefore restrict our discussion to the central difference and upwind method.

If we introduce the discretised form of the flux, $\sum F\phi_f$ which will be defined later, we now have a mass flux F and a face flux. ϕ_f. In the central differencing scheme a linear variation of ϕ between P and N is assumed and the expression can be written as:

$$\phi_f = f_x\phi_P + (1 - f_x)\phi_N. \tag{3.4}$$

The interpolation factor f_x is defined by the topological information and reads $f_x = \frac{|\mathbf{x}_f - \mathbf{x}_N|}{|\mathbf{x}_f - \mathbf{x}_N| + |\mathbf{x}_f - \mathbf{x}_P|}$. This scheme is second order accurate due to the spatial linear variation.

The upwind differencing scheme uses the direction of the flow to ensure boundedness of the solution but is only first-order accurate. The formulation is given:

$$\phi_f = \begin{cases} \phi_P & \text{for } F \geq 0 \\ \phi_N & \text{for } F < 0. \end{cases} \tag{3.5}$$

3.3.2 Gradient

Green-Gauss gradient can be used to evaluate the gradient of the function ϕ_i.

$$\int_{V_P} \nabla\phi \mathrm{dV} = \int_{\partial V_P} \phi \mathrm{d}\mathbf{S} \approx \sum_f \phi_f \mathbf{S}_f, \tag{3.6}$$

where the variation of the face flux, ϕ_f can be evaluated by a number of schemes - here we use the central differencing scheme.

The face normal gradient is the inner product of the face gradient and the unit normal vector to the face, i.e. $\nabla_f^\perp = \mathbf{n} \cdot \nabla_f^\perp \phi$. Where $\nabla_f^\perp \phi$ is the gradient at the face. The face normal gradient can be evaluated using:

$$\nabla_f^\perp \phi = \frac{\phi_N - \phi_P}{|\mathbf{d}|}. \tag{3.7}$$

This approach is second order accurate when the vector $\mathbf{d}$ is orthogonal to the face plane i.e $\mathbf{S}_f$. For non-orthogonal meshes a correction can be introduced, of which there are a few options, the method adopted in this work will be presented later.

3.3.3 Convection term

The convective term is discretised by integrating over the control volume and employing the Gauss' theorem to transform the volume integral into a surface integral. This reads:

$$\begin{aligned} \int_{V_P} \nabla \cdot (\rho\mathbf{u}\phi) \mathrm{dV} &= \sum_f (\rho\mathbf{u}\phi)_f \cdot \mathbf{S}_f \\ &= \sum_f (\rho\mathbf{u})_f \cdot \mathbf{S}_f \phi_f \\ &= \sum_f F\phi_f, \end{aligned} \tag{3.8}$$

where the mass flux through the face is defined as, $F = (\rho \mathbf{u})_f \cdot \mathbf{S}_f$ and ϕ_f is the face flux. These quantities can be evaluated using the interpolation schemes outlined in §3.3.1.

3.3.4 Diffusion term

The diffusion terms are discretised in a similar way to convection. Employing the linear variation of the function ϕ, it can be written as:

$$\int_{V_P} \nabla \cdot (\gamma \nabla \phi) dV = \int_{\partial V} (\gamma \nabla \phi) \cdot d\mathbf{S} \approx \sum_f \gamma_f (\nabla_f^{\perp} \phi \cdot \mathbf{S}_f). \tag{3.9}$$

On orthogonal meshes, the face normal gradient $\nabla_f^{\perp} \phi_i$ is a second order accurate approximation due to the linear variation assumed. The vectors, $\mathbf{d}$ and $\mathbf{S}_f$, that are defined in the schematic below, are parallel and then the following expression can be used:

$$\nabla_f^{\perp} \phi |\mathbf{\Delta}| = |\mathbf{S}_f| \frac{\phi_N - \phi_P}{|\mathbf{d}|}. \tag{3.10}$$

As mentioned previously, for non-orthogonal grids a correction can be introduced to preserve the second order accuracy. The corrected face normal flux approximation can be written as

$$\nabla_f \phi \cdot \mathbf{S}_f = \nabla_f^{\perp} \phi |\mathbf{\Delta}| + (\nabla \phi)_f \cdot \mathbf{k}, \tag{3.11}$$

where $|\mathbf{\Delta}|$ and $\mathbf{k}$ are vectors that are defined in the schematic below.

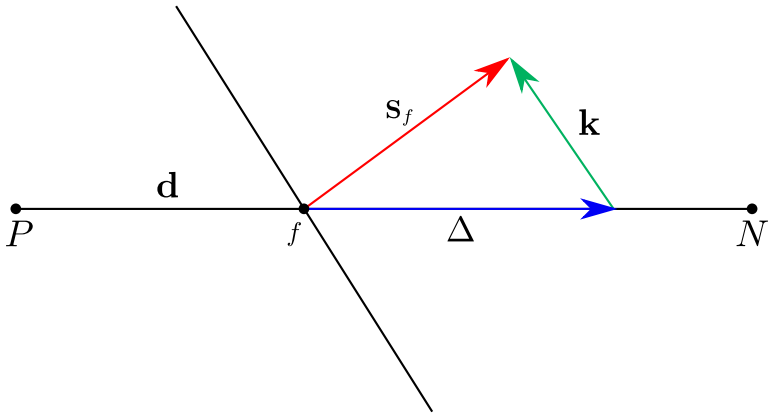

Figure 3.2: Over-relaxed approach adapted from Jasak [92].

In general each vector must satisfy the condition,

$$\mathbf{S}_f = \Delta + \mathbf{k}, \tag{3.12}$$

where in the over-relaxed approach of Jasak [92] we define,

$$\Delta = \frac{\mathbf{d}}{\mathbf{d} \cdot \mathbf{S}_f} |\mathbf{S}_f|^2. \tag{3.13}$$

If the mesh is orthogonal the equation reduces to the first term on the RHS regardless of the non-orthogonality approach. In this work non-orthongonal mesh cells are not employed but if they were the over-relaxed approach of Jasak [92] would be used.

3.3.5 Source term

Any term that is not written as convection or diffusion are treated as a source or sink. Before employing a discretisation approach its physical behaviour should be assessed to ensure the correct approach is used. Qualities such as boundedness, positive-definiteness (e.g. energy) and accuracy should ascertained. Here we follow a relatively generic approach to source terms:

$$S_\phi(\phi) = \phi S_p + S_u, \tag{3.14}$$

where S_p & S_u can depend on ϕ. Then integrating the term over the control volume:

$$\int_{V_P} S_\phi(\phi) dV = \phi S_p V_P + S_u V_P, \tag{3.15}$$

the source term has been linearised to enhance convergence - this is achieved by splitting the source term into an implicit and explicit contribution. Here the first term on the RHS is treated implicitly and the second term is treated explicitly. This enhances convergence by the implicit part of the source being negative enhancing diagonal dominance in the solution matrix.

3.3.6 Time derivative

The time derivative is discretised by integrating over the control volume. In this work the Euler implicit time differencing is used. Again, assuming a linear variation of ϕ within a time step reads:

$$\int_{V_P} \frac{\partial \rho \phi}{\partial t} dV \approx \frac{\rho_P^n \phi_P^n - \rho_P^o \phi_P^o}{\Delta t} V_P, \tag{3.16}$$

where $\phi^n = \phi(t + \Delta t)$ denotes the value at the time step that is being solved for i.e updated value and $\phi^o = \phi(t)$ which is the value from the previous time step. This scheme is first order accurate and is unconditionally stable.

3.4 Boundary conditions

The system of PDEs and consequently the system of algebraic equations require suitable initial and boundary conditions to solve. The two main types of boundary conditions, from which most are derived, are Dirichlet or Neumann boundary conditions. The former prescribes the value of the dependent variable on the boundary and is termed a 'fixed value' boundary condition. The latter prescribes the gradient of the variable that is normal to the boundary and is termed a 'fixed gradient' boundary condition.

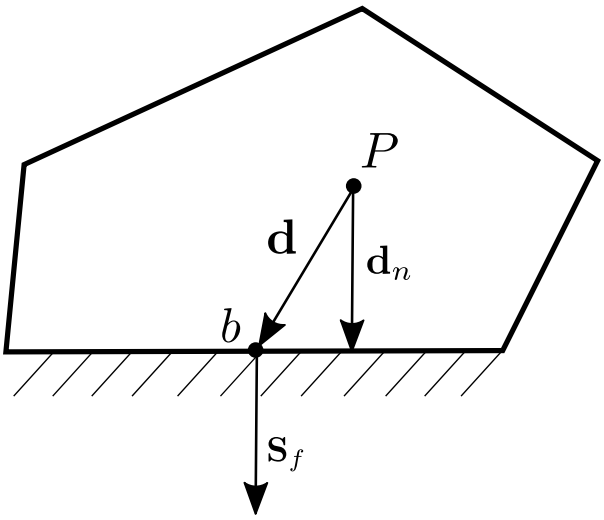

Figure 3.3: Schematic of a finite volume discretisation in the presence of a boundary

When discretising a convective or diffusive term for example an operation is carried out that sums over the faces of that particular control volume. When a sum operation, $\sum_f$ includes the boundary face then the boundary condition is invoked and it follows that this condition must be specified for each boundary face that is discretised.

Fig. 3.3 shows a control volume sharing one face with a boundary. Here the cell centre is labelled P, the face is labelled b, the vector connecting the cell centre P and the centre of the boundary face is $\mathbf{d}$ and its corresponding component normal to the boundary is denoted $\mathbf{d}_n$.

When one prescribes a fixed value at the boundary i.e. ϕ_B.

- It is substituted in cases where the discretisation procedure requires the value on a boundary face e.g. $\phi_f = \phi_B$ in the convection discretisation;
- In the diffusive terms where the face gradient $\nabla^{\perp}\phi$ is required the boundary value replaces the neighbour like so:

$$\nabla_f^{\perp}\phi \cdot \mathbf{S}_f = \frac{\phi_B - \phi_P}{|\mathbf{d}|}|\mathbf{S}_f|. \tag{3.17}$$

This method is second order accurate if the variation of ϕ_B is constant along the

face. It reduces to first order if it varies across the face and the mesh is non-orthogonal - again a correction can be included to improve this.

When one prescribes a fixed gradient condition at the boundary, then the face normal gradient $g_B = \nabla_f^{\perp}\phi$ is specified at the boundary

- When the discretisation requires the value ϕ_f on a boundary face the cell centre is extrapolated to the boundary:

$$\begin{aligned} \phi_f &= \phi_P + \mathbf{d}_n \cdot \nabla_f^{\perp}\phi \\ &= \phi_P + |\mathbf{d}_n| g_B; \end{aligned} \tag{3.18}$$

- g_B can be directly substituted into cases where the discretisation requires the face gradient i.e. the diffusive term and be written as:

$$\nabla_f^{\perp}\phi \cdot \mathbf{S}_f = g_B |\mathbf{S}_f|. \tag{3.19}$$

The discretisation for a fixed gradient is second order if g_B is constant along the face. Again, it reduces to first order accuracy if ϕ_B varies and the mesh is non-orthogonal.

Finally, the 'zero-gradient' boundary condition is essentially a fixed gradient boundary condition with $g_B = 0$ which means that the boundary face value is replaced with the cell centre value.

3.5 Temporal discretisation

Looking at generic multiphase transport Eq. 3.3 in its volume integral form once again:

$$\begin{aligned} \int_t^{t+\Delta t} \Big[\frac{\partial}{\partial t} \int_{V_P} \rho\phi \, \mathrm{dV} + \int_{V_P} \nabla \cdot (\rho \mathbf{u} \phi) \mathrm{dV} - \int_{V_P} \nabla \cdot (\Gamma \nabla \phi) dV \Big] \mathrm{dt} \\ = \int_t^{t+\Delta t} \Big(\int_{V_P} S_\phi \mathrm{dV} \Big) \mathrm{dt}. \end{aligned} \tag{3.20}$$

Assuming fixed control volumes with an incompressible system and employing the discretisation practises presented in the proceeding sections the equation can be re-written in a 'semi-discretised' form.

$$\int_t^{t+\Delta t} \left[\rho_P \frac{\phi_P^n - \phi_P^o}{\Delta t} V_P + \sum_f F\phi_f - \sum_f \gamma_f (\nabla_f^\perp \phi_i \cdot \mathbf{S}_f)\right] \mathrm{dt} = \int_t^{t+\Delta t} \Big(\phi S_p V_P + S_u V_P\Big) \mathrm{dt}. \tag{3.21}$$

From this form of the multiphase transport equation the time integrals need to be evaluated. The temporal variation of the cell centre value ϕ, face values and gradient terms are assumed to be constant during a time step. Although their formulation in terms of new and old values needs to be addressed.

In this work the Euler implicit scheme is employed. This scheme uses implicit discretisation of the spatial varying terms i.e. their new values are expressed as:

$$\phi_P = \phi_P^n, \tag{3.22a}$$

$$\phi_f = \phi_f^n, \tag{3.22b}$$

$$\nabla_f^\perp \phi \cdot \mathbf{S}_f = \nabla_f^\perp \phi^n \cdot \mathbf{S} = \nabla_f^\perp \phi^n |\mathbf{\Delta}| + (\nabla \phi^o)_f \cdot \mathbf{k}, \tag{3.22c}$$

which gives a first order accurate time discretisation. It guarantees boundedness of the solution and is unconditionally stable. For boundedness to be ensured the non-orthogonal correction has to be treated explicitly i.e. by using the old time step value.

Finally, the discretised generic transport equation now reads:

$$\rho_P \frac{\phi_P^n - \phi_P^o}{\Delta t} V_P + \sum_f F\phi_f - \sum_f \gamma_f (\nabla_f^\perp \phi \cdot \mathbf{S}_f) = \phi S_p V_P + S_u V_P. \tag{3.23}$$

The previous equation produces a linear algebraic equation for an arbitrary control volume, V_P. Given a system of control volumes a generic form of the equation can be written as:

$$a_p \phi_P^n + \sum_N a_N \phi_N^n = b_P. \tag{3.24}$$

The value ϕ_N^n depends on the neighbouring cells, given by the discretisation stencil, which creates a system of linear algebraic equations with each row representing each cell centre in the domain. As a control volume can only share faces with a finite number of other cells, depending on its shape, the system of equations will be sparse. The system of linear algebraic equations can then be rewritten in matrix form

$$\mathbf{A}\mathbf{x} = \mathbf{b}, \tag{3.25}$$

where $\mathbf{A}$ is a sparse matrix with coefficients a_P and a_N on the diagonal and off-diagonal respectively. $\mathbf{x}$ is the vector of variables to solve for and $\mathbf{b}$ is the source vector. From this point a number of approaches are available to solve the system although they broadly fall into two categories: direct or iterative. The direct method hinges on the matrix inversion of $\mathbf{A}$ and gives the solution to the system of equations in a finite number of arithmetic operations. The number of operations necessary to reach the solution scales with the cube of the number of equations thus making a solution computational very expensive. Iterative methods begin from an initial guessed solution and begins to iterate towards a more accurate solution until a user defined tolerance is reached.

In this work two main matrix solvers are employed which fit broadly into the categories of basic matrix solvers and multigrid algorithms. In both the system $\mathbf{A}\mathbf{x} = \mathbf{b}$ is solver for to find a series of approximations to $\mathbf{x}^n$. The iterations are stopped after some user defined or solver defined tolerance. Throughout this work the matrix solvers based on the method of steepest descent [90] are employed. The biconjugate gradient stabilised solver (BiCGSTAB) [196] is used for asymmetric matrices and the Incomplete Cholesky preconditioned Conjugate Gradient (ICCG) [81] solver for symmetric matrices is used.

When the size of the algebraic system increases dramatically the rate of convergence is adversely affected in the aforementioned methods. In these situations mulitgrid methods are often sought as they are capable of solving the large system of equations efficiently. Typically, the basic matrix solver is used to smooth

out high frequency sources of errors and then the coarsening of the mesh forming multiple 'grids' the low frequency errors are reduced resulting in a more efficient and convergent solution technique [162, 165]. This technique is often called the generalised algebraic multi-grid (GAMG) and is used throughout this work. For a full treatise on the solution procedure within the linear matrix solvers readers are refereed to Ferziger and Peric [64], Press et al. [143], Ruge and Stüben [162], Saad [165] .

3.6 Closure

In this chapter the basis for the finite volume discretisation used throughout this work have been described. The continuous PDEs were first presented and then discretised term by term. Additionally, the boundary condition discretisation has been outlined. Finally, the discretised generic transport equation was presented as a system of linear algebraic equations.

This page is intentionally left blank.

4 Solution algorithms for the E-E model

4.1 Overview

In this chapter the numerical implementation and solution algorithm of the RA-TFM governing equations are detailed. Both the segregated and coupled implementations are provided in which a pressure-correction approach is employed. For the coupled implementation the block-coupled matrix architecture is given. Lastly, the discretisation practices for the phase-energy system are described.

This chapter comprises of:

- Solution algorithm for the segregated solution of the governing equations;
- Solution algorithm for the coupled solution of the governing equations;
- Block-coupled matrix architecture;
- Discretisation practices for the phase-energy system.

4.2 Segregated solution algorithm

In this section the segregated implementation of the RA-TFM is presented, this constitutes the CFD code `ratfmFoam` and can be found in Appendix D.

4.2.1 Phase intensive momentum equations

It is important to note that in the formulation used throughout this work that the volume fraction of the particle phase is solved everywhere in the domain. This is achieved by prescribing a small value of α_p of $\mathcal{O}(10^{-6})$ and is chosen to be several orders of magnitude less than the mass loading. For alternative methods, such as the semi- and fully-conservative formulations where the volume fraction is not divided out the reader is refereed to Li and Christian [110], Park et al. [134], Passalacqua and Fox [135].

The continuity and momentum equations for the particle and fluid-phase are presented below. Throughout, the simplifying assumptions shown in §2.3 have been employed and these represent the governing equations that are used throughout this work. They read:

$$\frac{\partial(\alpha_p\rho_p)}{\partial t} + \nabla\cdot(\alpha_p\rho_p\mathbf{u}_p) = 0, \tag{4.1}$$

$$\frac{\partial(\alpha_p\rho_p\mathbf{u}_p)}{\partial t} + \nabla\cdot(\alpha_p\rho_p\mathbf{u}_p\mathbf{u}_p) = \nabla\cdot(\alpha_p\rho_p\overline{\mathbf{R}}_{\text{eff,p}}) + \beta\left[(\mathbf{u}_f-\mathbf{u}_p) - \frac{\nu_{ft}}{\text{Sc}_{fs}\alpha_p\alpha_f}\nabla\alpha_p\right] - \nabla p_p - \alpha_p\nabla p_f + \alpha_p\rho_p\mathbf{g}, \tag{4.2}$$

$$\frac{\partial(\alpha_f\rho_f)}{\partial t} + \nabla\cdot(\alpha_f\rho_f\mathbf{u}_f) = 0, \tag{4.3}$$

$$\frac{\partial(\alpha_f\rho_f\mathbf{u}_f)}{\partial t} + \nabla\cdot(\alpha_f\rho_f\mathbf{u}_f\mathbf{u}_f) = \nabla\cdot(\alpha_f\rho_f\overline{\mathbf{R}}_{\text{eff,f}}) + \beta\left[(\mathbf{u}_p-\mathbf{u}_f) + \frac{\nu_{ft}}{\text{Sc}_{fs}\alpha_p\alpha_f}\nabla\alpha_p\right] - \alpha_f\nabla p_f + \alpha_f\rho_f\mathbf{g}. \tag{4.4}$$

Here we follow the phase intensive formulation of Rusche [164], Weller [210]. For simplicity the turbulent dispersion term is now denoted as $\mathscr{D} = \nu_{ft}/(\mathrm{Sc}_{fs}\alpha_p\alpha_f)$, then separating the drag contributions into explicit and implicit terms and dividing by both the phase fraction and density we are left with:

$$\frac{\partial \mathbf{u}_p}{\partial t} + \nabla\cdot(\mathbf{u}_p\mathbf{u}_p) - \mathbf{u}_p\nabla\cdot\mathbf{u}_p + \frac{\nabla\alpha_p}{\alpha_p^*}\cdot\overline{\mathbf{R}}^c_{\mathrm{eff,p}} + \nabla\cdot\overline{\mathbf{R}}^c_{\mathrm{eff,p}} - \nabla\cdot(\nu_{\mathrm{eff,p}}\nabla\mathbf{u}_p) + \frac{\beta\mathbf{u}_p}{\alpha_p\rho_p} - \nabla\cdot\left(\nu_{\mathrm{eff,p}}\frac{\nabla\alpha_p}{\alpha_p^*}\mathbf{u}_p\right) + \mathbf{u}_p\nabla\cdot\left(\nu_{\mathrm{eff,p}}\frac{\nabla\alpha_p}{\alpha_p^*}\right) = \frac{\beta\mathbf{u}_f}{\alpha_p\rho_p} - \frac{\beta\mathscr{D}\nabla\alpha_p}{\alpha_p\rho_p} - \frac{\nabla p_p}{\alpha_p^*\rho_p} - \frac{\nabla p_f}{\rho_p} + \mathbf{g}, \tag{4.5}$$

$$\frac{\partial \mathbf{u}_f}{\partial t} + \nabla\cdot(\mathbf{u}_f\mathbf{u}_f) - \mathbf{u}_f\nabla\cdot\mathbf{u}_f + \frac{\nabla\alpha_f}{\alpha_f^*}\cdot\overline{\mathbf{R}}^c_{\mathrm{eff,f}} + \nabla\cdot\overline{\mathbf{R}}^c_{\mathrm{eff,f}} - \nabla\cdot(\nu_{\mathrm{eff,f}}\nabla\mathbf{u}_f) + \frac{\beta\mathbf{u}_f}{\alpha_f\rho_f} - \nabla\cdot\left(\nu_{\mathrm{eff,f}}\frac{\nabla\alpha_f}{\alpha_f^*}\mathbf{u}_f\right) + \mathbf{u}_f\nabla\cdot\left(\nu_{\mathrm{eff,f}}\frac{\nabla\alpha_f}{\alpha_f^*}\right) = \frac{\beta\mathbf{u}_p}{\alpha_f\rho_f} + \frac{\beta\mathscr{D}\nabla\alpha_p}{\alpha_f\rho_f} - \frac{\nabla p_f}{\rho_f} + \mathbf{g}, \tag{4.6}$$

where $\alpha_p^* = \alpha_p + \delta$ and $\alpha_f^* = \alpha_f + \delta$, and δ is introduced to avoid a division by zero and is $\mathcal{O}(10^{-6})$. It is important to clarify the behaviour of terms with the volume fraction in their denominator. The drag terms containing the phase-velocities i.e. β in which the numerator contains $\alpha_p\alpha_f$ which ensures the correct behavior of the function as $\alpha_p \to 0$. The turbulent dispersion term contains the gradient of volume fraction which in the limit $\alpha_p \to 0$ means that the ratio approaches zero. This ensures that the momentum equations are able to be solved everywhere within the domain despite diminishing particle volume fractions.

From the original system of equations presented in Chapter 2 - Eqs. 2.39 & 2.45 contain no diffusive flux that can be treated implicitly. This can have advantages when solving the equations i.e enhanced diagonal dominance. Therefore, following Rusche [164], Weller [210] the Reynolds stress term can be rewritten into a diffusive and corrective component:

$$\begin{aligned}\overline{\mathbf{R}}_{\text{eff,i}} &= \overline{\mathbf{R}}_{\text{eff,i}} + \nu_{\text{eff,i}}\nabla\mathbf{u}_i - \nu_{\text{eff,i}}\nabla\mathbf{u}_i \\ &= -\nu_{\text{eff,i}}(\nabla\mathbf{u}_i + \nabla^T\mathbf{u}_i) + \frac{2}{3}\nu_{\text{eff,i}}\mathbf{I}\nabla\cdot\mathbf{u}_i \\ &+ \nu_{\text{eff,i}}\nabla\mathbf{u}_i - \nu_{\text{eff,i}}\nabla\mathbf{u}_i \\ &= (-\nu_{\text{eff,i}}\nabla^T\mathbf{u}_i + \frac{2}{3}\nu_{\text{eff,i}}\mathbf{I}\nabla\cdot\mathbf{u}_i) - \nu_{\text{eff,i}}\nabla\mathbf{u}_i \\ &= \overline{\mathbf{R}}^c_{\text{eff,i}} - \nu_{\text{eff,i}}\nabla\mathbf{u}_i.\end{aligned} \tag{4.7}$$

4.2.2 Discretisation of the intensive momentum equations

First, we discretise the left hand side of the equation which contains the convective, diffusive and implicit-drag transport terms:

$$\begin{aligned}\mathcal{T}_p := \Big[\!\Big[\frac{\partial[\![\mathbf{u}_p]\!]}{\partial t}\Big]\!\Big] + \Big[\!\Big[\nabla\cdot(\mathbf{u}_p[\![\mathbf{u}_p]\!])\Big]\!\Big] - \Big[\!\Big[(\nabla\cdot\mathbf{u}_p)[\![\mathbf{u}_p]\!]\Big]\!\Big] + \frac{\nabla\alpha_p}{\alpha_p^*}\cdot\overline{\mathbf{R}}^c_{\text{eff,p}} + \nabla\cdot\overline{\mathbf{R}}^c_{\text{eff,p}} \\ -\Big[\!\Big[\nabla\cdot(\nu_{\text{eff,p}}\nabla[\![\mathbf{u}_p]\!])\Big]\!\Big] - \Big[\!\Big[\nabla\cdot(\nu_{\text{eff,p}}\frac{\nabla\alpha_p}{\alpha_p^*}[\![\mathbf{u}_p]\!])\Big]\!\Big] \\ -\Big[\!\Big[\nabla\cdot(\nu_{\text{eff,p}}\frac{\nabla\alpha_p}{\alpha_p^*})[\![\mathbf{u}_p]\!])\Big]\!\Big] + \Big[\!\Big[\frac{\beta[\![\mathbf{u}_p]\!]}{\alpha_p\rho_p}\Big]\!\Big],\end{aligned} \tag{4.8}$$

$$\begin{aligned}\mathcal{T}_f := \Big[\!\Big[\frac{\partial[\![\mathbf{u}_f]\!]}{\partial t}\Big]\!\Big] + \Big[\!\Big[\nabla\cdot(\mathbf{u}_f[\![\mathbf{u}_f]\!])\Big]\!\Big] - \Big[\!\Big[(\nabla\cdot\mathbf{u}_f)[\![\mathbf{u}_f]\!]\Big]\!\Big] + \frac{\nabla\alpha_f}{\alpha_f^*}\cdot\overline{\mathbf{R}}^c_{\text{eff,f}} + \nabla\cdot\overline{\mathbf{R}}^c_{\text{eff,f}} \\ -\Big[\!\Big[\nabla\cdot(\nu_{\text{eff,f}}\nabla[\![\mathbf{u}_f]\!])\Big]\!\Big] - \Big[\!\Big[\nabla\cdot(\nu_{\text{eff,f}}\frac{\nabla\alpha_f}{\alpha_f^*}[\![\mathbf{u}_f]\!])\Big]\!\Big] \\ -\Big[\!\Big[\nabla\cdot(\nu_{\text{eff,f}}\frac{\nabla\alpha_f}{\alpha_f^*})[\![\mathbf{u}_f]\!])\Big]\!\Big] + \Big[\!\Big[\frac{\beta[\![\mathbf{u}_f]\!]}{\alpha_f\rho_f}\Big]\!\Big],\end{aligned} \tag{4.9}$$

where $[\![\cdot]\!]$ is the implicit dicretisation of the term, $\mathcal{T}_p$ & $\mathcal{T}_f$ represents the numerical coefficients of each respective algebraic system given by the discretisation. The second and third terms on the RHS represent convection and have been split up into a convection term minus a divergence terms as it enhances boundedness of the solution i.e. the third term represents a source term.

The discretised momentum equations, $\mathcal{T}_p$ & $\mathcal{T}_f$ represents the system of algebraic equations which are written in the form,

$$(\mathcal{T}_p)_{coeffs}\mathbf{u}_p = (\mathcal{T}_p)_s, \tag{4.10a}$$

$$(\mathcal{T}_f)_{coeffs}\mathbf{u}_f = (\mathcal{T}_f)_s, \tag{4.10b}$$

where $()_{coeffs}$ represents the diagonal and off-diagonal coefficients and $()_s$ represents the source terms i.e. explicit terms. This discretised form of the momentum equations will be revisited once the source terms on the RHS have been addressed.

Now addressing the RHS of Eq. 4.5 & 4.6 which read,

$$\ldots = \frac{\beta\mathbf{u}_f}{\alpha_p\rho_p} - \frac{\beta\mathscr{D}\nabla\alpha_p}{\alpha_p\rho_p} - \frac{\nabla p_p}{\alpha_p^*\rho_p} - \frac{\nabla p_f}{\rho_p} + \mathbf{g}, \tag{4.11a}$$

$$\ldots = \frac{\beta\mathbf{u}_p}{\alpha_f\rho_f} + \frac{\beta\mathscr{D}\nabla\alpha_p}{\alpha_f\rho_f} - \frac{\nabla p_f}{\rho_f} + \mathbf{g}. \tag{4.11b}$$

Following the solution procedure of Weller [210] all terms on the RHS are evaluated at cell faces. In order to avoid checker-boarding in the solution, which is a prevalent problem on collocated grids due to the storage of values at cell centres and interpolating onto the face, the group of terms on the RHS are treated in a Rhie-Chow like manner [154].

4.2.3 Phase momentum flux correction equations

Now a semi-discretised formulation of both the particle- and fluid-phase can be written. Invoking Eqs. 4.10 and splitting up the total coefficients appearing in each system into a diagonal, $\mathbf{A}_i$ and an explicit, $\mathbf{H}_i$ [92] contribution. The latter consisting of two parts, the neighbouring coefficients, $()_N$ multiplied by its respective phase velocity and the source terms, $\mathbf{H}_i = -(\mathbf{A}_i)_N\mathbf{u}_i + (\mathbf{A}_i)_S$. The equations can then be written as:

$$\mathbf{A}_p\mathbf{u}_p = \mathbf{H}_p + \frac{\beta\mathbf{u}_f}{\alpha_p\rho_p} - \frac{\beta\mathscr{D}\nabla\alpha_p}{\alpha_p\rho_p} - \frac{\nabla p_f}{\rho_p} - \frac{\nabla p_p}{\alpha_p^*\rho_p} + \mathbf{g}, \tag{4.12a}$$

$$\mathbf{A}_f\mathbf{u}_f = \mathbf{H}_f + \frac{\beta\mathbf{u}_p}{\alpha_f\rho_f} + \frac{\beta\mathscr{D}\nabla\alpha_p}{\alpha_f\rho_f} - \frac{\nabla p_f}{\rho_f} + \mathbf{g}. \tag{4.12b}$$

Rearranging Eqs. 4.12 gives the phase momentum correction equations, note these equations are not used in the solution algorithm, but are required to derive a flux predictor and corrector:

$$\mathbf{u}_p = \frac{\mathbf{H}_p}{\mathbf{A}_p} + \frac{\beta \mathbf{u}_f}{\alpha_p \rho_p \mathbf{A}_p} - \frac{\beta \mathscr{D} \nabla \alpha_p}{\alpha_p \rho_p \mathbf{A}_p} - \frac{\nabla p_f}{\rho_p \mathbf{A}_p} - \frac{\nabla p_p}{\alpha_p^* \rho_p \mathbf{A}_p} + \frac{\mathbf{g}}{\mathbf{A}_p}, \tag{4.13a}$$

$$\mathbf{u}_f = \frac{\mathbf{H}_f}{\mathbf{A}_f} + \frac{\beta \mathbf{u}_p}{\alpha_f \rho_f \mathbf{A}_f} + \frac{\beta \mathscr{D} \nabla \alpha_p}{\alpha_f \rho_f \mathbf{A}_f} - \frac{\nabla p_f}{\rho_f \mathbf{A}_f} + \frac{\mathbf{g}}{\mathbf{A}_f}. \tag{4.13b}$$

4.2.4 Construction of the pressure equation

In order to derive a pressure equation the continuity equation is enforced globally. The global continuity equation thus reads:

$$\nabla \cdot [(\alpha_p)_f \phi_p + (\alpha_f)_f \phi_f] = 0, \tag{4.14}$$

where the subscript $()_f$ denotes the face value which is found through linear interpolation i.e. central differencing and $\phi_i = \mathbf{u}_{i,f} \cdot \mathbf{S}_f$ is the volumetric face flux where subscript f is used to denote variables that are evaluated at the control volume's face. From here the face fluxes are found by interpolating the momentum correction equation (Eqs. 4.13) onto face centres using Rhie-Chow interpolation [154]. The interpolation increases pressure-velocity coupling by introducing cell-to-cell pressure coupling by evaluating the gradient of pressure on cell faces using the neighbouring cell centre contribution. Using central differencing and denoting the gradient at a face as, ∇_f, we can write

$$\phi_p = \phi_p^* - \frac{1}{\rho_p (\mathbf{A}_p)_f} \nabla_f^\perp p_f |\mathbf{S}_f|, \tag{4.15a}$$

$$\phi_f = \phi_f^* - \frac{1}{\rho_f (\mathbf{A}_f)_f} \nabla_f^\perp p_f |\mathbf{S}_f|, \tag{4.15b}$$

where $\nabla_f^\perp \phi_i$ is the face normal gradient which is the inner product of the face gradient, $\mathbf{n} \cdot \nabla_f \phi_i$.

The flux prediction terms, ϕ_p^* & ϕ_f^* are written as:

$$\phi_p^* = \left(\frac{\mathbf{H}_p}{\mathbf{A}_p}\right)_f \cdot \mathbf{S}_f + \frac{(\beta)_f}{(\alpha_p)_f \rho_p (\mathbf{A}_p)_f}\phi_f - \frac{(\beta)_f (\mathscr{D})_f}{(\alpha_p)_f \rho_p (\mathbf{A}_p)_f}\nabla_f^\perp \alpha_p |\mathbf{S}_f| - \frac{1}{(\alpha_p^*)_f \rho_p (\mathbf{A}_p)_f}\nabla_f^\perp p_p |\mathbf{S}_f| + \frac{\mathbf{g}}{(\mathbf{A}_p)_f} \cdot \mathbf{S}_f, \tag{4.16}$$

$$\phi_f^* = \left(\frac{\mathbf{H}_f}{\mathbf{A}_f}\right)_f \cdot \mathbf{S}_f + \frac{(\beta)_f}{(\alpha_f)_f \rho_f (\mathbf{A}_f)_f}\phi_p - \frac{(\beta)_f (\mathscr{D})_f}{(\alpha_f)_f \rho_f (\mathbf{A}_f)_f}\nabla_f^\perp \alpha_p |\mathbf{S}_f| + \frac{\mathbf{g}}{(\mathbf{A}_f)_f} \cdot \mathbf{S}_f. \tag{4.17}$$

Now the pressure equation can be constructed by substituting Eqs. 4.15 into Eq. 4.14 which reads:

$$\left[\!\left[\nabla \cdot \left(D_p \nabla_f [\![p_f]\!] \cdot \mathbf{S}_f\right)\right]\!\right] = \nabla \cdot \left((\alpha_p)_f \phi_p^* + (\alpha_f)_f \phi_f^*\right), \tag{4.18}$$

where

$$D_p = \frac{(\alpha_p)_f}{\rho_p (\mathbf{A}_p)_f} + \frac{(\alpha_f)_f}{\rho_f (\mathbf{A}_f)_f}, \tag{4.19}$$

is the pressure diffusivity matrix and the pressure gradient has been discretised implicitly on the LHS as a diffusion term i.e. Laplacian. Essentially a shared or mixture pressure field is solved for, this ensures that continuity is obeyed throughout as the coupling is provided through the pressure equation.

Once this equation has been solved, the phase fluxes need to be updated to satisfy continuity, as in the predictor step the influence of the pressure gradient is removed, this can be achieved by solving Eqs. 4.15. From this stage the solution does not completely satisfy continuity as the velocities, which are stored at the cell centres, need to be corrected with the influence of the pressure gradient.

This is achieved by invoking:

$$\mathbf{u}_p = \frac{\mathbf{H}_p}{\mathbf{A}_p} + \left[\phi_p^* - \frac{1}{\rho_p (\mathbf{A}_p)_f}\nabla_f^\perp p_f |\mathbf{S}_f|\right]_{f\to c}, \tag{4.20a}$$

$$\mathbf{u}_f = \frac{\mathbf{H}_f}{\mathbf{A}_f} + \left[\phi_f^* - \frac{1}{\rho_f (\mathbf{A}_f)_f}\nabla_f^\perp p_f |\mathbf{S}_f|\right]_{f\to c}, \tag{4.20b}$$

where the subscript $f \rightarrow c$ denotes a vector field reconstruction from face flux values to cell centre values. The influence of the gradient of pressure is incorporated into the reconstruction of the phase velocity - this ensures the phase velocity obeys continuity.

4.2.5 Solution of the phase-mixed continuity equation

In practice the phase-mixed continuity equation is solved first based on the initial conditions but for the sake of logical progression is given here. Following Weller [210] the particle-phase continuity equation Eq. 4.14 can be reformulated as:

$$\frac{\partial \alpha_p}{\partial t} + \nabla \cdot (\mathbf{u}_T \alpha_p) + \nabla \cdot (\mathbf{u}_r \alpha_p \alpha_f) = 0, \tag{4.21}$$

where $\mathbf{u}_T = \alpha_p \mathbf{u}_p + \alpha_f \mathbf{u}_f$ is the mixture velocity and $\mathbf{u}_r = \mathbf{u}_p - \mathbf{u}_f$ is the relative velocity. This equation can then be discretised as

$$\left[\!\left[\frac{\partial [\![\alpha_p]\!]}{\partial t} \right]\!\right] + \left[\!\left[\nabla \cdot \left(\phi [\![\alpha_p]\!] \right) \right]\!\right] + \left[\!\left[\nabla \cdot \left(\phi_{r,p} [\![\alpha_p]\!] \right) \right]\!\right] = 0, \tag{4.22}$$

where $\phi_{r,p} = (\alpha_f)_f \phi_r$ and $\phi_r = \phi_p - \phi_f$. The second term on the LHS is ensured to be bounded between 0 and 1 due to the mixture flux, $\phi = \mathbf{u}_{p,f} \cdot \mathbf{S}_f + \mathbf{u}_{f,f} \cdot \mathbf{S}_f$ satisfying the mixture continuity equation. The third term is now non-linear and requires a Total Variation Diminishing (TVD) scheme to ensure the term is bounded between 0 and 1. As an aside the particles volume fraction should be bounded at a much lower value i.e. its maximum packing limit ≈ 0.62. This can be achieved by including the particle pressure calculation directly in the continuity equation. Interested readers are referred to Passalacqua et al. [136].

An overview of the numerical procedure can be found below:

The numerical procedure adopted in the segregated algorithm:

1. Solve the volume fraction (Eq. 4.22).
2. Construct $\mathbf{A}_i$ in each phase (Eqs. 4.10).
3. Enter PISO-Loop:
   (a) Predict fluxes using Eqs. 4.16 & 4.17.
   (b) Construct and solve the pressure equation (Eq. 4.18).
   (c) Correct the phase fluxes using Eqs. 4.15.
   (d) Reconstruct the phase velocities using Eqs. 4.20.
4. Solve the system of phase energy equations.
5. Advance in time.

4.3 Coupled solution algorithm

In this section the coupled implementation of the RA-TFM is presented, this constitutes the CFD code `ratfmCoupledFoam` and can be found in Appendix D.

4.3.1 Semi-discretised momentum equations

First, we start at the semi-discretised equations as presented previously:

$$\mathbf{A}_p\mathbf{u}_p = \mathbf{H}_p + \frac{\beta\mathbf{u}_f}{\alpha_p\rho_p} - \frac{\beta\mathscr{D}\nabla\alpha_p}{\alpha_p\rho_p} - \frac{\nabla p_f}{\rho_p} - \frac{\nabla p_p}{\alpha_p^*\rho_p} + \mathbf{g}, \tag{4.23a}$$

$$\mathbf{A}_f\mathbf{u}_f = \mathbf{H}_f + \frac{\beta\mathbf{u}_p}{\alpha_f\rho_f} + \frac{\beta\mathscr{D}\nabla\alpha_p}{\alpha_f\rho_f} - \frac{\nabla p_f}{\rho_f} + \mathbf{g}. \tag{4.23b}$$

From here we follow Cubero et al. [44] and separate out the temporal and drag coefficients from the semi-discretised equations. Additionally, the turbulent dispersion and gravity are absorbed into the $\mathbf{H}_i$ operator as well as the particle pressure for the particle-phase. Which now reads as:

$$[\mathbf{A}_p + \mathbf{A}_{Tp} + \mathbf{A}_{Dp}]\mathbf{u}_p = \mathbf{H}_p + \mathbf{H}_{Tp} + \frac{\beta\mathbf{u}_f}{\alpha_p\rho_p} - \frac{\nabla p_f}{\rho_p} \tag{4.24a}$$

$$[\mathbf{A}_f + \mathbf{A}_{Tf} + \mathbf{A}_{Df}]\mathbf{u}_f = \mathbf{H}_f + \mathbf{H}_{Tf} + \frac{\beta\mathbf{u}_p}{\alpha_f\rho_f} - \frac{\nabla p_f}{\rho_f} \tag{4.24b}$$

where the time coefficient for each phase, considering a first-order Euler scheme with a fixed time step, and the drag coefficient is defined as:

$$\mathbf{A}_{Tp} = \frac{\mathbf{H}_{Tp}}{\mathbf{u}_p^{t-1}}, \qquad \mathbf{A}_{Dp} = \frac{\beta}{\alpha_p\rho_p} \tag{4.25a}$$

$$\mathbf{A}_{Tf} = \frac{\mathbf{H}_{Tf}}{\mathbf{u}_f^{t-1}}, \qquad \mathbf{A}_{Df} = \frac{\beta}{\alpha_f\rho_f} \tag{4.25b}$$

Now we divide each side of Eq. 4.24 by the diagonal coefficient, $\mathbf{A}_i$ that contains the advection and the implicit contribution of the shear stress terms, which now reads:

$$[1 + \mathrm{d}_{Tp} + \mathrm{d}_{Dp}]\mathbf{u}_p = \tilde{\mathbf{u}}_p + \mathrm{d}_{Tp}\mathbf{u}_p^{t-1} + \mathrm{d}_{Dp}\mathbf{u}_f - \frac{\nabla p_f}{\rho_p \mathbf{A}_p} \tag{4.26a}$$

$$[1 + \mathrm{d}_{Tf} + \mathrm{d}_{Df}]\mathbf{u}_f = \tilde{\mathbf{u}}_f + \mathrm{d}_{Tf}\mathbf{u}_f^{t-1} + \mathrm{d}_{Df}\mathbf{u}_p - \frac{\nabla p_f}{\rho_f \mathbf{A}_f} \tag{4.26b}$$

with the pseudo-velocities defined as:

$$\tilde{\mathbf{u}}_p = \frac{\mathbf{H}_p}{\mathbf{A}_p}, \qquad \tilde{\mathbf{u}}_f = \frac{\mathbf{H}_f}{\mathbf{A}_f} \tag{4.27}$$

and the coefficients for time, which give a ratio of the temporal to steady coefficients, are defined as:

$$\mathrm{d}_{Tp} = \frac{\mathbf{A}_{Tp}}{\mathbf{A}_p}, \qquad \mathrm{d}_{Tf} = \frac{\mathbf{A}_{Tf}}{\mathbf{A}_f} \tag{4.28}$$

and the coefficients for drag, which give a ratio of the drag to steady coefficients, are defined as:

$$\mathrm{d}_{Dp} = \frac{\mathbf{A}_{Dp}}{\mathbf{A}_p}, \qquad \mathrm{d}_{Df} = \frac{\mathbf{A}_{Df}}{\mathbf{A}_f} \tag{4.29}$$

Then the approximations for each phase velocity can be obtained as:

$$\mathbf{u}_p = \frac{1}{1 + \mathrm{d}_{Tp} + \mathrm{d}_{Dp}} \left[\tilde{\mathbf{u}}_p + \mathrm{d}_{Tp}\mathbf{u}_p^{t-1} + \mathrm{d}_{Dp}\mathbf{u}_f - \frac{\nabla p_f}{\rho_p \mathbf{A}_p} \right] \tag{4.30a}$$

$$\mathbf{u}_f = \frac{1}{1 + \mathrm{d}_{Tf} + \mathrm{d}_{Df}} \left[\tilde{\mathbf{u}}_f + \mathrm{d}_{Tf}\mathbf{u}_f^{t-1} + \mathrm{d}_{Df}\mathbf{u}_p - \frac{\nabla p_f}{\rho_f \mathbf{A}_f} \right] \tag{4.30b}$$

4.3.2 Momentum interpolation

Following Cubero and Fueyo [43], Cubero et al. [44], the velocities at the cell faces can be written as:

$$\mathbf{u}_{i,f} = (\mathbf{u}_i)_f + \langle \mathbf{u}_i \rangle \tag{4.31}$$

where $(\mathbf{u}_i)_f$ is the linearly interpolated velocity at the face and $\langle \mathbf{u}_i \rangle$ is the velocity correction term. The correction term can be obtained by rewriting Eq. 4.31 as:

$$\langle \mathbf{u}_i \rangle = \mathbf{u}_{i,f} - (\mathbf{u}_i)_f \tag{4.32}$$

From here, Eqs. 4.30 can be substituted into the above equation to give:

$$\begin{aligned}
\langle \mathbf{u}_p \rangle = & \frac{\tilde{\mathbf{u}}_{p,f}}{1 + \mathrm{d}_{Tp,f} + \mathrm{d}_{Dp,f}} - \left(\frac{\tilde{\mathbf{u}}_p}{1 + \mathrm{d}_{Tp} + \mathrm{d}_{Dp}} \right)_f \\
& + \frac{\mathrm{d}_{Tp,f} \mathbf{u}^{t-1}_{p,f}}{1 + \mathrm{d}_{Tp,f} + \mathrm{d}_{Dp,f}} - \left(\frac{\mathrm{d}_{Tp} \mathbf{u}^{t-1}_{p}}{1 + \mathrm{d}_{Tp} + \mathrm{d}_{Dp}} \right)_f \\
& + \frac{\mathrm{d}_{Dp,f} \mathbf{u}_{f,f}}{1 + \mathrm{d}_{Tp,f} + \mathrm{d}_{Dp,f}} - \left(\frac{\mathrm{d}_{Dp} \mathbf{u}_{f}}{1 + \mathrm{d}_{Tp} + \mathrm{d}_{Dp}} \right)_f \\
& - \frac{\nabla p_{f,f}}{[1 + \mathrm{d}_{Tp,f} + \mathrm{d}_{Dp,f}] \rho_p \mathbf{A}_{p,f}} + \left(\frac{\nabla p_f}{[1 + \mathrm{d}_{Tp} + \mathrm{d}_{Dp}] \rho_p \mathbf{A}_p} \right)_f
\end{aligned} \tag{4.33}$$

$$\begin{aligned}
\langle \mathbf{u}_f \rangle = & \frac{\tilde{\mathbf{u}}_{f,f}}{1 + \mathrm{d}_{Tf,f} + \mathrm{d}_{Df,f}} - \left(\frac{\tilde{\mathbf{u}}_f}{1 + \mathrm{d}_{Tf} + \mathrm{d}_{Df}} \right)_f \\
& + \frac{\mathrm{d}_{Tf,f} \mathbf{u}^{t-1}_{f,f}}{1 + \mathrm{d}_{Tf,f} + \mathrm{d}_{Df,f}} - \left(\frac{\mathrm{d}_{Tf} \mathbf{u}^{t-1}_{f}}{1 + \mathrm{d}_{Tf} + \mathrm{d}_{Df}} \right)_f \\
& + \frac{\mathrm{d}_{Df,f} \mathbf{u}_{p,f}}{1 + \mathrm{d}_{Tf,f} + \mathrm{d}_{Df,f}} - \left(\frac{\mathrm{d}_{Df} \mathbf{u}_{p}}{1 + \mathrm{d}_{Tf} + \mathrm{d}_{Df}} \right)_f \\
& - \frac{\nabla p_{f,f}}{[1 + \mathrm{d}_{Tf,f} + \mathrm{d}_{Df,f}] \rho_f \mathbf{A}_{f,f}} + \left(\frac{\nabla p_f}{[1 + \mathrm{d}_{Tf} + \mathrm{d}_{Df}] \rho_f \mathbf{A}_f} \right)_f
\end{aligned} \tag{4.34}$$

which leads to exact corrections of each face value. However, due to the linear interpolation of many of these variables their respective face values already contain their best approximation. As shown in Cubero et al. [44], approximating the

pseudo-velocities through a linear interpolation reduces them to zero. The cell face values of the momentum-weighted coefficients and the numerical coefficients can be approximated as:

$$\mathrm{d}_{Ti,f} = (\mathrm{d}_{Ti})_f; \qquad \mathrm{d}_{Di,f} = (\mathrm{d}_{Di})_f; \qquad \mathbf{A}_{i,f} = (\mathbf{A}_i)_f \tag{4.35}$$

The face pressure is calculated from the cell centre assuming central differencing, so that

$$\nabla p_{f,f} = \nabla_f^{\perp} p_f \tag{4.36}$$

In Finite Volume CFD codes we can simplify the face interpolation by writing $(\mathcal{A}_i\phi_i)_f = \mathcal{A}_i(\phi_i)_f$ essentially taking the independent variables outside of the interpolation and leaving the dependant variable. This is utilised throughout each correction term.

Applying the above simplifications and invoking Eq. 4.33 & Eq. 4.34, which now reads as:

$$\langle \mathbf{u}_p \rangle = \langle \mathbf{u}_p \rangle_T + \langle \mathbf{u}_p \rangle_D + \langle \mathbf{u}_p \rangle_{\nabla p_f} \tag{4.37a}$$

$$\langle \mathbf{u}_f \rangle = \langle \mathbf{u}_f \rangle_T + \langle \mathbf{u}_f \rangle_D + \langle \mathbf{u}_f \rangle_{\nabla p_f} \tag{4.37b}$$

where the shared coefficients in each phase are $\langle \mathbf{u}_i \rangle_T$, temporal corrections are:

$$\langle \mathbf{u}_i \rangle_T = \frac{(\mathrm{d}_{Ti})_f [\mathbf{u}_{i,f}^{t-1} - (\mathbf{u}^{t-1})_f]}{1 + (\mathrm{d}_{Ti})_f + (\mathrm{d}_{Di})_f}, \tag{4.38}$$

and $\langle \mathbf{u}_i \rangle_D$, drag corrections are:

$$\langle \mathbf{u}_i \rangle_D = \frac{(\mathrm{d}_{Di})_f [\mathbf{u}_{j,f} - (\mathbf{u}_j)_f]}{1 + (\mathrm{d}_{Ti})_f + (\mathrm{d}_{Di})_f}, \tag{4.39}$$

and $\langle \mathbf{u}_f \rangle_{\nabla p_f}$, pressure correction are:

$$\langle \mathbf{u}_i \rangle_{\nabla p_f} = \frac{-\nabla_f^{\perp} p_f + (\nabla p_f)_f}{[1 + (\mathrm{d}_{Ti})_f + (\mathrm{d}_{Di})_f] \rho_i (\mathbf{A}_i)_f}, \tag{4.40}$$

4.3.3 Construction of implicit pressure equation

Analogous to the segregated implementation an equation for the mixture pressure can be found by inserting the phase-fluxes into the continuity equation (Eq. 4.14). Here we introduce the velocity-corrected flux to read:

$$\phi_{i,f} = [(\mathbf{u}_i)_f + \langle \mathbf{u}_i \rangle] \cdot \mathbf{S}_f \tag{4.41}$$

then inserting the relation into the continuity equation (Eq. 4.14) reading:

$$\nabla \cdot \Big((\alpha_p)_f [(\mathbf{u}_p)_f + \langle \mathbf{u}_p \rangle] \cdot \mathbf{S}_f + (\alpha_f)_f [(\mathbf{u}_f)_f + \langle \mathbf{u}_f \rangle] \cdot \mathbf{S}_f \Big) \tag{4.42}$$

then inserting the corrections velocities in Eqs. 4.37 results in the full pressure equation:

$$\nabla \cdot [D_p \nabla_f^{\perp} p_f |\mathbf{S}_f|] = \nabla \cdot \left(\sum_{k=1}^{P} (\alpha_k)_f (\mathbf{u}_k)_f \cdot \mathbf{S}_f \right) + \nabla \cdot [D_p (\nabla p_f)_f \cdot \mathbf{S}_f]$$
$$+ \nabla \cdot \left[\sum_{k=1}^{P} (\alpha_k)_f \left(\frac{(\mathrm{d}_{Tk})_f [\phi_k^{t-1} - (\mathbf{u}_k^{t-1})_f \cdot \mathbf{S}_f]}{1 + (\mathrm{d}_{Tk})_f + (\mathrm{d}_{Dk})_f} + \frac{\sum_{m=1}^{P} (\mathrm{d}_{mi})_f [\phi_m - (\mathbf{u}_m)_f \cdot \mathbf{S}_f]}{1 + (\mathrm{d}_{Tm})_f + (\mathrm{d}_{Dm})_f} \right) \right] \tag{4.43}$$

where the pressure diffusivity coefficient reads as

$$D_p = \sum_{k=1}^{P} \frac{(\alpha_k)_f}{[1 + (\mathrm{d}_{Tk})_f + (\mathrm{d}_{Dk})_f] \rho_k (\mathbf{A}_k)_f} \tag{4.44}$$

4.3.4 Discretised momentum equations

Here we present the phase-momentum equations in their implemented form as they will be referenced later when discussing the block-coefficients.

$$\begin{aligned}
&\left[\!\left[\frac{\partial[\![\mathbf{u}_p]\!]}{\partial t}\right]\!\right] + \left[\!\left[\nabla\cdot(\mathbf{u}_p[\![\mathbf{u}_p]\!])\right]\!\right] - \left[\!\left[(\nabla\cdot\mathbf{u}_p)[\![\mathbf{u}_p]\!]\right]\!\right] - \left[\!\left[\nabla\cdot(\nu_{\text{eff,p}}\nabla[\![\mathbf{u}_p]\!])\right]\!\right] \\
&\quad -\left[\!\left[\nabla\cdot(\nu_{\text{eff,p}}\frac{\nabla\alpha_p}{\alpha_p+\delta}[\![\mathbf{u}_p]\!])\right]\!\right] - \left[\!\left[\nabla\cdot(\nu_{\text{eff,p}}\frac{\nabla\alpha_p}{\alpha_p^*})[\![\mathbf{u}_p]\!])\right]\!\right] \\
&\quad +\left[\!\left[\frac{\beta[\![\mathbf{u}_p]\!]}{\alpha_p\rho_p}\right]\!\right] - \left[\!\left[\frac{\beta[\![\mathbf{u}_f]\!]}{\alpha_p\rho_p}\right]\!\right] + \left[\!\left[\frac{1}{\rho_p}[\![\nabla p_f]\!]\right]\!\right] \\
&= -\frac{\nabla\alpha_p}{\alpha_p+\delta}\cdot\overline{\mathbf{R}}^c_{\text{eff,p}} - \nabla\cdot\overline{\mathbf{R}}^c_{\text{eff,p}} - \frac{\beta\mathscr{D}\nabla\alpha_p}{\alpha_p\rho_p} - \frac{\nabla p_p}{\alpha_p^*\rho_p} + \mathbf{g}
\end{aligned} \tag{4.45}$$

$$\begin{aligned}
&\left[\!\left[\frac{\partial[\![\mathbf{u}_f]\!]}{\partial t}\right]\!\right] + \left[\!\left[\nabla\cdot(\mathbf{u}_f[\![\mathbf{u}_f]\!])\right]\!\right] - \left[\!\left[(\nabla\cdot\mathbf{u}_f)[\![\mathbf{u}_f]\!]\right]\!\right] - \left[\!\left[\nabla\cdot(\nu_{\text{eff,f}}\nabla[\![\mathbf{u}_f]\!])\right]\!\right] \\
&\quad -\left[\!\left[\nabla\cdot(\nu_{\text{eff,f}}\frac{\nabla\alpha_f}{\alpha_f+\delta}[\![\mathbf{u}_f]\!])\right]\!\right] - \left[\!\left[\nabla\cdot(\nu_{\text{eff,f}}\frac{\nabla\alpha_f}{\alpha_f^*})[\![\mathbf{u}_f]\!])\right]\!\right] \\
&\quad +\left[\!\left[\frac{\beta[\![\mathbf{u}_f]\!]}{\alpha_f\rho_f}\right]\!\right] - \left[\!\left[\frac{\beta[\![\mathbf{u}_p]\!]}{\alpha_f\rho_f}\right]\!\right] + \left[\!\left[\frac{1}{\rho_f}[\![\nabla p_f]\!]\right]\!\right] \\
&= -\frac{\nabla\alpha_f}{\alpha_f+\delta}\cdot\overline{\mathbf{R}}^c_{\text{eff,f}} - \nabla\cdot\overline{\mathbf{R}}^c_{\text{eff,f}} + \frac{\beta\mathscr{D}\nabla\alpha_p}{\alpha_p\rho_p} + \mathbf{g}
\end{aligned} \tag{4.46}$$

4.3.5 Discretised pressure equation

The final implemented pressure equation is presented below. The approach outlined in Cubero and Fueyo [43], Darwish et al. [46], Ferreira et al. [63] is followed to arrive at a pressure equation for the implicit solution of the phase-velocity-pressure coupling. The implicit divergence of the phase-velocities are corrected with the addition of the opposing drag contribution, as shown in Ferreira et al. [63]. Additionally, the whole equation is multiplied by -1 to force all the coefficients along the main diagonal to have the same sign which is advantageous when employing a linear matrix solver. The implemented pressure equation thus reads:

$$-\nabla\cdot[\![D_p\nabla_f^{\perp}[\![p_f]\!]|\mathbf{S}_f|]\!]+\nabla\cdot\left[\!\!\left[(\alpha_k)_f-\sum_{m=1}^{P}\frac{(\alpha_m)_f(\mathrm{d}_{Dm})_f}{1+(\mathrm{d}_{Tm})_f+(\mathrm{d}_{Dm})_f}([\![\mathbf{u}_k]\!])_f\cdot\mathbf{S}_f\right]\!\!\right]$$
$$=\nabla\cdot[D_p(\nabla p_f)_f\cdot\mathbf{S}_f]$$
$$+\nabla\cdot\left[\sum_{k=1}^{P}(\alpha_k)_f\left(\frac{(\mathrm{d}_{Tk})_f[\phi_k^{t-1}-(\mathbf{u}_k^{t-1})_f\cdot\mathbf{S}_f]}{1+(\mathrm{d}_{Tk})_f+(\mathrm{d}_{Dk})_f}+\frac{\sum_{m=1}^{P}(\mathrm{d}_{Dm})_f\phi_m}{1+(\mathrm{d}_{Tk})_f+(\mathrm{d}_{Dk})_f}\right)\right] \tag{4.47}$$

4.3.6 Correction of the phase fluxes

From the solution of the block-coupled matrix, we find new values for the phase-velocity and pressure. Then the face fluxes need to be updated by including the corrections to the phase-velocity that were added to the pressure equation.

$$\phi_p=(\mathbf{u}_p)_f\cdot\mathbf{S}_f+\frac{(\mathrm{d}_{Tp})_f[\phi_p^{t-1}-(\mathbf{u}_p^{t-1})_f\cdot\mathbf{S}_f]}{1+(\mathrm{d}_{Tp})_f+(\mathrm{d}_{Dp})_f}+\frac{(\mathrm{d}_{Dp})_f[\phi_f^{n-1}-(\mathbf{u}_f^{n})_f\cdot\mathbf{S}_f]}{1+(\mathrm{d}_{Tp})_f+(\mathrm{d}_{Dp})_f}$$
$$+\frac{[-\nabla_f^{\perp}p_f^n|\mathbf{S}_f|+(\nabla p_f^{n-1})_f\cdot\mathbf{S}_f]}{[1+(\mathrm{d}_{Tp})_f+(\mathrm{d}_{Dp})_f]\rho_p(\mathbf{A}_p)_f} \tag{4.48}$$

$$\phi_f=(\mathbf{u}_f)_f\cdot\mathbf{S}_f+\frac{(\mathrm{d}_{Tf})_f[\phi_f^{t-1}-(\mathbf{u}_f^{t-1})_f\cdot\mathbf{S}_f]}{1+(\mathrm{d}_{Tf})_f+(\mathrm{d}_{Df})_f}+\frac{(\mathrm{d}_{Df})_f[\phi_p^{n-1}-(\mathbf{u}_p^{n})_f\cdot\mathbf{S}_f]}{1+(\mathrm{d}_{Tf})_f+(\mathrm{d}_{Df})_f}$$
$$+\frac{[-\nabla_f^{\perp}p_f^n|\mathbf{S}_f|+(\nabla p_f^{n-1})_f\cdot\mathbf{S}_f]}{[1+(\mathrm{d}_{Tf})_f+(\mathrm{d}_{Df})_f]\rho_f(\mathbf{A}_f)_f} \tag{4.49}$$

where the superscripts n and $n-1$ denote the value from the present iteration and the previous iteration, respectively. The outline of the solution procedure can be found below.

The numerical procedure adopted in the coupled algorithm:

1. Solve the volume fraction (Eq. 4.22).
2. Construct $\mathbf{A}_i$ and $\mathbf{H}_i$ in each phase.
3. Update the temporal and drag coefficients in Eqs. 4.25.
4. Update the momentum-weighted coefficients in Eq. 4.28 & 4.29.
5. Update the correction velocities in each phase using Eq. 4.37.
6. Assemble and solve the 7x7 block-coupled matrix.
   (a) Feed in the phase momentum equations.
   (b) Feed in the pressure equation.
   (c) Remove cross-coupling source and place in implicit off-diagonal.
7. Apply the flux update using Eqs. 4.48 & 4.49.
8. Solve the system of phase energy equations
9. Advance in time.

4.3.7 Block-coupled solver

The block-coupled system of linear algebraic equations discretised in a Finite Volume framework can be written as:

$$A_{i,j}x_i = b_i \tag{4.50}$$

where $A_{i,j}$ is the matrix representing diagonal and off-diagonal coefficients. x_i is the solution variable and finally b_i is the source vector. This discretisation, within a block-coupled solution, can be easier expressed in two steps [193]: the first level, represents the spatial coupling across the computational domain (Eq. 4.51) and the second level, which represents the inter-equation coupling i.e. phase-velocity-pressure coupling. Expressing a system with N unknowns, in which N is denoted as the number of cells, Eq. 4.50 can be written as:

$$\begin{bmatrix} a_{1,1} & a_{1,2} & \dots & a_{1,N} \\ a_{2,1} & a_{2,2} & \dots & a_{2,N} \\ \vdots & \vdots & \ddots & \vdots \\ a_{N,1} & a_{N,2} & \dots & a_{N,N} \end{bmatrix} \begin{bmatrix} x_1 \\ x_2 \\ \vdots \\ x_N \end{bmatrix} = \begin{bmatrix} b_1 \\ b_2 \\ \vdots \\ b_N \end{bmatrix} \tag{4.51}$$

where $a_{i,j}$ represents a block-coefficient and is spatially coupled between cells i and j, the solution vector, x_i contains the unknowns at cell i and finally, b_i is the source vector for cell i. As mentioned previously, a second level of discretisation is present within a block-coupled matrix.

The solution vector, at cell i now reads:

$$x_i = \begin{bmatrix} u_{p,xi} \\ u_{p,yi} \\ u_{p,zi} \\ u_{f,xi} \\ u_{f,yi} \\ u_{f,zi} \\ p_{f,i} \end{bmatrix}, \qquad b_i = \begin{bmatrix} b_{u_{p,xi}} \\ b_{u_{p,yi}} \\ b_{u_{p,zi}} \\ b_{u_{f,xi}} \\ b_{u_{f,yi}} \\ b_{u_{f,zi}} \\ b_{p_{f,i}} \end{bmatrix} \tag{4.52}$$

where $u_{k,xi}$ represents the x component of the respective phase velocity in cell i, similarly, $u_{k,yi}$ and $u_{k,zi}$ represents the y and z components of the respective phase velocity and finally $p_{f,i}$ represents the pressure field in cell i. In the source vector, the source term for each variable is found following the same notation as the solution vector.

Each block-matrix coefficient, $a_{i,j}$ is a sub-matrix representing the coupling between the phase-velocity-pressure components which comprises of a 7x7 block matrix which can be written as follows:

$$a_{i,j} = \begin{bmatrix} a_{u_{p,xi},u_{p,xj}} & 0 & 0 & a_{u_{p,xi},u_{f,xj}} & 0 & 0 & a_{u_{p,xi},p_{f,j}} \\ 0 & a_{u_{p,yi},u_{p,yj}} & 0 & 0 & a_{u_{p,yi},u_{f,yj}} & 0 & a_{u_{p,yi},p_{f,j}} \\ 0 & 0 & a_{u_{p,zi},u_{p,zj}} & 0 & 0 & a_{u_{p,zi},u_{f,zj}} & a_{u_{p,zi},p_{f,j}} \\ a_{u_{f,xi},u_{p,xj}} & 0 & 0 & a_{u_{f,xi},u_{f,xj}} & 0 & 0 & a_{u_{f,xi},p_{f,j}} \\ 0 & a_{u_{f,yi},u_{p,yj}} & 0 & 0 & a_{u_{f,yi},u_{f,yj}} & 0 & a_{u_{f,yi},p_{f,j}} \\ 0 & 0 & a_{u_{f,zi},u_{p,zj}} & 0 & 0 & a_{u_{f,zi},u_{f,zj}} & a_{u_{f,zi},p_{f,zj}} \\ a_{p_{f,i},u_{p,xj}} & a_{p_{f,i},u_{p,yj}} & a_{p_{f,i},u_{p,zj}} & a_{p_{f,i},u_{f,xj}} & a_{p_{f,i},u_{f,yj}} & a_{p_{f,i},u_{f,zj}} & a_{p_{f,i},p_{f,j}} \end{bmatrix} \tag{4.53}$$

Given the structure of the block-coefficient, a description of the coefficients and their physical meaning is required. We will now focus our attention on four sections of the block-coefficient and for brevity concern ourselves with the particle-phase coefficients.

$$\begin{bmatrix} a_{u_{p,xi},u_{p,xj}} & 0 & 0 \\ 0 & a_{u_{p,yi},u_{p,yj}} & 0 \\ 0 & 0 & a_{u_{p,zi},u_{p,zj}} \end{bmatrix}; \quad \begin{bmatrix} a_{u_{p,xi},u_{f,xj}} & 0 & 0 \\ 0 & a_{u_{p,yi},u_{f,yj}} & 0 \\ 0 & 0 & a_{u_{p,zi},u_{f,zj}} \end{bmatrix} \tag{4.54}$$

The first 3x3 block represents the coupling between the velocity components. These coefficients are filled by the implicitly discretised directional momentum equations pertaining to the time derivative, convection, diffusion and drag in Eqs. 4.45 & 4.46. The explicitly discretised terms are moved to the source vector, Eq. 4.52 i.e. the terms found on the RHS of Eqs. 4.45 & 4.46. The second 3x3 block introduces the cross-coupling coefficients. These represent the implicit treatment

of drag which includes the phase-velocity of the opposing phase and is the eighth term on the LHS of Eqs. 4.45 & 4.46. It is useful to note that in this work the geometry is 2D and therefore the coefficients denoted by the z subscript are zero.

$$\begin{bmatrix} a_{u_{p,xi},p_{f,j}} \\ a_{u_{p,yi},p_{f,j}} \\ a_{u_{p,zi},p_{f,j}} \end{bmatrix}; \qquad \begin{bmatrix} a_{p_{f,i},u_{p,xj}} & a_{p_{f,i},u_{p,yj}} & a_{p_{f,i},u_{p,zj}}. \end{bmatrix} \tag{4.55}$$

The first 1x3 block in Eq. 4.55 denotes the phase-velocity-pressure coupling in the momentum equation. This pertains to the implicit treatment of the pressure gradient, the ninth term in Eqs. 4.45 & 4.46. The second block, 3x1 denotes the phase-velocity-pressure coupling in the pressure equation. This pertains to the implicit treatment of the terms inside in the divergence operator in Eq. 4.47 i.e. the second term, with explicit boundary contributions populating the source vector, $b_{p_{f,i}}$.

The implicitly treated pressure on the LHS of Eq. 4.47 is fed into the coefficient $a_{p_{f,i},p_{f,j}}$ with the explicit boundary contributions being fed into the corresponding source vector $b_{p_{f,i}}$. Finally, the explicit terms on the RHS of Eq. 4.47 are fed into the source vector, $b_{p_{f,i}}$.

Within the community driven branch of OpenFOAM called `foam-extend` several numerical tools have been developed to house coupled solvers [33, 42, 91]. The block-matrix machinery is extended in order to construct a 7x7 block matrix and ensure the correct populating of matrix coefficients. The coupled matrix solvers are then used to solve the phase-velocity-pressure coupled system.

4.4 Solution of the phase energies

Upon completion of the phase-continuity and phase-velocity-pressure equations the phase energy equations are then solved. The system of phase energies, like their momentum counterpart, are put into a phase-intensive form although this is not essential. Due to the form of the drag term the division by the volume fraction does not cause any numerical issues, as outlined in previous sections. Thus, the phase energies can be readily discretised.

$k_f - \varepsilon_f$ model equations:

$$\begin{aligned}\left[\!\left[\frac{\partial[k_f]}{\partial t}\right]\!\right] + \left[\!\left[\nabla\cdot(\phi_f[k_f]_f)\right]\!\right] - \left[\!\left[\nabla\cdot(\phi_f)([k_f])\right]\!\right] - \left[\!\left[\nabla\cdot\left[\left(\nu_f+\frac{\nu_{ft}}{\sigma_{fk}}\right)\nabla[k_f]\right]\right]\!\right] \\ = \Pi_f - \left[\!\left[\frac{\varepsilon_f}{k_f}[k_f]\right]\!\right] + 2\frac{\beta}{\alpha_f\rho_f}k_{fp} - \left[\!\left[2\frac{\beta}{\alpha_f\rho_f}[k_f]\right]\!\right]\end{aligned} \tag{4.56}$$

$$\begin{aligned}\left[\!\left[\frac{\partial[\varepsilon_f]}{\partial t}\right]\!\right] + \left[\!\left[\nabla\cdot(\phi_f[\varepsilon_f]_f)\right]\!\right] - \left[\!\left[\nabla\cdot(\phi_f)([\varepsilon_f])\right]\!\right] - \left[\!\left[\nabla\left[\cdot\left(\nu_f+\frac{\nu_{ft}}{\sigma_{fk}}\right)\nabla[\varepsilon_f]\right]\right]\!\right] \\ = C_1\Pi_f\frac{\varepsilon_f}{k_f} - \left[\!\left[C_2\frac{\varepsilon_f}{k_f}[\varepsilon_f]\right]\!\right] + 2C_3\frac{\beta}{\alpha_f\rho_f}\varepsilon_{fp} - \left[\!\left[2C_3\frac{\beta}{\alpha_f\rho_f}[\varepsilon_f]\right]\!\right]\end{aligned} \tag{4.57}$$

$\overline{v_f^2} - f$ model equations:

$$\begin{aligned}\left[\!\left[\frac{\partial[\overline{v_f^2}]}{\partial t}\right]\!\right] + \left[\!\left[\nabla\cdot(\phi_f[\overline{v_f^2}]_f)\right]\!\right] - \left[\!\left[\nabla\cdot(\phi_f)([\overline{v_f^2}])\right]\!\right] - \left[\!\left[\nabla\cdot\left[\left(\nu_f+\frac{\nu_{ft}}{\sigma_{fk}}\right)\nabla[\overline{v_f^2}]\right]\right]\!\right] \\ = \overline{v_f^2}_{source} - \left[\!\left[6\frac{\varepsilon_f}{k_f}[\overline{v_f^2}]\right]\!\right] + 2\frac{\beta}{\alpha_f\rho_f}\overline{v_{fp}^2} - \left[\!\left[2\frac{\beta}{\alpha_f\rho_f}[\overline{v_f^2}]\right]\!\right]\end{aligned} \tag{4.58}$$

$$-\left[\!\left[\nabla^2[f]\right]\!\right] = -\left[\!\left[\frac{1}{L^2}[f]\right]\!\right] - \frac{1}{L^2}\left[\frac{C_1}{T}\left(\frac{\overline{v_p^2}}{k_f}-\frac{2}{3}\right) - C_2\frac{\Pi_p}{k_f} - \frac{1}{T}\left(6\frac{\overline{v_f^2}}{k_f}-\frac{2}{3}\right)\right] \tag{4.59}$$

$k_p - \varepsilon_p$ model equations:

$$\begin{aligned}\left[\!\left[\frac{\partial[k_p]}{\partial t}\right]\!\right] + \left[\!\left[\nabla\cdot(\phi_p[k_p]_f)\right]\!\right] - \left[\!\left[\nabla\cdot(\phi_p)([k_p])\right]\!\right] - \left[\!\left[\nabla\cdot\left(\nu_p+\frac{\nu_{pt}}{\sigma_{pk}}\right)\nabla[k_p]\right]\!\right] \\ = \Pi_p - \left[\!\left[\frac{\varepsilon_p}{k_p}\varepsilon_p\right]\!\right] + 2\frac{\beta}{\alpha_p\rho_p}k_{fp} - \left[\!\left[2\frac{\beta}{\alpha_p\rho_p}[k_p]\right]\!\right]\end{aligned} \tag{4.60}$$

$$\begin{aligned}\left[\!\left[\frac{\partial[\varepsilon_p]}{\partial t}\right]\!\right]+\left[\!\left[\nabla\cdot(\phi_p[\varepsilon_p]_f)\right]\!\right]-\left[\!\left[\nabla\cdot(\phi_p)([\varepsilon_p])\right]\!\right]-\left[\!\left[\nabla\cdot\left(\nu_p+\frac{\nu_{pt}}{\sigma_{pk}}\right)\nabla[\varepsilon_p]\right]\!\right]\\ =C_1\Pi_p\frac{\varepsilon_p}{k_p}-\left[\!\left[C_2\frac{\varepsilon_p}{k_p}[\varepsilon_p]\right]\!\right]+2C_3\frac{\beta}{\alpha_p\rho_p}\varepsilon_{fp}-\left[\!\left[2C_3\frac{\beta}{\alpha_p\rho_p}[\varepsilon_p]\right]\!\right]\end{aligned} \tag{4.61}$$

$\overline{v_p^2}-f$ model equations:

$$\begin{aligned}\left[\!\left[\frac{\partial[\overline{v_p^2}]}{\partial t}\right]\!\right]+\left[\!\left[\nabla\cdot(\phi_p[\overline{v_p^2}]_f)\right]\!\right]-\left[\!\left[\nabla\cdot(\phi_p)([\overline{v_p^2}])\right]\!\right]-\left[\!\left[\nabla\cdot\left[\left(\nu_p+\frac{\nu_{pt}}{\sigma_{fk}}\right)\nabla[\overline{v_p^2}]\right]\right]\!\right]\\ =\overline{v_{p_{source}}^2}-\left[\!\left[6\frac{\varepsilon_p}{k_p}[\overline{v_p^2}]\right]\!\right]+2\frac{\beta}{\alpha_p\rho_p}\overline{v_{fp}^2}-\left[\!\left[2\frac{\beta}{\alpha_p\rho_p}[\overline{v_p^2}]\right]\!\right]\end{aligned} \tag{4.62}$$

$$-\left[\!\left[\nabla^2[f]\right]\!\right]=-\left[\!\left[\frac{1}{L_p^2}[f]\right]\!\right]-\frac{1}{L_p^2}\left[\frac{C_1}{T_p}\left(\frac{\overline{v_p^2}}{k_p}-\frac{2}{3}\right)-C_2\frac{\Pi_p}{k_p}-\frac{1}{T_p}\left(6\frac{\overline{v_p^2}}{k_p}-\frac{2}{3}\right)\right] \tag{4.63}$$

An exception is made for the granular temperature equation. As the constitutive relations for p_p, μ_p, κ_Θ and γ are a function of volume fraction and density, dividing by these would result in unnecessary division by small values as $\alpha_p \to 0$. Therefore, the equations are implemented in their multiphase form like so:

$$\begin{aligned}\frac{3}{2}\left[\!\left[\frac{\partial(\alpha_p\rho_p[\Theta])}{\partial t}\right]\!\right]+\left[\!\left[\nabla\cdot(\alpha_{p,f}\rho_p\phi_p[\Theta]_f)\right]\!\right]-\left[\!\left[\nabla\cdot(\alpha_{p,f}\rho_p\phi_p)([\Theta])\right]\!\right]+\left[\!\left[3\beta[\Theta]\right]\!\right]+\left[\!\left[\gamma[\Theta]\right]\!\right]\\ -\left[\!\left[\nabla\cdot\left[\left(\kappa_\Theta+\frac{3\mu_{pt}}{2Pr_{pt}}\right)\nabla[\Theta]\right]\right]\!\right]=2\mu_p\overline{\mathbf{S}}_\mathbf{p}:\overline{\mathbf{S}}_\mathbf{p}-p_p\nabla\cdot\mathbf{u}_p+\alpha_p\rho_p\varepsilon_p\end{aligned} \tag{4.64}$$

Once the phase energy system is solved the algorithm is completed. It should be noted that upon the solution of the granular temperature equation the variables of interest are updated in their incompressible form to ensure the correct calculation for the particle pressure and viscosity is employed within the particle-phase momentum equation.

4.5 Closure

This chapter has detailed the solution procedure adopted for solving the RA-TFM system of equations. The governing equations were presented and recast into their implemented form. A segregated and coupled implementation has been outlined

with particular attention paid to the treatment of the solution algorithm on collocated grids of which are used in OpenFOAM. Additionally, the numerical treatment of the momentum coupling force and the mixed-phase continuity equation was detailed. Finally, the discretisation practice for the phase-energy system was presented.

This page is intentionally left blank.

5 Prediction of fluid-particle flow over a backward-facing step

5.1 Overview

In this chapter the Reynolds-Averaged Two-Fluid Model (RA-TFM) for modelling of turbulent fluid-particle flow is applied to a vertically orientated backward-facing step. The model is compared and contrasted against the Modified Peirano Model [141]. Three particle classes with varying mass loadings (10-40%) and different Stokes number are investigated. The prediction of mean flow statistics are in good agreement with the benchmark experimental data of Fessler and Eaton [65, 66] and show a distinct improvement over the MPM predictions - an implementation that is rife in open-source and commercial CFD codes. This improvement was due to the separation of the particle turbulent kinetic energy k_p, and the granular temperature Θ, in which the large scale correlated motion and small scale uncorrelated motion are governed by separate transport equations. For each case simulated in this work, turbulence attenuation was accurately predicted, a finding that is attributed to separate coupling terms in both transport equations of k_p and ε_p.

The contributions of this chapter are as follows:

- The RA-TFM segregated implementation detailed in Chapter 4 is implemented with OpenFOAM and applied to a vertically orientated backward-facing step of Fessler and Eaton [65, 66];
- In order to accommodate the new particle turbulence statistics, k_p, ϵ_p & Θ, boundary conditions of Johnson and Jackson [97] (presented in Chapter 2 - §2.7) that represent their interaction with the wall are implemented within OpenFOAM;
- The modelling methodology is compared and contrasted against the current methodology that is prevalent in open-source and commercial CFD codes i.e. the Peirano model [141];
- The RA-TFM is validated on three different particle classes with increasing mass loading. This enhances the influence of turbulence production terms within the model and demonstrates the model is capable of capturing different particle behaviours;
- Agreement across mean particle-phase velocities and the fluctuating intensity of both the particle and fluid phases are found to be satisfactory with stark improvements over the MPM model;
- The influence of the wall boundary conditions were ascertained through a parametric study of the specularity coefficient.
- The separation of the particle fluctuation energy into two separate contributions was vital in predicting the presence of the shear layer in the backward-facing step configuration;
- The particle-fluid velocity coupling terms, k_{fp} and ϵ_{fp} were shown to be capable of predicting two-way coupled effects resulting in a good agreement with the experimental data.

5.2 Introduction

To date, there have been numerous experimental studies investigating small heavy particles in wall-bounded, high Reynolds number flow [18, 32, 106, 192]. One valuable study is that of Fessler and Eaton [66] in which mean and turbulence statistics of moderately dilute fluid-particle flow were recorded in a vertically orientated backward-facing step. Velocities and their statistics were sampled with laser Doppler anemometry (LDA) which is capable of recording the particles within its field of view. They report turbulence attenuation across three particle classifications (different Stokes number and mass loadings) and provide valuable insights into the particle behaviour in the free shear layer. Traditionally, the backward-facing step has been used as a benchmark for validation of single-phase turbulence models, as flow separation, reattachment and redevelopment are common in engineering applications. Due to the complex nature of turbulence attenuation, the challenging physics in a backward-facing step configuration and high Reynolds number flow, its successful prediction has proven difficult for E-E models [36, 127, 128, 198, 221]. These models are exclusively based on the MPM methodology presented in §2.4 in which the distinction between the separating effect of the particles inertia is not catered for within the particle-phase energy modelling.

In this chapter, the RA-TFM and its segregated implementation as detailed in Chapters 2 & 4 are employed throughout. The model is applied to the experimental data of Fessler and Eaton [65, 66] in which a turbulent vertically orientated backward-facing step is used to investigate two-way coupling effects with volume fractions in the $\mathcal{O}(10^{-4})$. This case is often sought in the literature for validation and as discussed previously represents a challenging case for E-E models. The predictions of the RA-TFM are contrasted and compared against the MPM Peirano and Leckner [141] presented in §2.4. Additionally, in order to accommodate the new particle-phase turbulent variables, k_p, ϵ_p and Θ wall boundary conditions that were presented in Chapter 2 - §2.7 are employed and their influenced ascertained.

5.3 Geometry and case setup

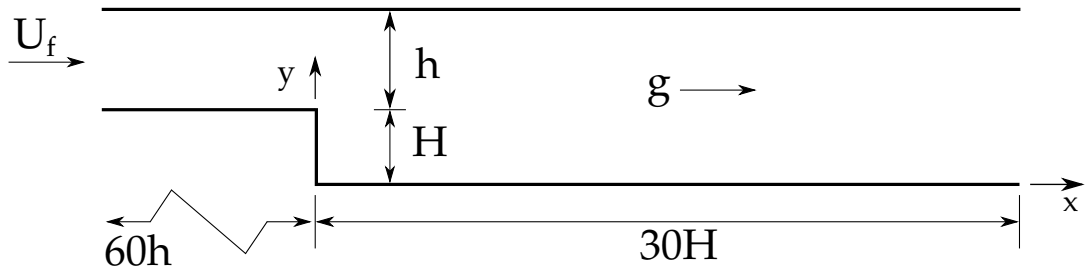

Figure 5.1: Schematic detailing the geometry used throughout, with h = 0.04 m and H = 0.0267 m.

The computational domain is a two-dimensional channel section as seen in Fig. 5.1 which starts at 60h upstream of the step to allow the flow to fully develop and extends 30H downstream. The material constants for each respective case can be found in Table 5.1. As reported in the experiments the centreline velocity, U_0 is 10.5 m s^{-1} at the step (x/H =0) and this corresponded to an inlet value of 9.4 m s^{-1}. Based on the reported centreline velocity and the channel half-height i.e. h/2, the Reynolds number was 13, 800. Mass loading is given by a uniform particle volume fraction across the inlet, this is achieved by assuming a constant particle-to-fluid velocity ratio. Wall functions for the fluid-phase are used throughout and the effect of the particles on the boundary layer is not considered. For the particle-phase, the boundary conditions described in §2.7 are used for the turbulent quantities. At the inlet a first estimate of the two turbulent quantities is determined as follows; $k_p = 1/3k_f$ and $\varepsilon = 1/3\varepsilon_f$ (for a more elaborate approach see [71]). For the granular temperature a small value is specified; $\Theta = 1\,\mathrm{x}\,10^{-10}$ m^2 s^{-2} [198]. Calculations are carried out on a fully structured hex dominated mesh consisting of 11,253 cells with $y^+ > 30$ along both walls. Lastly, the model constants can be found in Appendix C - §C.3.

Table 5.1: Table of simulated cases.

Case	Material	d_p [μ m]	ρ_p [kg m^{-3}]	Mass loading	St	Re_p
1	glass	150	2500	20% and 40%	7.9	10.1
2	glass	90	2500	20%	3.8	2.9
3	copper	70	8800	10% and 40%	7.4	4.4

5.4 Results and discussion

The simulated results from the RA-TFM and the modified Peirano model (MPM) are compared against two sets of experimental data given by Fessler and Eaton [66] & Fessler and Eaton [65]. Mean quantities of particle velocity, fluid turbulence intensity and particle turbulence intensity are presented across three cases focusing on three particle classes (see Table 5.1). The measured velocity profiles start at the recirculation region (x/H = 2), continue through to the reattachment zone (x/H = 5), and finally the redevelopment region (x/H = 14) with measurements being taken in between.

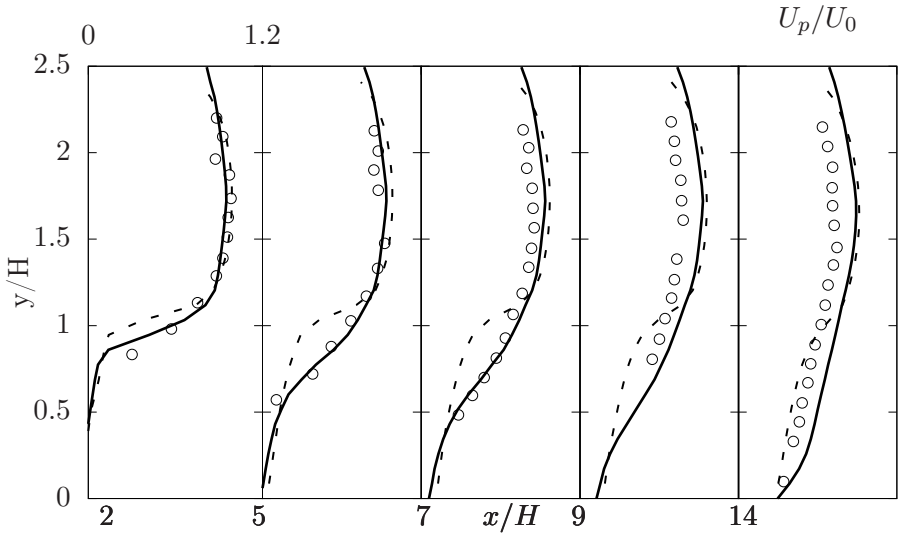

Figure 5.2: Stream-wise particle mean velocity for case 1. Solid line showing the RA-TFM and the dashed line showing the MPM. Data from Fessler and Eaton [65] with a mass-loading of 40%.

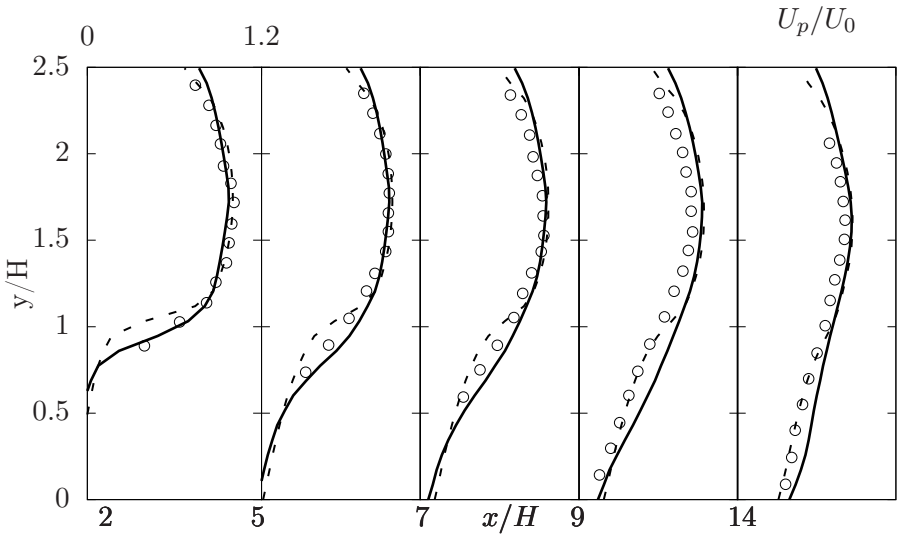

Figure 5.3: Stream-wise particle mean velocity for case 2. Solid line showing the RA-TFM and the dashed line showing the MPM. Data from Fessler and Eaton [65] with a mass-loading of 20%.

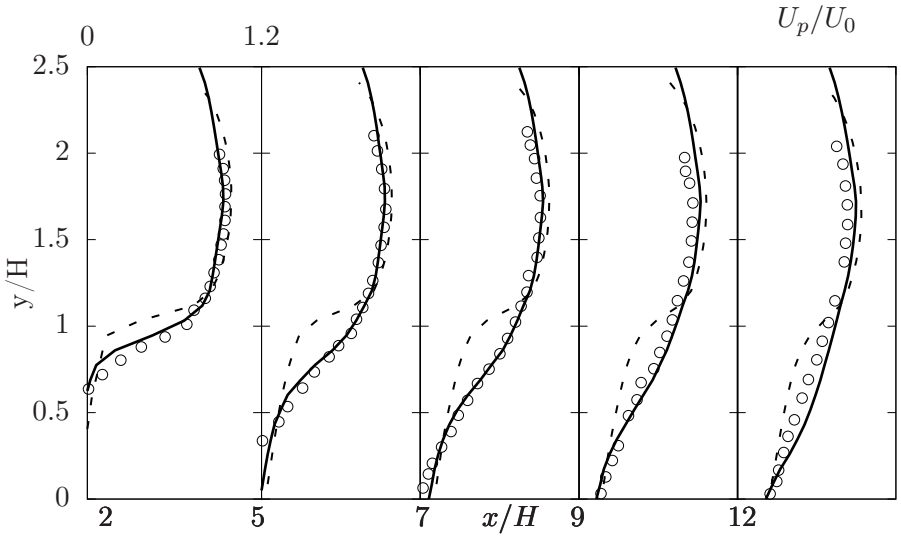

Figure 5.4: Stream-wise particle mean velocity for case 3. Solid line showing the RA-TFM and the dashed line showing the MPM. Data from Fessler and Eaton [66] with a mass-loading of 10%.

5.4.1 Mean particle stream-wise velocity

It is evident that across all three Figs. 5.2, 5.3 and 5.4 the prediction of the RA-TFM mean particle velocity profiles are in good agreement with the measured results. The model captures the affects of varying St and mass loading on the mean velocity profile, especially in the recirculation region corresponding to locations (x/H = 2) and (x/H = 5). The MPM shows a marked difference around the step ($0.5 < \text{y/H} \leq 1$) as it does not include the correlated particle turbulent kinetic fluctuations. These stresses are responsible for forming the shear layer and leading to the production of turbulent viscosity.

Figures 5.2, 5.3 and 5.4 show particle velocities with a flatter gradient across the depth of the pipe when compared to the fluid velocities, a feature that is not predicted by the MPM. This is attributed to the calculation of the particle-phase viscosity. In the RA-TFM the calculation of the turbulent viscosity μ_{pt} appearing in the momentum equation is given by the $k_p - \varepsilon_p$ turbulence model, which accounts for the correlated turbulent kinetic particle fluctuations that are dominant due to the shear layer. In the MPM the viscosity is calculated directly from the granular temperature equation which relies on constitutive closures of particle pressure, thermal conductivity and viscosity [141]. As a result, a small value of both is predicted due to the dilute nature of the flow and this leads to a gross under-prediction of the particle viscosity. This then allows the momentum coupling term β to dominate in this region, which is why the mean velocity profiles tend to closely follow the fluid-phase mean velocity profile.

Figures 5.2 & 5.4 reveal the largest variation between the predicted mean particle velocity profiles in the shear layer. This is attributed to the particles St, which varies considerably over the shear layer as shown in both Figs (y/H < 1). When the particles $St \gg 1$ the particles tend to escape from the eddy they are in and ignore the influence of external eddies. This can either unite small eddies to create larger more energetic eddies or it can destroy large eddies which dissipate to smaller eddies. As a consequence of this for $St \gg 1$ we can expect the particle to take

longer to react to the fluid. Therefore, when considering the shear layer the fluid response time, τ_f will be small in comparison with the channel flow resulting in a much higher local St. As a result the particle mean velocity profile does not show the sharp gradient across the (y/H $>$ 1) and becomes much flatter.

Figure 5.2 shows the case denoting both a high St (7.9) and a large mass loading (40%). It also corresponds to the largest over-prediction in the mean particle velocities at locations (x/H = 9 & 14) for the RA-TFM. These locations correspond to the redevelopment region which indicate that the energy in the particle-phase is recovering too quickly in comparison to the measured data. This overestimation is difficult to explain as the predictions for case 3 with a large St are in good agreement. One potential source of error could be due to the distribution of the particles across the width of the pipe. As the particles pass the step they are redistributed inhomogeneously (clustered) which reduces the slip velocity and as a result the drag. As the particles reach the redevelopment region they begin to redistribute homogeneously which increases the drag in this region. However neither model considers the effects of clustering in their drag model and are only representative of one particle. This can cause the observed over-estimation of the mean stream-wise velocities in the redevelopment region.

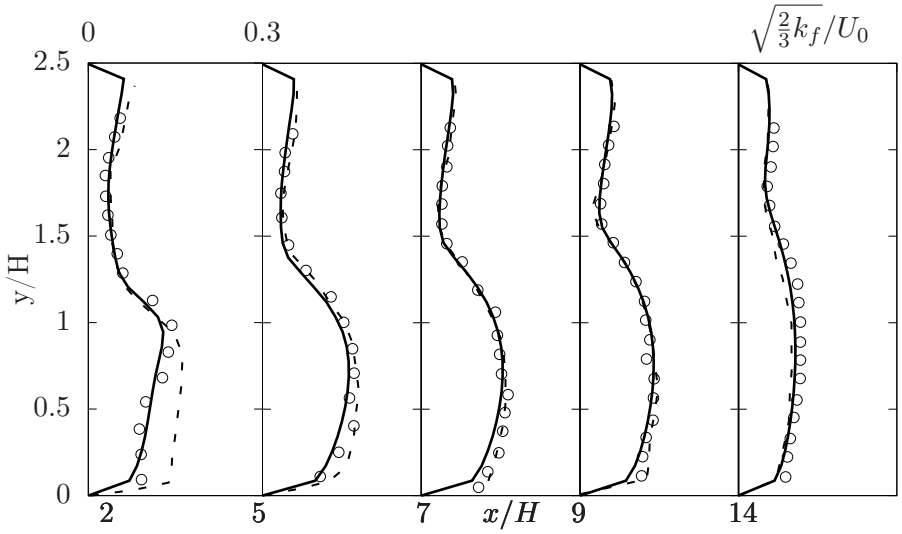

Figure 5.5: Fluid turbulent intensity for case 1. Solid line showing the RA-TFM and the dashed line showing the MPM. Data from Fessler and Eaton [66] with a mass-loading of 40%.

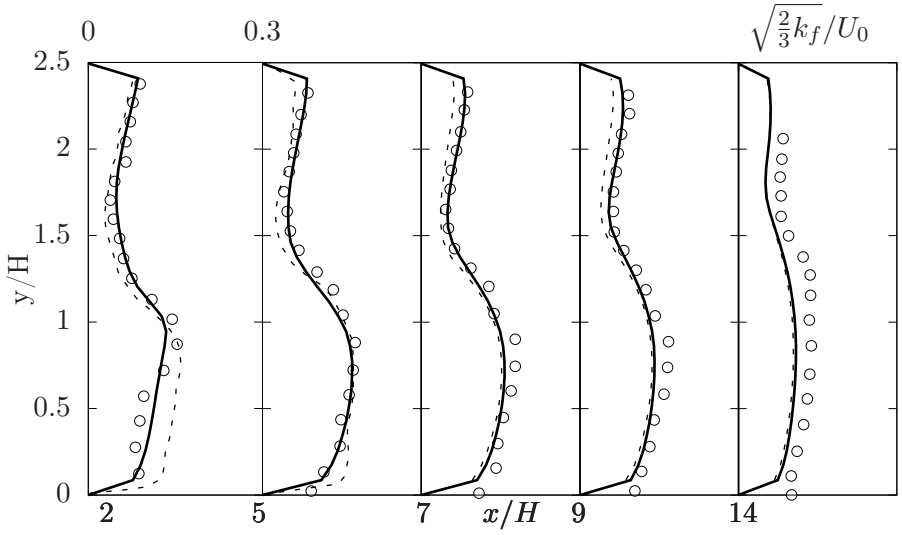

Figure 5.6: Fluid turbulent intensity for case 2. Solid line showing the RA-TFM and the dashed line showing the MPM. Data from Fessler and Eaton [66] with a mass-loading of 20%.

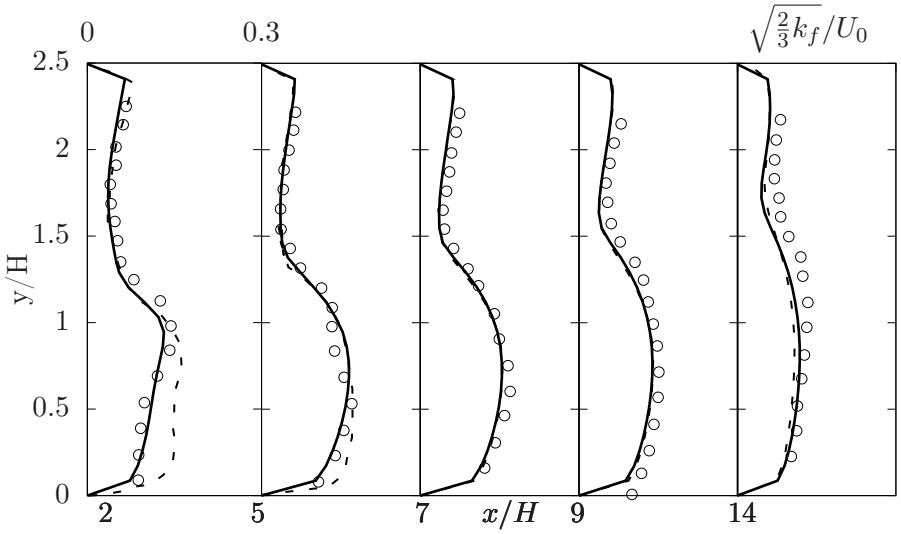

Figure 5.7: Fluid turbulent intensity for case 3. Solid line showing the RA-TFM and the dashed line showing the MPM. Data from Fessler and Eaton [66] with a mass-loading of 40%.

5.4.2 Fluid-phase turbulence

As shown in the experiment of Fessler and Eaton [66], distinct turbulence attenuation was found for the two larger St cases (1 & 3). Over the region of (y/H $>$ 1) extensive turbulence attenuation is shown across all five plots (corresponds to Fig. 9 in Fessler and Eaton [66]). Across locations (x/H = 2 & 5) there is attenuation across the range (y/H $>$ 1) which shows that as mass loading is increased the turbulence is suppressed and below this range (y/H $<$ 1) the turbulence is unaffected. This behaviour of turbulence attenuation was accurately predicted by the RA-TFM and the corresponding plots to those in [66] are Figs 5.5 & 5.7. The predictions are in good agreement with the experimental measurements. The turbulence attenuation for case 1 is as much as 35% showing a large reduction over the region of (y/H $>$ 1) at (x/H = 2) on Fig. 5.7.

Below (y/H $<$ 1) very little turbulence attenuation was observed, this corresponds to the shear layer and recirculation zone. From the simulations carried out, the particle turbulent quantities k_p & ε_p are produced and dissipated primarily near and at the wall and step (shear layer), with the contribution in the recirculation zone (y/H $<$ 1) being several orders of magnitudes smaller. When considering the form of the coupling terms (see §2.3) it is evident why the turbulence attenuation is small in this region. This also follows from the lack of particles within the recirculation region due to the large St of all cases ($St > 1$) as the particles are not dragged into the eddy in the same way a particle of ($St < 1$) would.

The turbulence attenuation was accurately captured across all three particle classes for the RA-TFM. For the MPM an over-prediction of the fluid turbulent kinetic energy was observed. It was found that the form of the velocity correlation coupling term posed two major problems, the first being that as the term $k_{fp} = \sqrt{k_f \Theta}$ contains Θ directly the evolution of the term is adversely affected as the granular temperature equation evolves too quickly. This behaviour is recognised in two fluid model codes, and typically an upper limit is employed to constrain the initial stages of the solution to increase robustness.

Secondly, the source term of this form exists in both the k_f & ε_f transport equations (Eq. 2.65 & 2.66), this leads to the formulation of the turbulent kinetic energy dissipation equation given by Elghobashi and Abou-Arab [61], which has been shown to yield incorrect behaviour [71], mainly as a consequence of failing to differentiate between the correlated and uncorrelated turbulent kinetic energy. Conversely, two coupling source terms for the macroscale energy exchange are used within the RA-TFM, k_{fp} and ε_{fp} respectively.

This has several benefits. Firstly, it allows the coupling of the turbulent kinetic energy k_i and dissipation ε_i equations of both phases to contain source terms that are of the same physical attribute i.e. particle turbulent kinetic energy and particle turbulence kinetic energy dissipation both contain separate coupling terms, which ensures conservation of energy between the two phases. Secondly, this essentially means that the particles can become correlated with the carried phase at the macroscale level i.e. turbulence scale and also dissipate its energy at a characteristic length scale. Lastly, this dissipation appears as a source term within the granular temperature equation thus ensuring an energy cascade across scales (Fig. 2.1). As this approach forms a physically correct treatise of the particles energy the need for numerical limiting of the phase energy is alleviated. This increases the numerical robustness and stability of the transient solution as the evolution of the solution is limited by physical processes. Additionally, the linear solvers used to solve the equations require fewer iterations to reach tolerance before advancing the solution in time - thus decreasing the solution time.

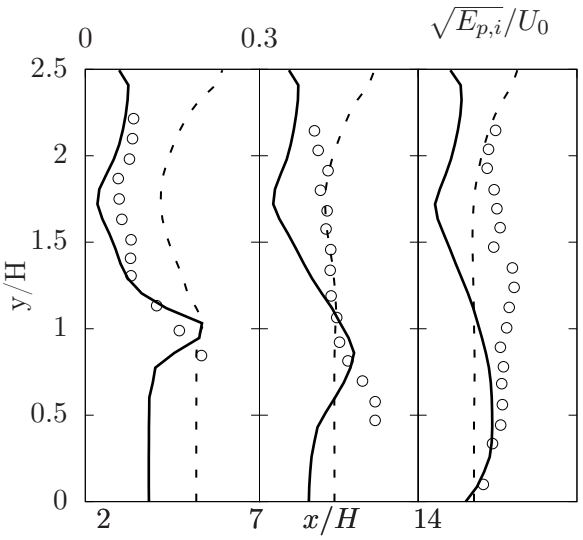

Figure 5.8: Particle turbulent intensity for case 1. Solid line showing the RA-TFM and the dashed line showing the MPM. Data from Fessler and Eaton [65] with a mass-loading of 40%.

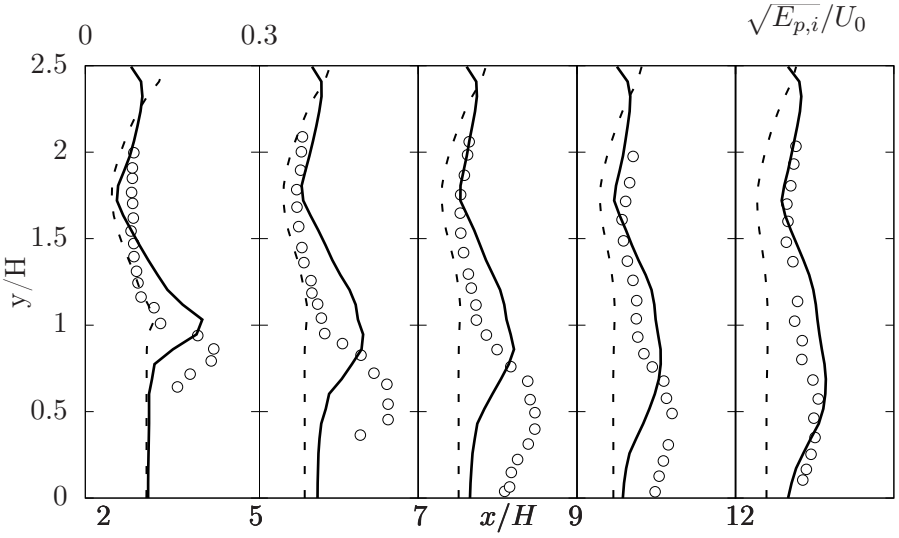

Figure 5.9: Particle turbulent intensity for case 3. Solid line showing the RA-TFM and the dashed line showing the MPM. Data from Fessler and Eaton [66] with a mass-loading of 10%.

5.4.3 Particle-phase turbulence

From the experimental measurements it can be seen that the particles are being heavily influenced by the fluid-phase's shear layer. This is true for both cases involving large St as shown in Figs. 5.8 & 5.9. Looking at the results from the MPM the prediction of the shear layer can not be seen across each location. Conversely, the RA-TFM is able to predict the presence of the shear layer and, crucially, convect it downstream. This feature is difficult to predict as the particles disperse and their fluctuating energy becomes more uniform across the profile. This result was almost exclusively attributed to the solution of the $k_p - \varepsilon_p$ transport equation.

As shown in Février et al. [67] the decomposition of the particle fluctuation energy into two components which reads, $\kappa_p = k_p + 3/2\Theta$ was needed when accounting for the particle's overall motion. Due to the step, turbulent scales at the integral scale are dominating the flow and as a result the large scale motions are the most relevant. This is reflected in the predictions of this model and highlighted when contrasted with the predictions of the MPM. Without the $k_p - \varepsilon_p$ transport model, the influence of the step is not captured and an under-prediction of the turbulent particle kinetic energy is seen.

Table 5.2 shows the integral time scales associated with both flow regimes. This characteristic time scale associated with the particle turbulent kinetic energy enables the prediction of the shear layer and allows for the successful prediction of the predominant turbulent behaviour found in experiment across both Figs. 5.8 & 5.9.

Table 5.2: Table of integral time scales for each phase.

Flow regime	T_p	T_f
Channel flow centre line	0.04s	0.04s
Shear layer	4.09ms	5.12ms

In the MPM this definition of the particle-phase time scale is not present. The calculation of 'turbulent kinetic energy' (granular temperature Θ) is heavily reliant on the constitutive relation of thermal conductivity, shear viscosity and bulk viscosity. As shown in both Figs. 5.8 & 5.9 the absence of the shear layer is demonstrated. The profiles are within the correct order of magnitude but the profile remains flat and largely unaffected by the step.

The $k_p - \varepsilon_p$ transport equation is modelled in an analogous manner to the single-phase $k - \varepsilon$ turbulence model using similar closure relations [142]. As a result some of the models well-known limitations are directly inherited. The Boussinesq approximation is one such limitation of RANS models of this form and introduces isotropy into the model; specifically the Reynolds stresses are assumed to be a scalar function of the mean velocity gradients. This introduction of isotropy has quite clear implications for the prediction of turbulent structures. The shear layer simulated in this studied is dominated by both the production term, Π_p and the turbulent dissipation term, ε_p; the former is where the isotropy is introduced and that is why it is so influential.

It has been shown by Simonin [173, 174] that the particle turbulence Reynolds stresses are highly anisotropic and require transport equations for each term. This is a clear limitation of the current model and from the performance of the current RA-TFM an introduction of anisotropy for at least the particle-phase is vital in an accurate prediction of the particle-phase energy behaviour.

5.4.4 Particle wall boundary conditions

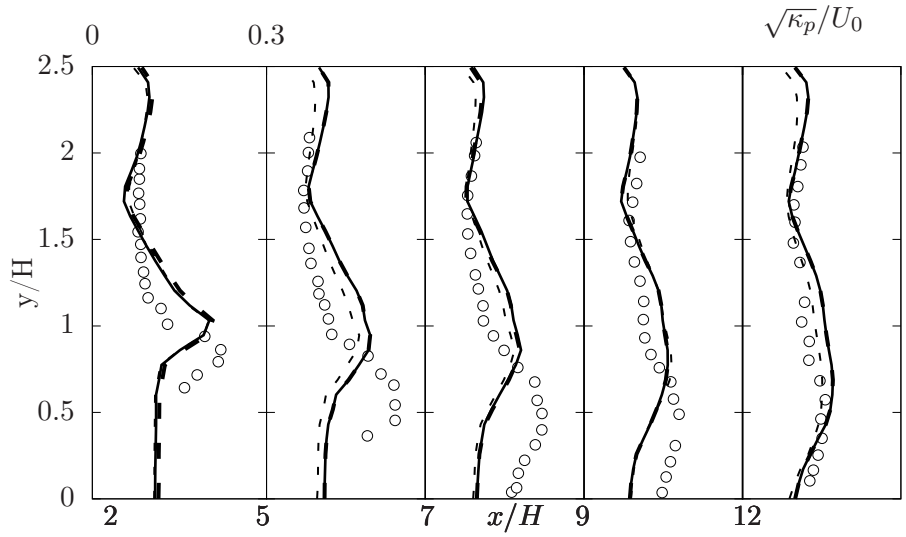

Figure 5.10: Particle turbulent intensity for case 3. Solid line showing the $\phi_{spec} = 0.001$, thick dashed line showing $\phi_{spec} = 0.01$ and the thin dashed line showing $\phi_{spec} = 0$. Data from Fessler and Eaton [66] with a mass-loading of 10%.

As noted in Fessler and Eaton [66], the particles tend to conserve almost all their energy when interacting with the wall. As a consequence of this observation the specularity coefficient was varied from 0-0.01 in order to ascertain its effect on the numerical predictions.

Fig. 5.10 shows the particle turbulent intensity prediction of the RA-TFM with varying specularity coefficients. Immediately a general observation can be made; the particle-phase wall boundary conditions have a relatively small impact on the prediction of particle fluctuation energy. This is to be expected as the particles spend very little time interacting with the wall and the particle fluctuation energy is dominated by the production in the shear layer.

The biggest difference can be seen by comparing $\phi_{spec} = 0$ with $\phi_{spec} = 0.01 - 0.001$, and looking at locations (x/H = 5 - x/H = 12). The free slip condition exerts its influence on the prediction immediately downstream of the shear layer, this results in an underestimation in comparison with the larger ϕ_{spec} values. When comparing

this result with the experimental data it seems that the prediction lies closer to the measured values, this is seen most clearly at location (x/H = 5) across (y/H > 1) and across the whole profile at location (x/H = 12).

When comparing the near wall predictions of particle fluctuation energy it can be seen that there is a slight under-prediction when comparing $\phi_{spec} = 0$ and $\phi_{spec} = 0.01 - 0.001$. This is to be expected as a higher specularity coefficient will result in a higher value of particle fluctuation energy due to the production of mean particle shear.

All three simulations under-predict the near wall behaviour. This result is attributed to the lack of particle-phase fluctuation anisotropy, but put more explicitly the experimental observations show that the particle fluctuation energy is stretched in the wall-normal direction. This stretching continues up to the wall (at x/H = 7), the RA-TFM used in this work can not predict this behaviour due to the inherit assumptions made throughout.

A specularity coefficient value of 0.1 was tested but yielded unphysical results. [14, 227] also found that a low specularity coefficient was representative of high velocity, dilute fluid-particle flow. The unphysical results were due to the lowering of the slip velocity near the wall. The mean velocity profiles for the fluid and particle-phase tend to converge as the no slip condition ($\phi_{spec} = 1$) is approached. At the relatively high speed velocities used in this study this resulted in a gross overestimation of the particle fluctuation energy. An explanation for this behavior is as follows, the high specularity coefficient at the wall promotes "sticking" of the particles. As these particles are stuck at the wall and then released they begin to produce mean shear in the particle-phase momentum equation. This shearing which is imposed by the boundary condition results in an overestimation of turbulence production resulting in excessively large values of the particle-phase fluctuation energy.

5.4.5 RA-TFM limitations

As shown in §2.2.1 the hydrodynamic model (volume fraction. particle velocity and granular temperature) is derived from the mesoscale model i.e the Boltzmann equation, using a Chapman-Enskog expansion. It is owing to this mathematical linearisation that the hydrodynamical model is not valid for large values of Knudsen number (Kn $>$ 1). The hydrodynamical model, as hinted at, is therefore most accurate for small values of Knudsen number (Kn $\ll$ 1), a feature of collisionally dominated flows (see Appendix C for Kn).

The flow regime used in this study is characterized as moderately dilute where collisions are expected. For the smallest mass loading (case 3), the Knudsen number was found to be (Kn $< 10^{-4}$) across the pipe, whilst for higher mass loadings the Knudsen number was much lower. As this constraint is one across the whole domain this can not always be fulfilled. When considering a fluidised bed for example, the upper region of the chamber will not fulfill this criteria as no collisions are present as there are no particles. For this study the recirculating region posed a problem as only a small number of particles were present in the region. This meant that in this region the Knudsen number would fluctuate, due to the vortex shedding, and temporarily be $\mathcal{O}(1)$, compromising the validity of the solution. Although as has been noted by others [152, 213] the hydrodynamic equations work well beyond their range of validity. Violating the small Knudsen assumption is often unavoidable throughout the whole domain. For a more flexible approach, kinetic-based equations can be formulated in their high order moments and solved for using an appropriate numerical technique (see [24, 104, 122, 137]).

5.5 Closure

The current chapter has investigated turbulent attenuation of fluid-particle flow in a vertically orientated backward-facing step using a Reynolds-Averaged Two-Fluid model. The model results were compared against benchmark experimental data

of Fessler and Eaton [65, 66] and also against the model of Peirano and Leckner [141]. The RA-TFM was validated against the experimental data as well as showing marked improvements over the MPM model. The inclusion of the correlated k_p and uncorrelated Θ particle motion was crucial in accurately predicting the behaviour of the turbulent shear layer. This was further highlighted when compared to the turbulent particle kinetic energy predictions from the modified Peirano model. The form of the velocity coupling terms proved crucial in a correct prediction of the particle-phase mean, turbulence quantities and turbulence attenuation. Lastly, changes in the specularity coefficient ($\phi_{spec} < 0.01$) had very little effect on the particle fluctuation energy prediction.

6 Near-wall modelling in Eulerian-Eulerian simulations

6.1 Overview

The near-wall region in turbulent Eulerian-Eulerian (E-E) simulations has hitherto received little to no attention. A standard approach to modelling this region is through the employment of single-phase wall-functions in the fluid-phase although it is uncertain whether such an approach is capable of capturing turbulent fluid-particle behaviour. In order to both investigate and alleviate E-E models reliance on single-phase wall-functions we propose an E-E elliptic relaxation model (presented in Chapter 2 - §2.5) to account for the near-wall non-homogeneity which arises in wall-bounded flows. The proposed model is derived within an E-E framework and enables the full resolution of the boundary layer and arbitrary wall sensitivity. The model is then compared against the conventional $k_f - \varepsilon_f$ turbulence model with standard single-phase wall-functions. The elliptic relaxation model is implemented within the open-source CFD toolbox OpenFOAM, applied to a vertical downward-facing channel and validated against the benchmark experimental data of Kulick et al. [106]. Model results show marked improvements over the conventional tur-

bulence model across mean flow and turbulence statistics predictions. The use of conventional single-phase wall functions were shown to negatively impede on the prediction of the velocity covariance coupling term and as a result the particle fluctuation energy. Moreover, this also lead to an underestimation of the near-wall volume fraction accumulation.

The main contributions of the chapter are as follows:

- The elliptic relaxation model for the fluid-phase derived in Chapter 2 - §2.5 is implemented in OpenFOAM and compared against the benchmark experimental data of Kulick et al. [106];
- Predictions for the elliptic relaxation model and the $k_f - \varepsilon_f$ model are compared and contrasted to highlight the effect of the particles within the boundary layer;
- The new modelling has been validated against benchmark experimental data with differing mass loading and Stokes number as well as being corroborated with Euler-Lagrange results;
- The elliptic relaxation model has shown a high level of validation, in line with those from Euler-Lagrange, offering a viable way of achieving accurate results at a lower computational cost;
- The elliptic relaxation model proposed in this chapter enables the prediction of the correct near-wall behaviour of the mean and turbulence statistics - paving the way for more advanced modelling of the complex boundary layer fluid-particle behaviour;
- The use of single-phase wall functions in E-E simulations can result in an under-prediction of the velocity covariance coupling term which impedes on the particle fluctuation energy prediction. This is expected to be exacerbated with increasing mass loading;
- The elliptic relaxation model enabled the migration of particles towards the near-wall region, a result that was not replicated using the conventional tur-

bulence model;

- The approach presented herein offers a novel way of accounting for the near-wall region in E-E simulations.

6.2 Introduction

Many researchers have investigated turbulent wall-bounded fluid-particle flow through experimentation [32, 66, 77, 106, 109, 192]. Owing to their turbulent nature such flows exhibit complex physical behaviour giving rise to turbulence modulation which can be caused by: particle-particle, fluid-particle and/or particle-wall interactions. Thus, research has been ongoing to understand and model these phenomena; most of which are common in engineering processes, e.g. pneumatic conveyance and coal particle combustion. The aforementioned experimental studies provide invaluable physical insights and validation data for the development of predictive models. One notable study is that of Kulick et al. [106] which has received considerable attention from researchers developing, predominantly Euler-Lagrange (E-L), models [105, 113, 161, 180, 203, 207, 217]. This study is particularly attractive as there are several particle classes giving rise to various particle-fluid and particle-wall interactions which contribute to turbulence modulation.

Having identified the aspects of physical behaviour which are significant in these flows, researchers can investigate them separately in a reductionist approach. We now highlight some studies that contribute to the understanding of particle behaviour within the case of Kulick et al. [106]; starting with the so-called feedback-force of the particle phase on the fluid turbulence in the flow. Vreman [203] recently examined the effect of the mean feedback-force and how it is exacerbated by wall roughness. An increase in wall roughness enhances turbulence attenuation i.e. a reduction in fluid-phase velocity fluctuations. This explains the over prediction of the mean particle velocities seen in previous studies Kubik and Kleiser [105], Wang and Squires [207], Yamamoto et al. [217] as smooth walls were simulated.

Another phenomenon that has been investigated is turbophoresis, which refers to the tendency of particles in the flow to migrate towards regions of lower turbulence. The turbophoresis force is responsible for particles drifting from regions of high turbulence intensity to low turbulence intensity [120, 149], which often results in particles accumulating in the near-wall region characterised by low-speed streaks [140, 146]. This accumulation in the near-wall region is referred to as deposition and has been researched numerically by [112, 120, 126, 132]. One of the first models for particle deposition by Young and Leeming [220] showed that the turbophoretic velocity depends on the gradient of wall-normal fluctuating velocities and provided one of the first physical basis for explaining the turbophoresis force. Strömgren et al. [180] investigated the effect of the turbophoresis force within an Eulerian-Eulerian (E-E) framework and found that even for small volume fractions, $\alpha_p = 2\text{x}10^{-4}$, two-way coupling effects are non-negligible and the near-wall region may require special attention. This is due to the accumulation of particles in the near-wall region i.e viscous sub layer, leading to higher volume fractions in which two-way coupling effects become more relevant [76].

In turbulent single-phase simulations the near-wall region is typically modelled. Wall functions are applied to turbulence quantities, ε_f & ν_{ft} with a zero gradient condition given to k_f. The near-wall region is then modelled to avoid the computational overhead of resolving the flow. Such wall functions are based on the so-called law-of-the-wall, which is that the dimensionless velocity, u^+ varies through some function expressed generically as, $u^+ = f_{log}(\text{y}^+)$. The function f_{log} is logarithmic representing the outer log-law region of the turbulent boundary layer. This corresponds to the constant-stress layer in which the turbulent shear stress is proportional to the friction velocity [168]. In turbulent quantity terms this means that the production and dissipation of turbulent kinetic energy are equal.

The law-of-the-wall is assumed to be universal and is found through dimensional reasoning, this then leads to a description of the near-wall region through dimensionless variables i.e. velocity and wall-normal coordinates. The dimensionless wall-normal coordinate is defined as $\text{y}^+ = \text{y}u_\tau/\nu_f$ and the log-law is applicable

in the range of $30 < y^+ < 300$, this then gives a universal relation that can be applied to turbulent wall-bounded flows. This criterion places a requirement on the first computational cell i.e. the distance of the cell centre must be further than $y^+ > 30$. As can already be deduced, the calculation of y^+ depends on the friction velocity, which is not known *a priori*. Hence, this quantity is estimated prior to calculation using standard skin friction relations and informs mesh generation. This approach then sacrifices near-wall resolution for a computationally cheaper simulation. An important assumption about the nature of the law-of-the-wall has been made throughout i.e. its universal nature. This is in fact not true as it has been shown experimentally that the boundary layer is affected by adverse pressure gradients and geometric changes [78].

The viability of single-phase wall functions applied to multiphase simulations has attracted some interest from researchers. A theoretical study by Rizk and Elghobashi [158] showed that increasing volume fraction can adversely effect the mean profile prediction. It was found that with increasing particle volume fraction the log layer broke down resulting in an overestimation. Interestingly, a similar relationship between an increasing mass loading and a reduction in the mean log-layer momentum was recently found experimentally by Saber et al. [166]. Benyahia et al. [14] included the effect of the particle phase directly into the wall function. An additional term that contains the drag and velocity fluctuation covariance is introduced in the log-law relation. This formulation allows the presence of the particles to influence the velocity profile, although when extended to more complex geometries the short-comings of single-phase wall functions remain.

Attempts to circumvent the reliance on single-phase wall functions have been made by several authors [16, 49, 158, 226] in which a low-Re number turbulence model is used. This allows the transport equations to be integrated up to the wall. This approach has proven fruitful for numerous authors as without the use of wall functions, the presence of the particles within the boundary layer can exert their influence [158, 226]. The low-Re turbulence model uses a damping function and a near wall correction of Kolmogorov scaling [139]. The damping of the viscosity can

be somewhat arbitrary and validated on relatively simple flow leading to a range of different models [41, 107, 159, 172] with an extensive summary found in Patel et al. [139]. The damping functions used in [139] are often non-linear and can lead to numerical stiffness further complicating their application.

Durbin [56], Durbin and Reif [58] propose another way of accounting for wall-induced non-homogeneity. The quantity $\overline{v_f^2}$, which represents the turbulence-stress normal to streamlines, is introduced. This quantity is derived from the exact Reynolds-stress transport equation and contains a source term that accounts for the redistribution of turbulence kinetic energy. This inclusion explicitly accounts for the wall-induced non-homogeneity and enables the wall-normal component to be dampened. The energy redistribution is governed by an *elliptic relaxation* equation f, that is free of geometric dependence or arbitrary fitting. The $\overline{v_f^2} - f$ elliptic relaxation model has been validated across various challenging single-phase flows [12, 50, 114, 130, 182] highlighting the benefit of such a modelling technique.

There are two closely linked issues with the current E-E modelling approaches: the modelling of the near-wall region, through single-phase wall functions, and the subsequent consequences of such an approach i.e. the prediction of turbulence modulation and turbophoresis. In this work we seek to investigate this by carrying out a side-by-side comparison of a conventional E-E simulation method with a newly-derived elliptic relaxation model in which the near-wall region has been resolved. The main aim then is to reveal the consequences of modelling the near-wall region whilst proposing new modelling to circumvent these consequences.

In this chapter the elliptic relaxation model, presented in Chapter 2 - §2.5, is applied to the vertical downward facing channel of Kulick et al. [106]. The elliptic relaxation model alleviates the use of wall functions and/or the use of ad-hoc damping functions as well as being geometry independent. To ascertain the consequences of a conventional E-E simulation, the RA-TFM with the solution of the $k_f - \varepsilon_f$ model, is compared and contrasted against the newly proposed elliptic relaxation model, $\overline{v_f^2} - f$.

6.3 Geometry and case setup

Table 6.1: Table of simulated cases.

Case	Material	d_p [μm]	ρ_p [kg m^{-3}]	Mass loading, ϕ	St
1	glass	50	2500	2%	0.57
2	copper	70	8800	10%	3

The cases used throughout are based on two experiments from Kulick et al. [106] which include separately both glass and copper particles, the details of which can be found in Table 6.1. For both cases the the channel half-width is H = 0.02 m with a corresponding length of 5.2 m and a wall friction velocity u_τ = 0.49 m s^{-1}. The viscosity of gas is ν_f = 15.11 x 10^{-5} m^2 s^{-1} with a density of ρ_f = 1.2kg m^{-3}. At the inlet the velocity of both the fluid- and particle-phase are set at 9.4 m s^{-1}. A Neumann boundary condition is used for f together with Dirichlet boundary conditions for all turbulent statistics. At the outlet a Dirichlet boundary condition for pressure is set whilst a Neumann boundary condition is prescribed for all remaining variables.

At the wall, the wall boundary conditions for the elliptic relaxation model presented in §2.5 are employed. For the particle-phase Neumann boundary conditions are applied to all variables. For the $k_f-\varepsilon_f$ model, standard wall functions are employed. Both k_p and ε_p are initialised as 1/3rd of their fluid counterpart with Θ = 1.0 x 10^{-10}m^2 s^{-2}. The flow is orientated vertically with a uniform body force of gravity acting in the direction of the flow (g = 9.8 m s^{-2}), this configuration resulted in a centerline velocity of U_{cl} = 10.5 m s^{-1}. The mass loading is defined as $\phi = \frac{\alpha_p \rho_p}{\alpha_f \rho_f}$, and assuming uniform velocity at the inlet.

Table 6.3 shows the complete phase-energy system used in the elliptic relaxation model. The main momentum equations of the RA-TFM presented in Chapter 2 are used throughout where the buoyancy induced terms have been neglected due

to the high density ratio. Lastly, the model constants can be found in Appendix C - §C.3 & §C.4.

Owing to the different modelling approaches used throughout two different meshes are employed and are detailed in Table 6.2. Mesh 1 is associated with the $\overline{v_f^2} - f$ model and is resolved to $y^+ < 1$ ensuring that the resolution of the boundary layer is captured. Mesh 2 is associated with the $k_f - \varepsilon_f$ model and is resolved up to $y^+ > 30$ ensuring that the wall functions can be applied across the correct section of the boundary layer (i.e. log-layer). The final column refers to the computational time spent for a typical run consisting of 30 seconds of real flow time. For ease of reference the $\overline{v_f^2} - f$ formulation will hereafter be referred to as V2F and the $k_f - \varepsilon_f$ formulation as KE.

Table 6.2: Properties of each mesh, f_x, f_y refer to mesh stretching with Mesh 1 [$f_x = 1.1, f_y = 1.1$] and Mesh 2 [$f_x = 1.2, f_y = 1.2$].

Mesh	$\Delta x_{min}, \Delta x_{max}$[m]	$\Delta y_{min}, \Delta y_{max}$[m]	Mesh size	Comp time
1	1.2×10^{-3}, 0.02	1.2×10^{-5}, 1.2×10^{-3}	202,761	32 hrs
2	7×10^{-4}, 9×10^{-4}	7×10^{-4}, 9×10^{-4}	66,481	4 hrs

Table 6.3: Phase energy equations.

Phase energy equations for the fluid-phase:

$$\frac{\partial(\alpha_f\rho_f k_f)}{\partial t}+\nabla\cdot(\alpha_f\rho_f k_f\mathbf{u}_f)=\nabla\cdot\left[\left(\mu_f+\frac{\mu_{ft}}{\sigma_{fk}}\right)\nabla k_f\right]+\alpha_f\rho_f\Pi_f-\alpha_f\rho_f\varepsilon_f \\ +2\beta(k_{fp}-k_f) \tag{6.1}$$

$$\frac{\partial(\alpha_f\rho_f\varepsilon_f)}{\partial t}+\nabla\cdot(\alpha_f\rho_f\varepsilon_f\mathbf{u}_f)=\nabla\cdot\left[\left(\mu_f+\frac{\mu_{ft}}{\sigma_{f\epsilon}}\right)\nabla\varepsilon_f\right]+\frac{\varepsilon_f}{k_f}\left[\frac{C_{\varepsilon1}\alpha_f\rho_f\Pi_f-C_{\varepsilon2}\alpha_f\rho_f\varepsilon_f}{T}\right] \\ +2C_3\beta(\varepsilon_{fp}-\varepsilon_f) \tag{6.2}$$

$$\frac{\partial(\alpha_f\rho_f\overline{v_f^2})}{\partial t}+\nabla(\cdot\alpha_f\rho_f\overline{v_f^2})\mathbf{u}_f=\nabla\cdot\left[\left(\mu_f+\frac{\mu_{ft}}{\sigma_{fk}}\right)\nabla\overline{v_f^2}\right]+\alpha_f\rho_f\overline{v_f^2}_{source}-\alpha_f\rho_f 6\frac{\overline{v_f^2}}{k_f}\varepsilon_f \\ +2\beta(\overline{v_{fp}^2}-\overline{v_f^2}) \tag{6.3}$$

$$L^2\frac{\partial^2 f}{\partial x^2}-f=\frac{C_1}{T}\left(\frac{\overline{v_f^2}}{k_f}-\frac{2}{3}\right)-C_2\frac{\Pi_f}{k_f}-\frac{1}{T}\left(6\frac{\overline{v_f^2}}{k_f}-\frac{2}{3}\right) \tag{6.4}$$

Phase energy equations for the particle-phase:

$$\frac{\partial(\alpha_p\rho_p k_p)}{\partial t}+\nabla\cdot(\alpha_p\rho_p k_p\mathbf{u}_p)=\nabla\cdot\left[\left(\mu_p+\frac{\mu_{pt}}{\sigma_{pk}}\right)\nabla k_p\right]+\alpha_p\rho_p\Pi_p-\alpha_p\rho_p\varepsilon_p \\ +2\beta(k_{fp}-k_p) \tag{6.5}$$

$$\frac{\partial(\alpha_p\rho_p\varepsilon_p)}{\partial t}+\nabla\cdot(\alpha_p\rho_p\varepsilon_p\mathbf{u}_p)=\nabla\cdot\left[\left(\mu_p+\frac{\mu_{pt}}{\sigma_{pk}}\right)\nabla\varepsilon_p\right]+\frac{\varepsilon_p}{k_p}\left[C_1\alpha_p\rho_p\Pi_p-C_2\alpha_p\rho_p\varepsilon_p\right] \\ +2C_3\beta(\varepsilon_{fp}-\varepsilon_p) \tag{6.6}$$

$$\frac{3}{2}\left[\frac{\partial(\alpha_p\rho_p\Theta)}{\partial t}+\nabla\cdot(\alpha_p\rho_p\Theta\mathbf{u}_p)\right]=\nabla\cdot\left[\left(\kappa_\Theta+\frac{3\mu_{pt}}{2Pr_{pt}}\right)\nabla\Theta\right]+2\mu_p\overline{\mathbf{S}}_\mathbf{p}:\overline{\mathbf{S}}_\mathbf{p} \\ -p_p\nabla\cdot\mathbf{u}_p+\alpha_p\rho_p\varepsilon_p-3\beta\Theta-\gamma \tag{6.7}$$

6.4 Results and discussion

6.4.1 Mean fluid stream-wise velocity profiles

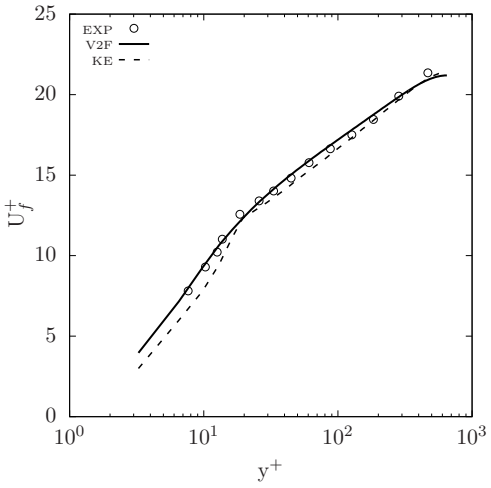

Figure 6.1: C1 - Mean fluid velocity profile.

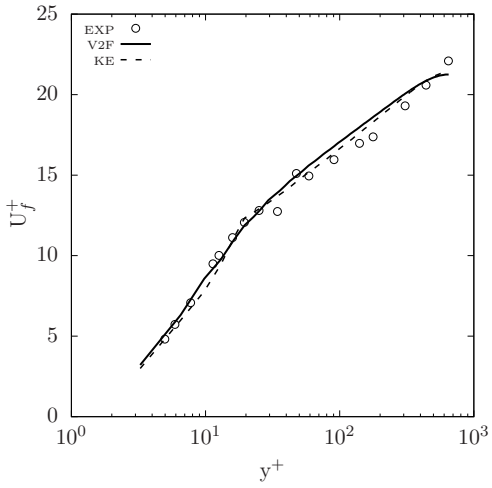

Figure 6.2: C2 - Mean fluid velocity profile.

Figures 6.1 & 6.2 show the mean fluid velocity profiles for each case. It is evident from both plots that the prediction of both V2F & KE models are in good agreement with the experimental data of Kulick et al. [106]. For both C1 & C2 the mean fluid velocity profile remains unchanged, behaviour that is consistent with the experimental observations. Moreover, the experimental uncertainty was reported by the authors to be $\approx 2\%$ and it can be seen that across both profiles the numerical prediction lies well within this range.

When comparing both the V2F & KE model predictions there is only a small discrepancy between each result. This disparity is at its most obvious at $y^+ < 30$ in Fig. 6.1. Owing to the wall function the turbulence statistics are integrated to the wall from the first computational cell at $y^+ \approx 30$ which results in an over-prediction of turbulence viscosity. This over-prediction is felt in the mean velocity profile as an under-prediction. This trend is seen across the profile for both plots as the KE consistently under-predicts the mean velocity profile in comparison with

V2F although this difference is small.

6.4.2 Mean particle stream-wise velocity profiles

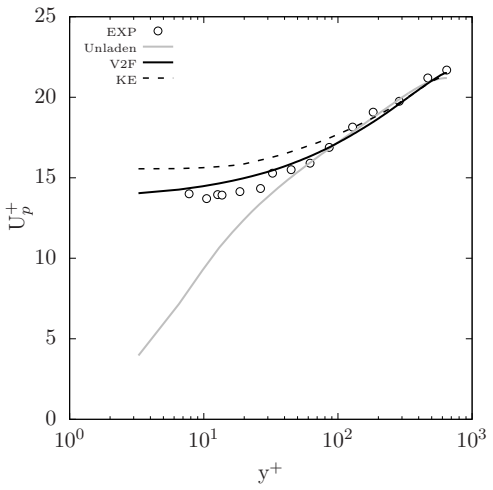

Figure 6.3: C1 - Mean particle velocity profile.

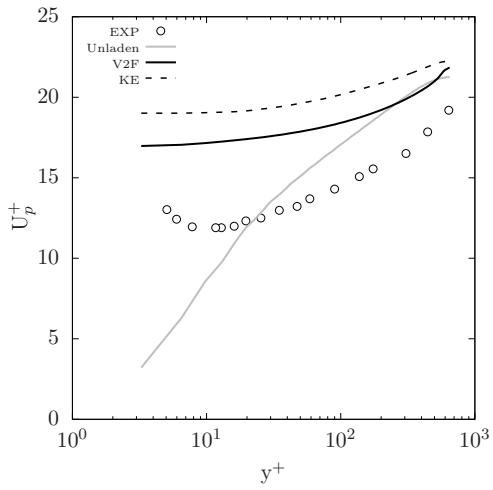

Figure 6.4: C2 - Mean particle velocity profile.

The mean particle velocity profiles are shown in Figs. 6.3 & 6.4. Focusing on the former it can be seen that both V2F & KE models accurately predict the experimental behavior which is characterised by a flatter profile as it approaches the wall. As the particle velocities need not be zero at the wall unlike the fluid-phase, a large slip value exists. The particles deviate from the fluid-phase velocities at around $y^+ < 100$ and maintain their momentum, leading to a flattening of the profile as the wall is approached.

In Fig. 6.3 the profile predicted by the V2F model is in good agreement with the experimental data. This is also true for the KE model up until the near-wall region is approached. Over the range $y^+ < 100$ the KE prediction deviates from both the experimental and V2F results as the momentum is over-predicted. The cause of this overestimation is attributed to the lack of particle fluctuation energy production resulting in a lack of momentum loss. This finding will be discussed at length in §6.4.5 where the particle-phase fluctuation energy results are presented.

Looking at Fig. 6.4 it can be seen that there is an over-estimation in the mean particle velocities across both models. This discrepancy was also predicted in the E-L results of Yamamoto et al. [217] and Wang and Squires [207]. A recent study by Vreman [203] suggests that this global reduction in the particle velocities is due to the so-called 'non-uniform feedback force' which is exacerbated by wall roughness. This results in an additional drag force exerted on the particles leading to increased turbulence attenuation.

This additional force would result in a much flatter profile as shown in Vreman [203] and lead to results that closely align with the experimental data in Fig. 6.4. As wall roughness has not been modelled in this study, and similar results have been reported by other researchers using higher resolution methods i.e. E-L [207, 217], it is plausible to conclude that this is the source of the overestimation. It is instructive to note that despite this, the qualitative behaviour of the profile is captured by both numerical models resulting in a comparable trend across the profile.

6.4.3 Fluid stream-wise turbulence intensity

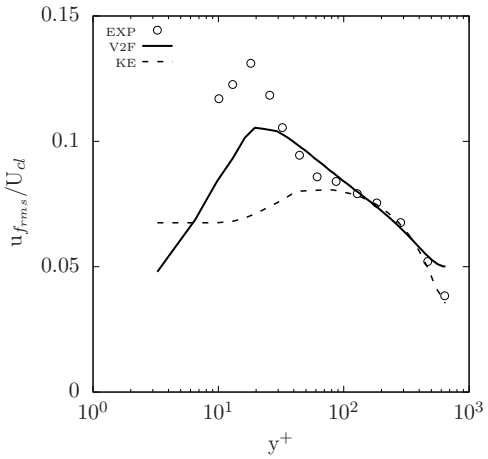

Figure 6.5: C1 - Fluid stream-wise turbulence intensity profile.

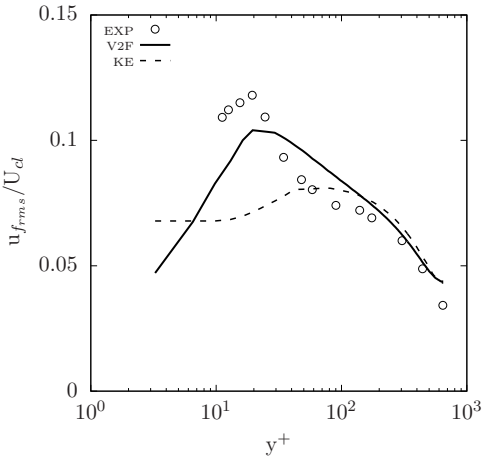

Figure 6.6: C2 - Fluid stream-wise turbulence intensity profile.

Figures 6.5 & 6.6 show the fluid-phase turbulence intensity for each case. When comparing the V2F & KE model across both cases it is apparent that there is a clear difference between the two. The V2F model is capable of predicting a strong peak at $y^+ \approx 20$ and then dissipating off into the core of the channel. This is not seen by the KE model as the first computational cell is placed at $y^+ > 30$ with the turbulence statistics being integrated up to the wall assuming a log-law variation. This then omits the presence of the peak and results in a near constant value of $u_{f_{rms}}$ as the wall is approached. In the core of the flow, over the region ($y^+ > 70$), there is better agreement with the experimental data as the dominant transport terms are correctly modelled.

The KE models dependency on the wall function results in a deterioration of the turbulence intensity prediction. This will be shown to have important consequences when predicting the particle fluctuation energy behaviour. The V2F model then shows excellent agreement across both plots with the under prediction being confined to the turbulence peak and dissipation towards the wall. It has been suggested [56, 58] that the $\overline{v_f^2} - f$ model performs best at high Re number. In this work a relatively small Re number of 14,000 is simulated which could be the cause of the under-prediction. This could be improved with a manipulation of the turbulence constant i.e. C_2 although this remains out of the scope of this study.

Kulick et al. [106] reports turbulence attenuation in C2. As discussed in §6.4.2 this is due to the lack of wall roughness modelled in this work. Across both Figs. the behaviour is similar with the velocity covariance terms contributing little to the prediction. This finding is also consistent with those of Wang and Squires [207], Yamamoto et al. [217] in which negligible attenuation was reported.

6.4.4 Fluid wall-normal turbulence intensity

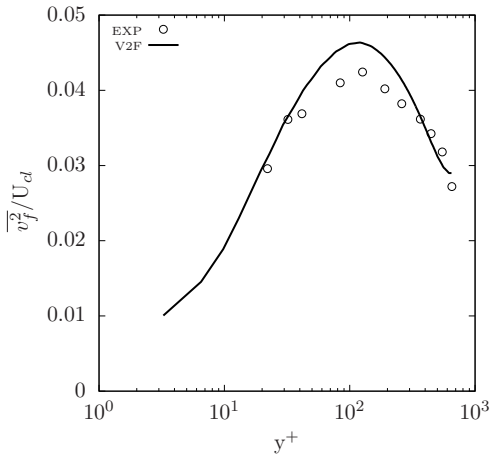

Figure 6.7: C1 - Fluid wall-normal turbulence intensity profile.

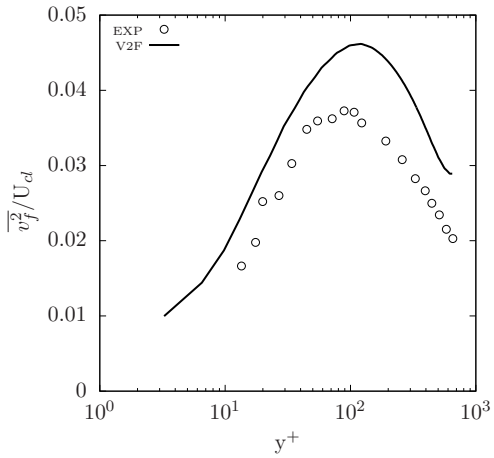

Figure 6.8: C2 - Fluid wall-normal turbulence intensity profile.

Figures 6.7 & 6.8 show the fluctuating wall-normal component. This component is explicitly modelled in the V2F model as $\overline{v_f^2}$ and is crucial in enabling the resolution of the boundary layer. As it can be seen from Fig. 6.7 the distribution is in good agreement with the experimental predictions. The V2F model shows the correct dampening of the wall-normal component through the elliptic relaxation equation and enables a strong turbulence production peak as seen in §6.4.3. For C2 the wall-normal intensity was also attenuated in the same way the stream-wise intensity was. As previously discussed it is clear why no attenuation was reported in these results.

6.4.5 Particle fluctuation energy

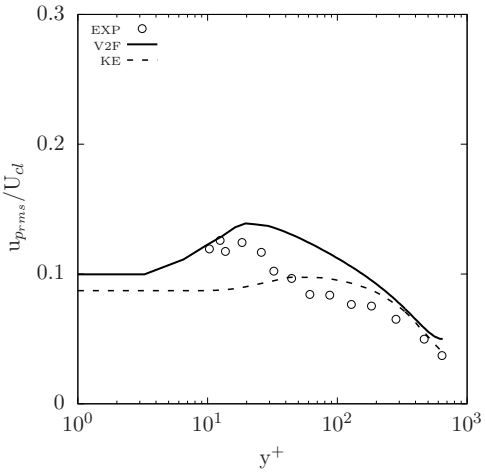

Figure 6.9: C1 - Particle fluctuation energy profile.

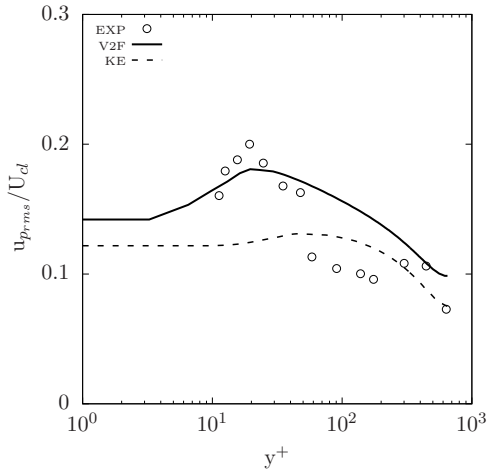

Figure 6.10: C2 - Particle fluctuation energy profile.

In the RA-TFM we explicitly account for two contributions to the particle fluctuation energy [67], $\kappa_p = k_p + 1.5\Theta$ where Θ represents the small-scale kinetic collisional energy i.e. uncorrelated energy and k_p represents the large-scale turbulent kinetic energy i.e. correlated energy. Broadly speaking Θ is relevant at high St number and high mass loading, and k_p is relevant at low St number and low mass loading. This distinction has already proven crucial in the literature [67, 100, 156, 157, 199].

Figures 6.9 & 6.10 show the particle fluctuation energy for each case. As is evident from both plots the V2F model outperforms the KE model. This is a direct consequence of the poor prediction in the fluid turbulence intensity. Owing to the relatively low St number in the core of the flow the particles are tightly correlated therefore they are governed by the velocity covariance term which arises due to drag. The fluctuation energy distribution is dominated by k_p up until the near-wall region is approached - this is confirmed by comparing the distribution with that of Fig. 6.5. For C2 this is not strictly true as the St number is larger in the core of the flow resulting in a contribution acting across the half-width of the channel, this can be seen by comparing the two figures.

In the near-wall region the St number increases dramatically. This ensures that the particles become uncorrelated with the main carrier flow and Θ is produced in the region $y^+ < 10$. Additionally, an energy cascade exists in which the large-scale $k_p - \varepsilon_p$ equations dissipated energy into the Θ transport equation through a source term. The particle turbulence kinetic dissipation energy is then highest in the near-wall region thus contributing to the loss of correlation with the carrier flow.

6.4.6 Volume fraction distribution

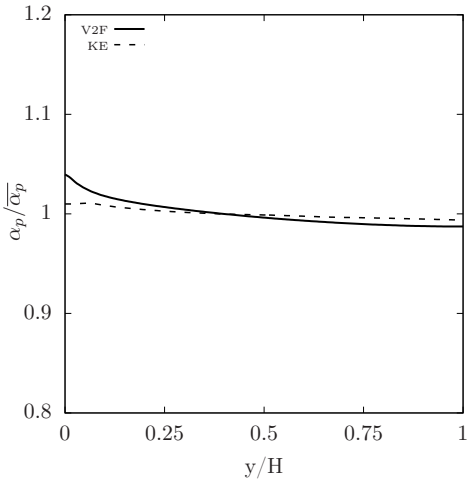

Figure 6.11: C1 - Volume fraction distribution normalised by mean values.

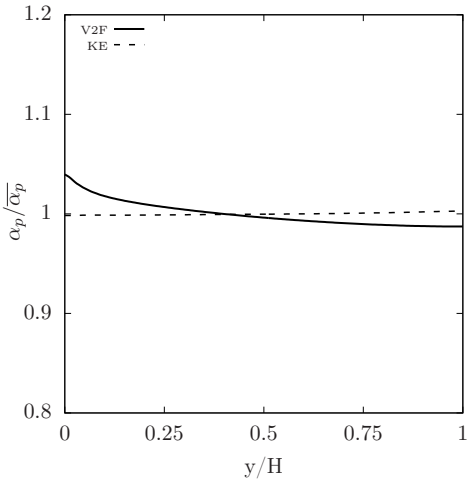

Figure 6.12: C2 - Volume fraction distribution normalised by mean values.

Figures 6.11 & 6.12 show the volume fraction distribution for both cases. It is clear from both plots that the V2F model predicts an accumulation of particles in the near-wall. The particles tend to drift across the channel width and reside in the near-wall region - characteristic behaviour of turbophoresis. As the force is determined by the fluctuating wall normal component, of which is explicitly modelled in the V2F model and coupled to the particle-phase correlated energy, the particles are able to drift down the gradients of turbulent kinetic energy.

The KE model predictions reveal a slightly different picture. In C1 an accumulation

of particles in the near-wall region is seen but the sharp peak is not replicated, instead these particles are found in the main core of the flow. The prediction for C2 reveals a breakdown in the volume fraction distribution in comparison to the V2F model. The particles are nearly uniformly distributed with a higher concentration in the main core of the flow. Due to the higher St number in C2 the particles are less correlated with the carrier flow, therefore in order to migrate towards the wall a larger dispersion is required. As the wall-normal component has not been explicitly modelled the particles can not overcome the turbulent kinetic energy gradient and remain in the main core of flow. Moreover, this can be a symptom of the mesh resolution as the wall function constraint ensures the near-wall region can not be resolved.

6.5 Closure

This current chapter has proposed a generic approach for accounting for near-wall induced non-homogeneity in Eulerian-Eulerian simulations. An E-E elliptic relaxation model, namely the $\overline{v_f^2} - f$ model, has been derived with in a Reynolds-Averaged Two-Fluid model framework and applied to a downward-facing vertical channel. Predictions are validated against the benchmark experimental data of Kulick et al. [106] and compared against the conventional $k_f - \varepsilon_f$ turbulence model. It has been shown that the E-E elliptic relaxation model shows improved prediction of fluid- and particle-phase turbulence statistics when compared with the conventional $k_f - \varepsilon_f$ formulation. The new modelling has been validated against benchmark experimental data with differing mass loading and Stokes number as well as being corroborated with Euler-Lagrange results.The elliptic relaxation model has shown a high level of validation, in line with those from Euler-Lagrange, offering a viable way of achieving accurate results at a lower computational cost. One of the most significant findings was that the use of single-phase wall functions in E-E simulations can result in an under-prediction of the velocity covariance coupling term which impedes on the particle fluctuation energy prediction. This is expected

to be exacerbated with increasing mass loading. Moreover, the elliptic relaxation model enabled the migration of particles towards the near-wall region, a result that was not replicated using the conventional turbulence model. Finally, the approach presented herein offers a novel way of accounting for the near-wall region in E-E simulations.

7 Inhomogeneity and anisotropy in Eulerian-Eulerian modelling

7.1 Overview

This chapter tackles the issue of image vorticity in turbulent Eulerian-Eulerian simulations. In Chapter 2 - §2.6 a pressure-velocity model to account for the no permeability constraint on the particle-phase wall normal stress components was proposed. Throughout this chapter we demonstrate that this approach is capable of accounting for the strong near-wall inhomogeneity, a flow feature that hitherto has been neglected in Eulerian-Eulerian modelling. Simulation predictions are validated against benchmark Direct Numerical Simulation (DNS) data of Marchioli et al. [121] in which turbulent channel flow at $Re_\tau = 150$ with one-way coupling is presented. Mean and turbulent statistics for the stream-wise and wall-normal components are also shown. The results in this chapter show a promising step forward in near-wall modelling in Eulerian-Eulerian simulations. The predictions reveal that the approach proposed herein can lead to a satisfactory agreement across all turbulence statistics, stream-wise and wall normal, paving the way for the correct prediction of more complex mechanisms. Additionally, the St dependant

behaviour was predicted by the model, adding to the validity of the approach.

The main contributions of this chapter are:

- The elliptic relaxation model for the particle-phase derived in Chapter 2 - §2.6 is implemented in OpenFOAM and compared with the benchmark DNS data of Marchioli et al. [121];
- The combined solution of the elliptic relaxation models $\overline{v_p^2} - f$ & $\overline{v_f^2} - f$ resulted in excellent agreement with the DNS data, showing agreement across turbulence statistics that have hitherto eluded E-E frameworks;
- The co-variance coupling form showed the correct behaviour across the width of the channel incorporating the Stokes dependant behaviour;
- Taking advantage of the shared pressure field and the correlated phase-energy in turbulent E-E simulations can lead to advantageous modelling approaches;
- A mesh sensitive study was conducted to ascertain the influence of grid resolution, a restraint was placed on the refinement in the near-wall region due to the aspect ratio of the mesh;
- The methodology presented herein has highlighted the potential for boundary-layer resolved simulations within E-E frameworks leading to satisfactory results.

7.2 Introduction

The near-wall behaviour of particle-laden fluid behaviour has been a challenging topic for researchers over the preceding decades. Modelling the highly inhomogeneous near-wall region in a turbulent shear flow has proved difficult even in single phase flows [142]. One phenomenon in particular that has proven challenging is the so-called image vorticity [86, 190] that is caused by the kinematic blocking by the wall. This non-local effect on the Reynolds stress arises due to the physical inviscid boundary condition i.e. the no-flux condition on the normal component of velocity $\mathbf{u} \cdot \mathbf{n} = 0$. This effect results in a highly anisotropic distribution amongst the Reynolds stress components in the vicinity of a wall, mainly it is felt as a suppression of energy transfer into the wall-normal component.

To circumvent these issues Durbin [56] proposed a pressure-velocity model based on the Reynolds-Stress wall-normal component and an elliptical relaxation function to account for the kinematic blocking effect. In single-phase simulations this approach has proven fruitful [12, 50, 56, 58, 114, 182], with results showing distinct improvements over simulations with damping-functions and in particular wall-functions, as neither can account for the so-called stagnation-point anomaly or imposed pressure gradients.

Owing largely to its maturity and complexity, research in turbulent near-wall fluid-particle modelling in an E-E framework has been sparse. One notably study is that of Rizk and Elghobashi [158] in which a theoretical study was carried out to ascertain the effects of increasing volume fraction on the mean velocity profile. They found that the log-layer broke down in their model speculating that a standard wall-function may not be representative of particle-laden flow. This postulation was somewhat corroborated by Vreman et al. [204] who showed that the log-layer was retained but resulted in an adjustment of the von Karman 'constant'. In addition to this, Benyahia et al. [14] showed that the effect of the particle-phase could be included in the wall-function in an ad-hoc manner which allows the particle-phase

to influence the fluid-phase velocity when the particle-fluid co-variance remained correlated. In Chapter 6 the consequences of employing single-phase wall functions in wall-bounded high Re number E-E simulations were revealed. It was found that its arbitrary employment can result in a breakdown of the phase-energy exchange mechanisms which impede on the particles fluctuation energy, co-variance and volume fraction distribution.

The use of single-phase wall functions in E-E simulations are abundant in literature [13, 48, 151, 171, 180]. The wall functions are applied to the fluid-phase regardless of the volume fraction in which complicated one- or two-way coupling effects can play a role. Moreover, the universal form of the log-layer neglects pressure gradients, with the addition of particles an induced hydro-static pressure gradient can commonly be found in the boundary layer. Attempts to circumvent this issue through damping functions have been used [16, 49, 158, 226]. This introduces further complications with arbitrarily matching experimental/Direct Numerical Simulation (DNS) in new or more complicated geometries. The drawbacks of damping-functions are well known i.e. their arbitrariness and dampening the incorrect scale [139].

In the literature E-E simulations in the near-wall region rarely predict the correct turbulence statistics in the particle-phase. Moreover, the particle-phase wall normal component can not be correctly predicted due to the $k-\varepsilon$ modelling assumptions i.e. the eddy-viscosity approximation for the pressure-velocity redistribution terms. In the particle-phase this is particularly problematic as the wall-normal component is known to govern segregation towards the wall [149, 217] and can inhibit the correct volume fraction distribution.

A more fundamental explanation can be given when considering E-E (Two-Fluid Models) models. In the current E-E the correlated fluctuating component of the particle-phase is equated to the uncorrelated fluctuating energy of the particle-phase. This error was first identified by Février et al. [67] in which the partitioning effect of particle inertia was shown to give rise to two different contributions to the

particle-phase energy, namely correlated and uncorrelated energy. This distinction is crucial in both collisional and non-collisional flow Février et al. [67], Fox [71] and has been shown to predict the correct physics in comparison with the current E-E models in which the distinction is not made as shown in Chapter 5.

In the near-wall region this distinction can prove particularly crucial. As the St number increases as the wall is approached the correlated particle-phase energy k_p is dissipated into uncorrelated particle-phase energy Θ. This Stokes dependent behaviour is vital to predicting the correct distribution of particle-phase energy in the near-wall region. Without accounting for this behaviour, in combination with wall-functions or damping functions it is clear why the near-wall region has proven particularly challenging and has received little attention Peirano and Leckner [141].

Within the context of near-wall modelling the turbulence constants may need to be changed to account for the presence of the particles. Bolio et al. [16] reported no significant changes in C_1, C_2, σ_k and σ_ε. Despite this, Fox [71] has shown that there in fact a small dependence of C_2 on the Stokes number for homogeneous-shear flow. In the near-wall region the picture is complicated further and no experimental or DNS data exists. In this study we do not consider the influence of the turbulent constants but it is recognised here that with increased mass loading and Stokes number the constants may need to be changed. Within the near-wall region this is particularly uncertain and more research needs to be done.

In this chapter the elliptic relaxation model for the particle-phase (proposed in Chapter 2 - §2.6) is solved in tandem with the elliptic relaxation model for the particle phase proposed in Chapter 2 - §2.5. Simulation predictions are validated against benchmark Direct Numerical Simulation (DNS) data of Marchioli et al. [121] in which turbulent channel flow at $Re_\tau = 150$ with one-way coupling is presented. Mean and turbulent statistics for the stream-wise and wall-normal components are also shown. Additionally, the St dependant behaviour is determined via an increase in particle diameter.

7.3 Geometry and case setup

Table 7.1: Table of simulated cases.

Case	d_p [μm]	ρ_p [kg/m^3]	St
1	20.4	1000	1
2	45.6	1000	5

The geometry comprises of two flat parallel walls. The computational domain of size $16\pi h$ x $2h$, with x-, y- axes in the stream-wise and wall-normal directions, respectively. Four mesh resolutions are investigated with $y^+ = 0.5$ kept constant throughout with an inflation ratio of 1.1 in the y direction. The carrier flow has a density of $\rho_f = 1.3\text{kg}\,\text{m}^{-3}$ and kinematic viscosity of $\nu_f = 15.7\text{x}10^{-6}\text{m}^2\,\text{s}^{-1}$. The shear Reynolds number is defined as $Re_\tau = \mathbf{u}_\tau h/\nu_f$ where $\mathbf{u}_\tau$ is the friction velocity and h is the half channel height. The shear velocity, $\mathbf{u}_\tau h/\nu_f = (\overline{\tau}_w/\rho_f)^2$ where $\overline{\tau}_w$ is the mean shear stress at the wall. All variables are reported in their dimensionless form, denoted by the superscript $+^2$ and expressed in wall units - these can be obtained by combining $\mathbf{u}_\tau, \rho_f$ and ν_f.

The wall boundary condition for ε_f can be found in §2.5. For the remaining model variables the following boundary conditions at the wall are prescribed, $\mathbf{u}_f = k_f = \overline{v_f^2} = f = 0$. For the particulate phase a Neumann boundary condition is prescribed for the velocity and turbulence statistics. Both k_p and ε_p are initialised as 1/3rd of their fluid counterpart with $\Theta = 1.0$ x $10^{-10}\text{m}^2\,\text{s}^{-2}$. At the inlet a Dirichlet boundary condition is prescribed for both phase velocities and a Neumann condition for pressure. At the outlet a Dirichlet boundary condition is prescribed for pressure and a Neumann condition for both phase velocities.

Details of the simulated cases can be found in Table 7.1. The full system of phase energies used in this chapter is shown in Table 7.2. The main momentum equations of the RA-TFM presented in Chapter 2 are used throughout, where the buoyancy

induced terms have been neglected due to the high density ratio. Lastly, the model constants can be found in Appendix C - §C.4.

Table 7.2: Phase-energy equations.

$$\frac{\partial(\alpha_f\rho_f k_f)}{\partial t}+\nabla\cdot(\alpha_f\rho_f k_f\mathbf{u}_f)=\nabla\cdot\Big[\Big(\mu_t+\frac{\mu_{ft}}{\sigma_{fk}}\Big)\nabla k_f\Big]+\alpha_f\rho_f\Pi_f-\alpha_f\rho_f\varepsilon_f \\ +2\beta(k_{fp}-k_f) \tag{7.1}$$

$$\frac{\partial(\alpha_f\rho_f\varepsilon_f)}{\partial t}+\nabla\cdot(\alpha_f\rho_f\varepsilon_f\mathbf{u}_f)=\nabla\cdot\Big[\Big(\mu_t+\frac{\mu_{ft}}{\sigma_{fk}}\Big)\nabla\varepsilon_f\Big]+\frac{\varepsilon_f}{k_f}\Big[\frac{C_{\varepsilon1}\alpha_f\rho_f\Pi_f-C_{\varepsilon2}\alpha_f\rho_f\varepsilon_f}{T}\Big] \\ +2C_3\beta(\varepsilon_{fp}-\varepsilon_f) \tag{7.2}$$

$$\frac{\partial(\alpha_f\rho_f\overline{v_f^2})}{\partial t}+\nabla\cdot(\alpha_f\rho_f\overline{v_f^2}\mathbf{u}_f)=\nabla\cdot\Big[\Big(\mu_f+\frac{\mu_{ft}}{\sigma_{fk}}\Big)\nabla\overline{v_f^2}\Big]+\overline{v_f^2}_{source}-\alpha_f\rho_f 6\frac{\overline{v_f^2}}{k_f}\varepsilon_f \\ +2\beta(\overline{v_{fp}^2}-\overline{v_f^2}) \tag{7.3}$$

$$L^2\frac{\partial^2 f}{\partial x^2}-f=\frac{C_1}{T}\left(\frac{\overline{v_f^2}}{k_f}-\frac{2}{3}\right)-C_2\frac{\Pi_f}{k_f}-\frac{1}{T}\left(6\frac{\overline{v_f^2}}{k_f}-\frac{2}{3}\right) \tag{7.4}$$

$$\frac{\partial(\alpha_p\rho_p k_p)}{\partial t}+\nabla\cdot(\alpha_p\rho_p k_p\mathbf{u}_p)=\nabla\cdot\Big[\Big(\mu_p+\frac{\mu_{pt}}{\sigma_{pk}}\Big)\nabla k_p\Big]+\alpha_p\rho_p\Pi_p-\alpha_p\rho_p\varepsilon_p \\ +2\beta(k_{fp}-k_p) \tag{7.5}$$

$$\frac{\partial(\alpha_p\rho_p\varepsilon_p)}{\partial t}+\nabla\cdot(\alpha_p\rho_p\varepsilon_p\mathbf{u}_p)=\nabla\cdot\Big[\Big(\mu_p+\frac{\mu_{pt}}{\sigma_{pk}}\Big)\nabla\varepsilon_p\Big]+\frac{\varepsilon_p}{k_p}\Big[\frac{C_1\alpha_p\rho_p\Pi_p-C_2\alpha_p\rho_p\varepsilon_p}{T_p}\Big] \\ +2C_3\beta(\varepsilon_{fp}-\varepsilon_p) \tag{7.6}$$

$$\frac{\partial(\alpha_p\rho_p\overline{v_p^2})}{\partial t}+\nabla\cdot(\alpha_p\rho_p\overline{v_f^2}\mathbf{u}_p)=\nabla\cdot\Big[\Big(\mu_p+\frac{\mu_{pt}}{\sigma_{pk}}\Big)\nabla\overline{v_p^2}\Big]+\overline{v_p^2}_{source}-\alpha_p\rho_p 6\frac{\overline{v_p^2}}{k_p}\varepsilon_p \\ +2\beta(\overline{v_{fp}^2}-\overline{v_p^2}) \tag{7.7}$$

$$L_p^2\frac{\partial^2 f}{\partial x^2}-f=\frac{C_1}{T_p}\left(\frac{\overline{v_p^2}}{k_p}-\frac{2}{3}\right)-C_2\frac{\Pi_p}{k_p}-\frac{1}{T_p}\left(6\frac{\overline{v_p^2}}{k_p}-\frac{2}{3}\right) \tag{7.8}$$

$$\frac{3}{2}\Big[\frac{\partial(\alpha_p\rho_p\Theta)}{\partial t}+\nabla\cdot(\alpha_p\rho_p\Theta\mathbf{u}_p)\Big]=\nabla\cdot\Big[\Big(\kappa_\Theta+\frac{3\mu_{pt}}{2Pr_{pt}}\Big)\nabla\Theta\Big]+2\mu_p\overline{\mathbf{S}}_\mathbf{p}:\overline{\mathbf{S}}_\mathbf{p} \\ -p_p\nabla\cdot\mathbf{u}_p+\alpha_p\rho_p\varepsilon_p-3\beta\Theta-\gamma \tag{7.9}$$

7.4 Results and discussion

7.4.1 Influence of mesh resolution

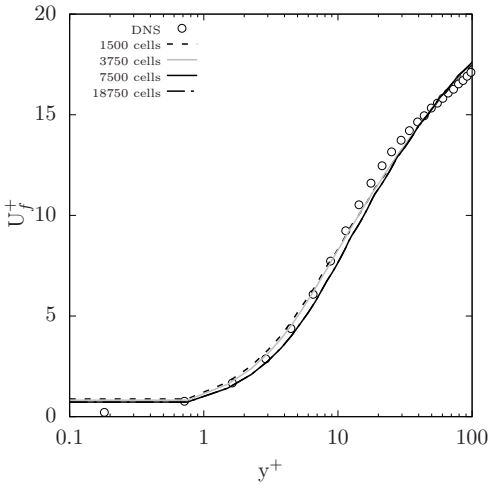

Figure 7.1: Mean fluid stream-wise velocity convergence.

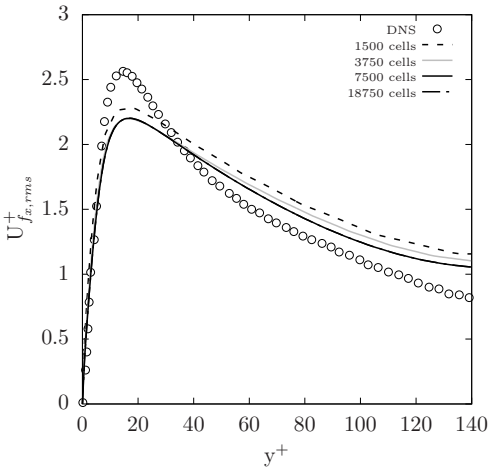

Figure 7.2: Fluid stream-wise fluctuation velocity convergence.

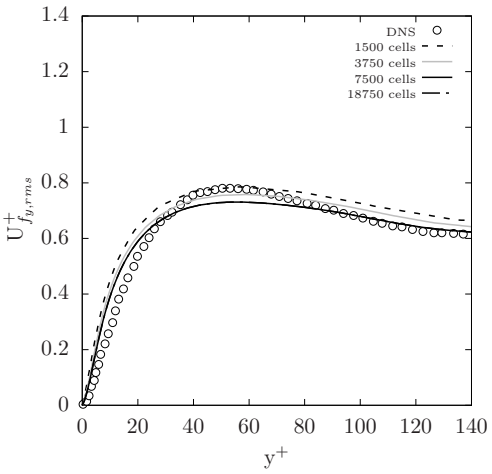

Figure 7.3: Fluid wall-normal fluctuation velocity convergence.

To ascertain the influence of the mesh's resolution four different mesh sizes are compared; 1500, 3750, 7500 and 18750 cells pertaining to 25x50, 50x75, 75x100 and 1250x150 in the x- and y- direction, respectively. Simulations are run for 500 s of real flow time with all flow statistics being averaged through flow sampling. Flow sampling takes place after 100 s and is used to ascertain temporal sensitivity of the solution. It is expected that the steady state would be reached well before this as $16\pi h/\mathbf{u}_f \approx 27$s and therefore the flow has travelled down the channel over 15 times.

Figures 7.1 - 7.3 show that with incremental increases in mesh resolution the results tend towards a converged solution. The final two mesh resolutions reveal no change across all three flow variables and lie on top of each other in each plot. These two mesh resolutions indicate that the solution is mesh independent and no further enhancement of the resolution will influence the solution. As the flow is one-way coupled and the particles tend to remain correlated with the flow i.e. the drag from the fluid-phase is main coupling mechanism, only the fluid-phase statistics are shown here. In conclusion then, with a mind to reduce the computational cost, and with no loss of accuracy, the mesh consisting of 7500 cells is employed throughout this chapter.

It is worth noting that the solution of the RA-TFM momentum equations and the full system of phase energies i.e. the solution of 12 transport equations is relatively cheap on a grid for $Re_\tau = 150$. The average solution time on the selected grid was between 60-120 seconds on a computer with 8GB of RAM and an i5-7200u processor with base frequency 2.9GHz. With the increase in computing power relatively large systems of algebraic equations become quite feasible. Although as processing power seems to be peaking with only incremental advances, a RAM intensive coupled matrix formulation may be a better alternative in the future. For more complex and higher Re number flow this computational cost would indubitably increase, perhaps out of feasibility. For the investigation of the near-wall behaviour, in a certain section or geometric aspect of an application, of fluid-particle flow this approach remains quite feasible and could elucidate the fluid-particle behaviour in

the boundary layer without imposing a huge computational cost.

7.4.2 Fluid-phase statistics

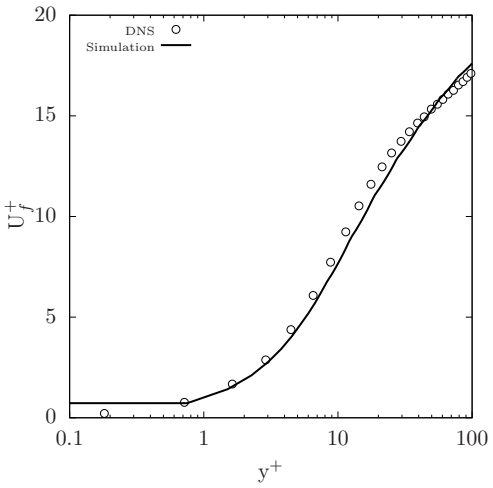

Figure 7.4: Mean fluid stream-wise velocity.

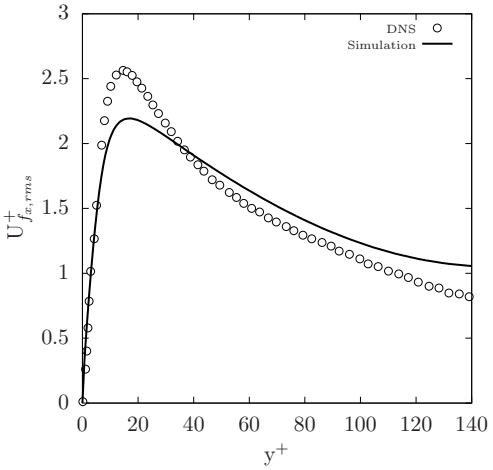

Figure 7.5: Fluid stream-wise fluctuation velocity.

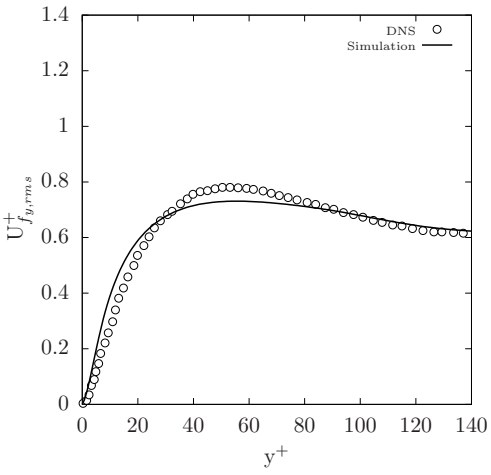

Figure 7.6: Fluid wall-normal fluctuation velocity.

Figure 7.4 shows the calculation of the mean fluid-phase velocity. There is a satisfactory prediction of the mean velocity spanning from the viscous wall region to the log-law region. This crucial region for predicting a number of phenomena i.e. heat

transfer, particle-wall interaction and compressible flows can be accurately modelled with the $\overline{v_f} - f$ model. From $y^+ < 1$ there exists two mesh cells which explains the perceived lack of gradient in this region, as mentioned in §7.3 a computational limit is set for small values of y^+, although the fluid-phase velocity components do correctly tend to 0 as the wall is approached. It is an artifact of the lack of resolution for very small values of y^+ and the logarithmic scaling.

In Fig. 7.5 the stream-wise fluctuation velocity is shown. Qualitatively the model is in good agreement especially for an E-E simulation. Despite this, two main discrepancies can be seen: the under-prediction in the peak of fluid-phase turbulent kinetic energy and the over-prediction of the turbulence decay in the free-stream. Two explanations that perhaps feed into each other can be suggested. The first, if one invokes continuity across the span of the channel it can be imagined that if the production was increased the decay would increase. Thus we can postulate that if the production was increased a larger peak would be displayed and as a result a steeper gradient of decay would be shown.

The peak is governed by the production term, Π_f which is a function of the fluid-phase turbulent viscosity and mean velocity gradients. The latter can be influenced through numerical schemes - in particular the calculation of the gradient [64]. Secondly, due to the relatively small Reynolds number of the flow, $Re_\tau = 150$ the turbulence model can fail to capture the correct turbulent kinetic energy behaviour. This is due to the model being calibrated for high Reynolds number. In Durbin [56] it is shown that for low Reynolds number flow the model over-predicts turbulence in the free stream - a finding that is consistent with damping functions. It should be noted that they also over-predicted the peak which was not the case in this study. It would seem that an element of both are at work, therefore with calibrating of the turbulence constants a more accurate fit could be obtained. It is also worth mentioning that in the data of Marchioli et al. [121] the peak is the region in which the greatest variance was reported. This is true of both phases and highlights the difficulty in predicting a reliable value.

The near-wall behaviour of the wall-normal component has been accurately captured in Fig. 7.6. A slight underproduction is seen in the peak across the range $40 < y^+ < 80$ which is expected as the value of the stream-wise fluctuating component is also under-predicted. As discussed the wall-normal component receives turbulent kinetic energy through redistribution - therefore the under-prediction is experienced in both components. Overall excellent agreement with the DNS data is found, this provides promising evidence for the application of the $v^2 - f$ model to E-E modelling.

7.4.3 Particle-phase statistics

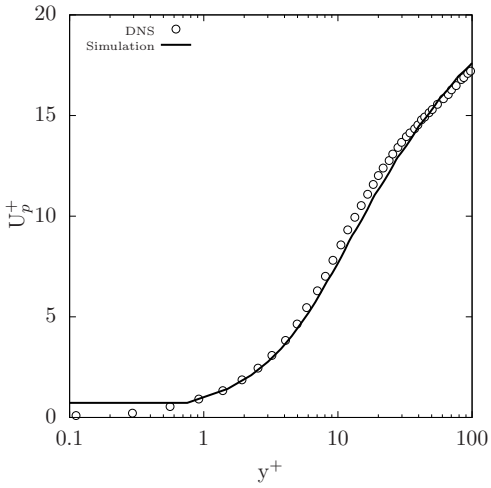

Figure 7.7: Mean particle stream-wise velocity, St = 1.

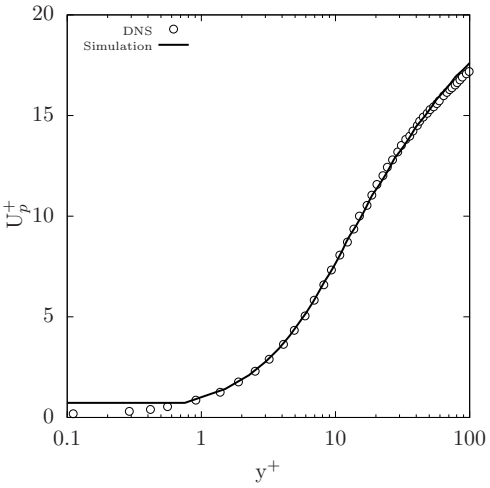

Figure 7.8: Mean particle stream-wise velocity, St = 5.

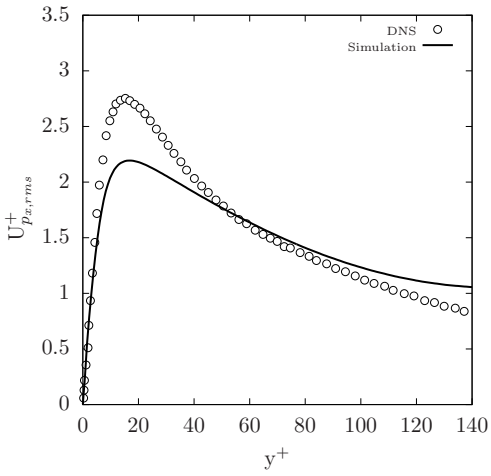

Figure 7.9: Particle stream-wise fluctuation velocity, St = 1.

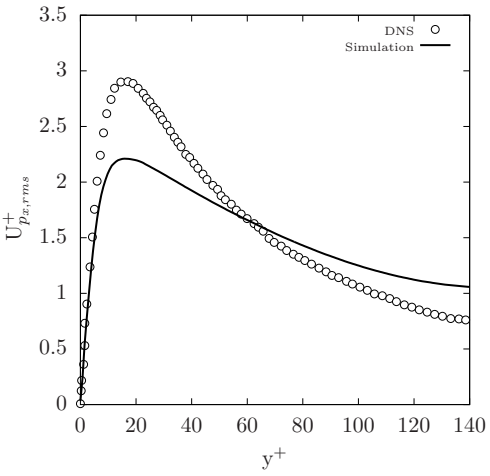

Figure 7.10: Particle stream-wise fluctuation velocity, St = 5.

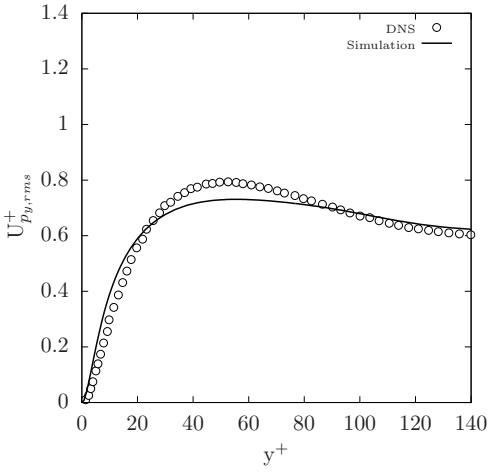

Figure 7.11: Particle wall-normal fluctuation velocity, St = 1.

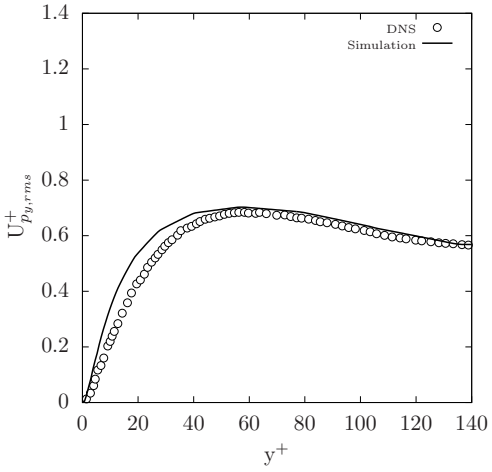

Figure 7.12: Particle wall-normal fluctuation velocity, St = 5.

For the channel flow simulated in the work of Marchioli et al. [121] the fluid-particle co-variance terms dominate the particle-phase energy by providing the major contribution to their production via drag. As the particle-phase is one-way coupled with the fluid-phase the particles will be dragged along by the fluid and experience no feedback effect on the fluid-phase. Even in such a flow it has been shown the need to partition the particle inertia into correlated and uncorrelated motion Février et al. [67]. In the model used throughout this partitioning is denoted by k_p and Θ, respectively.

Figs. 7.7 & 7.8 shows the prediction of the particle-phase mean velocity of which shows excellent agreement with the DNS data. The prediction of the mean velocity is well captured across the range of y^+ with the main discrepancy coming from the mesh resolution as discussed previously. Due to the close to non-existent slip velocity, owing to the geometry and governing physics, it is apparent that the Neumann wall boundary condition results in the correct near-wall behaviour. Owing to the smoothness of the channel no effects due to roughness were incorporated, for further discussion the reader is referred to Vreman [203].

Figs. 7.9-7.10 reveal that the model is capable of capturing the Stokes dependent

behaviour, which manifests itself in an increase in the peak of turbulent kinetic energy, although the increase is not as large as that seen in the DNS. We recognise here that this increase of particle-phase turbulent kinetic energy is due to the increase in uncorrelated energy, Θ. As the particle response time increases the particles become uncorrelated with the main flow. This phenomenon has also been reported by Février et al. [67], Vance et al. [199] who showed that with increasing Stokes number an increasing fraction of the fluctuating energy was found in the random-uncorrelated motion, Θ. We find that the increase in particle response time coupled with the dispersion enhances the 'de-correlation' which is why the main increase is seen across $y^+ < 60$. The energy is re-partitioned into the near wall region showing an increase in the peak of the turbulent kinetic energy. As a result over the $y^+ > 60$ there is an increase in the gradient of turbulent kinetic energy decay, a feature that was not captured. It is interesting to note that this re-partitioning of the particle-phase energy is not especially felt in the mean-velocity profile.

In Fig. 7.10, even though an increase in the peak seen at $y^+ \approx 11.6$ is apparent the behaviour approaching the free-stream is at odds with the DNS data. The lack of turbulent kinetic energy decay is most apparent across $y^+ > 60$. It is clear that the distribution of the turbulence energy changes quite considerably with larger response times and a sharper gradient of decay is shown. This suggests that an adjustment of the the turbulent decay constant could be made a function of the particle Stokes number.

As shown in Marchioli et al. [121] preferential concentration is shown for Stokes number 5, a feature that was also seen in the simulation. It was revealed in our simulations that with increasing particle response time, particles tended to drift towards the wall becoming preferentially concentrated. A phenomenon that is well-established in the literature Reeks [149]. This behaviour was determined by the drift velocity as expected, which is a function the gradient of volume fraction and Stokes number. Figs. 7.11 & 7.12 show the particle-wall normal fluctuation velocity components. A satisfactory prediction across both simulations can be seen. The

main discrepancy is the lack of peak in the former although the trend is captured elsewhere. The increase in St number tends to dampen this peak as it is felt as an increase in the stream-wise component. This behaviour is present within the current simulations but to a much less pronounced extent. As previously mentioned this area provided the greatest variance in the DNS data and the magnitude of the error may not be as pronounce as suggested here.

7.5 Closure

The current chapter presented a derivation of a pressure-velocity model for both the particle-phase for use in Eulerian-Eulerian simulations. The turbulence model was derived within a Reynolds-Averaged Two-Fluid Model framework and applied to channel flow. Both pressure-velocity models derived within this thesis were applied to a wall bounded turbulent flow. Throughout it has been shown that accounting for the kinematic blocking effect leads to promising results. Across both fluid and particle turbulence statistics a good agreement was shown, in particular the wall-normal energy component of each respective phase was well produced. A result that has hitherto alluded E-E simulations. The results were validated against benchmark Direct Numerical Simulation of Marchioli et al. [121] and show good agreement with the experimental data. The RA-TFM shows the correct Stokes dependence behaviour exhibited in the particle-phase turbulence statistics. The current predictions show encouraging results and efforts should be made to extend the approach for more complex flow regimes i.e. two-way coupling.

This page is intentionally left blank.

8 A fully-coupled pressure-based two-fluid solver

8.1 Overview

In this chapter, the block-coupled solution algorithm, presented in Chapter 4 - Sec. 4.3, is verified against the segregated algorithm, presented in Chapter 4 - Sec. 4.2, and validated against the benchmark experimental data of Tsuji and Morikawa [192]. The coupled solver shows marked improvements in convergence, stability and solution time. The coupled implementation is capable of solving to a tolerance that is six orders of magnitudes smaller in residual error and 1.7 times quicker than the segregated solver. The implicit treatment of phase-velocity-pressure and inter-phase momentum transfer enabled the simulation to be accelerated as larger time steps could be taken. Additionally, the sequentially solved system of phase-energies experienced performance improvements when solved in conjunction with the coupled solver.

The main contributions of this chapter are:

- The coupled two-fluid implementation is verified against the segregated implementation;
- The coupled two-fluid implementation is validated against benchmark experimental data of Tsuji and Morikawa [192];
- The performance of the coupled implementation is contrasted and compared against the segregated implementation.
- The coupled implementation, in general, provides superior performance:
  - Solving to a tolerance that is six orders of magnitude smaller in residual error;
  - Completing the simulation 1.7 times quicker than the segregated solver;
  - Able to increase the Courant number to 2.5 further accelerating the simulation as opposed to 1.5 in the segregated solver.
- As an auxiliary benefit to the implicit treatment of the phase-velocity-pressure coupling the system of phase-energy equations, of which are solved sequentially, are solved to a tolerance that is seven times smaller in magnitude.

8.2 Introduction

Traditionally, the governing equations in E-E simulations are solved in a sequential manner. This essentially means decoupling the phase-velocity-pressure and inter-phase drag and solving for them explicitly i.e. an equation for momentum and pressure-correction as shown in Chapter 4. As discussed previously, this often leads to slow convergence and arbitrary under-relaxation values. An alternative approach to the solution of the E-E governing equations exists - the block-coupled approach.

The approach relies on constructing a single block-matrix in which the influence of the phase-velocity-pressure coupling can be introduced through inter-equation coupling terms. The solution of which leads to dramatic improvements in convergence, stability and robustness. Approaches that are based on the solution of the single-phase governing equations have been proposed in the literature [20, 34, 39, 46, 47, 87, 99, 116, 124, 125, 147, 200, 208, 209, 215] and have been extended to E-E models by Burns et al. [25], Darwish et al. [45] and Ferreira et al. [63].

Darwish et al. [45] has recently proposed a two-fluid fully-coupled pressure-based solver in which their single-phase framework [46, 47] is extended to a multiphase framework. The governing equations are solved within a fully conservative formulation i.e. the volume fraction and density are left in the momentum equations, typically used to capture compressibility effects. They derived their model in a 2D framework and verify their results on 1D laminar test cases showing a rate of solution acceleration between 1.3 and 4.6. More recently. Ferreira et al. [63] proposed a fully-coupled pressure-based multi-fluid framework. In their work they solve the phase-intensive formulation i.e. dividing out by volume fraction and density and employ the Compact Momentum Interpolation (CMI) practice of Cubero et al. [44] and guess-and-correct procedure shown in Darwish et al. [45]. Overall, this treatment was shown to enhance stability and convergence through the correct treatment of the temporal, drag and body force interpolation especially when

a large drag force was present. The multi-fluid solver is verified on 2D laminar test cases showing superior performance when compared to the segregated solver.

In this chapter we verify and validate the fully-coupled pressure-based two-fluid algorithm presented in Chap. 4 - §4.3. The framework is implemented within the open-source tool-box `foam-extend` which is a community driven fork of OpenFOAM. The algorithm is verified against the segregated implementation (see Chap. 4 - §4.2) and validated against the turbulent benchmark experimental data of Tsuji and Morikawa [192]. Additionally, the performance of the coupled and segregated solvers are compared and contrasted.

8.2.1 Governing equations

We begin with a simplified set of equations from the RA-TFM. The coupling terms through buoyancy have been neglected.

The continuity and momentum equations of the particle- and fluid-phases are as follows:

$$\frac{\partial(\alpha_p\rho_p)}{\partial t} + \nabla\cdot(\alpha_p\rho_p\mathbf{u}_p) = 0, \tag{8.1}$$

$$\frac{\partial(\alpha_f\rho_f)}{\partial t} + \nabla\cdot(\alpha_f\rho_f\mathbf{u}_f) = 0, \tag{8.2}$$

$$\frac{\partial(\alpha_p\rho_p\mathbf{u}_p)}{\partial t} + \nabla\cdot(\alpha_p\rho_p\mathbf{u}_p\mathbf{u}_p) = \nabla\cdot(\alpha_p\rho_p\overline{\mathbf{R}}_{\text{eff,p}}) + \beta(\mathbf{u}_f-\mathbf{u}_p) - \beta\frac{\nu_{ft}}{\text{Sc}_{fs}\alpha_p\alpha_f}\nabla\alpha_p \\ -\nabla p_p - \alpha_p\nabla p_f + \alpha_p\rho_p\mathbf{g}, \tag{8.3}$$

$$\frac{\partial(\alpha_f\rho_f\mathbf{u}_f)}{\partial t} + \nabla\cdot(\alpha_f\rho_f\mathbf{u}_f\mathbf{u}_f) = \nabla\cdot(\alpha_f\rho_f\overline{\mathbf{R}}_{\text{eff,f}}) + \beta(\mathbf{u}_p-\mathbf{u}_f) + \beta\frac{\nu_{ft}}{\text{Sc}_{fs}\alpha_p\alpha_f}\nabla\alpha_p \\ -\alpha_f\nabla p_f + \alpha_f\rho_f\mathbf{g}. \tag{8.4}$$

The accompanying phase-energy transport equations that make up the complete RA-TFM can be found in Table 8.1. In this chapter they are treated sequentially and are therefore not given special treatment here.

Table 8.1: Phase-energy equations.

The fluid-phase energy transport equations:

$$\frac{\partial \alpha_f \rho_f k_f}{\partial t} + \nabla \cdot (\alpha_f \rho_f k_f \mathbf{u}_f) = \nabla \cdot \left[\left(\mu_f + \frac{\mu_{ft}}{\sigma_{fk}} \right) \nabla k_f \right] + \alpha_f \rho_f \Pi_f - \alpha_f \rho_f \varepsilon_f + \beta(k_{fp} - k_f) \tag{8.5}$$

$$\frac{\partial \alpha_f \rho_f \varepsilon_f}{\partial t} + \nabla \cdot (\alpha_f \rho_f \varepsilon_f \mathbf{u}_f) = \nabla \cdot \left[\left(\mu_f + \frac{\mu_{ft}}{\sigma_{fk}} \right) \nabla \varepsilon_f \right] + \frac{\varepsilon_f}{k_f} \left[C_1 \alpha_f \Pi_f - C_2 \alpha_f \rho_f \varepsilon_f \right] + C_3 \beta(\varepsilon_{fp} - \varepsilon_f) \tag{8.6}$$

The particle-phase energy transport equations:

$$\frac{\partial \alpha_p \rho_p k_p}{\partial t} + \nabla \cdot (\alpha_p \rho_p k_p \mathbf{u}_p) = \nabla \cdot \left[\left(\mu_p + \frac{\mu_{pt}}{\sigma_{pk}} \right) \nabla k_p \right] + \alpha_p \rho_p \Pi_p - \alpha_p \rho_p \varepsilon_p + \beta(k_{fp} - k_p) \tag{8.7}$$

$$\frac{\partial \alpha_p \rho_p \varepsilon_p}{\partial t} + \nabla \cdot (\alpha_p \rho_p \varepsilon_p \mathbf{u}_p) = \nabla \cdot \left[\left(\mu_p + \frac{\mu_{pt}}{\sigma_{pk}} \right) \nabla \varepsilon_p \right] + \frac{\varepsilon_p}{k_p} \left[C_1 \alpha_p \rho_p \Pi_p - C_2 \alpha_p \rho_p \varepsilon_p \right] + \beta(\varepsilon_{fp} - \varepsilon_p) \tag{8.8}$$

$$\frac{3}{2} \left[\frac{\partial \alpha_p \rho_p \Theta}{\partial t} + \nabla \cdot (\alpha_p \rho_p \Theta \mathbf{u}_p) \right] = \nabla \cdot \left[\left(\kappa_\Theta + \frac{3\mu_{pt}}{2Pr_{pt}} \right) \nabla \Theta \right] + 2\mu_p \overline{\mathbf{S}}_\mathbf{p} : \overline{\mathbf{S}}_\mathbf{p} - p_p \nabla \cdot \mathbf{u}_p + \alpha_p \rho_p \varepsilon_p - 3\beta\Theta \tag{8.9}$$

8.3 Geometry and case setup

The geometry used in the experiment of Tsuji and Morikawa [192] comprises of a vertically facing pipe with a diameter (D) of 0.035m and can be seen schematically in Fig. 8.1. The length of the pipe (L) including the development section is, L = 5.2m. The mesh size is 50 cells in the x direction and 20 in the y direction with adequate spacing to ensure a $y^+ > 30$ for the wall function. Due to the computational power available and the number of coefficients that need to be stored for each cell in the coupled solver, the mesh size had to be limited.

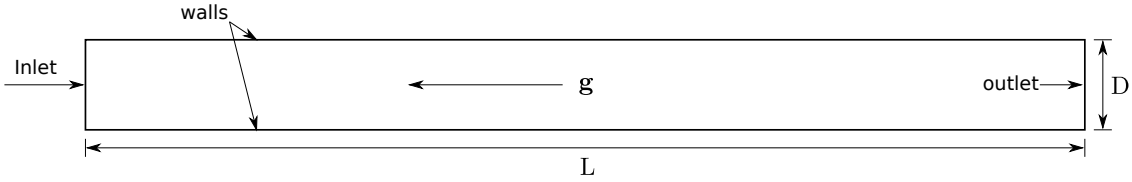

Figure 8.1: Schematic of the computational domain.

At the inlet a Dirichlet boundary condition is prescribed for both phase velocities and a Neumann condition for pressure. At the outlet a Dirichlet boundary condition is prescribed for pressure and a Neumann condition for both phase velocities. For the particulate phase wall boundary conditions a Neumann boundary condition is prescribed for the velocity and turbulence statistics. For the fluid-phase, the no slip wall condition is prescribed for velocity and the standard wall functions are employed for the turbulence statistics. Both k_p and ε_p are initialised as 1/3rd of their fluid counterpart with $\Theta = 1.0 \text{ x } 10^{-10}\text{m}^2\text{s}^{-2}$.

Table 8.2 details the cases simulated in this work. For the majority of the cases the centreline velocities were not recorded therefore the bulk velocities have been used. The mean velocity ($U_i^+ = u_x/u_m$) and turbulence intensity ($u_i^+ = (0.5k_i)^{1/2}/u_m$) are normalised by the bulk velocity, u_m which is taken from the simulation due to the lack of recorded values in the experiment.

Table 8.2: Table of simulated cases.

Case	Mass loading	d_p [μm]	Density [$\mathrm{kg\,m^{-3}}$]	U_m [$\mathrm{m\,s^{-1}}$]
1	1	0.2	1020	15.6
2	2.1	〃	〃	15.3
3	1.3	0.5	〃	10.8
4	2.9	〃	〃	10.8

Both the coupled and segregated solvers solve the phase-energy system of equations in a sequential manner using generic relaxation factors of 0.7 and a PGiCG solver. The coupled solver employs the ILU preconditioner and the biconjugate gradient stabilised solver (BiCGSTAB) with no relaxation factors. For the segregated system of equations the pressure equation was solved using the generalised algebraic multi-grid (GAMG) with a relaxation factor of 0.3. The volume fraction is solved using Multi-dimensional Universal Limiter with Explicit Solution (MULES) [222] which is a flux-corrected transport algorithm which ensures robustness, stability and convergence. Time derivative terms are discretised using the first order accurate implcit Euler scheme, gradients are discretised using the Gauss linear scheme, convective terms are discretised using the first order upwind scheme. Finally, Laplacians are discretised with the second order accurate central differencing scheme.

8.4 Results and discussion

8.4.1 Verification of the coupled solver

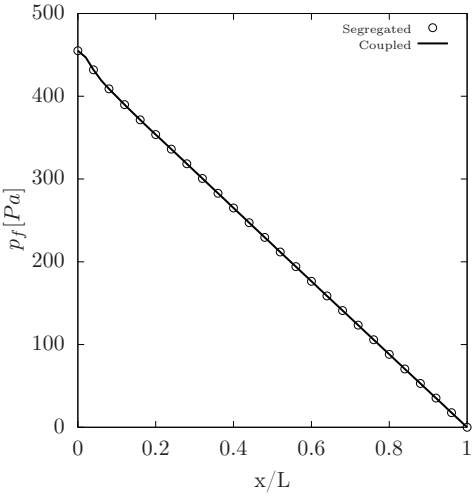

Figure 8.2: Distribution of pressure across the horizontal midsection of the pipe.

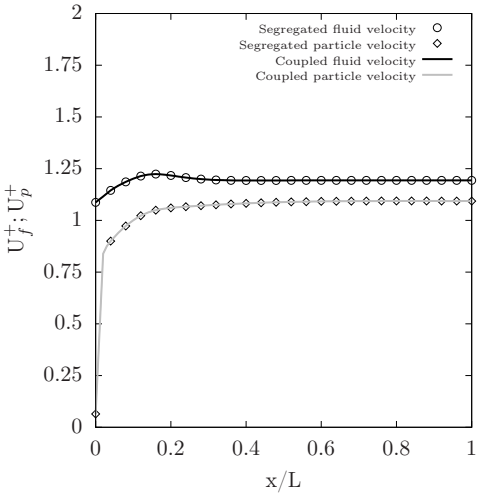

Figure 8.3: Distribution of velocity across the horizontal midsection of the pipe.

Fig. 8.2 shows a comparison of the pressure drop across the pipe in both the coupled and segregated solver. Both solvers show identical behaviour with a linear drop across the length of the pipe. From the authors experience, this was greatly influenced by the momentum interpolation technique of Cubero et al. [44] and implicit treatment of the drag correction in the divergence operator (Eq. 4.47). In particular the behaviour of the pressure drop in cells close to the inlet proved particularly challenging and could not be realised without the CMI of Cubero and Fueyo [43].

Fig. 8.3 shows a comparison of the phase-velocities across the pipe in both the coupled and segregated solver. To highlight the influence of the inter-phase momentum transfer the inlet velocity for the particle-phase is a $\approx 10\%$ of the fluid-phase. Again identical behaviour between solvers is demonstrated.

8.4.2 Validation of the coupled solver

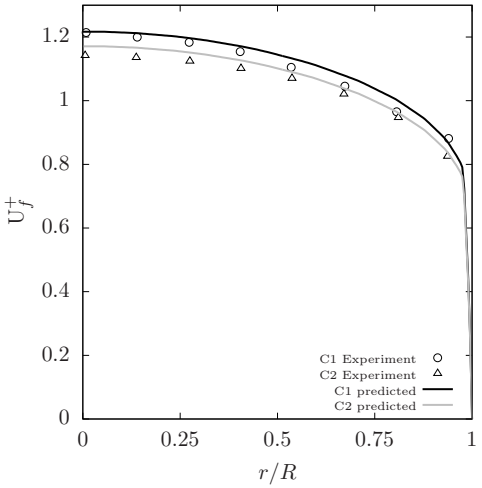

Figure 8.4: Mean fluid velocity. Symbols Tsuji and Morikawa [192]; curves are predictions for Case 1 & 2.

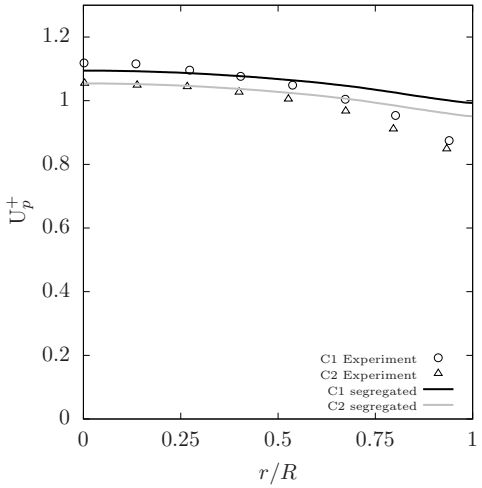

Figure 8.5: Mean particle velocity. Symbols Tsuji and Morikawa [192]; curves are predictions for Case 1 & 2.

Figure 8.4 shows the mean fluid velocity profiles. Overall, the trend of the fluid behaviour is captured, with the increase in mass loading resulting in a global reduction of fluid velocity (due to the direction of the body force) in both experimental and numerical predictions. In Case 1, there is an almost global over-prediction of the mean velocity albeit small. In the near-wall region ($r/R > 0.75$) the momentum loss is difficult to capture correctly. The experimental results suggest that the numerical model is not producing enough mean shear. This would result in a higher rate of change in the near-wall region thus falling in line with the experimental data. This lack of momentum loss can also be affected by the co-variance coupling term. As the particles are tightly coupled with the fluid-phase the main mechanism for momentum transfer is drag. An under-prediction in the co-variance term will reduce momentum loss - which would result an over-prediction of mean velocity.

For Case 2 this over-prediction is exacerbated and with an increased mass loading, in particular across ($r/R < 0.5$). In the region ($r/R > 0.75$) a substantial rela-

tive velocity between Case 1 and Case 2 was observed in the experimental data. Throughout the simulations this behaviour was qualitatively predicted showing reasonable agreement. It should be noted that the instrument used to measure the flow statistics, namely the laser Doppler Velocimeter (LDV) can be an intrusive way of measuring velocity and turbulence statistics. Additionally, in the near-wall region it becomes particularly challenging to record reliably.

Figure 8.5 shows the mean particle velocity predictions for Case 1 & 2. In the near wall region the slip condition enables a relative velocity between both phases to develop. Experimentally this resulted in a negative, $\mathbf{u}_r = \mathbf{u}_f - \mathbf{u}_p$ in the region $(r/R > 0.75)$ and a positive $\mathbf{u}_r$ in the $(r/R < 0.75)$ region. The slip boundary condition exhorts its influence over a quarter of the pipe - a finding that is consistent with the numerical prediction. The main discrepancy between the experimental and numerical results is across the near-wall region. The experimental results indicate that the particles remain largely correlated with the fluid-phases boundary layer. This is expected due to their tight coupling through drag and can be partly predicted by the model as the influence of the fluid-phase is felt across the particle velocities across $(r/R > 0.75)$.

Two explanations for this lack of momentum loss can be offered. Firstly, this behaviour indicates that the turbophoresis force that is responsible for wall-normal migration of particles is being under predicted. Without the redistribution of particles across the width of the pipe a more uniform velocity distribution is seen [157]. Secondly, the wall boundary condition was taking as slip assuming smooth walls. This is a speculative assumption and with the inclusion of boundary conditions that incorporate the effect of wall roughness the momentum loss in the boundary layer would be enhanced resulting in a closer prediction.

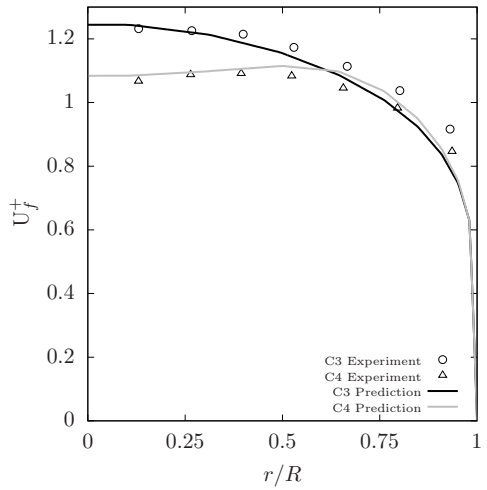

Figure 8.6: Mean fluid velocity. Symbols Tsuji and Morikawa [192]; curves are predictions for Case 3 & 4.

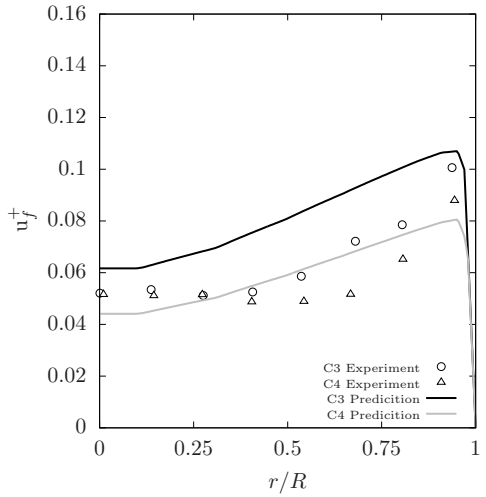

Figure 8.7: Mean fluid turbulent kinetic energy. Symbols Tsuji and Morikawa [192]; curves are predictions for Case 3 & 4.

Figures 8.6 & 8.7 show the results from Cases 3 & 4. In the former, the predicted mean fluid-velocities are in relatively good agreement with the experimental data with the main discrepancies being seen in the near-wall region. With increased mass loading, the difficult to capture [118] reduction of fluid velocities in the core region ($r/R < 0.5$) is reproduced. The increase in particle diameter and mass loading results in an accumulation of particles within the core of the pipe which are being dragged down by gravity. Due to the increase in Stokes number and increased likelihood of particle collisions, the uncorrelated energy, Θ experiences an increase in the core of the flow. This ensures that the particles are no longer closely correlated with the carrier flow, i.e. increased dissipation in the correlated energy equations $k_p - \varepsilon_p$. Through the co-variance coupling terms, as well as the inter-phase momentum transfer term, this behaviour can be captured. This results in the fluid-phase velocity being 'dragged' by the particle-phase - a complex two-way coupled mechanism that is apparent in the numerical prediction and in the experimental observation. Due to the conservation of momentum across the pipe this results in an increase in the velocities in the region ($0.5 > r/R > 0.75$).

For Case 3, good agreement is found with the centreline velocity but the main

bulk of the velocities leading up to the near-wall region are under-predicted. This behaviour can be better explained by looking at Fig. 8.7. The fluid intensity result for Case 3 illuminates the situation. The over-prediction of the intensity across the centreline would manifest itself in an over-prediction in the turbulent viscosity calculation resulting in the predicted behaviour. Due to the non-linear profile of the experimental turbulence intensity the behaviour is difficult to capture within a Reynolds-Averaged methodology, in particular the use of the wall function also limits the situation further. To this end a near-wall pressure-velocity model has been recently proposed that can circumvent these problems in two-fluid simulations - see Chapter 2.

8.4.3 Performance of the coupled solver vs segregated solver

In this section both the coupled and segregated solvers are run for 30 seconds of actual flow time on Case 1 under identical conditions with the Courant number kept constant at 0.5.

In order to ascertain the magnitude of the estimated error, the normalised residual error estimate is calculated according to Jasak [92]. The residual is normalised by the dominant diagonal coefficients in order to ascertain the behaviour of each variable more readily. This enables the formulation of a relative error.

$$\varepsilon_r(\phi) = \frac{|b_i - A_{i,j}x_i|}{|A^n_{i,j}x^k_i - A^{n-1}_{i,j}x^{n-1}_i| + |b^k_i - A^{n-1}_{i,j}x^{n-1}_i|}. \tag{8.10}$$

A convergence criterion can be set as:

$$\varepsilon_r(\phi) \leq \varepsilon_{res}. \tag{8.11}$$

Although we do not set a stop criterion in this study it should be noted that conventionally residuals are set between $\varepsilon_r < 10^{-3} - 10^{-6}$. If we take the latter value as our convergence criterion the two-fluid coupled solver converges in 161s whereas the segregated solver fails to reach values near $\varepsilon_r(\phi) = 10^{-6}$ and oscillate in the order of $\varepsilon_r(\phi) = 10^{-3} - 10^{-4}$.

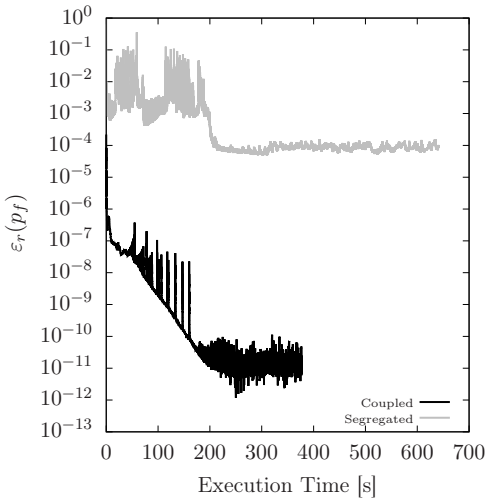

Figure 8.8: Pressure residual behaviour for coupled and segregated solver.

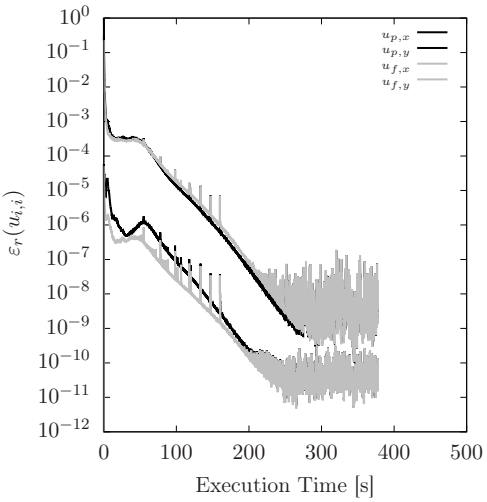

Figure 8.9: Velocity component behaviour for the coupled solver.

Figures 8.8 and 8.9 show the normalised residual behaviour for pressure and phase velocity components. Due to the segregated solution algorithm used the phase velocity components are not explicitly solved for and are instead used to predict and correct, hence no data is available for a comparison. Fig. 8.8 reveals some quite striking behaviour about the residual behaviour. The coupled two-fluid solver's initial residual, due to the implicit treatment of the pressure correction, starts at the $\varepsilon_r(p_f) = \mathcal{O}(10^{-4})$ - as the flow is driven by inlet condition for velocity, the pressure coefficients do not contain a substantial source. This residual error is driven down by several orders of magnitude within the first few iterations before reaching an oscillatory steady state at $\varepsilon_r(p_f) = \mathcal{O}(10^{-11})$.

In the segregated solver, typical residual behaviour is observed, showing saw-toothed behaviour, due to the relaxation factor. After some time, similar to the coupled solver, the solution reaches a steady-state with the residual remaining oscillatory until the simulation ends. The main contributor to the extension in time is the explicit calculation of the pressure equation. In the segregated solver crucial terms, drag and gravity, are moved to the pressure calculation - this increases the stability of the solution but puts a penalty on the computational time. This often results in a hefty amount of iterations to drive the pressure residual down to its

prescribed tolerance before advancing the solution in time.

Figure 8.9 shows the four phase velocity components. It can be seen how the normalised residual behaviour follows the same qualitative behaviour of the pressure residual - a natural consequence of the block-coupled solution. Throughout the solution, small spikes and oscillatory behaviour were present, a feature that was also apparent in Uroić and Jasak [193] and was shown to be an artifact of the linear solver BiCGSTAB. The two largest residuals are the momentum variables in the flow direction, this is expected due to their diagonal coefficients containing the dominant momentum flux and implicit drag correction. It is evident that the implicit treatment of the phase-velocity-pressure has positive benefits on the normalised residual error showing substantial improvements over the explicit treatment.

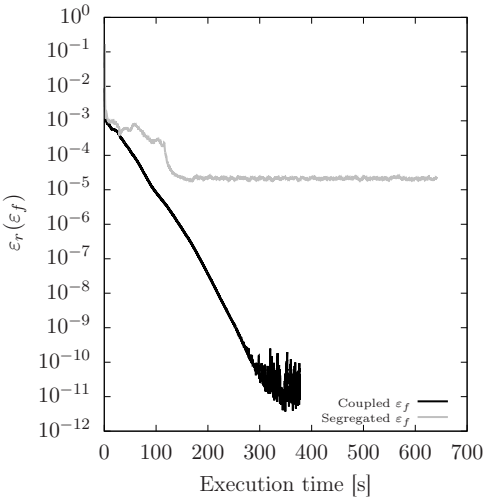

Figure 8.10: Turbulent dissipation residual behaviour.

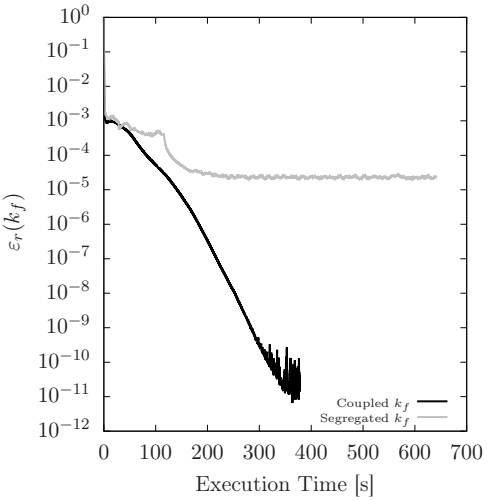

Figure 8.11: Turbulent kinetic energy residual behaviour.

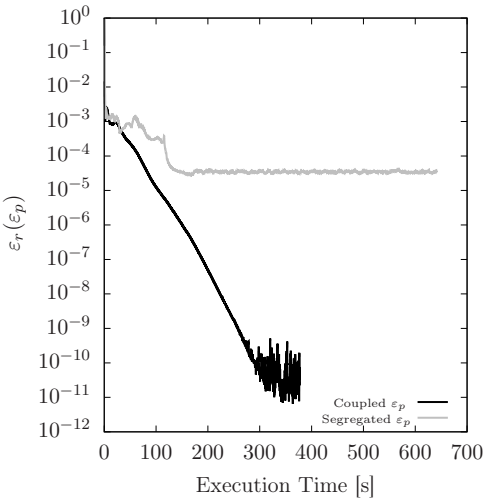

Figure 8.12: Particle turbulent kinetic energy execution time.

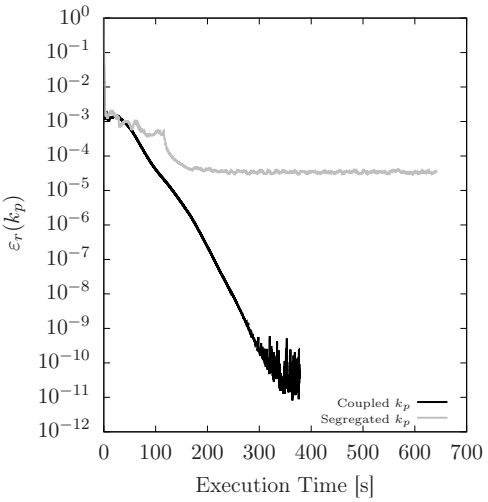

Figure 8.13: Particle turbulent kinetic energy dissipation convergence.

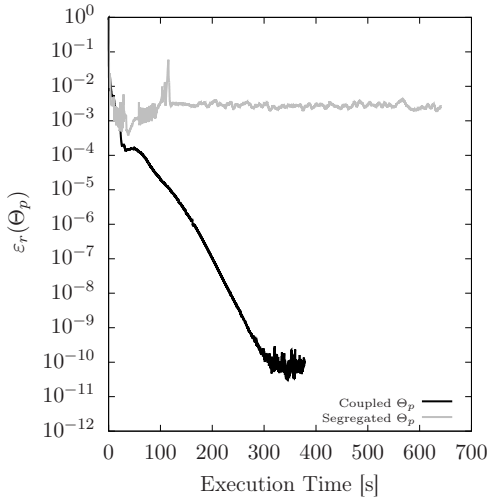

Figure 8.14: Granular temperature convergence.

Figures 8.10 - 8.14 show the residual behaviour for the phase-energy system. Overall, it can be seen that the coupled solver reduces the residual error across all turbulence variables resulting in a comparative drop of several orders of magnitude. The benefits of the implicit treatment of the phase-velocity-pressure coupling is carried over into the solution of phase-energies despite them being solved using a segregated solution algorithm. This auxiliary benefit can be best highlighted by looking at the residual behaviour for the granular temperature, Fig. 8.14. In the

segregated approach the residual fails to converge to a reasonable tolerance whereas in the implicitly coupled solution the residual shows a dramatic reduction in line with the accompanying phase-energy residuals. The reason for this relatively large residual of granular temperature is due to the particle turbulent dissipation. ε_p appearing as an explicit positive source term in its transport equation. Without the particle turbulent dissipation residual being reduced this behaviour will always be present, a feature that is alleviated within the coupled solution residual.

8.4.4 Courant number variation

One benefit of an implicitly coupled phase-velocity-pressure solution is that the solution can be accelerated due to the implicit treatment of hitherto explicit terms, unlike in the segregated solver. The implicit treatment of the phase-velocity-pressure coupling and the inter-phase momentum transfer in particular enables the Courant number to be increased beyond conventional limits. In this section the simulations are rerun with incrementally increasing Courant number to ascertain the performance of both solvers.

Table 8.3: Total execution time of the coupled and segregated solvers under increasing Courant Number.

Courant No.	Coupled Exe. [s]	Segregated Exe. [s]
0.25	541	1022
0.5	377	641
1	235	320
1.5	216	255
2	176	N/A
2.5	149	N/A

Table 8.3 details the solution execution time of each solver under increasing Courant number. Overall, it can be seen that the coupled solver out performs the segregated solver across each increment of Courant number. In addition, the coupled solver is

able to achieve higher Courant numbers due to its implicit solution. This results in the coupled solver being 1.7 times quicker than than the segregated solver. Above Courant numbers of 1.5 the segregated solution becomes unstable and the solution is compromised. This is due to the explicit treatment of the phase-velocity-pressure coupling and the semi-explicit implementation of the inter-phase momentum transfer.

For the solution of the block-matrix a fairly conventional matrix solver is employed i.e. ILU preconditioner with BiCGSTAB. Recently, a more sophisticated approach has been developed: a block-selective algebraic multigrid algorithm [193]. We note here that an aggregative algebraic multigrid algorithm exists within `foam-extend` but its performance was found to be unsatisfactory in comparison to BiCGSTAB. The block-selective algorithm has shown to provide substantial increases in the performance of the linear solver. In some cases completing the solution within half the time of the BiCGSTAB algorithm. This could further improve the results of the coupled solver with a further reduction in execution time.

Simulations above Courant number 2.5 were not feasible due to the solution of the phase-energy equations. This can be circumvented with the block-coupled solution of the phase-energy equations as the the explicit terms that enforce the time step dependency can be treated implicitly. The most obvious candidates would be the production and dissipation of turbulent kinetic energy and the inter-phase momentum transfer. Recently, Keser [101] has shown that single-phase turbulence models can also benefit from such a block-coupled solution.

8.5 Closure

The current chapter has verified and validated the fully-coupled pressure-based two-fluid framework presented in Chapter 4 - §4.3. The coupled implementation was verified against the segregated implementation, additionally the former was validated against benchmark experimental data. The approach is directly contrasted with the segregated approach in order to compare key differences in the solution algorithm. The coupled two-fluid solver shows far superior performance in terms of solution time, stability and convergence, often converging to a residual error of several magnitudes smaller than its segregated counterpart. Additionally, the algorithm was capable of being accelerated due to the implicit treatment of the phase-velocity-pressure and inter-phase drag.

This page is intentionally left blank.

9 Closure

9.1 Summary and Conclusions

The overarching aim of this study has been to advance the current Eulerian-Eulerian modelling methodologies for the solution of turbulent fluid-particle flows. The underpinning philosophy of the approach was recognising the partitioning effect of particle inertia - this was shown, if neglected, to result in the incorrect prediction of the particle's behaviour in high Re number flows. As the particle's inertia increases from a non-zero value the particles can be broadly separated into correlated and uncorrelated motion with the carrier phase.

When the inertia is small the particles are aligned with the turbulent kinetic energy in the carrier phase - as the particles inertia increases, depending on a range of criteria e.g. α_p and St, the particles begin to become uncorrelated with the carrier flow and contain their own energy from inter-particle collisions, drag with the carrier phase and dissipation from the correlated particles. This cascade of particle energy has been proven to be vital for the correct prediction of the turbulence statistics - showing validation across a range of particle classifications, flow configurations and coupling mechanisms.

The near-wall region within E-E modelling methodologies have been an often neglected area. Throughout this work modelling advancements have been proposed in order to resolve the near-wall region in E-E simulations. The approaches are completely arbitrary and can be applied to any wall bounded flow and nor is the approach confined to the E-E modelling used in this work. It was shown that the elliptic relaxation models proposed herein resulted in a satisfactory approach to resolving this region showing hitherto out of reach agreement with the available experimental data. Following such an approach can open the way to new modelling in the near-wall region as our understanding of this region expands.

Typical E-E solution algorithms have relied on the decoupling of phase-velocity-pressure and inter-phase drag in order to solve the system of equations in a segregated manner. This often leads to lengthy solution times and poor convergence, even more so than in single-phase segregated algorithms due to the inter-phase drag decoupling. In this work it has been shown that the implicit treatment of the phase-velocity-pressure and inter-phase drag, through a block-coupled solution, can result in dramatic improvements in simulation solution time, stability and convergence.

9.2 Current E-E modelling

It has been demonstrated how pivotal the partitioning effect of particle inertia is to achieving an accurate prediction of the particle-phase turbulence statistics. Starting from a mesoscale kinetic equation one can arrive at a Reynolds-Averaged macroscale equation that can account for a distinction between the particle-phase energies i.e. Θ and k_p. These quantities provide separate contributions to the total fluctuation energy and represent small scale uncorrelated energy and large scale correlated energy, respectively. This proved crucial throughout and resulted in a high level of validation across a range of flow regimes.

This study presented a Reynolds-Averaged Two-Fluid model for the solution of

turbulent fluid-particle flows. Throughout the work, particular emphasis has been placed on the derivation of the model from the kinetic equation through to the RA transport equations for the E-E model. The coupling mechanisms and correct separation of the phase energy has been detailed. The modelling methodology has been implemented within the open-source CFD tool-box OpenFOAM. The approach has been applied to numerous benchmark experimental cases which has highlighted the modelling philosophies validity especially when compared to the conventional E-E modelling methodologies. The breakdown in the prediction of the conventional methodologies have been elucidated with the aid of the RA-TFM.

This breakdown was seen at its most stark in Chapter 5. Particle-phase turbulence statistics of the RA-TFM were compared against the methodology of Peirano [141], a model that has widespread use in open-source and commercial codes alike, showing a disparity with the experimental data. This error was attributed to the coupling of the mesoscale kinetic equation with the macroscale turbulence in the Peirano model. It was revealed that the standard model was not capable of capturing key flow features e.g. recirculating region. This had a dramatic impact on the particle mean flow statistics resulting in an under prediction across the step. This fed into the inter-energy transfer mechanism leading to an incorrect prediction of the two-way coupling effect - attenuation.

9.3 Near-wall modelling in E-E simulations

Special attention has been paid to the near-wall region, in Chapters 6 & 7, resulting in elliptic relaxation models for the fluid- and particle-phases, respectively. The inclusion of this additional modelling has elucidated various aspects of E-E modelling. An aspect of E-E simulations that has remained largely untouched.

In the near-wall region, where an accumulation of particles can occur, a correct calculation of the fluid-phase turbulent kinetic energy is crucial. In order to predict the particle deposition in the boundary layer, the turbophoresis force must be

accounted for - this force is dependant on the wall-normal stress component [150]. As the wall-normal stress components are overestimated in conventional turbulence modelling e.g. $k - \varepsilon$, the particles can not overcome the wall-normal gradient. As the wall-normal component should be suppressed owing to image vorticity the particles can reassemble themselves and overcome the relatively flat gradient in the near wall region. Once trapped they rarely overcome the opposing gradient and are deposed. With the use of the proposed elliptic relaxation model this behaviour can be predicted as shown in Chapter 6.

It was also shown that without predicting this behaviour the particle physics can be inhibited. Using wall-functions in conjunction with the conventional turbulence model resulted in an incorrect prediction of the volume fraction across the width of the pipe. It tended to force particles into the core of the flow and this aspect was missed. The knock-on effect was the loss of two-way coupling effects in the near-wall region. These issues were also shown to be alleviated with the elliptic relaxation model as well as falling in line with the experimental data.

In Chapter 7, the elliptic relaxation model is applied to the particle-phase. As the fluid- and particle-phase share a pressure field and both phases are tightly coupled at the macroscale the approach remains valid. The modelling is validated against benchmark DNS data and shows good agreement across particle mean flow, turbulent kinetic energy and crucially wall-normal kinetic energy. The model was applied to channel flow in the one-way coupled regime although it is applicable to two-way coupling. Additionally, the boundary conditions provided in Chapter 5 can be employed to model particle-wall interaction which can also lead to two-way coupling effects i.e. attenuation. The level of agreement is particularly satisfying given that E-E modelling was used throughout this work.

9.4 Numerical solution of E-E models

In Chapters 4 & 8, a block-coupled solution algorithm for the E-E governing equations was presented, verified and validated. The phase-velocity-pressure and inter-phase drag terms were treated implicitly resulting in tight coupling between the primary variables. In comparison to the segregated approach in which the primary variables are decoupled by treating them explicitly as each variable is solved. The implicit treatment of the phase-velocity-pressure and inter-phase drag was shown to give far superior performance over the explicit treatment found in the segregated implementation.

The block-coupled solution algorithm was shown to be capable of reaching residual errors in $\mathbf{u}_i$ - p_f in the $\mathcal{O}(10^{-11})$. This was $\approx$ 7 orders of magnitude smaller than the segregated solvers residual tolerance. In addition, the solution time was found to be 1.7 times faster than its segregated counterpart. Due to the implicit treatment of the phase-velocity-pressure and inter-phase drag the simulation could be accelerated via the CFL criterion. This resulted in a further speed up of the simulation. Due to the solution of the phase-energies i.e. segregated this was limited at a CFL of 2.5 but with the block-coupled solution of the phase-energies this could be increased further.

It was shown that with a block-coupled solution the phase-energy system of equations experienced an auxiliary benefit. Due to the presence of cascade effect in the particles energy i.e. the correlated turbulence dissipation appearing as a source term in the granular temperature equation, convergence can be adversely affected due to cross-equation dependency. Within the block-coupled solution this was alleviated resulting in a residual error of several orders of magnitude lower showing enhanced stability and robustness throughout the solution process. Moreover, the whole-system of phase-energy showed enhanced stability and convergence reaching residual errors in the $\mathcal{O}(10^{-10})$.

9.5 Future work

The results of this work can be improved on in a number of ways, in particular introducing more complex mechanisms such as virtual-mass, lift, heat transfer etc. Given the approaches used herein, the inclusion of these additional physics would be straight forward, and some of these advances could be applied to engineering relevant cases and elucidate our current 'toolbox' for tackling these problems.

Another suggestion and perhaps most obvious is investigating more complex geometries. As the near-wall modelling is completely arbitrary it is applicable for any wall-bounded flow of which there are a wide variety in industry. Currently there is not a large database of experimental turbulent fluid-particle wall-bounded flows making validation and modelling difficult. As the particle classes and physics and vary widely it is challenging to develop a framework for how each system will behave. Even at the discrete level i.e. E-L this results in a lot of difficulty.

More work to refute the current E-E models in which the partitioning effect of particle inertia is not made needs to be carried out. Although efforts have been made at recognising unresolved structures by using filtered equations [131, 144, 169] although this is typically for dense flows. This will improve model predictions in existing CFD codes and promote the use of the current methodology.

The block-coupled implementation was applied to a relatively simple and computationally cheap regime, largely due to to computational restraints. Moreover, a standard matrix solver was employed for want of a better alternative. Exploration of the implementation on denser and more complex meshes are required to solidify its use and validity. The matrix solver used throughout was not optimised for the solution of block matrices. Recently, more optimised and efficient block-matrix solution algorithms have been presented [193]. It is thought that with these additional factors the results reported here could be further improved.

Some suggestions for further work are as follows:

- The coupling between both phases is given by the fluid-particle velocity co-variance i.e. k_{fp} and ε_{fp}. This term has been shown to give satisfactory agreement with experimental and DNS data. This has only been shown in a limited amount of flows, it would be particularly interesting to investigate this term for more complex flows and more importantly for higher volume fractions. This would accelerate the 'decorrelation' between the fluid- and particle-phase and could lead to a slightly different form of the closure;
- The closure for the fluid-particle velocity covariance is used for point particles which are well known to dissipate energy at a rate slightly higher than in true DNS [181, 216]. This is another aspect of modelling that could be explored;
- Throughout high density ratios were employed which resulted in the exclusion of the buoyancy terms. If this were not the case there would exist regimes in which a mixture of turbulence production by shear and buoyancy would occur - a particular interesting prospect;
- Application of the block-coupled implementation to more complex and challenging geometries. In particular with the use of more complex boundary conditions;
- An avenue exists in which the E-E phase-energy system can be block-coupled i.e. through inter-phase coupling of turbulence production, dissipation and drag. Moreover, the co-variance coupling terms that provided cross-phase coupling could also benefit from such a treatment;
- The modelling of both phases suffer from the classic eddy-viscosity assumption constraint i.e. isotropy. This can be alleviated by the use of a Reynolds-Stress Model (RSM) of which would be a reasonable next step as the particle Reynolds stress component have been shown to be highly anisotropic [173, 174];
- A particularly interesting approach would be to use the elliptic relaxation models proposed in this work with a Reynolds-Stress Model (as has been done

in single-phase flows [57]). This does pose a challenge in terms of stability and convergence due to the reliance of Reynolds-Stress components on each other;

- In connection to the previous suggestion, a block-coupled approach to solving the system of algebraic equations was shown in Chapter 4, if this approach was successfully applied to a RSM, one of the main drawback of RSM (in single-phase flow) would be alleviated. This approach would be best suited to this type of model as the Reynolds stress components are implicitly coupled - this would possibly pave the way to its wide spread use in industrial applications.

9.6 List of publications

A full list of publications which have been produced throughout this PhD are as follows:

Paper 1 Riella, M., Kahraman, R., Tabor, G. (2018).
'Reynolds-Averaged Two-Fluid Model prediction of moderately dilute fluid-particle flow over a backward-facing step'
Int. J. Multiphase Flow, 106:95-108.

Paper 2 Riella, M., Kahraman, R., Tabor, G. (2019).
'Near-wall modelling in Eulerian-Eulerian Simulations'
Computers and Fluids. 190:206-216.

Paper 3 Riella, M., Kahraman, R., Tabor, G. (2019).
'Inhomogeneity and anisotropy in Eulerian-Eulerian near-wall modelling'
Int. J. Multiphase Flow, 114:9-18.

Paper 4 Riella, M., Kahraman, R., Tabor, G. (2019).
'Fully-coupled pressure-based two-fluid solver for the solution of turbulent fluid-particle systems'
Computer and Fluids. (Under review).

This page is intentionally left blank.

A Appendix

A.1 RA equations for fluid-particle flows

Beginning from the equations found in §2.2.2 Reynolds-Averaging is applied to find the exact (unclosed) RA transport equations for each phase. This results in exact (unclosed) RA transport equations for each statistic in each phase. These are:

- the RA particle-phase volume fraction $\langle\alpha\rangle$;
- the PA velocities $\langle\mathbf{u}_p''\rangle_p$ and $\langle\mathbf{u}_f''\rangle_f$;
- the PA granular temperature $\langle\Theta\rangle_p$;
- the PA Reynolds stress tensors $\langle\mathbf{u}_p''\mathbf{u}_p''\rangle_p$ and $\langle\mathbf{u}_f'''\mathbf{u}_f'''\rangle_f$;
- the PA total granular energy $\langle e\rangle_p = 1/2(\langle\mathbf{u}_p\cdot\mathbf{u}_p\rangle_p + 3\langle\Theta\rangle_p)$

The PA turbulent kinetic energy for both phases are defined as:

$$k_p = \frac{1}{2}\langle\mathbf{u}_p''\cdot\mathbf{u}_p''\rangle_p \tag{A.1}$$

$$k_f = \frac{1}{2}\langle\mathbf{u}_f'''\cdot\mathbf{u}_f'''\rangle_f \tag{A.2}$$

where the fluctuations are averaged with respect to the PA mean. The PA total granular energy can be rewritten as:

$$\langle e \rangle_p = 1/2 \langle \mathbf{u}_p \rangle_p \cdot \langle \mathbf{u}_p \rangle_p + k_p + 3/2 \langle \Theta \rangle_p \tag{A.3}$$

The form of this equation is quite informative. It clearly demonstrates that total particle turbulent kinetic energy can have two contributions i.e. correlated and uncorrelated energy. The total particle turbulent kinetic energy can be defined as $\kappa_p = k_p + 3/2 \langle \Theta \rangle_p$ which means that k_p and $\langle \Theta \rangle_p$ can be solved for to find the energy - which is done in this model.

A.2 RA particle-phase equations

A.2.1 Particle-phase volume fraction

Taking the Reynolds average of Eq. 2.31 gives:

$$\frac{\partial \langle \alpha_p \rangle}{\partial t} + \nabla \cdot \langle \alpha_p \rangle \langle \mathbf{u}_p \rangle_p = 0 \tag{A.4}$$

with no unclosed terms appearing in the continuity equation.

A.2.2 Particle-phase velocity

Taking the Reynolds average of Eq. 2.32 gives:

$$\frac{\partial \langle \alpha_p \rangle \langle \mathbf{u}_p \rangle_p}{\partial t} + \nabla \cdot (\langle \alpha_p \rangle_p \langle \mathbf{u}_p \rangle_p \langle \mathbf{u}_p \rangle_p + \langle \mathbf{u}_p'' \mathbf{u}_p'' \rangle_p + \langle \mathbf{P} \rangle_p) = \langle \alpha_p \rangle (\langle \mathcal{A} \rangle_p + \mathbf{g}) \tag{A.5}$$

There are several unclosed terms, the most recognisable is the particle-phase Reynolds tress tensor $\langle \mathbf{u}_p'' \mathbf{u}_p'' \rangle_p$. This can be combined with $\langle \mathbf{P} \rangle_p$ by defining a particle-phase turbulent stress tensor $\langle \mathcal{P} \rangle_p = \langle \mathbf{P} \rangle_p + \langle \mathbf{u}_p'' \mathbf{u}_p'' \rangle_p$. Employing the definition of $\mathcal{A}$, we arrive at

$$\langle \mathcal{A} \rangle_p = \frac{1}{\tau_p}(\langle \mathbf{u}_f \rangle_p - \langle \mathbf{u}_p \rangle) - \frac{1}{\rho_p}\langle \nabla p_f \rangle_p \tag{A.6}$$

where $\langle \mathbf{u}_f \rangle_p$ and $\langle \nabla p_f \rangle_p$ are mixed averages which arise due to phase coupling. This refers to the primarily quantity being averaged with respect to the opposite phase. For the former term (which is of great importance) this is a measure of how "correlated" the particle-phase is with the fluid-phase. This is also described as the fluid-phase seen by the particle. Using the properties of the Reynolds average (see Sec. B.1) and phase average (see Sec. B.2), this can be rewritten as

$$\langle \mathcal{A} \rangle_p = \frac{1}{\tau_p}\left(\langle \mathbf{u}_f \rangle_f - \langle \mathbf{u}_p \rangle_p + \frac{\langle \alpha_p' \mathbf{u}_f''' \rangle}{\langle \alpha_p \rangle \langle \alpha_f \rangle}\right) - \frac{1}{\rho_p}\langle \nabla p_f \rangle - \frac{1}{\rho_p \langle \alpha_p \rangle}\langle \alpha_p' \nabla p_f' \rangle \tag{A.7}$$

which leads to an extra term respective to each quantity that determines how uncorrelated the statistic is. Ozel et al. [131] reports a similar term. The final form of the PA particle-phase velocity thus reads

$$\begin{aligned}\frac{\partial \langle \alpha_p \rangle \langle \mathbf{u}_p \rangle_p}{\partial t} + \nabla \cdot \langle \alpha_p \rangle (\langle \mathbf{u}_p \rangle_p \langle \mathbf{u}_p \rangle_p + \langle \mathcal{P} \rangle_p) = \frac{\langle \alpha_p \rangle}{\tau_p}\left(\langle \mathbf{u}_f \rangle_f - \langle \mathbf{u}_p \rangle_p + \frac{\langle \alpha_p' \mathbf{u}_f''' \rangle}{\langle \alpha_p \rangle \langle \alpha_f \rangle}\right) \\ - \frac{\langle \alpha_p \rangle}{\rho_p}\nabla \langle p_f \rangle - \frac{1}{\rho_p}\langle \alpha_p' \nabla p_f' \rangle + \langle \alpha_p \rangle \mathbf{g}\end{aligned} \tag{A.8}$$

A.2.3 Granular temperature

The Reynolds average of the granular temperature is

$$\begin{aligned}\frac{3}{2}\left[\frac{\partial \langle \alpha_p \rangle \langle \Theta \rangle_p}{\partial t} + \nabla \cdot \langle \alpha_p \rangle \left(\langle \Theta \rangle_p \langle \mathbf{u}_p \rangle_p + \langle \mathbf{u}_p'' \Theta \rangle_p + \frac{2}{3}\langle \mathbf{q} \rangle_p\right)\right] \\ = -\langle \alpha_p \rangle \langle \mathbf{P} \rangle_p : \nabla \langle \mathbf{u} \rangle_p - \langle \alpha_p \rangle \langle \mathbf{P} : \nabla \mathbf{u}'' \rangle_p + \frac{3\langle \alpha_p \rangle}{\tau_p}\left(\langle \Theta_f \rangle_f - \langle \Theta \rangle_p + \frac{\langle \alpha_p' \Theta_f \rangle}{\langle \alpha_p \rangle \langle \alpha_f \rangle}\right)\end{aligned} \tag{A.9}$$

In this equation, $\langle \mathbf{u}_p'' \Theta \rangle_p$ is the turbulent granular temperature flux, which is combined with the granular temperature flux $\langle \mathbf{q} \rangle_p$ to recover the total granular temperature flux. The first two terms on the right hand side are the granular source/sink terms due to the mean flow gradients. The second term is particularly important as it represents the production of the PA granular temperature due to the dissipation

of turbulent kinetic energy. It will be shown that this term with an positive sign arises in the transport equation for turbulent kinetic energy dissipation. The last term is the momentum coupling term which exchanges energy with the fluid-phase, exclusively due to drag.

A.2.4 Total granular energy

Taking the Reynolds average of Eq. 2.33

$$\frac{\partial\langle\alpha_p\rangle\langle e\rangle_p}{\partial t} + \nabla\cdot\langle\alpha_p\rangle(\langle e\rangle_p\langle\mathbf{u}_p\rangle_p + \langle\mathbf{u}_p''e\rangle_p + \langle\mathbf{P}\rangle_p\cdot\langle\mathbf{u}_p\rangle_p + \langle\mathbf{P}\cdot\mathbf{u}_p''\rangle_p + \langle\mathbf{q}\rangle_p) = \langle\alpha_p\rangle(\langle\mathcal{E}\rangle_p + \langle\mathbf{u}_p\rangle_p\cdot\mathbf{g}) \tag{A.10}$$

There are several unclosed terms, the most notable of which is the turbulent total granular energy flux: $\langle\mathbf{u}_p''e\rangle_p$. Using the properties of the phase average (Sec. B.2) this term can be rewritten as:

$$\begin{aligned}
\langle\mathbf{u}_p''e\rangle_p &= \frac{1}{2}\langle\mathbf{u}_p''(\mathbf{u}_p\cdot\mathbf{u}_p + 3\Theta)\rangle_p \\
&= \frac{1}{2}\langle\mathbf{u}_p''\mathbf{u}_p\cdot\mathbf{u}_p\rangle_p + \frac{3}{2}\langle\mathbf{u}_p''\Theta\rangle_p \\
&= \frac{1}{2}\langle\mathbf{u}_p''(\mathbf{u}_p'' + \langle\mathbf{u}_p\rangle_p)\cdot(\mathbf{u}_p'' + \langle\mathbf{u}_p\rangle_p)\rangle_p + \frac{3}{2}\langle\mathbf{u}_p''\Theta\rangle_p \\
&= \frac{1}{2}\langle\mathbf{u}_p''(\mathbf{u}_p''\cdot\mathbf{u}_p'' + 2\langle\mathbf{u}_p\rangle_p\cdot\mathbf{u}_p'' + \langle\mathbf{u}_p\rangle_p\cdot\langle\mathbf{u}_p\rangle_p)\rangle_p + \frac{3}{2}\langle\mathbf{u}_p''\Theta\rangle_p \\
&= \frac{1}{2}\langle\mathbf{u}_p''\mathbf{u}_p''\cdot\mathbf{u}_p''\rangle_p + \langle\mathbf{u}_p''\mathbf{u}_p''\rangle_p\cdot\mathbf{u}_p + \frac{3}{2}\langle\mathbf{u}_p''\Theta\rangle_p
\end{aligned} \tag{A.11}$$

where $\langle\mathbf{u}_p''\mathbf{u}_p''\cdot\mathbf{u}_p''\rangle_p$ is the particle-phase kinetic energy flux. From the definition of $\mathcal{E}$ in Eq. 2.25 we arrive at

$$\begin{aligned}
\langle\mathcal{E}\rangle_p &= \frac{1}{\tau_p}(\langle\mathbf{u}_p\cdot\mathbf{u}_f\rangle_p - \langle\mathbf{u}_p\cdot\mathbf{u}_p\rangle_p) + \frac{3}{\tau_p}(\langle\Theta_f\rangle_p - \langle\Theta\rangle_p) - \frac{1}{\rho_p}\langle\mathbf{u}_p\cdot\nabla p_f\rangle_p \\
&= \frac{1}{\tau_p}(\langle\mathbf{u}_p\rangle_p\cdot\langle\mathbf{u}_f\rangle_p - \langle\mathbf{u}_p\rangle_p\cdot\langle\mathbf{u}_p\rangle_p + \langle\mathbf{u}_p''\rangle_p\cdot\langle\mathbf{u}_f''\rangle_p - 2k_p) \\
&+\frac{3}{\tau_p}\left(\langle\Theta_f\rangle_f - \langle\Theta\rangle_p + \frac{\langle\alpha_p'\Theta_f\rangle}{\langle\alpha_f\rangle\langle\alpha_f\rangle}\right) - \frac{1}{\rho_p}\langle\mathbf{u}_p\rangle_p\cdot\langle\nabla p_f\rangle_p - \frac{1}{\rho_p}\langle\mathbf{u}_p''\cdot\nabla p_f\rangle_p
\end{aligned} \tag{A.12}$$

There are several mixed averages in $\langle\mathcal{E}\rangle_p$. Using the definitions of the Reynolds average (Sec B.1) and the phase average (Sec. B.2) it can be rewritten as:

$$\langle \mathcal{E} \rangle_p = \langle \mathcal{A} \rangle_p \cdot \langle \mathbf{u}_p \rangle_p + \frac{1}{\tau_p}(\langle \mathbf{u}_p'' \cdot \mathbf{u}_f'' \rangle_p - 2k_p) + \frac{3}{\tau_p}\left(\langle \Theta_f \rangle_f - \langle \Theta \rangle_p + \frac{\langle \alpha_p' \Theta_f \rangle}{\langle \alpha_p \rangle \langle \alpha_f \rangle} \right) - \frac{1}{\rho_p} \langle \mathbf{u}_p'' \cdot \nabla p_f' \rangle_p \tag{A.13}$$

Combining the particle-phase Reynolds stress tensor and $\langle \mathbf{P} \rangle_p$, the final form for the PA total granular energy is

$$\begin{aligned} &\frac{\partial \langle \alpha_p \rangle \langle e \rangle_p}{\partial t} \\ &+ \nabla \cdot \langle \alpha_p \rangle \left(\langle e \rangle_p \langle \mathbf{u}_p \rangle_p + \frac{1}{2} \langle \mathbf{u}_p'' \mathbf{u}_p'' \cdot \mathbf{u}_p'' \rangle_p + \frac{3}{2} \langle \mathbf{u}_p'' \Theta \rangle_p + \langle \mathcal{P} \rangle_p \cdot \langle \mathbf{u}_p \rangle_p + \langle \mathbf{P} \cdot \mathbf{u}_p'' \rangle_p + \langle \mathbf{q} \rangle_p \right) \\ &= \langle \alpha_p \rangle \langle \mathcal{A} \rangle_p \cdot \langle \mathbf{u}_p \rangle_p + \frac{\langle \alpha_p \rangle}{\tau_p}(\langle \mathbf{u}_p'' \cdot \mathbf{u}_f''' \rangle_p - 2k_p) + \frac{3\langle \alpha_p \rangle}{\tau_p}\left(\langle \Theta_f \rangle_f - \langle \Theta \rangle_p + \frac{\langle \alpha_p' \Theta_f \rangle}{\langle \alpha_p \rangle \langle \alpha_f \rangle} \right) \\ &- \frac{\langle \alpha_p \rangle}{\rho_p} \langle \mathbf{u}_p'' \cdot \nabla p_f' \rangle_p + \langle \alpha_p \rangle \langle \mathbf{u}_p \rangle_p \cdot \mathbf{g} \end{aligned} \tag{A.14}$$

On the RHS of this equation there are three contributions due to drag: exchange of mean kinetic energy, turbulent kinetic energy and granular energy.

A.2.5 Particle-phase mean kinetic energy

The particle-phase mean kinetic energy is defined as:

$$K_p = \frac{1}{2} \langle \mathbf{u}_p \rangle_p \cdot \langle \mathbf{u}_p \rangle_p \tag{A.15}$$

In order to derive the transport equation for k_p one needs the mean kinetic energy owing to the definition of the Reynolds average. Clearly, these quantities do not need their own transport equation as the particle-phase velocities are already solved. Nevertheless, starting from Eq. A.5 an equation can be written as:

$$\frac{\partial \langle \alpha_p \rangle K_p}{\partial t} + \nabla \cdot \langle \alpha_p \rangle (K_p \langle \mathbf{u}_p \rangle_p + \langle \mathcal{P} \rangle_p \cdot \langle \mathbf{u}_p \rangle_p) = \langle \alpha_p \rangle [\langle \mathcal{P} \rangle_p : \nabla \langle \mathbf{u}_p \rangle_p + \langle \mathbf{u}_p \rangle_p \cdot (\langle \mathcal{A} \rangle_p + \mathbf{g})] \tag{A.16}$$

The first term on the right hand side represent energy transfer from the mean kinetic energy to the particle-phase fluctuation energy. This is inclusive of the

turbulent kinetic energy and the mean granular temperature. From here a transport equation for the particle-phase fluctuation energy can be found.

A.2.6 Particle-phase fluctuation energy

We can define the particle-phase fluctuation energy as

$$\kappa_p = k_p + \frac{3}{2}\langle\Theta\rangle_p \tag{A.17}$$

such that $\langle e\rangle_p = K_p + \kappa_p$. The transport equation for κ_p is then found by subtracting Eq. A.16 from Eq. A.14.

$$\begin{aligned}\frac{\partial\langle\alpha_p\rangle\kappa_p}{\partial t} + \nabla\cdot\langle\alpha_p\rangle\Big(\kappa_p\langle\mathbf{u}_p\rangle_p + \frac{1}{2}\langle\mathbf{u}_p''\mathbf{u}_p''\cdot\mathbf{u}_p''\rangle_p + \frac{3}{2}\langle\mathbf{u}_p''\Theta\rangle_p + \langle\mathcal{P}\rangle_p + \langle\mathbf{q}\rangle_p\Big) \\ = -\langle\alpha_p\rangle\langle\langle\mathcal{P}\rangle_p : \nabla\langle\mathbf{u}_p\rangle_p + \frac{\langle\alpha_p\rangle}{\tau_p}(\langle\mathbf{u}_p''\cdot\mathbf{u}_f'''\rangle_p - 2k_p) \\ + \frac{3\langle\alpha_p\rangle}{\tau_p}\Big(\langle\Theta_f\rangle_f - \langle\Theta\rangle_p + \frac{\langle\alpha_p'\Theta_f\rangle}{\langle\alpha_p\rangle\langle\alpha_f\rangle}\Big) - \frac{\langle\alpha_p\rangle}{\rho_p}\langle\mathbf{u}_p''\cdot\nabla p_f'\rangle_p\end{aligned} \tag{A.18}$$

The first term on the right hand side is the production due to mean flow gradients. The remaining terms are a result of inter-phase coupling. These fluctuation energy exchange terms are only governed by drag and buoyancy and thus the overall energy in the system does not contain any viscous dissipation. This means that the overall fluctuation energy can only be reduced through exchanges with the fluid-phase.

A.2.7 Particle-phase turbulent kinetic energy

The transport equation for the particle-phase turbulent kinetic energy k_p can be found by subtracting Eq. A.9 from Eq. A.17.

$$\begin{aligned}\frac{\partial\langle\alpha_p\rangle k_p}{\partial t} + \nabla\cdot\langle\alpha_p\rangle\Big(k_p\langle\mathbf{u}_p\rangle_p + \frac{1}{2}\langle\mathbf{u}_p''\mathbf{u}_p''\cdot\mathbf{u}_p''\rangle_p + \langle\mathbf{P}\cdot\mathbf{u}_p''\rangle_p\Big) \\ = -\langle\alpha_p\rangle\langle\langle\mathbf{u}_p''\mathbf{u}_p''\rangle_p : \nabla\langle\mathbf{u}_p\rangle_p + \langle\alpha_p\rangle\langle\mathbf{P}:\nabla\mathbf{u}_p''\rangle_p \\ + \frac{\langle\alpha_p\rangle}{\tau_p}(\langle\mathbf{u}_p''\cdot\mathbf{u}_f'''\rangle_p - 2k_p) - \frac{\langle\alpha_p\rangle}{\rho_p}\langle\mathbf{u}_p''\cdot\nabla p_f'\rangle_p\end{aligned} \tag{A.19}$$

The first term on the RHS is the production term due to particle phase Reynolds stresses and the particle phase mean velocity gradients. The second term contains the turbulent kinetic energy dissipation rate ε_p. As noted this appears as a production term in the PA granular temperature (see Eq. A.9). Therefore, it is clear to see that as energy is produced in the large scale turbulent kinetic energy it dissipates until it cascades down to the PA granular temperature. The final two terms are the covariance coupling with the fluid phase through drag and buoyancy respectively.

A.2.8 Particle-phase mean velocity tensor product

Starting from Eq. A.5 and invoking $\langle \mathcal{P} \rangle_p = \langle \mathbf{P} \rangle_p + \langle \mathbf{u}_p'' \mathbf{u}_p'' \rangle_p$ a transport equation for the particle-phase mean velocity tensor product is given by

$$\begin{aligned} \frac{\partial \langle \alpha_p \rangle \langle \mathbf{u}_p \rangle_p \otimes \langle \mathbf{u}_p \rangle_p}{\partial t} + \nabla \cdot \langle \alpha_p \rangle [\langle \mathbf{u}_p \rangle_p \otimes \langle \mathbf{u}_p \rangle_p \otimes \langle \mathbf{u}_p \rangle_p + (\langle \mathcal{P} \rangle_p \otimes \langle \mathbf{u}_p \rangle_p)] \\ = \langle \alpha_p \rangle [\langle \mathcal{P} \rangle_p \cdot \nabla \langle \mathbf{u}_p \rangle_p + \langle \mathbf{u}_p \rangle_p \otimes (\langle \mathcal{A} \rangle_p + \mathbf{g})] \end{aligned} \tag{A.20}$$

As ultimately we want to derive an equation for the Reynolds stress tensor we now present the transport equation for the particle-phase velocity tensor product. Note this is prior to averaging, as invoking the decomposition, to find the Reynolds stress tensor. Beginning at Eq. 2.32 we can multiply through by the cross product of the particle phase velocity.

$$\frac{\partial (\alpha_p \mathbf{u}_p \otimes \mathbf{u}_p)}{\partial t} + \nabla \cdot (\alpha_p \mathbf{u}_p \otimes \mathbf{u}_p \otimes \mathbf{u}_p) + [\mathbf{u}_p \otimes \nabla \cdot (\alpha_p \mathbf{P})] = \alpha_p [\mathbf{u}_p \otimes (\mathcal{A} + \mathbf{g})] \tag{A.21}$$

A.2.9 Particle-phase Reynolds stress tensor

The transport equation is found by subtracting Eq. A.20 from the RA of Eq. A.21 resulting in

$$\frac{\partial\langle\alpha_p\rangle\langle\mathbf{u}_p''\otimes\mathbf{u}_p''\rangle_p}{\partial t}+\nabla\cdot\langle\alpha_p\rangle(\langle\mathbf{u}_p\rangle_p\otimes\langle\mathbf{u}_p''\otimes\mathbf{u}_p''\rangle_p+\langle\mathbf{u}_p''\otimes\mathbf{u}_p''\otimes\mathbf{u}_p''\rangle_p+\langle\mathbf{P}\otimes\mathbf{u}_p''\rangle_p)$$
$$=-\langle\alpha_p\rangle(\langle\mathbf{u}_p''\otimes\mathbf{u}_p''\rangle_p\cdot\nabla\langle\mathbf{u}_p\rangle_p)+\langle\alpha_p\rangle\langle\mathbf{P}\cdot\nabla\mathbf{u}_p''\rangle$$
$$+\langle\alpha_p\rangle\beta(\langle\mathbf{u}_f'''\otimes\mathbf{u}_p''\rangle_p-\langle\mathbf{u}_p''\otimes\mathbf{u}_p''\rangle_p) \tag{A.22}$$

where the first term on the second line represents the production due to the particle-phase Reynolds stress and the mean flow gradients. The second term is responsible for redistribution and dissipation of the Reynolds stresses. Then finally terms are the energy exchange processes through drag.

A.3 RA fluid-phase equations

A.3.1 Fluid-phase volume fraction

Taking the Reynolds average of Eq. 2.34 gives:

$$\frac{\partial\langle\alpha_f\rangle}{\partial t}+\nabla\cdot\langle\alpha_f\rangle\langle\mathbf{u}_f\rangle_f=0 \tag{A.23}$$

with no unclosed terms appearing in the continuity equation.

A.3.2 Fluid-phase velocity

Taking the Reynolds average of Eq. 2.35 gives:

$$\begin{aligned}&\frac{\partial\langle\alpha_f\rangle\langle\mathbf{u}_f\rangle_f}{\partial t}+\nabla\cdot\left(\langle\alpha_f\rangle\langle\mathbf{u}_f\rangle_f\langle\mathbf{u}_f\rangle_f+\langle\alpha_f\rangle\langle\mathbf{u}_f''\mathbf{u}_f''\rangle_f+\frac{1}{\rho_f}\langle\sigma_f\rangle\right)+\frac{1}{\rho_f}\nabla\langle p_f\rangle\\&=\frac{\rho_p\langle\alpha_p\rangle}{\rho_f\tau_p}\left(\langle\mathbf{u}_p\rangle_p-\langle\mathbf{u}_f\rangle_f-\frac{\langle\alpha'\mathbf{u}_f'\rangle}{\langle\alpha\rangle\langle\alpha_f\rangle}\right)+\frac{\langle\alpha\rangle}{\rho_f}\nabla\langle p_f\rangle+\frac{1}{\rho_f}\langle\alpha'\nabla p_f'\rangle+\langle\alpha_f\rangle\mathbf{g}\end{aligned} \tag{A.24}$$

New unclosed terms are $\langle\alpha_f\rangle\langle\mathbf{u}_f''\mathbf{u}_f''\rangle_f$ the fluid-phase Reynolds stress tensor and $\langle\sigma_f\rangle$ which is the RA fluid-phase viscous stress tensor. Using the definition of the fluid-phase viscous tensor the RA fluid-phase viscous tensor can be written as

$$\langle\sigma_f\rangle=\rho_f\left\langle(\nu_f+\nu_f^*)\left(\nabla\mathbf{u}_f+(\nabla\mathbf{u}_f)^t-\frac{2}{3}\nabla\cdot\mathbf{u}_f\mathbf{I}\right)\right\rangle \tag{A.25}$$

A.3.3 Fluid-phase turbulent kinetic energy

The transport equation for the fluid-phase turbulent kinetic energy has a similiar form to that of the particle phase. It reads:

$$\begin{aligned}\frac{\partial\langle\alpha_f\rangle k_f}{\partial t}+\nabla\cdot\Big[\langle\alpha_f\rangle k_f\langle\mathbf{u}_f\rangle_f+\langle\alpha_f\rangle\frac{1}{2}\langle\mathbf{u}_f'''\mathbf{u}_f'''\cdot\mathbf{u}_f'''\rangle_f+\frac{1}{\rho_f}(\langle p_f\mathbf{u}_f'''\rangle-\langle\sigma_f\cdot\mathbf{u}_f'''\rangle)\Big]\\ =-\langle\alpha_f\rangle\langle\langle\mathbf{u}_f'''\mathbf{u}_f'''\rangle_f:\nabla\langle\mathbf{u}_f\rangle_f+\frac{1}{\rho_f}\Big(\langle p_f\nabla\cdot\mathbf{u}_f'''\rangle-\langle\sigma_f:\nabla\mathbf{u}_f'''\rangle\Big)\\ +\frac{\rho_p\langle\alpha_p\rangle}{\rho_f\tau_p}\Big[\langle\mathbf{u}_f'''\cdot\mathbf{u}_p''\rangle_p-\langle\mathbf{u}_f'''\cdot\mathbf{u}_f'''\rangle_p+\langle\mathbf{u}_f'''\rangle_p\cdot(\langle\mathbf{u}_p\rangle-\langle\mathbf{u}_f'''\rangle_f\Big]\\ +\frac{\langle\alpha_p\rangle}{\rho_f}\langle\mathbf{u}_f'''\rangle_p\cdot\nabla\langle p_f\rangle+\frac{\langle\alpha_p\rangle}{\rho_f}\langle\mathbf{u}_f'''\cdot\nabla p_f'\rangle_p\end{aligned} \tag{A.26}$$

The terms in the first two lines are common to compressible turbulent flows and can be modelled in a similar manner [163, 212]. The terms in the last two lines involve coupling with the particle phase that are all nearly unclosed because they involve mixed averages. The coupling terms in the fluid phase are rather cumbersome due to their coupling through α_p' - this physically means that the particles exhibit preferential segregation.

A useful identity can be employed to re-express the particles-phase averages as fluid-phase averages plus a term involving a correlation with the volume fraction fluctuations. E.g.

$$\langle\mathbf{u}_f\rangle_p=\langle\mathbf{u}_f\rangle_f+\frac{\langle\alpha_p'\mathbf{u}_f'''\rangle}{\langle\alpha_p\rangle\langle\alpha_f\rangle} \tag{A.27}$$

$$\langle\mathbf{u}_f'''\rangle_p=\frac{\langle\alpha_p'\mathbf{u}_f'''\rangle}{\langle\alpha_p\rangle\langle\alpha_f\rangle} \tag{A.28}$$

$$\langle\mathbf{u}_f'''\cdot\mathbf{u}_p'''\rangle_p=2k_f+\frac{\langle\alpha_p'\mathbf{u}_f'''\cdot\mathbf{u}_f'''\rangle}{\langle\alpha_p\rangle\langle\alpha_f\rangle} \tag{A.29}$$

and

$$\langle\mathbf{u}_f'''\cdot\nabla p_f'\rangle_p=\langle\mathbf{u}_f'''\cdot\nabla p_f'\rangle_f+\frac{1}{\langle\alpha_p\rangle\langle\alpha_f\rangle}\langle\alpha_p'\mathbf{u}_f'''\cdot\nabla p_f'\rangle \tag{A.30}$$

The terms $\langle \alpha_p' \mathbf{u}_f''' \rangle$ and $\langle \alpha_p' \mathbf{u}_f''' \cdot \nabla p_f' \rangle$ require additional modelling and will be discussed later on.

Using these results one arrives at the exact (unclosed) transport equations

$$\begin{aligned}
\frac{\partial \langle \alpha_f \rangle k_f}{\partial t} + \nabla \cdot \Big[\langle \alpha_f \rangle k_f \langle \mathbf{u}_f \rangle_f + \langle \alpha_f \rangle \frac{1}{2} \langle \mathbf{u}_f''' \mathbf{u}_f''' \cdot \mathbf{u}_f''' \rangle_f + \frac{1}{\rho_f} (\langle p_f \mathbf{u}_f''' \rangle - \langle \sigma_f \cdot \mathbf{u}_f''' \rangle) \Big] \\
= -\langle \alpha_f \rangle \langle \langle \mathbf{u}_f''' \mathbf{u}_f''' \rangle_f : \nabla \langle \mathbf{u}_f \rangle_f + \frac{1}{\rho_f} \Big(\langle p_f \nabla \cdot \mathbf{u}_f''' \rangle - \langle \sigma_f : \nabla \mathbf{u}_f''' \rangle \Big) \\
+ \frac{\rho_p \langle \alpha_p \rangle}{\rho_f \tau_p} \Big[\langle \mathbf{u}_f''' \cdot \mathbf{u}_p'' \rangle_p - 2k_f + \frac{\langle \alpha_p' \mathbf{u}_f''' \rangle}{\langle \alpha_p \rangle \langle \alpha_f \rangle} \cdot (\langle \mathbf{u}_p \rangle_p - \langle \mathbf{u}_f \rangle_f) - \frac{\langle \alpha_p' \mathbf{u}_f''' \cdot \mathbf{u}_f''' \rangle}{\langle \alpha_p \rangle \langle \alpha_f \rangle} \Big] \\
+ \frac{1}{\rho_f \langle \alpha_f \rangle} \langle \alpha_p' \mathbf{u}_f''' \rangle_p \cdot \nabla \langle p_f \rangle + \frac{\langle \alpha \rangle}{\rho_f} \Big(\langle \mathbf{u}_f''' \cdot \nabla p_f' \rangle_f + \frac{1}{\langle \alpha_p \rangle \langle \alpha_f \rangle} \langle \alpha_p' \mathbf{u}_f''' \cdot \nabla p_f' \rangle \Big)
\end{aligned} \tag{A.31}$$

It is interesting to note that the coupling terms in the fluid-phase are asymmetric with respect to those in the particle phase. This asymmetry enables alternative turbulence generation mechanisms. One example is homogeneous gravity-driven fluid-particle flows which exhibit volume fraction and velocity fluctuations with turbulent like characteristics [3, 28].

A.3.4 Fluid-phase Reynolds stress tensor

An identical approach to how the transport equation was derived for the particle-phase is followed. This results in

$$\begin{aligned}
\frac{\partial \langle \alpha_f \rangle \langle \mathbf{u}_f''' \otimes \mathbf{u}_f''' \rangle_f}{\partial t} + \nabla \cdot \langle \alpha_f \rangle (\langle \mathbf{u}_f \rangle_f \otimes \langle \mathbf{u}_f''' \otimes \mathbf{u}_f''' \rangle_f + \langle \mathbf{u}_f''' \otimes \mathbf{u}_f''' \otimes \mathbf{u}_f''' \rangle_f) \\
= -\langle \alpha_f \rangle (\langle \mathbf{u}_f''' \otimes \mathbf{u}_f''' \rangle_f \cdot \nabla \langle \mathbf{u}_f \rangle_f) + \frac{1}{\rho_f} \nabla \cdot \langle \overline{\boldsymbol{\sigma}}_f \otimes \mathbf{u}_f''' \rangle - \frac{1}{\rho_f} \nabla \langle p_f \mathbf{u}_f''' \rangle \\
+ \frac{1}{\rho_f} \langle p_f \nabla \mathbf{u}_f''' \rangle - \frac{1}{\rho_f} \langle \overline{\boldsymbol{\sigma}}_f \cdot \nabla \mathbf{u}_f''' \rangle + \langle \alpha_f \rangle \beta (\langle \mathbf{u}_f''' \otimes \mathbf{u}_p'' \rangle_p - \langle \mathbf{u}_f''' \otimes \mathbf{u}_f''' \rangle_p)
\end{aligned} \tag{A.32}$$

where the first term on the second line represents the production due to the fluid-phase Reynolds stress and the mean flow gradients. The second term comprises the first part of the fluid pressure and dissipative forces. The first two represent the flux with the first two terms on the next line representing the source term. They

are responsible for redistribution and dissipation of the Reynolds stresses. Then finally terms are the energy exchange processes through drag.

A.4 Closure of fluid-phase turbulence terms

As the fluid-phase behaves like a (weakly) compressible gas the closure models are adopted from turbulence models used for variable-density turbulence Pope [142], Wilcox [212].

A.4.1 Fluid-velocity flux

In the fluid-phase velocity Eq. A.24, the unclosed flux terms are

$$\langle \mathbf{u}_f''' \mathbf{u}_f''' \rangle_f - \frac{1}{\rho_f \langle \alpha_f \rangle} \langle \sigma_f \rangle \tag{A.33}$$

the unclosed term $\langle \sigma_f \rangle$ can be written in the form found in A.25. Using a turbulent-viscosity model to close the fluid-phase stress tensor yields

$$\begin{aligned} &\langle \mathbf{u}_f''' \mathbf{u}_f''' \rangle_f - \frac{1}{\rho_f \langle \alpha_f \rangle} \langle \sigma_f \rangle \\ &= -\frac{2}{\langle \alpha_f \rangle} (\nu_f + \langle \nu_f^* \rangle + \langle \alpha_f \rangle \nu_{ft}) \Big(\overline{\mathbf{S}}_f - \frac{1}{3} \nabla \cdot \langle \mathbf{u}_f \rangle_f \mathbf{I} \Big) + \frac{2}{3} k_f \mathbf{I} \end{aligned} \tag{A.34}$$

where

$$\overline{\mathbf{S}}_f = \frac{1}{2} [\nabla \langle \mathbf{u}_f \rangle_f + (\nabla \langle \mathbf{u}_f \rangle_f)^T] \tag{A.35}$$

where the turbulent viscosity is defined by

$$\nu_{ft} = C_{f\mu} \frac{k_f^2}{\varepsilon_f} \tag{A.36}$$

The pseudo-turbulent kinematic viscosity, which is due to particle wakes, can be modelled as

$$\langle \nu_f^* \rangle = c_\mu d_p \Big(\phi f(Re_p) [\frac{1}{3} (\langle \mathbf{u}_p \rangle_p - \langle \mathbf{u}_f \rangle_f)^2 + \langle \Theta \rangle_p] \Big)^{1/2} \tag{A.37}$$

In this work this effect is neglected as the particle Reynolds number is below 10. As the reader will not the closure adopted here is relatively simple. A plethora of more advanced models are available in the literature which can account for the anistropic nature of the Reynolds stresses [108, 159].

A.4.2 Fluid-phase turbulent kinetic energy flux

Consistent with the velocity flux, the turbulent flux term in Eq. A.31

$$\frac{1}{2}\langle \mathbf{u}_f'''\mathbf{u}_f''' \cdot \mathbf{u}_f'''\rangle_f + \frac{1}{\rho_f\langle\alpha_f\rangle}(\langle p_f\mathbf{u}_f'''\rangle - \langle\sigma_f \cdot \mathbf{u}_f'''\rangle) \tag{A.38}$$

using the classic gradient-diffusion hypothesis

$$\frac{1}{2}\langle \mathbf{u}_f'''\mathbf{u}_f''' \cdot \mathbf{u}_f'''\rangle_f + \frac{1}{\rho_f\langle\alpha_f\rangle}(\langle p_f\mathbf{u}_f'''\rangle - \langle\sigma_f \cdot \mathbf{u}_f'''\rangle) = -\left(\frac{\nu_f + \langle\nu_f^*\rangle}{\langle\alpha_f\rangle} + \frac{\nu_{ft}}{\sigma_{fk}}\right)\nabla k_f \tag{A.39}$$

where $\sigma_{fk} = 5/3$ is a model constant Rumsey [163], Wilcox [212].

A.4.3 Fluid-phase kinetic energy production

The fluid-phase kinetic energy production terms are

$$-\langle \mathbf{u}_f'''\mathbf{u}_f'''\rangle_f : \nabla\langle\mathbf{u}_f\rangle_f + \frac{1}{\rho_f\langle\alpha_f\rangle}\langle p_f\nabla\cdot\mathbf{u}_f'''\rangle \tag{A.40}$$

where the first contribution is due to mean shear and the second is due to the correlation between pressure fluctuations and the dilation of the fluctuating fluid velocity. The mean-shear contribution is closed:

$$\begin{aligned} -\langle \mathbf{u}_f'''\mathbf{u}_f'''\rangle_f : \nabla\langle\mathbf{u}_f\rangle_f &= 2\nu_{ft}\left(\mathbf{S}_f - \frac{1}{3}\nabla\cdot\langle\mathbf{u}_f\rangle_f\mathbf{I}\right) : \nabla\langle\mathbf{u}_f\rangle_f - \frac{2}{3}k_f\nabla\cdot\langle\mathbf{u}_f\rangle_f \\ &= 2\nu_{ft}\overline{\mathbf{S}}_f : \overline{\mathbf{S}}_f - \frac{2}{3}k_f\nabla\langle\mathbf{u}_f\rangle_f \end{aligned} \tag{A.41}$$

where $\overline{\mathbf{S}}_f$ is the traceless part of $\mathbf{S}_f$:

$$\overline{\mathbf{S}}_f = \mathbf{S}_f - \frac{1}{3}\nabla\cdot\langle\mathbf{u}_f\rangle_f\mathbf{I} \tag{A.42}$$

The pressure-dilation term depends on the fluid-phase Mach number and is usually neglected in the fluid-phase kinetic energy equation Rumsey [163].

A.4.4 Fluid-phase turbulent kinetic energy dissipation

$$\begin{aligned}\frac{1}{\rho_f\langle\alpha_f\rangle}\langle\sigma_f : \nabla\mathbf{u}_f'''\rangle &= \frac{1}{\langle\alpha_f\rangle}\Big\langle(\nu_f+\nu_f^*)\Big[\nabla\mathbf{u}_f+(\mathbf{u}_f)^T-\frac{2}{3}\nabla\cdot\mathbf{u}_f\mathbf{I}\Big] : \nabla\mathbf{u}_f'''\Big\rangle \\ &\approx (\nu_f+\langle\nu_f^*\rangle)\Big\langle\Big[\nabla\mathbf{u}_f+(\mathbf{u}_f)^T-\frac{2}{3}\nabla\cdot\mathbf{u}_f\mathbf{I}\Big] : \nabla\mathbf{u}_f'''\Big\rangle_f\end{aligned} \tag{A.43}$$

where the second form comes from neglecting the correlations in $\nu * f_f$ and α_p' at small scales. By introducing the fluctuating vorticity vector ω_f''' which is defined as $\omega_{fi}''' = \varepsilon_{ijk}\omega_{jjk}'''$ where ε_{ijk} is the Levi-Civita tensor and

$$\omega_{jjk}''' = \frac{1}{2}\Big(\frac{\partial u_{fi}'''}{\partial x_j}-\frac{\partial u_{fj}'''}{\partial x_i}\Big) \tag{A.44}$$

this term can then be rewritten as Canuto [26]

$$\begin{aligned}\frac{1}{\rho_f\langle\alpha_f\rangle}\langle\sigma_f : \nabla\mathbf{u}_f'''\rangle &= (\nu_f+\nu_f^*)\Big(\langle\omega_f'''\cdot\omega_f'''\rangle_f+\frac{4}{3}\langle(\nabla\cdot\mathbf{u}_f''')^2\rangle_f\Big) \\ &+2(\nu_f+\langle\nu_f^*\rangle)\nabla\cdot(\nabla\cdot\langle\mathbf{u}_f'''\mathbf{u}_f'''\rangle_f-2\langle\mathbf{u}_f'''\nabla\cdot\mathbf{u}_f'''\rangle_f)\end{aligned} \tag{A.45}$$

where the inhomogeneous term, second term on the RHS, is assumed negligible relative to the first term. The latter is decomposed into two parts:

- solenoidal turbulent dissipation rate, $\varepsilon_{fs} = (\nu_f+\langle\nu_f^*\rangle)\langle\omega_f'''\cdot\omega_f'''\rangle_f$;
- dilatational turbulent dissipation rate, $\varepsilon_{fd} = (\nu_f+\langle\nu_f^*\rangle)\frac{4}{3}\langle(\nabla\cdot\mathbf{u}_f''')^2\rangle_f$

However, as the turbulent dissipation rate is modelled using scaling arguments, in the turbulence model methodology used in this work, both terms are not treated separately i.e. the turbulent dissipation rate will dissipate at a singular rate Pope [142]. Thus the fluid-phase kinetic energy dissipation can be closed as:

$$\frac{1}{\rho_f\langle\alpha_f\rangle}\langle\sigma_f : \nabla\mathbf{u}_f'''\rangle = \varepsilon_f \tag{A.46}$$

where ε_f is the fluid-phase turbulent dissipation rate.

A.5 Closure of particle-phase turbulence terms

As the particle-phase behaves like a compressible gas the closure models are adopted from turbulence models used for compressible turbulence [163, 212]. At the macroscale level i.e. two-equation turbulence model level, the closures are very similar to the fluid phase.

A.5.1 Particle-phase velocity flux

In the particle-phase velocity equation (Eq. A.5) the velocity flux is $\langle P \rangle_p = \langle \mathbf{u}_p'' \mathbf{u}_p'' \rangle_p + \langle \overline{\mathbf{P}}_p \rangle_p$. The particle-phase Reynolds stress tensor can be modelled as

$$\langle \mathbf{u}_p'' \mathbf{u}_p'' \rangle_p = -2\nu_{pt}(\mathbf{S}_p - \frac{1}{3}\nabla \cdot \langle \mathbf{u}_p \rangle_p \mathbf{I}) + \frac{2}{3}k_p \mathbf{I} \tag{A.47}$$

where

$$\mathbf{S}_f = \frac{1}{2}[\nabla \langle \mathbf{u}_p \rangle_p + (\nabla \langle \mathbf{u}_p \rangle_p)^T] \tag{A.48}$$

where the turbulent viscosity is defined by

$$\nu_{pt} = C_{p\mu} \frac{k_p^2}{\varepsilon_p} \tag{A.49}$$

The granular contribution the velocity flux is defined by

$$\overline{\mathbf{P}}_p = \frac{1}{\rho_p \alpha}(p_p \mathbf{I} - \sigma_p) \tag{A.50}$$

where the particle-pressure can be found from Jenkins and Savage [94]

$$p_p = \rho_p \alpha_p \Theta + 2(1+e)\rho_p \alpha_p^2 g_0 \Theta \tag{A.51}$$

the first term on the right hand side is the kinetic contribution and the second term is a collisional contribution. In the hydrodynamic limit, the particle-phase viscous stress tensor is defined by

$$\overline{\sigma}_p = \mu_p[\nabla \mathbf{u} + (\nabla \mathbf{u})^T] - \frac{1}{3}\mu_p \nabla \cdot \mathbf{u}\mathbf{I} \tag{A.52}$$

with the particle-phase viscosity

$$\mu_p = \alpha_p \rho_p \nu_p = \frac{2\mu_{p_{dil}}}{(1+e)g_0}\left[1 + \frac{4}{5}(1+e)g_0\alpha_p\right]^2 + \frac{4}{5}\alpha_p^2 \rho_p d_p g_0 (1+e)\left(\frac{\Theta}{\pi}\right)^{1/2} \tag{A.53}$$

and

$$\mu_{p_{dil}} = \frac{5\sqrt{\pi}}{96}\rho_p d_p \Theta^{1/2} \tag{A.54}$$

The terms involving the radial distribution function, g_0 represent particle collisions. Meaning that this term is near unity for dilute flow and very large for high collisional flow. The viscosity given by the granular contribution is characterised by the velocity, $\Theta^{1/2}$, this is due to granular contributions representing a particle-particle collision, and is not $k_p^{1/2}$ as these contributions do not arise due to particle-phase turbulence.

It is instructive to note then that in the particle-phase momentum equation there exists separate contributions from the mesoscale granular contribution i.e. granular pressure and viscosity, and the macroscale turbulence contribution i.e. Reynolds stress.

A.5.2 Granular temperature flux

The PA granular temperature flux is $\langle \mathbf{u}_p'' \Theta \rangle_p + 2/3 \langle \mathbf{q} \rangle_p$ where the first term is the turbulent granular-temperature flux and the second is the granular-temperature flux. The turbulent flux is closed using a gradient-diffusion model Pope [142]:

$$\langle \mathbf{u}_p'' \Theta \rangle_p = -\frac{\nu_{pt}}{Pr_{pt}} \nabla \langle \Theta \rangle_p \tag{A.55}$$

where Pr_{pt} is the turbulent Prandtl number. The granular contribution is closed in a similar manner:

$$\langle \mathbf{q} \rangle_p = -\frac{k_\Theta(\langle \alpha_p \rangle, \langle \Theta \rangle_p)}{\rho_p \langle \alpha_p \rangle} \nabla \langle \Theta \rangle_p \tag{A.56}$$

where k_Θ is the granular conductivity and is a function of both particle volume fraction and granular temperature. An expression for which can be found for with the KT of granular flow Jenkins and Savage [94] and is expressed as:

$$\kappa_\Theta = \frac{2}{(1+e)g_0}\left[1 + \frac{6}{5}(1+e)g_0\alpha_p\right]^2 \kappa_{\Theta,dil} + 2\alpha_p^2 \rho_p d_p g_0 (1+e)\left(\frac{\Theta}{\pi}\right)^{\frac{1}{2}} \tag{A.57}$$

and

$$\kappa_{\Theta,dil} = \frac{75}{384}\sqrt{\pi}\rho_p d_p \Theta^{1/2} \tag{A.58}$$

A.5.3 Particle-phase turbulent kinetic energy flux

The particle-phase turbulent kinetic energy flux is modelled as

$$\frac{1}{2}\langle \mathbf{u}_p'' \mathbf{u}_p'' \cdot \mathbf{u}_p'' \rangle_p + \langle \overline{\mathbf{P}}_p \cdot \mathbf{u}_p'' \rangle_p = -\left(\nu_p + \frac{\nu_{pt}}{\sigma_{pk}}\right)\nabla k_p \tag{A.59}$$

where $\sigma_{pk} = 5/3$ is a model constant Rumsey [163] and

$$\nu_p = \frac{(\langle \alpha_p \rangle, \langle \Theta \rangle_p)}{\rho_p \langle \alpha_p \rangle} \tag{A.60}$$

is the particle-phase kinematic viscosity.

A.5.4 Particle-phase kinetic energy production due to mean shear

The particle-phase kinetic energy production term due to mean shear is $-\langle \mathbf{u}_p'' \mathbf{u}_p'' \rangle_p : \nabla \langle \mathbf{u}_p \rangle_p$. This term is closed as

$$-\langle \mathbf{u}_p'' \mathbf{u}_p'' \rangle_p : \nabla \langle \mathbf{u}_p \rangle_p = 2\nu_{pt} \overline{\mathbf{S}}_p : \overline{\mathbf{S}}_p - \frac{2}{3} k_p \nabla \cdot \langle \mathbf{u}_p \rangle_p \tag{A.61}$$

where $\overline{\mathbf{S}}_p$ is traceless part of $\mathbf{S}_p$:

$$\overline{\mathbf{S}}_p = \mathbf{S}_p - \frac{1}{3}\nabla \cdot \langle \mathbf{u}_p \rangle_p \mathbf{I} \tag{A.62}$$

A.5.5 Particle-phase turbulent kinetic energy dissipation

The particle-phase turbulent kinetic energy dissipation results from

$$\langle \overline{\mathbf{P}}_p : \nabla \mathbf{u}_p'' \rangle_p = \frac{1}{\rho_p \langle \alpha \rangle} \langle p_p \nabla \cdot \mathbf{u}_p'' \rangle - \frac{1}{\rho_p \langle \alpha \rangle} \langle \sigma_p : \nabla \mathbf{u}_p'' \rangle \tag{A.63}$$

where the first term is due to pressure dilation and the second term is due to viscous effects. The viscous term is modelled as

$$\frac{1}{\rho_p \langle \alpha \rangle} \langle \sigma_p : \nabla \mathbf{u}_p'' \rangle = \varepsilon_p \tag{A.64}$$

In this work the pressure dilation is neglected as in other works Rumsey [163], Wilcox [212].

A.6 Coupling terms

The coupling terms involve the Reynolds average with respect to both particle and fluid properties. This leads to mixed averages that require closure.

A.6.1 Covariance of volume fraction and fluid velocity

This term is often described as the drift velocity, turbulent drag flux or dispersion velocity. It is often modelled as a turbulent flux Zuber and Findlay [228]

$$\frac{\langle \alpha_p' \mathbf{u}_f''' \rangle}{\langle \alpha_p \rangle \langle \alpha_f \rangle} = \frac{\nu_{ft}}{Sc_{fp}} (C_f \nabla \ln \langle \alpha_f \rangle - C_p \nabla \ln \langle \alpha_p \rangle) \tag{A.65}$$

Now setting both constants C_f and C_p to unity the closure simplifies to

$$\langle \alpha_p' \mathbf{u}_f''' \rangle = \frac{\nu_{ft}}{Sc_{fp}} \nabla \langle \alpha_p \rangle \tag{A.66}$$

where Sc_{fp} is a turbulent Schmidt number that depends on the particle Stokes number. This closure has the added benefit that when $\tau_p \to 0$ the correct turbulent diffusivity term is generated Fox [71].

A.6.2 Covariance of volume fraction and fluid-pressure gradient

This term represents the fluctuations in the buoyancy force, it can be rewritten as a flux and source term $\langle \alpha_p' \nabla p_f' \rangle = \nabla \langle \alpha_p' p_f' \rangle - \langle p_f' \nabla \alpha_p' \rangle$. For gravity driven flows, the fluctuating fluid-pressure gradient can be decomposed into static and dynamic components:

$$\nabla p_f' = \nabla p_f - \nabla \langle p_f \rangle = \rho_{mix}' \mathbf{g} + \nabla p' \tag{A.67}$$

where $\rho_{mix}' = (\rho_p - \rho_f)\alpha_p'$. The static component of the mean pressure is $\langle \nabla p_f \rangle_s = \langle \rho_{mix} \rangle \mathbf{g}$ with $\langle \rho_{mix} \rangle = \rho_p \langle \alpha_p \rangle + \rho_f \langle \alpha_f \rangle$ and $\nabla p_f = \nabla p + \rho_{mix} \mathbf{g}$ where the mean dynamic pressure $\langle p \rangle$ is zero under static conditions.) Using this decomposition we can write:

$$\langle \alpha_p' \nabla p_f' = (\rho_p - \rho_f) \langle (\alpha_p')^2 \rangle \mathbf{g} + \langle \alpha_p' \nabla p' \rangle \tag{A.68}$$

where the first term involves the variance of the volume fraction through the non-linear fluctuation. In large stokes number flows this is expected to be large.

A.6.3 Fluid-particle velocity covariance

The covariance appears in the drag term for the turbulent kinetic energy and is one of the most important terms in E-E modelling. Using the definition of phase average, we can write

$$\langle \mathbf{u}_p'' \cdot \mathbf{u}_f \rangle_p = \langle \mathbf{u}_p'' \cdot \mathbf{u}_f''' \rangle_f + \frac{\langle \alpha' \mathbf{u}_p'' \cdot \mathbf{u}_f''' \rangle}{\langle \alpha \rangle \langle \alpha_f \rangle} \tag{A.69}$$

in a statistically homogeneous system the latter term is null and thus we are left with just the covariance between velocity fluctuations in the two phases. There is much debate over the appropriate closure of this term - the one adopted in this work is

$$\langle \mathbf{u}_p'' \cdot \mathbf{u}_f''' \rangle_p = \sqrt{2k_p \langle \mathbf{u}_f''' \cdot \mathbf{u}_f''' \rangle_p} \tag{A.70}$$

which in this work is denoted as $k_{fp} = \sqrt{k_f k_p}$. For further discussion on this term the reader is referred to Fox [71], Xu and Subramaniam [216**?**].

A.6.4 Velocity-fluid-pressure-gradient covariance

These terms arise due to buoyancy and, using the decomposition in Sec. A.6.2 they can be rewritten as

$$\langle \mathbf{u}_f''' \cdot \nabla p_f' \rangle_p = (\rho_p - \rho_f) \langle \alpha_p' \mathbf{u}_f''' \rangle_p \cdot \mathbf{g} + \langle \mathbf{u}_f''' \cdot \nabla p' \rangle_p \tag{A.71}$$

$$\langle \mathbf{u}_p'' \cdot \nabla p_f' \rangle_p = (\rho_p - \rho_f) \langle \alpha_p' \mathbf{u}_p'' \rangle_p \cdot \mathbf{g} + \langle \mathbf{u}_p'' \cdot \nabla p' \rangle_p \tag{A.72}$$

The terms involving p' are likely to be negligible, wile the first term on the LHS of each equation can be written as:

$$\langle \alpha_p' \mathbf{u}_f''' \rangle_p = \langle \alpha_p' \mathbf{u}_f''' \rangle + \frac{\langle (\alpha_p')^2 \mathbf{u}_f''' \rangle}{\langle \alpha_p \rangle} \tag{A.73}$$

$$\langle \alpha_p' \mathbf{u}_p'' \rangle_p = \langle \alpha_p' \mathbf{u}_p'' \rangle + \frac{\langle (\alpha_p')^2 \mathbf{u}_p'' \rangle}{\langle \alpha_p \rangle} \tag{A.74}$$

The fluxes $\langle \alpha_p' \mathbf{u}_f''' \rangle$ and $\langle \alpha_p' \mathbf{u}_p'' \rangle$ can be modelled analogous to the turbulent dispersion term in Sec. A.6.1.

This page is intentionally left blank.

B Appendix

B.1 Reynolds averaging

As in single-phase turbulence modelling a Reynolds average is defined as an ensemble average over multiple realisations of the same flow Pope [142]. A Reynolds average of a quantity $(\cdot)$ will by denoted as $\langle(\cdot)\rangle$.

The following decomposition of an arbitrary quantity A, e.g. scalar, vector tensor, is as follows: RA decomposition: $\mathrm{A} = \langle \mathrm{A} \rangle + \mathrm{A}'$ where $\langle \mathrm{A}' \rangle = 0$ and the angle-bracket operator $\langle \cdot \rangle$ denotes the Reynolds average.

Within the context of this work the most important properties of the Reynolds average are as follows.

1. The Reynolds average commutes with time derivatives: $\langle \partial(\cdot)/\partial t \rangle = \partial \langle(\cdot)\rangle / \partial t$.
2. The Reynolds average commutes with space derivatives: $\langle \nabla(\cdot) \rangle = \nabla \langle(\cdot)\rangle$.
3. The Reynolds average is used to decompose a quantity into its mean and fluctuations: $(\cdot) = \langle(\cdot)\rangle + (\cdot)'$.
4. The Reynolds average of the fluctuations is null: $\langle(\cdot)'\rangle = 0$.
5. The Reynolds average of the mean is the mean: $\langle\langle(\cdot)\rangle\rangle = \langle(\cdot)\rangle$.

6. The Reynolds average of a product can be decomposed as

$$\langle \mathrm{AB} \rangle = \langle \mathrm{A}'\mathrm{B}' \rangle + \langle \mathrm{A} \rangle \langle \mathrm{B} \rangle \tag{B.1}$$

7. The Reynolds average of a product with a derivative can be rewritten in terms of mean and fluctuating quantities.

$$\left\langle \mathrm{A} \frac{\partial \mathrm{B}}{\partial t} \right\rangle = \langle \mathrm{A} \rangle \frac{\partial \langle \mathrm{B} \rangle}{\partial t} + \frac{\partial \langle \mathrm{A}'\mathrm{B}' \rangle}{\partial t} - \left\langle \mathrm{B}' \frac{\partial \mathrm{A}'}{\partial t} \right\rangle \tag{B.2}$$

B.2 Phase/Conditional averaging

In variable-density turbulent flows the Favre average is used to define density-weighted statistics. The Favre average is related to the Reynolds average by $\langle \rho \mathrm{A} \rangle = \langle \rho \rangle \langle \mathrm{A} \rangle_F$ where ρ is the density and $\langle \mathrm{A} \rangle_F$ is the Favre average of A. In fluid-particle flows, the phase volume fractions play the role of density. The decomposition definitions as follows:

Particle-PA decomposition: $\mathrm{A} = \langle \mathrm{A} \rangle_p + \mathrm{A}''$ where $\langle \mathrm{A} \rangle_p \equiv \langle \alpha_p \mathrm{A} \rangle / \langle \alpha_p \rangle$.

Particle-PA decomposition: $\mathrm{A} = \langle \mathrm{A} \rangle_f + \mathrm{A}'''$ where $\langle \mathrm{A} \rangle_f \equiv \langle \alpha_f \mathrm{A} \rangle / \langle \alpha_f \rangle$.

We define the PA quantities as

$$\langle \mathrm{A} \rangle_p = \frac{\langle \alpha \mathrm{A} \rangle}{\langle \alpha \rangle} \tag{B.3}$$

$$\langle \mathrm{A} \rangle_f = \frac{\langle \alpha_f \mathrm{A} \rangle}{\langle \alpha_f \rangle} \tag{B.4}$$

Unlike the Reynolds average, the phase average does not commute with derivative: $\langle \nabla \mathrm{A} \rangle_p \neq \nabla \langle \mathrm{A} \rangle_p$. In addition there are two types of phase average with respect to each phase. Using the above definitions it is trivial to show that

$$\langle \mathrm{A} \rangle = \langle \alpha_p \rangle \langle \mathrm{A} \rangle_p + \langle \alpha_f \rangle \langle \mathrm{A} \rangle_f \tag{B.5}$$

excluding derivatives, the phase average have similar properties to the Reynolds average. The PA decomposition in each phase results in a PA mean and fluctuating

quantity. Using the definition of the PA fluctuations, we can now write PA first-derivative terms as

$$\langle \nabla \mathrm{A} \rangle_p = \nabla \langle \mathrm{A} \rangle_p - \frac{1}{\langle \alpha_p \rangle} \langle \mathrm{A}'' \nabla \alpha_p \rangle \tag{B.6}$$

where the last term is unclosed. Another useful identity is $\langle \alpha' \mathrm{A} \rangle = \langle \alpha_p' \mathrm{A}' \rangle = \langle \alpha_p' \mathrm{A}'' \rangle = \langle \alpha_p' \mathrm{A}''' \rangle$ for any A. This identity holds because in each case the difference between A and the primed quantities is an additive constant and $\langle \alpha_p' \rangle = 0$. Thus, in the RA transport equations, where primed quantities are present this is employed.

Another identity is relating the phase average of a quantity to its covariance with respect to the volume fraction. First, using Eq. B.5 we rewrite it such that

$$\langle \mathrm{A} \rangle_p = \langle \mathrm{A} \rangle_f + \frac{1}{\langle \alpha_p \rangle} (\langle \mathrm{A} \rangle - \langle \mathrm{A} \rangle_f) \tag{B.7}$$

Similarly, we find $\langle \alpha_f \rangle \langle A \rangle_f = \langle \alpha_f A \rangle = \langle (\langle \alpha_f \rangle - \alpha_p') A \rangle = \langle \alpha_f \rangle \langle A \rangle - \langle \alpha_p' A \rangle$ so that

$$\langle \mathrm{A} \rangle - \langle \mathrm{A}_f \rangle_f = \frac{\langle \alpha_p' \mathrm{A} \rangle}{\langle \alpha_f \rangle} \tag{B.8}$$

Combining these two results to eliminate $\langle \mathrm{A} \rangle$ yields

$$\langle \mathrm{A} \rangle_p = \langle \mathrm{A} \rangle_f + \frac{\langle \alpha_p' \mathrm{A} \rangle}{\langle \alpha_f \rangle \langle \alpha_p \rangle} \tag{B.9}$$

where A is arbitrary. Likewise, using $\langle \mathrm{A}'' \rangle_p = 0$ and $\langle \mathrm{A}''' \rangle_f = 0$ to show that

$$\langle \alpha_p' \mathrm{A} \rangle = \langle \alpha_p' \mathrm{A}'' \rangle = \langle \alpha_p' \mathrm{A}''' \rangle = -\langle \alpha_p \mathrm{A}'' \rangle = \langle \alpha_f \mathrm{A}''' \rangle \tag{B.10}$$

In the literature the phase average on the LHS of Eq. B.9 is referred to as the average seen by the particles, with the RHS is the average seen by the fluid. The second term on the RHS in Eq. B.9 dictates how correlated they are depends on the fluctuations within the volume fraction. An example of this is the preferential concentration exhibited by two way coupling effects Ahmed and Elghobashi [6].

This page is intentionally left blank.

C Appendix

C.1 Tables of definitions and variables

Table C.1: Definition of variables.

$$\mu_f = \rho_f \nu_f$$

$$\mu_{ft} = \alpha_f \rho_f \nu_{ft} = \alpha_f \rho_f C_{f\mu} \frac{k_f^2}{\varepsilon_f}$$

$$\mu_p = \alpha_p \rho_p \nu_p = \frac{2\mu_{p_{dil}}}{(1+e)g_0}\Big[1 + \frac{4}{5}(1+e)g_0\alpha_p\Big]^2 + \frac{4}{5}\alpha_p^2 \rho_p d_p g_0 (1+e)\Big(\frac{\Theta}{\pi}\Big)^{1/2}$$

$$\mu_{p_{dil}} = \frac{5\sqrt{\pi}}{96}\rho_p d_p \Theta^{1/2}$$

$$\mu_{pt} = \alpha_p \rho_p \nu_{pt} = \alpha_p \rho_p C_{p\mu} \frac{k_p^2}{\varepsilon_p}$$

$$p_p = \rho_p \alpha_p \Theta + 2(1+e)\rho_p \alpha_p^2 g_0 \Theta$$

$$\gamma = \frac{12(1-e^2)g_o}{\sqrt{\pi} d_p}\alpha_p^2 \rho_p \Theta^{3/2}$$

$$\kappa_\Theta = \frac{2}{(1+e)g_0}\Big[1 + \frac{6}{5}(1+e)g_0\alpha_p\Big]^2 \kappa_{\Theta,dil} + 2\alpha_p^2 \rho_p d_p g_0 (1+e)\Big(\frac{\Theta}{\pi}\Big)^{\frac{1}{2}}$$

$$\kappa_{\Theta,dil} = \frac{75}{384}\sqrt{\pi}\rho_p d_p \Theta^{1/2}$$

$$g_0 = \Big[1 - \Big(\frac{\alpha_p}{\alpha_{p,max}}\Big)^{\frac{1}{3}}\Big]^{-1}$$

$$\overline{\mathbf{S}}_\mathbf{p} = \frac{1}{2}[\nabla \mathbf{u}_p + (\nabla \mathbf{u}_p)^T] - \frac{1}{3}\nabla \cdot \mathbf{u}_p \mathbf{I}$$

$$\overline{\mathbf{S}}_\mathbf{f} = \frac{1}{2}[\nabla \mathbf{u}_f + (\nabla \mathbf{u}_f)^T] - \frac{1}{3}\nabla \cdot \mathbf{u}_f \mathbf{I}$$

$$k_{fp} = \beta_k \sqrt{k_f k_p}$$

$$\varepsilon_{fp} = \beta_\varepsilon \sqrt{\varepsilon_f \varepsilon_p}$$

$$\mathrm{Kn} = \frac{\sqrt{\pi} d_p}{12\alpha_p g_0 L}$$

$$u_{p_{rms}} = \sqrt{(2/3)\kappa_p}$$

$$u_{f_{rms}} = \sqrt{(2/3)k_f}$$

Table C.2: Definition of phase-averaged variables.

$\alpha_p = \langle \alpha_p \rangle$

$\alpha_f = \langle \alpha_f \rangle$

$\mathbf{u}_p = \langle \mathbf{u} \rangle_p$

$\mathbf{u}_f = \langle \mathbf{u} \rangle_f$

$\Theta = \langle \Theta \rangle_p$

$k_p = \frac{1}{2} \langle \mathbf{u}_p'' \cdot \mathbf{u}_p'' \rangle_p$

$k_f = \frac{1}{2} \langle \mathbf{u}_f''' \cdot \mathbf{u}_f''' \rangle_f$

$\varepsilon_p = \frac{1}{\rho_p \alpha_p} \langle \bar{\boldsymbol{\sigma}}_p : \nabla \mathbf{u}_p'' \rangle$

$\varepsilon_f = \frac{1}{\rho_f \alpha_f} \langle \bar{\boldsymbol{\sigma}}_f : \nabla \mathbf{u}_f''' \rangle$

$\overline{\boldsymbol{\sigma}}_p = \mu_p [\nabla \mathbf{u}_p + (\nabla \mathbf{u}_p)^T] - \frac{1}{3} \mu_p \nabla \cdot \mathbf{u}_p \mathbf{I}$

$\overline{\boldsymbol{\sigma}}_f = \mu_f [\nabla \mathbf{u}_f + (\nabla \mathbf{u}_f)^T] - \frac{1}{3} \mu_f \nabla \cdot \mathbf{u}_f \mathbf{I}$

$\mathbf{u}_p'' = \mathbf{u}_p - \langle \mathbf{u}_p \rangle_p$

$\mathbf{q}_\Theta = \langle \mathbf{q}_\Theta \rangle_p = \frac{\kappa_\Theta}{\alpha_p \rho_p} \nabla \Theta_p$

$\mathbf{u}_f''' = \mathbf{u}_f - \langle \mathbf{u}_f \rangle_f$

$\langle \mathbf{u}_p \rangle_p = \langle \alpha_p \mathbf{u}_p \rangle / \langle \alpha_p \rangle$

$\langle \mathbf{u}_f \rangle_f = \langle \alpha_f \mathbf{u}_f \rangle / \langle \alpha_f \rangle$

$\mathbf{u}_p'' \mathbf{u}_p'' = \langle \mathbf{u}_p'' \mathbf{u}_p'' \rangle_p$

Table C.3: Turbulence model parameters for RA-TFM.

C_p	C_g	C_ρ	C_1	C_2	C_3	C_4	C_5	β_k	β_ε	$C_{f\mu}$	$C_{p\mu}$
0	0	1	1.44	1.92	1	1	1	1	1	0.09	0.09

Table C.4: Turbulence model parameters for RA-TFM velocity pressure models.

$C_{\varepsilon 1}$	$C_{\varepsilon 2}$	C_μ	C_1	C_2	C_L	C_η	β_ϵ	$C_{f\mu}$	$C_{p\mu}$	σ_k	σ_ϵ
1.6	1.9	0.22	1.4	0.3	0.23	70	1	0.09	0.09	1	1

D Appendix

D.1 Code repository

The source code of both `ratfmFoam` and `ratfmCoupledFoam` and supplementary material can be downloaded from www.github.com/mjriella/RA-EE.

This page is intentionally left blank.

Bibliography

[1] Existence and smoothness of the navier-stokes equation. http://www.claymath.org/sites/default/files/navierstokes.pdf. Charles L. Fefferman.

[2] Abrahamson, J. (1975). Collision rates of small particles in a vigorously turbulent fluid. *Chemical Engineering Science*, 30(11):1371 – 1379.

[3] Agrawal, K., Loezos, P. N., Syamlal, M., and Sundaresan, S. (2001). The role of meso-scale structures in rapid gas-solid flows. *Journal of Fluid Mechanics*, 445:151–185.

[4] Ahmadi, G. and Ma, D. (1990). A thermodynamical formulation for dispersed multiphase turbulent flows: Basic theory. *International Journal of Multiphase Flow*, 16(2):323 – 340.

[5] Ahmed, A. and Elghobashi, S. (2001). Direct numerical simulation of particle dispersion in homogeneous turbulent shear flows. *Physics of Fluids*, 13(11):3346–3364.

[6] Ahmed, A. M. and Elghobashi, S. (2000). On the mechanisms of modifying the structure of turbulent homogeneous shear flows by dispersed particles. *Physics of Fluids*, 12(11):2906–2930.

[7] Anderson, T. B. and Jackson, R. (1967). Fluid mechanical description of fluidized beds: Equations of Motion. *Industrial and Engineering Chemistry Fundamentals*, 6(4):527–539.

[8] Armstrong, L.-M., Luo, K., and Gu, S. (2010). Two-dimensional and three-dimensional computational studies of hydrodynamics in the transition from bubbling to circulating fluidised bed. *Chemical Engineering Journal*, 160(1):239–248.

[9] Bagchi, P. and Balachandar, S. (2003). Effect of turbulence on the drag and lift of a particle. *Physics of fluids*, 15(11):3496–3513.

[10] Bagchi, P. and Balachandar, S. (2004). Response of the wake of an isolated particle to an isotropic turbulent flow. *Journal of Fluid Mechanics*, 518:95–123.

[11] Basset, A. B. (1888). *A treatise on hydrodynamics: with numerous examples*, volume 2. Deighton, Bell and Company.

[12] Behnia, M., Parneix, S., and Durbin, P. (1998). Prediction of heat transfer in an axisymmetric turbulent jet impinging on a flat plate. *International Journal of Heat and Mass Transfer*, 41(12):1845 – 1855.

[13] Benavides, A. and van Wachem, B. (2008). Numerical simulation and validation of dilute turbulent gas-particle flow with inelastic collisions and turbulence modulation. *Powder Technology*, 182:294–306.

[14] Benyahia, S., Syamlal, M., and O'Brien, T. J. (2005). Evaluation of boundary conditions used to model dilute, turbulent gas/solids flows in a pipe. *Powder Technology*, 156(2):62 – 72. Particle Technology Forum Special Issue.

[15] Bird, G. (1994). Molecular gas dynamics and the direct simulation of gas flows (oxford engineering science series). *Clarendon,*.

[16] Bolio, E. J., Yasuna, J. A., and Sinclair, J. L. (1995). Dilute turbulent gas-solid flow in risers with particle-particle interactions. *AIChE Journal*, 41(6):1375–1388.

[17] Boltzmann, L. (1970). Weitere studien über das wärmegleichgewicht unter gasmolekülen. In *Kinetische Theorie II*, pages 115–225. Springer.

[18] Borée, J. and Caraman, N. (2005). Dilute bidispersed tube flow: Role of interclass collisions at increased loadings. *Physics of Fluids*, 17(5):055108.

[19] Boussinesq, J. (1877). Essai sur la théeorie des eaux courante. *Mémoires préesentées par divers savants à l'Acadéemie des Sciences XXIII,*, 1:1–680.

[20] Braaten, M. and Patankar, S. (1989). A block-corrected subdomain solution procedure for recirculating flow calculations. *Numerical Heat Transfer, Part B: Fundamentals*, 15(1):1–20.

[21] Brey, J. J., Dufty, J. W., and Santos, A. (1997). Dissipative dynamics for hard spheres. *Journal of statistical physics*, 87(5-6):1051–1066.

[22] Brilliantov, N. V. and Pöschel, T. (2010). *Kinetic theory of granular gases*. Oxford University Press.

[23] Brooke, J. W., Kontomaris, K., Hanratty, T. J., and McLaughlin, J. B. (1992). Turbulent deposition and trapping of aerosols at a wall. *Physics of Fluids A: Fluid Dynamics*, 4(4):825–834.

[24] Buffo, A., Vanni, M., and Marchisio, D. L. (2016). On the implementation of moment transport equations in OpenFOAM : Boundedness and realizability. *International Journal of Multiphase Flow*, 85:223 – 235.

[25] Burns, A., Splawski, A., Lo, S., and Guetari, C. (2001). Application of coupled solver technology to cfd modeling of multiphase flows with cfx. *WIT Transactions on Engineering Sciences*, 30.

[26] Canuto, V. (1997). Compressible turbulence. *Astrophys. J.*, 482:827–851.

[27] Capecelatro, J., Desjardins, O., and Fox, R. O. (2015). On fluid-particle dynamics in fully developed cluster-induced turbulence. *Journal of Fluid Mechanics*, 780:578–635.

[28] Capecelatro, J., Desjardins, O., and Fox, R. O. (2016a). Strongly coupled fluid-

particle flows in vertical channels. I. Reynolds-averaged two-phase turbulence statistics. *Physics of Fluids*, 28(3).

[29] Capecelatro, J., Desjardins, O., and Fox, R. O. (2016b). Strongly coupled fluid-particle flows in vertical channels. II. Turbulence modeling. *Physics of Fluids*, 28(3).

[30] Capecelatro, J., Desjardins, O., and Fox, R. O. (2018). On the transition between turbulence regimes in particle-laden channel flows. *Journal of Fluid Mechanics*, 845:499–519.

[31] Caporaloni, M., Tampieri, F., Trombetti, F., and Vittori, O. (1975). Transfer of particles in nonisotropic air turbulence. *Journal of the Atmospheric Sciences*, 32(3):565–568.

[32] Caraman, N., Borée, J., and Simonin, O. (2003). Effect of collisions on the dispersed phase fluctuation in a dilute tube flow: Experimental and theoretical analysis. *Physics of Fluids*, 15(12):3602–3612.

[33] Cardiff, P., Tuković, Ž., Jasak, H., and Ivanković, A. (2016). A block-coupled finite volume methodology for linear elasticity and unstructured meshes. *Computers & structures*, 175:100–122.

[34] Caretto, L., Curr, R., and Spalding, D. (1972). Two numerical methods for three-dimensional boundary layers. *Computer Methods in Applied Mechanics and Engineering*, 1(1):39 – 57.

[35] Cercignani, C., Illner, R., and Pulvirenti, M. (2013). *The mathematical theory of dilute gases*, volume 106. Springer Science & Business Media.

[36] Chan, C. K., Zhang, H. Q., and Lau, K. S. (2001). Numerical simulation of gas-particle flows behind a backward-facing step using an improved stochastic separated flow model. *Computational Mechanics*, 27(5):412–417.

[37] Chao, Z., Wang, Y., Jakobsen, J. P., Fernandino, M., and Jakobsen, H. A.

(2011). Derivation and validation of a binary multi-fluid eulerian model for fluidized beds. *Chemical Engineering Science*, 66(16):3605 – 3616.

[38] Chapman, S. and Cowling, T. G. (1961). *The Mathematical Theory of Non-Uniform Gases*. Chambridge: University Press.

[39] Chen, Z. and Przekwas, A. (2010). A coupled pressure-based computational method for incompressible/compressible flows. *Journal of Computational Physics*, 229(24):9150 – 9165.

[40] Cheng, Y., Guo, Y., Wei, F., Jin, Y., and Lin, W. (1999). Modeling the hydrodynamics of downer reactors based on kinetic theory. *Chemical Engineering Science*, 54(13):2019 – 2027.

[41] Chien, K.-Y. (1982). Predictions of Channel and Boundary-Layer Flows with a Low-Reynolds-Number Turbulence Model. *AIAA Journal*, 20(1):33–38.

[42] Clifford, I., J. H. (2009). The application of a multi-physics toolkit to spatial reactor dynamics. In *International Conference on Mathematics, Computational Methods Reactor Physics, Curran Associates, Saratoga Springs, New York.*

[43] Cubero, A. and Fueyo, N. (2007). A compact momentum interpolation procedure for unsteady flows and relaxation. *Numerical Heat Transfer, Part B: Fundamentals*, 52(6):507–529.

[44] Cubero, A., SÃąnchez-Insa, A., and Fueyo, N. (2014). A consistent momentum interpolation method for steady and unsteady multiphase flows. *Computers Chemical Engineering*, 62:96 – 107.

[45] Darwish, M., Abdel Aziz, A., and Moukalled, F. (2015). A coupled pressure-based finite-volume solver for incompressible two-phase flow. *Numerical Heat Transfer, Part B: Fundamentals*, 67(1):47–74.

[46] Darwish, M., Sraj, I., and Moukalled, F. (2007). A coupled incompressible flow solver on structured grids. *Numerical Heat Transfer, Part B: Fundamentals*, 52(4):353–371.

[47] Darwish, M., Sraj, I., and Moukalled, F. (2009). A coupled finite volume solver for the solution of incompressible flows on unstructured grids. *Journal of Computational Physics*, 228(1):180–201.

[48] Dasgupta, S., Jackson, R., and Sundaresan, S. (1994). Turbulent gas-particle flow in vertical risers. *AIChE Journal*, 40(2):215–228.

[49] Dasgupta, S., Jackson, R., and Sundaresan, S. (1998). Gas-particle flow in vertical pipes with high mass loading of particles. *Powder Technology*, 96(1):6 – 23.

[50] Davidson, L., Nielsen, P. V., and Sveningsson, A. (2003). Modifications of the v2-f model for computing the flow in a 3d wall jet. In Hanjalić, K., Nagano, Y., and Tummers, M., editors, *Turbulence, heat and mass transfer*, pages 577–584.

[51] Desjardins, O., Fox, R. O., and Villedieu, P. (2008). A quadrature-based moment method for dilute fluid-particle flows. *Journal of Computational Physics*, 227(4):2514–2539.

[52] Di Giacinto, M., Sabetta, F., and Piva, R. (1982). Two-way coupling effects in dilute gas-particle flows. *Journal of Fluids Engineering*, 104(3):304–311.

[53] Drew, D. A. and Lahey, R. T. (1993). *In particulate Two-phase Flow*. Butterworth-Heinemann, Boston.

[54] Drew, D. A. and Segel, L. A. (1971). Averaged equations for two-phase flows. *Studies in Applied Mathematics*, 50(3):205–231.

[55] Dukowicz, J. K. (1980). A particle-fluid numerical model for liquid sprays. *Journal of computational Physics*, 35(2):229–253.

[56] Durbin, P. A. (1991). Near-wall turbulence closure modeling without "damping functions". *Theoretical and Computational Fluid Dynamics*, 3(1):1–13.

[57] Durbin, P. A. (1993). A reynolds stress model for near-wall turbulence. *Journal of Fluid Mechanics*, 249:465–498.

[58] Durbin, P. A. and Reif, B. A. P. (2010). *Statistical theory and modeling of turbulence flow*, pages 109–154. John Wiley & Sons, Ltd.

[59] Elghobashi, S. (1994). On predicting particle-laden turbulent flows. *Applied Scientific Research*, 52(4):309–329.

[60] Elghobashi, S. and Truesdell, G. C. (2006). Direct simulation of particle dispersion in a decaying isotropic turbulence. *Journal of Fluid Mechanics*, 242(-1):655.

[61] Elghobashi, S. E. and Abou-Arab, T. W. (1983). A two-equation turbulence model for two-phase flows. *Physics of Fluids*, 26(4):931.

[62] Enwald, H., Peirano, E., and Almstedt, A.-E. (1996). Eulerian two-phase flow theory applied to fluidization. *International Journal of Multiphase Flow*, 22:21–66.

[63] Ferreira, G. G., Lage, P. L., Silva, L. F. L., and Jasak, H. (2019). Implementation of an implicit pressure-velocity coupling for the eulerian multi-fluid model. *Computers Fluids*, 181:188 – 207.

[64] Ferziger, J. H. and Peric, M. (2002). *Computational Methods for Fluid Dynamics*. Springer.

[65] Fessler, J. R. and Eaton, J. K. (1995). Particle-turbulence interaction in a backward-facing step flow. *Rep. MD-70*, 394(1995):97–117.

[66] Fessler, J. R. and Eaton, J. K. (1999). Turbulence modification by particles in a backward-facing step flow. *Journal of Fluid Mechanics*, 394(1999):97–117.

[67] Février, P., Simonin, O., and Squires, K. D. (2005). Partitioning of particle velocities in gas–solid turbulent flows into a continuous field and a spatially uncorrelated random distribution: theoretical formalism and numerical study. *Journal of Fluid Mechanics*, 533:1–46.

[68] Feynman, R., Leighton, R., Sands, M., and Hafner, E. (1965). *The Feynman Lectures on Physics; Vol. I*, volume 33. AAPT.

[69] Fox, R. O. (2003). *Computational Models for Turbulent Reacting Flows*. Cambridge University Press.

[70] Fox, R. O. (2012). Large-eddy-simulation tools for multiphase flows. *Annual Review of Fluid Mechanics*, 44:47–76.

[71] Fox, R. O. (2014). On multiphase turbulence models for collisional fluid-particle flows. *Journal of Fluid Mechanics*, 742:368–424.

[72] Garzó, V. and Santos, A. (2013). *Kinetic theory of gases in shear flows: nonlinear transport*, volume 131. Springer Science & Business Media.

[73] Garzó, V., Tenneti, S., Subramaniam, S., and Hrenya, C. M. (2012). Enskog kinetic theory for monodisperse gas-solid flows. *Journal of Fluid Mechanics*, 712:129–168.

[74] Ge, W., Chen, F., Gao, J., Gao, S., Huang, J., Liu, X., Ren, Y., Sun, Q., Wang, L., Wang, W., et al. (2007). Analytical multi-scale method for multi-phase complex systems in process engineering-bridging reductionism and holism. *Chemical Engineering Science*, 62(13):3346–3377.

[75] Gibson, M. M. and Launder, B. E. (1978). Ground effects on pressure fluctuations in the atmospheric boundary layer. *Journal of Fluid Mechanics*, 86(3):491–511.

[76] Gidaspow, D. (1994). *Multiphase flow and fluidization*. Academic Press.

[77] Gore, R. and Crowe, C. (1989). Effect of particle size on modulating turbulent intensity. *International Journal of Multiphase Flow*, 15(2):279 – 285.

[78] Hanjalic, K. and Launder, B. (1980). Sensitizing the dissipation equation to irrotational strains. *Journal of Fluids Engineering*, 102(1):34–40.

[79] He, J. and Simonin, O. (1993). Non-equilibrium prediction of the particle-phase stress tensor in vertical pneumatic conveying. *Gas-Solid Flows, ASME FED*, 166:253–263.

[80] Helland, E., Occelli, R., and Tadrist, L. (2002). Computational study of

fluctuating motions and cluster structures in gas-particle flows. *International Journal of Multiphase Flow*, 28(2):199 – 223.

[81] Hestenes, M. R. and Stiefel, E. (1952). *Methods of conjugate gradients for solving linear systems*, volume 49.

[82] Hetsroni, G. (1989). Particles-turbulence interaction. *International Journal of Multiphase Flow*, 15(5):735 – 746.

[83] Hinze, J. O. (1975). *Turbulence*. McGraw-Hill.

[84] Hrenya, C. and Sinclair, J. (1997a). Effects of particle-phase turbulence in gas-solid flows. *AIChE Journal*, 43(4):853–869.

[85] Hrenya, C. M. and Sinclair, J. L. (1997b). Effects of particle-phase turbulence in gas-solid flows. *AIChE Journal*, 43(4):853–869.

[86] Hunt, J. C. R. and Graham, J. M. R. (1978). Free-stream turbulence near plane boundaries. *Journal of Fluid Mechanics*, 84(2):209–235.

[87] Hutchinson, B., Galpin, P., and Raithby, G. (1988). Application of additive correction multigrid to the coupled fluid flow equations. *Numerical Heat Transfer*, 13(2):133–147.

[88] Ishii, M. (1975). Thermo-fluid dynamic theory of two-phase flow. *NASA STI/Recon Technical Report A*, 75.

[89] Issa, R. I. (1986). Solution of the implicitly discretised fluid flow equations by operator-splitting. *Journal of Computational Physics*, 62(1):40–65.

[90] Jacobs, D. A. (1986). A generalization of the conjugate-gradient method to solve complex systems. *IMA journal of numerical analysis*, 6(4):447–452.

[91] Jareteg, K., Vukčević, V., and Jasak, H. (2014). pucoupledfoam-an open source coupled incompressible pressure-velocity solver based on foam-extend. In *9th OpenFOAM Workshop*.

[92] Jasak, H. (1996). *Error Analysis and Estimation for the Finite Volume Method with Applications to Fluid Flows*. PhD thesis, Imperial College London.

[93] Jenkins, J. T. and Mancini, F. (1989). Kinetic theory for binary mixtures of smooth, nearly elastic spheres. *Physics of Fluids A: Fluid Dynamics*, 1(12):2050–2057.

[94] Jenkins, J. T. and Savage, S. B. (1983). A theory for the rapid flow of identical, smooth, nearly elastic, spherical particles. *Journal of Fluid Mechanics*, 130:187–202.

[95] Jiménez, J. (2012). Cascades in wall-bounded turbulence. *Annual Review of Fluid Mechanics*, 44:27–45.

[96] Jiménez, J. and Pinelli, A. (1999). The autonomous cycle of near-wall turbulence. *Journal of Fluid Mechanics*, 389:335–359.

[97] Johnson, P. C. and Jackson, R. (1987). Friction-collisional constitutive relations for granular materials, with application to plane shearing. *Journal of Fluid Mechanics*.

[98] Jorgensen, S. and Johnsen, I. (1981). *Principles of Environmental Science and Technology*. Elsevier Scientific Publishing Co., New York, NY.

[99] Karki, K. C. and Mongia, H. C. Evaluation of a coupled solution approach for fluid flow calculations in body-fitted co-ordinates. *International Journal for Numerical Methods in Fluids*, 11(1):1–20.

[100] Kaufmann, A., Moreau, M., Simonin, O., and Helie, J. (2008). Comparison between lagrangian and mesoscopic eulerian modelling approaches for inertial particles suspended in decaying isotropic turbulence. *Journal of Computational Physics*, 227(13):6448–6472.

[101] Keser, R. (2016). Block-coupled soltuion algorithms for 2-equation turbulence models. *Masters Thesis - Faculty of Mechanical Engineering and Naval Architecture, University of Zagreb*.

[102] Klinzing, G. (1981). *Gas-solid transport*. New York, McGraw-Hill.

[103] Kolmogorov, A. (1941). The Local Structure of Turbulence in Incompressible Viscous Fluid for Very Large Reynolds' Numbers. *Akademiia Nauk SSSR Doklady*, 30:301–305.

[104] Kong, B. and Fox, R. O. (2017). A solution algorithm for fluid-particle flows across all flow regimes. *Journal of Computational Physics*, 344:575 – 594.

[105] Kubik, A. and Kleiser, L. (2006). Influence of mass loading on particle-laden turbulent channel flow. *PAMM*, 6(1):531–532.

[106] Kulick, J., Fessler, J. R., and Eaton, J. R. (1994). Particle response and turbulence modification in fully developed channel flow. *Journal of Fluid Mechanics*, 277:109–134.

[107] Launder, B. and Sharma, B. (1974). Application of the energy-dissipation model of turbulence to the calculation of flow near a spinning disc. *Letters in Heat and Mass Transfer*, 1(2):131 – 137.

[108] Launder, B. E., Reece, G. J., and Rodi, W. (1975). Progress in the development of a reynolds-stress turbulence closure. *Journal of Fluid Mechanics*, 68(3):537–566.

[109] Lee, S. and Durst, F. (1982). On the motion of particles in turbulent duct flows. *International Journal of Multiphase Flow*, 8(2):125 – 146.

[110] Li, D. and Christian, H. (2017). Simulation of bubbly flows with special numerical treatments of the semi-conservative and fully conservative two-fluid model. *Chemical Engineering Science*, 174:25–39.

[111] Li, J., Chen, A., Yan, Z., Xu, G., and Zhang, X. (1993). Particle–fluid contacting in circulating fluidized beds. *Preprint Volume for CFB-IV; Avidan, AA, Ed.; AIChE: New York*, pages 49–54.

[112] Li, T. (2009). Revisiting the Johnson and Jackson Boundary Conditions for Granular Flows. *IFAC Proceedings Volumes*.

[113] Li, Y., McLaughlin, J. B., Kontomaris, K., and Portela, L. (2001). Numerical simulation of particle-laden turbulent channel flow. *Physics of Fluids*, 13(10):2957–2967.

[114] Lien, F.-S. and Kalitzin, G. (2001). Computations of transonic flow with the v2-f turbulence model. *International Journal of Heat and Fluid Flow*, 22(1):53–61.

[115] Liu, X. and Xu, X. (2009). Modelling of dense gas-particle flow in a circulating fluidized bed by distinct cluster method (dcm). *Powder Technology*, 195(3):235 – 244.

[116] Lonsdale, R, D. (1991). An algebraic multigrid scheme for solving the navier-stokes equations on unstructured meshes. In *Proc. 7th Int. Conf. on Numerical Methods in Turbulent and Laminar Flows.*

[117] Lun, C., Savage, S. B., Jeffrey, D., and Chepurniy, N. (1984). Kinetic theories for granular flow: inelastic particles in couette flow and slightly inelastic particles in a general flowfield. *Journal of fluid mechanics*, 140:223–256.

[118] Lun, C. K. K. (2000). Numerical simulation of dilute turbulent gas–solid flows. *International Journal of Multiphase Flow*, 26(10):1707–1736.

[119] Marchioli, C. and Soldati, A. (2002a). Mechanisms for particle transfer and segregation in a turbulent boundary layer. *Journal of Fluid Mechanics*, 468:283–315.

[120] Marchioli, C. and Soldati, A. (2002b). Mechanisms for particle transfer and segregation in a turbulent boundary layer. *Journal of Fluid Mechanics*, 468:283–315.

[121] Marchioli, C., Soldati, A., Kuerten, J., Arcen, B., Tanière, A., Goldensoph, G., Squires, K., Cargnelutti, M., and Portela, L. (2008). Statistics of particle dispersion in direct numerical simulations of wall-bounded turbulence: Results of an international collaborative benchmark test. *International Journal of Multiphase Flow*, 34(9):879 – 893.

[122] Marchisio, D. L. and Fox, R. O. (2013). *Computational Models for Polydisperse Particulate and Multiphase Systems*. Cambridge Series in Chemical Engineering. Cambridge University Press.

[123] Masters, K. (1972). *Spray Drying: an introduction to principles, operational practice and applications*. Leonard Hill Books, London.

[124] Mazhar, Z. (2001). A procedure for the treatment of the velocity-pressure coupling problem in incompressible fluid flow. *Numerical Heat Transfer: Part B: Fundamentals*, 39(1):91–100.

[125] Mazhar, Z. (2016). A novel fully implicit block coupled solution strategy for the ultimate treatment of the velocity–pressure coupling problem in incompressible fluid flow. *Numerical Heat Transfer, Part B: Fundamentals*, 69(2):130–149.

[126] Mito, Y. and Hanratty, T. J. (2006). Effect of feedback and inter-particle collisions in an idealized gas-liquid annular flow. *International Journal of Multiphase Flow*, 32(6):692 – 716.

[127] Mohanarangam, K. and Tu, J. Y. (2007). Two-fluid model for particle-turbulence interaction in a backward-facing step. *AIChE Journal*, 53(9):2254–2264.

[128] Mukin, R. V. and Zaichik, L. I. (2012). Nonlinear algebraic Reynolds stress model for two-phase turbulent flows laden with small heavy particles. *International Journal of Heat and Fluid Flow*, 33(1):81–91.

[129] Oesterle, B. and Petitjean, A. (1993). Simulation of particle-to-particle interactions in gas solid flows. *International Journal of Multiphase Flow*, 19(1):199 – 211.

[130] Ooi, A., Iaccarino, G., Durbin, P., and Behnia, M. (2002). Reynolds averaged simulation of flow and heat transfer in ribbed ducts. *International Journal of Heat and Fluid Flow*, 23(6):750 – 757.

[131] Ozel, A., Fede, P., and Simonin, O. (2013). Development of filtered euler-

euler two-phase model for circulating fluidised bed: High resolution simulation, formulation and a priori analyses. *International Journal of Multiphase Flow*, 55:43 – 63.

[132] Pan, Y. and Banerjee, S. (1996). Numerical simulation of particle interactions with wall turbulence. *Physics of Fluids*, 8(10):2733–2755.

[133] Papadikis, K., Bridgwater, A., and Gu, S. (2008). Cfd modelling of the fast pyrolysis of biomass in fluidised bed reactors, part a: Eulerian computation of momentum transport in bubbling fluidised beds. *Chemical Engineering Science*, 63(16):4218–4227.

[134] Park, I., Cho, H., Yoon, H., and Jeong, J. (2009). Numerical effects of the semi-conservative form of momentum equations for multi-dimensional two-phase flows. *Nuclear Engineering and Design*, 239(11):2365 – 2371.

[135] Passalacqua, A. and Fox, R. (2011). Implementation of an iterative solution procedure for multi-fluid gas-particle flow models on unstructured grids. *Powder Technology*, 213(1):174 – 187.

[136] Passalacqua, A., Fox, R., Garg, R., and Subramaniam, S. (2010a). A fully coupled quadrature-based moment method for dilute to moderately dilute fluid–particle flows. *Chemical Engineering Science*, 65(7):2267–2283.

[137] Passalacqua, A., Fox, R., Garg, R., and Subramaniam, S. (2010b). A fully coupled quadrature-based moment method for dilute to moderately dilute fluid-particle flows. *Chemical Engineering Science*, 65(7):2267 – 2283. International Symposium on Mathematics in Chemical Kinetics and Engineering.

[138] Patankar, S. V. and Spalding, D. B. (1983). A calculation procedure for heat, mass and momentum transfer in three-dimensional parabolic flows. In *Numerical Prediction of Flow, Heat Transfer, Turbulence and Combustion*, pages 54–73. Elsevier.

[139] Patel, V. C., Rodi, W., and Scheuerer, G. (1985). Turbulence models for near-wall and low Reynolds number flows - A review. *AIAA Journal*, 23(9):1308–1319.

[140] Pedinotti, S. and Mariotti, G. (1992). Direct numerical simulation of particle behaviour in the wall region of turbulent flows in horizontal channels. 18(6):927–941.

[141] Peirano, E. and Leckner, B. (1998). Fundamentals of turbulent gas-solid flows applied to circulating fluidized bed combustion. *Doktorsavhandlingar vid Chalmers Tekniska Hogskola*, 24(1381):259–296.

[142] Pope, S. B. (2011). *Turbulent flows*. Cambridge Univ. Press, Cambridge.

[143] Press, W. H., Teukolsky, S. A., Vetterling, W. T., and Flannery, B. P. (2007). *Numerical recipes 3rd edition: The art of scientific computing*. Cambridge university press.

[144] Radl, S. and Sundaresan, S. (2014). A drag model for filtered euler–lagrange simulations of clustered gas–particle suspensions. *Chemical engineering science*, 117:416–425.

[145] Rao, A., Curtis, J. S., Hancock, B. C., and Wassgren, C. (2008). Numerical simulation of dilute turbulent gas-particle flow with turbulence modulation. *AIChE Journal*, 58(5):1381–1396.

[146] Rashidi, M., Hetsroni, G., and Banerjee, S. (1990). Particle-turbulence interaction in a boundary layer. *International Journal of Multiphase Flow*, 16(6):935–949.

[147] Raw, M. (1995). *A Coupled Algebraic Multigrid Method for the 3D Navier-Stokes Equations*, pages 204–215. Vieweg+Teubner Verlag, Wiesbaden.

[148] Reade, W. C. and Collins, L. R. (2000). Effect of preferential concentration on turbulent collision rates. *Physics of Fluids*, 12(10):2530–2540.

[149] Reeks, M. (1983). The transport of discrete particles in inhomogeneous turbulence. *Journal of Aerosol Science*, 14(6):729 – 739.

[150] Reeks, M. W. (1977). On the dispersion of small particles suspended in an isotropic turbulent fluid. *Journal of Fluid Mechanics*, 83(3):529–546.

[151] Reinhardt, Y. and Kleiser, L. (2015). Validation of Particle-Laden Turbulent Flow Simulations Including Turbulence Modulation. *Journal of Fluids Engineering*, 137(7):71303.

[152] Rericha, E. C., Bizon, C., Shattuck, M. D., and Swinney, H. L. (2001). Shocks in supersonic sand. *Physical review letters*, 88(1):014302.

[153] Reveillon, J. and Demoulin, F.-X. (2007). Effects of the preferential segregation of droplets on evaporation and turbulent mixing. *Journal of Fluid Mechanics*, 583:273–302.

[154] Rhie, C. M. and Chow, W. L. (1983). A numerical study of the turbulent flow past an isolated airfoil with trailing edge separation. *AIAA J.*, pages 1525–1532.

[155] Richardson, L. (1922). *Weather prediction by numerical process*. Cambridge, University Press.

[156] Riella, M., Kahraman, R., and Tabor, G. (2018). Reynolds-averaged two-fluid model prediction of moderately dilute fluid-particle flow over a backward-facing step. *International Journal of Multiphase Flow*, 106:95 – 108.

[157] Riella, M., Kahraman, R., and Tabor, G. (2019). Inhomogeneity and anisotropy in eulerian-eulerian near-wall modelling. *International Journal of Multiphase Flow*, 114:9 – 18.

[158] Rizk, M. A. and Elghobashi, S. E. (1989). A two-equation turbulence model for dispersed dilute confined two-phase flows. *International Journal of Multiphase Flow*, 15(1):119–133.

[159] Rodi, W. and Mansour, N. N. (1993). Low Reynolds number k-epsilon modelling with the aid of direct simulation data. *Journal of Fluid Mechanics*, 250:509–529.

[160] Rotta, J. (1951). Statistische theorie nichthomogener turbulenz. *Zeitschrift für Physik*, 129(6):547–572.

[161] Rouson, D. W. I. and Eaton, J. K. (2001). On the preferential concentration

of solid particles in turbulent channel flow. *Journal of Fluid Mechanics*, 428:149–169.

[162] Ruge, J. W. and Stüben, K. (1987). Algebraic multigrid. In *Multigrid methods*, pages 73–130. SIAM.

[163] Rumsey, C. L. (2010). Compressibility considerations for kw turbulence models in hypersonic boundary-layer applications. *Journal of Spacecraft and Rockets*, 47(1):11–20.

[164] Rusche, H. (2002). *Computational Fluid Dynamics of Dispersed Two-Phase Flows at High Phase Fractions*. PhD thesis, Imperial College London.

[165] Saad, Y. (2003). *Iterative methods for sparse linear systems*, volume 82. siam.

[166] Saber, A., Lundström, T., and Hellström, J. (2016). Influence of inertial particles on turbulence characteristics in outer and near wall flow as revealed with high resolution particle image velocimetry. *Journal of Fluids Engineering, Transactions of the ASME*, 138(9):1–12.

[167] Schiller, L. and Naumann, Z. (1933). Uber die grundlegenden berechnungenbei der schwerkraftaufbereitung. *Ver. Deut. Ing.*, 77:318âĂŞ320.

[168] Schlichting, H., Gersten, K., Krause, E., Oertel, H., and Mayes, K. (1955). *Boundary-layer theory*. Springer.

[169] Schneiderbauer, S. (2017). A spatially-averaged two-fluid model for dense large-scale gas-solid flows. *AIChE Journal*, 63(8):3544–3562.

[170] Schwarzkopf, J. D., Sommerfeld, M., Crowe, C. T., and Tsuji, Y. (2011). *Multiphase flows with droplets and particles*. CRC press.

[171] Shah, M. T., Utikar, R. P., Pareek, V. K., Tade, M. O., and Evans, G. M. (2015). Effect of closure models on eulerian-eulerian gas-solid flow predictions in riser. *Powder Technology*, 269:247 – 258.

[172] Shih, T. H. and Hsu, A. T. (1991). An improved k-epsilon model for near

wall turbulence. *Center for Modeling of Turbulence and Transition (CMOTT). Research Briefs: 1990*, 1:87–104.

[173] Simonin, O. (1991). Second-moment prediction of dispersed phase turbulence in particle-laden flows. *Proceedings of 8th International Symposium on Turbulent Shear Flows*, 1(4):741–746.

[174] Simonin, O. (1996). Continuum modeling of dispersed turbulent two-phase flows. Part 1: General model description. *Combustion and Turbulence in Two-phase Flows*.

[175] Simonin, O., Deutsch, E., and Minier, J. (1993). Eulerian prediction of the fluid/particle correlated motion in turbulent two-phase flows. *Applied Scientific Research*, 51(1-2):275–283.

[176] Sinclair, J. and Mallo, T. (1998). Describing particle-turbulence interaction in a two-fluid modeling framework. *Proceedings of FEDSM'98: ASME Fluids Engineering Division Summer Meeting*, 4:7–14.

[177] Soldati, A. and Marchioli, C. (2009). Physics and modelling of turbulent particle deposition and entrainment: Review of a systematic study. *International Journal of Multiphase Flow*, 35(9):827–839.

[178] Sommerfeld, M. (2000). Theoretical and experimental modeling of particulate flow: overview and fundamentals. *VKI for Fluid dynamics*, pages 2000–06.

[179] Soo, S. L. (1990). *Multiphase Fluid Dynamics*. Science Press, Gower Technical, New York.

[180] Strömgren, T., Brethouwer, G., Amberg, G., and Johansson, A. V. (2012). Modelling of turbulent gas-particle flows with focus on two-way coupling effects on turbophoresis. *Powder Technology*, 224:36–45.

[181] Sundaram, S. and Collins, L. R. (1997). Collision statistics in an isotropic particle-laden turbulent suspension. part 1. direct numerical simulations. *Journal of Fluid Mechanics*, 335(1):75–109.

[182] Sveningsson, A. (2003). Analysis of the Performance of Different v2f Turbulence Models in a Stator Vane Passage Flow. *PhD Thesis*.

[183] Syamlal, M. and Gidaspow, D. (1985). Hydrodynamics of fluidization: Prediction of wall to bed heat transfer coefficients. *AIChE Journal*, 31(1):127–135.

[184] Syamlal, M. and O'Brien, T. J. (1989). Computer simulation of bubbles in a fluidized bed. *AIChE Symposium Series*, 85(270):22–31.

[185] Tanaka, T. and Tsuji, M. (1991). Numerical simulation of gas-solid two-phase flow in a vertical pipe: On the effect of inter-particle collision. *ASME/FED Gas-Solid Flows*, 121:123–128.

[186] Tanaka, T., Yonemura, S., Kiribayashi, K., and Tsuji, Y. (1996). Cluster formation and particle-induced instability in gas-solid flows predicted by the dsmc method. *JSME International Journal Series B*, 39(2):239–245.

[187] Tang, L., Wen, F., Yang, Y., Crowe, C. T., Chung, J. N., and Troutt, T. R. (1992). Self-organizing particle dispersion mechanisms in a plane wake. *Phys.\ Fluids*, A4(1992):2244–2251.

[188] Ten Cate, A., Derksen, J. J., Portela, L. M., and Van Den Akker, H. E. (2004). Fully resolved simulations of colliding monodisperse spheres in forced isotropic turbulence. *Journal of Fluid Mechanics*, 519:233–271.

[189] Tenneti, S., Garg, R., Hrenya, C., Fox, R., and Subramaniam, S. (2010). Direct numerical simulation of gas-solid suspensions at moderate reynolds number: Quantifying the coupling between hydrodynamic forces and particle velocity fluctuations. *Powder Technology*, 203(1):57 – 69. Selected Papers from the 2009 NETL Multiphase Flow Workshop.

[190] Thomas, N. H. and Hancock, P. E. (1977). Grid turbulence near a moving wall. *Journal of Fluid Mechanics*, 82(3):481–496.

[191] Truesdell, G. C. and Elghobashi, S. (1994). On the two-way interaction

between homogeneous turbulence and dispersed solid particles. II. Particle dispersion. *Physics of Fluids*, 6(3):1405–1407.

[192] Tsuji, Y. and Morikawa, Y. (1984). LDV measurements of an air-solid two-phase flow in a vertical pipe. *Journal of Fluid Mechanics*, 120:385–409.

[193] Uroić, T. and Jasak, H. (2018). Block-selective algebraic multigrid for implicitly coupled pressure-velocity system. *Computers & fluids*, 167(1):100–110.

[194] Van den Akker, H. E. (2010). Toward a truly multiscale computational strategy for simulating turbulent two-phase flow processes. *Industrial & Engineering Chemistry Research*, 49(21):10780–10797.

[195] van der Hoef, M. A., van Sint Annaland, M., Deen, N., and Kuipers, J. (2008). Numerical simulation of dense gas-solid fluidized beds: a multiscale modeling strategy. *Annu. Rev. Fluid Mech.*, 40:47–70.

[196] Van der Vorst, H. A. (1992). Bi-cgstab: A fast and smoothly converging variant of bi-cg for the solution of nonsymmetric linear systems. *SIAM Journal on scientific and Statistical Computing*, 13(2):631–644.

[197] Van Wachem, B., Schouten, J., Krishna, R., and Van den Bleek, C. (1998). Eulerian simulations of bubbling behaviour in gas-solid fluidised beds. *Computers & chemical engineering*, 22:S299–S306.

[198] Van Wachem, B. G. M., Schouten, J. C., Van den Bleek, C. M., Krishna, R., and Sinclair, J. L. (2001). Comparative analysis of CFD models of dense gas-solid systems. *AIChE Journal*, 47(5):1035–1051.

[199] Vance, M. W., Squires, K. D., and Simonin, O. (2006). Properties of the particle velocity field in gas-solid turbulent channel flow. *Physics of Fluids*, 18(6):063302.

[200] Vanka, S. (1986). Block-implicit multigrid solution of navier-stokes equations in primitive variables. *Journal of Computational Physics*, 65(1):138 – 158.

[201] Viollet, P. L. and Simonin, O. (1994). Modelling dispersed two-phase flows: Closure, validation and software development. *Appl. Mech. Rev.*, 47:s80–s84.

[202] Vreman, A. W. (2007). Turbulence characteristics of particle-laden pipe flow. *Journal of Fluid Mechanics*, 584:235–279.

[203] Vreman, A. W. (2015). Turbulence attenuation in particle-laden flow in smooth and rough channels. *Journal of Fluid Mechanics*, 773:103–136.

[204] Vreman, B., Geurts, B. J., Deen, N. G., Kuipers, J. A. M., and Kuerten, J. G. M. (2009). Two- and four-way coupled euler–lagrangian large-eddy simulation of turbulent particle-laden channel flow. *Flow, Turbulence and Combustion*, 82(1):47–71.

[205] Wang, L.-P., Wexler, A. S., and Zhou, Y. (1998). On the collision rate of small particles in isotropic turbulence. i. zero-inertia case. *Physics of Fluids*, 10(1):266–276.

[206] Wang, L.-P., Wexler, A. S., and Zhou, Y. (2000). Statistical mechanical description and modelling of turbulent collision of inertial particles. *Journal of Fluid Mechanics*, 415:117–153.

[207] Wang, Q. and Squires, K. D. (1996). Large eddy simulation of particle-laden turbulent channel flow. *Physics of Fluids*, 8(5):1207–1223.

[208] Webster, R. An algebraic multigrid solver for navier-stokes problems. *International Journal for Numerical Methods in Fluids*, 18(8):761–780.

[209] Webster, R. (1996). An algebraic multigrid solver for navier-stokes problems in discrete second-order approximation. *International Journal for Numerical Methods in Fluids*, 22(11):1103–1123.

[210] Weller, H. (2002). Derivation, modelling and solution of the conditionally averaged two-phase flow equations. *Tech.Rep.OpenCFD Ltd.*

[211] Wen, C.-Y. and Yu, Y. (1966). Mechanics of fluidization. *Chemical Engineering Progress Symposium Series*, 62.

[212] Wilcox, D. (2004). *Turbulence Modeling for CFD*. DCW Industries.

[213] Wildman, R., Martin, T., Huntley, J., Jenkins, J., Viswanathan, H., Fen, X., and Parker, D. (2008). Experimental investigation and kinetic-theory-based model of a rapid granular shear flow. *Journal of Fluid Mechanics*, 602:63–79.

[214] Wu, Y., Wang, H., Liu, Z., Li, J., Zhang, L., and Zheng, C. (2006). Experimental investigation on turbulence modification in a horizontal channel flow at relatively low mass loading. *Acta Mechanica Sinica*, 22(2):99–108.

[215] Xiao, C.-N., Denner, F., and van Wachem, B. G. (2017). Fully-coupled pressure-based finite-volume framework for the simulation of fluid flows at all speeds in complex geometries. *Journal of Computational Physics*, 346:91–130.

[216] Xu, Y. and Subramaniam, S. (2007). Consistent modeling of interphase turbulent kinetic energy transfer in particle-laden turbulent flows. *Physics of Fluids*, 19(8):085101.

[217] Yamamoto, Y., Potthoff, M., Tanaka, T., Kajishima, T., and Tsuji, Y. (2001). Large-eddy simulation of turbulent gas-particle flow in a vertical channel: effect of considering inter-particle collisions. *Journal of Fluid Mechanics*, 442:303–334.

[218] Yang, N., Wang, W., Ge, W., Wang, L., and Li, J. (2004). Simulation of heterogeneous structure in a circulating fluidized-bed riser by combining the two-fluid model with the emms approach. *Industrial & Engineering Chemistry Research*, 43(18):5548–5561.

[219] Yin, X. and Sundaresan, S. (2009). Fluid-particle drag in low-reynolds-number polydisperse gas–solid suspensions. *AIChE journal*, 55(6):1352–1368.

[220] Young, J. and Leeming, A. (1997). A theory of particle deposition in turbulent pipe flow. *Journal of Fluid Mechanics*, 340:129–159.

[221] Yu, K., Lau, K., and Chan, C. (2004). Numerical simulation of gas-particle flow in a single-side backward-facing step flow. *Journal of Computational and*

Applied Mathematics, 163(1):319 – 331. Proceedings of the International Symposium on Computational Mathematics and Applications.

[222] Zalesak, S. T. (1979). Fully multidimensional flux-corrected transport algorithms for fluids. *Journal of Computational Physics*, 31(3):335–362.

[223] Zhang, D. and Prosperetti, A. (1994). Averaged equations for inviscid disperse two-phase flow. *Journal of Fluid Mechanics*, 267:185–219.

[224] Zhang, D. and Prosperetti, A. (1997). Momentum and energy equations for disperse two-phase flows and their closure for dilute suspensions. *International Journal of Multiphase Flow*, 23(3):425–453.

[225] Zhang, Y. and Reese, J. M. (2003). The drag force in two-fluid models of gas-solid flows. *Chemical Engineering Science*, 58(8):1641–1644.

[226] Zheng, Y., Wan, X., Qian, Z., Wei, F., and Jin, Y. (2001). Numerical simulation of the gas-particle turbulent flow in riser reactor based on k-ϵ-kp-ϵp-θ two-fluid model. *Chemical Engineering Science*, 56(24):6813–6822.

[227] Zhou, X., Gao, J., Xu, C., and Lan, X. (2013). Effect of wall boundary condition on CFD simulation of CFB risers. *Particuology*, 11(5):556 – 565.

[228] Zuber, N. and Findlay, J. (1965). Average volumetric concentration in two-phase flow systems. *Journal of heat transfer*, 87(4):453–468.